Advanced Electrolyte Design for Long-Life and High-Areal-Capacity Divalent Metal Batteries

by

Chang Li

A thesis
presented to the University of Waterloo
in fulfillment of the
thesis requirement for the degree of
Doctor of Philosophy
in
Chemistry

Waterloo, Ontario, Canada, 2024

Examining Committee Membership

The following served on the Examining Committee for this thesis. The decision of the Examining Committee is by majority vote.

External Examiner	Bruce Dunn Professor Dept. of Materials Science and Engineering, University of California, Los Angeles
Supervisor	Linda F. Nazar Professor Dept. of Chemistry, University of Waterloo
Internal Member	Holger Kleinke Professor Dept. of Chemistry, University of Waterloo
Internal-external Member	Michael Pope Associate Professor Dept. of Chemical Engineering, University of Waterloo
Other Members	Vivek Maheshwari Associate Professor Dept. of Chemistry, University of Waterloo
	Rodney Smith Associate Professor Dept. of Chemistry, University of Waterloo

Author's Declaration

I hereby declare that I am the sole author of this thesis. This is a true copy of the thesis, including any required final revisions, as accepted by my examiners.

I understand that my thesis may be made electronically available to the public.

Abstract

Net-zero carbon dioxide emission demands clean renewable energy, while harnessing it requires electrochemical storage devices with high energy density, safety and affordability. To achieve decarbonization, much effort is being devoted to new battery technologies beyond lithium-ion batteries (LIBs), which suffer from limited lithium resources and low safety. Rechargeable batteries based on divalent metal anodes (Zn, Mg and Ca) are promising systems due to their high abundance, high volumetric capacity and potentially high safety. Zn anode has a high standard redox potential (-0.76 V vs. standard hydrogen electrode (SHE)), resulting in its relatively good compatibility with aqueous electrolytes. Such inherent safety and potential low-cost make aqueous Zn metal batteries (AZMBs) desirable candidates for small and large-scale stationary grid storage. Mg or Ca anode, on the other hand, has a much lower standard redox potential (-2.37 V or -2.87 V vs. SHE, respectively) that is even comparable to lithium (-3.04 V vs. SHE). Therefore, high-voltage rechargeable Mg or Ca metal batteries (MMBs or CMBs) are potential alternatives to LIBs in a variety of areas ranging from portable electronic devices to electrical vehicles. However, the study of these divalent metal batteries is still at the early stages. Among many unaddressed challenges for practical divalent metal batteries, designing better electrolytes is one key to their successful commercialization. This thesis presents a comprehensive investigation on designing new electrolytes for both AZMBs (chapters 3, 4 and 5) and MMBs (chapters 6 and 7), by tuning the solvation structure of Zn^{2+} or Mg^{2+} ions and their interaction with solvents or anions. A series of electrolytes with precisely controlled interfacial electrolyte/electrode chemistry are developed to achieve rechargeable AZMBs and MMBs under practical conditions.

Chapter 3 reports a novel additive - N,N-dimethylformamidium trifluoromethanesulfonate (DOTf) - in a low-cost aqueous electrolyte that enable near 100% coulombic efficiency of Zn plating/striping at a combined high current density of 4 mA cm^{-2} and areal capacity of 4 mAh cm^{-2} over long-term cycling. The water-assisted dissociation of DOTf into triflic superacid creates a robust nanostructured SEI - as revealed by operando spectroscopy and cryo-microscopy - which excludes water and enables dense Zn deposition.

Zn||$Zn_{0.25}V_2O_5 \cdot nH_2O$ (ZVO) full cells based on this modified electrolyte retain ~83% of their capacity after 1000 cycles with mass-limited Zn anodes. By restricting the depth of discharge, the cathodes exhibit less proton intercalation and LDH formation with an extended lifetime of 2000 cycles.

Chapter 4 presents the electrochemical degradation mechanism of $LiV_2(PO_4)_3$ (LVP) as a host cathode in AZMBs. Phase conversion of LVP induced by H^+ intercalation is observed in 4 m $Zn(OTf)_2$ whereas dominant Zn^{2+} insertion is confirmed in $ZnCl_2$ water-in-salt electrolyte (WiSE). This disparity is ascribed to the complete absence of free water and the strong Zn^{2+}-H_2O interaction in the latter that interrupts the H_2O hydrogen bonding network, thus suppressing H^+ intercalation. Based on this strategy, a novel PEG-based hybrid electrolyte is designed to replace the corrosive $ZnCl_2$ WiSE. This system exhibits an optimized Zn^{2+} solvation sheath with a similar low free water content, showing not only much better suppression of H^+ intercalation but also highly reversible Zn plating/stripping with a CE of ~99.7% over 150 cycles.

Chapter 5 reveals the competition between Zn^{2+} *vs* proton intercalation chemistry of typical ZVO cathode using *ex-situ/operando* techniques, and alleviate side reactions by developing a cost-effective and non-flammable hybrid eutectic electrolyte. A fully hydrated Zn^{2+} solvation structure facilitates fast charge transfer at the solid/electrolyte interface, enabling dendrite-free Zn plating/stripping with a remarkably high average coulombic efficiency of 99.8% at commercially relevant areal capacities of 4 mAh cm^{-2} and function up to 1600 hours at 8 mAh cm^{-2}. By concurrently stabilizing Zn redox at both electrodes, we achieve a new benchmark in Zn-ion battery performance of 4 mAh cm^{-2} anode-free cells that retain 85% capacity over 100 cycles at 25 °C. Using this eutectic-design electrolyte, Zn||Iodine full cells are further realized with 86% capacity retention over 2500 cycles. The approach represents a new avenue for long-duration energy storage.

Chapter 6 reports a low-cost inorganic membrane that forms an effective protection film on the Mg surface to stabilize Mg plating/stripping. It significantly reduces the population (and hence decomposition) of free diglyme (G2) molecules at the Mg/interface, while allowing facile transport of Mg^{2+} cations, leading to dendrite-free Mg deposition in a magnesium

tetrakis(hexafluoroisopropyloxy)borate/G2 electrolyte. We demonstrate very stable Mg plating/stripping performance with a 750-fold extended lifetime (over 6000 hours) with a high coulombic efficiency of ~98%. The prototype Mo_3S_4 cathode paired with inorganic membrane-protected Mg anode shows 91% capacity retention over 200 cycles. More importantly, this membrane also protects soluble species in a high-voltage organic polymer cathode from being reduced at the anode via shuttling, achieving a full cell with a 3.5 V cutoff voltage and 1.4 V average discharge voltage. This results a high specific energy density of 320 Wh kg^{-1} and power density of 1320 W kg^{-1} based on cathode mass.

Chapter 7 report a new and easily accessible co-ethereal phosphate electrolyte system for high-voltage rechargeable MMBs, which very effectively solves the difficulty of ion pair dissociation and facilitates fast nanoscale Mg nucleation/growth for the first time, enabling facile interfacial charge transfer at current densities up to 10 mA cm^{-2}. Dendrite-free Mg plating/stripping is achieved for over 6000 hours (8.3 months) at a practical areal capacity of 2 mAh cm^{-2}. The four-volt oxidative stability of these electrolytes - in conjunction with a polyaniline cathode with an upper potential of 3.5 V and a Mg metal anode - enables cells with stable cycling at a 2C rate for over 400 cycles at 25 °C. We believe our work opens up new frontiers in developing low-cost and fast-charging MMBs with long life and high energy densities.

Acknowledgements

I would like to express my greatest gratitude to my supervisor Dr. Linda F. Nazar for her guidance and support during my doctoral study. Her intelligent ideas and scientific thinking have encouraged my research, and I have gained great experience on critical and independent thinking and planning in the past few years. I would like to thank my Ph. D. committee members Dr. Holger Kleinke, Dr. Vivek Maheshwari and Dr. Rodney Smith for their time and suggestions about my research. I would also like to thank Dr. Michael Pope and Dr. Bruce Dunn for being my internal-external member and external examiner, respectively, and their time to participate in my thesis defense.

I would like to thank all the Research collaborators for their help and the great collaboration. Dr. Ryan Kingsbury and Dr. Rishabh D. Guha from Dr. Kristin A. Persson group (Lawrence Berkeley National Laboratory) carried out theoretical calculation and modeling of electrolytes. Dr. Ryan Kingsbury performed modeling for aqueous Zn electrolytes (Chapter 4 and 5), and Dr Rishabh D. Guha performed modeling for Mg electrolytes (Chapter 7). I also appreciate the useful discussions with them. The HRTEM and EELS experiments as well as the data analysis of Zn anode surface (Chapter 3) were done by Dr. Daniel M. Long and Dr. Paul G. Kotula from Dr. Kevin R. Zavadil group (Sandia National Laboratories). The ATR-SEIRAS was carried and analyzed by Alexis Grace Hoane from Dr. Andrew A. Gewirth group (University of Illinois at Urbana-Champaign). The HRTEM and EELS experiments as well as the data analysis of ZVO (Chapter 5) were done by Dr. Arashdeep Singh Thind from Dr. Robert F. Klie group (University of Illinois - Chicago). The XAS measurements (Chapter 5) were performed by Dr. Timothy T. Fister (Argonne National Laboratory).

I would also like to extend my appreciation to Dr. Laidong Zhou and Abhinandan Shyamsunder, who helped me with the synthesis and characterization techniques when I first joined the Nazar group. The discussion with them always inspired me with new thoughts towards my experiments. Dr Laidong Zhou provides many useful suggestions during the design of experiments when a new project started. Abhinandan Shyamsunder conduced all

NMR experiments and analysis to understand the electrolyte network. Also many thanks to the rest of the group for their help and accompanying the lab.

I would like to thank my parents who raised me up and taught me as best as they can. I would like to thank my brother and his family for looking after our parents for all these years. Finally, I would also like to thank my wife, Fangzhou Yin, for her selfless support and choosing me as her husband, as well as my child about to be born for choosing me as his dad. You are the best part of this journey and I love you all!

Table of Contents

List of Figures

List of Tables

List of Abbreviations

AC	Activated Carbon
AZMBs	Aqueous Zinc Metal Batteries
CEPE	Co-Ethereal Phosphate Electrolyte
DOTf	N,N-Dimethylformamidium Trifluoromethanesulfonate
EDX	Energy Dispersive X-ray Spectroscopy
EELS	Electron Energy Loss Spectroscopy
EIS	Electrochemical Impedance Spectroscopy
EXAFS	Extended X-ray absorption fine structure
FTIR	Fourier Transform Infrared Spectroscopy
GITT	Galvanostatic Intermittent Titration Technique
HAADF	High-Angle Annular Dark-Field
HER	Hydrogen Evolution Reaction
LDHs	Layered Double Hydroxides
LIBs	Lithium-Ion Batteries
LSV	Linear sweep voltammetry
MMBs	Magnesium Metal Batteries
OER	Oxygen Evolution Reaction
SEI	Solid-Electrolyte-Interphase
SEM	Scanning Electron Microscopy
SEIRAS	Surface-Enhanced Infrared Absorption Spectroscopy
STEM	Scanning Transmission Electron Microscopy
TEM	Transmission Electron Microscopy
TGA	Thermogravimetric analysis
WiSE	Water-in-Salt Electrolyte
XRD	X-Ray Diffraction
XANES	X-ray Absorption Near Edge Structure
XAS	X-ray Absorption Spectroscopy

Chapter 1 Introduction

1.1 Electrochemical Energy Storage

The energy consumption caused by the ever-increasing population, economic development by human society has caused serious energy crises and environmental issues.[1] To alleviate the current tense situation, renewable and environmentally-friendly energies such as solar energy and wind energy gradually became the most promising energy resources in the past decades. However, these resources are intermittent and dispersed, thus are difficult to directly support population and industry consumption on a large scale.[2]

As an effective carrier of energy, electrochemical energy storage systems like rechargeable batteries are emerging to realize energy transfer from energy-producing industries to energy-assuming devices. Among all rechargeable batteries, lithium-ion batteries (LIBs) undoubtedly play a dominant role in a variety of areas ranging from portable electronic devices to electrical vehicles, due to their high-energy density, high energy efficiency, and excellent cyclic stability. However, conventional commercialized LIBs are not a promising candidate for large-scale energy storage, where low operational cost, high safety, and environmental benignity are highly anticipated.[3, 4] The major concerns also arise from the safety aspects of traditional LIBs that possibly incurred by lithium dendrite growths caused by organic electrolytes and the high cost resulted from limited lithium resources. Alternatively, "beyond Li-ion" battery technologies can provide new opportunities to address these concerns.

1.2 Lithium-ion batteries

A conventional LIB usually has three major components: positive electrode, negative electrode and electrolyte to separate these two electrodes. A typical commercial battery system can be represented by a lithium metal oxide cathode and a graphite anode, both of which rely on reversible Li^+-ion insertion/extraction mechanism. Take $LiCoO_2$ as a representative cathode (**Figure 1.1**),[5] during the charge process, an external power supply is needed to create an electric force field between two electrodes, where electrons flow from $LiCoO_2$ cathode to graphite anode. Such a loss of electrons in $LiCoO_2$ induces the oxidation of cobalt – the only

elements that can change oxidation states in the cathode – from Co^{3+} to Co^{4+}, where the Li^+ ions are extracted from the structure into electrolyte to balance the charge (**Equation 1.1**). In meantime, Li^+ ions from the electrolyte intercalate into graphite anode to compensate the

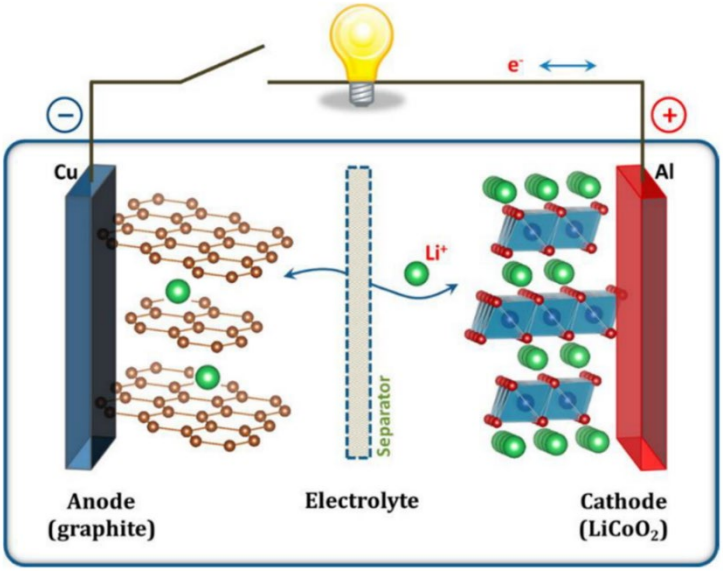

Figure 1.1. Schematic illustration of a conventional lithium-ion battery consists of a graphite anode, layered $LiCoO_2$ cathode, and a porous separator immersed in a liquid electrolyte, respectively. The electrolyte contains lithium salts dissolved in organic solvents. Adapted from Ref. 5. Copyright @ 2013 American Chemical Society.

obtained the electrons (**Equation 1.2**). At the end of charge, $LiCoO_2$ is at a higher chemical potential compared to that of graphite anode, leading to the spontaneous reaction of the reverse process named as the discharge process (**Equation 1.3** and **1.4**). During the whole process, electrons only travel through the external supplies or powers, while Li^+ ion only migrates in the electrolytes. Theoretically, electrolyte as a migration substance for Li^+ ion transport, do not participate in the any reaction processes during charge/discharge. However, due to the electrochemical/chemical instability of electrolyte components on electrode surface – including both salts and solvents, the chemical/physical properties of electrolytes have great impacts on battery performance, which will be discussed in detail in this thesis.

During charging:

Positive electrode (Cathode): $LiCoO_2 - x\ Li^+ - x\ e^- \rightarrow Li_{1-x}CoO_2$ **Equation 1.1**

Negative electrode (Anode): $C_6 + x\ Li^+ + x\ e^- \rightarrow Li_xC_6$ **Equation 1.2**

During Discharging:

Positive electrode (Cathode): $Li_{1-x}CoO_2 + x\ Li^+ + x\ e^- \rightarrow LiCoO_2$ **Equation 1.3**

Negative electrode (Anode): $Li_xC_6 - x\ Li^+ - x\ e^- \rightarrow C_6$ **Equation 1.4**

In this cell, the layered structure of $LiCoO_2$ can be maintained when $x < 0.5$, meaning only half of Li^+ can be extracted during the charge process, resulting in a theoretical specific capacity of 137 mAh g^{-1}. This is because deeper charging will lead to the structural degradation of $LiCoO_2$. This low specific capacity of $LiCoO_2$ and high toxicity/costs of cobalt, results in wide academic interests in developing alternative cathode candidates. Among all alternatives, one of most promising cathodes is $LiNi_{1-x-y}Mn_xCo_yO_2$ (NMC) family.[6] This material is synthesized by substituting Co with Ni and Mn, while maintaining the original layered structure of $LiCoO_2$. The highest capacity of this cathode class is around 200 mAh g^{-1}, which is achieved by a NMC cathode with high nickel contents (for example, $LiNi_{0.8}Mn_{0.1}Co_{0.1}O_2$). The major redox couples during charge/discharge are $Ni^{2+/4+}$ and $Co^{3+/4+}$, while Mn remains on its 4^+ oxidation state to stabilize the layered structure during electrochemical process.

As an alternative to graphite anode, lithium metal anode has been widely studied during the last decade. In fact, the early use of metallic Li as the anode in LIBs dates to 1970s by

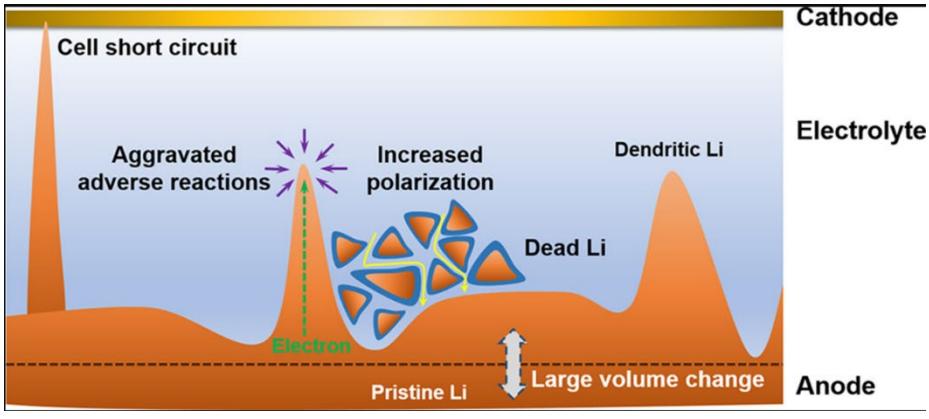

Figure 1.2. Scheme of issues of Li metal anode. Adapted from Ref. 8. Copyright @ 2013 American Chemical Society.

Stanely Whittingham at Exxon.[7] However, due to the frequent fire accidents caused by Li

dendrite formation, the academic investigation and commercialization of the Li metal anode was halted. Until in recent years, LIBs based on graphite anode approach the limit of their theoretical capacities, which leads to the reviving of the Li metal anode that has one magnitude higher capacity (3860 mAh g^{-1}) than that of graphite.[8] It also has the lowest standard electrode potential (-3.04 V versus standard hydrogen electrode (SHE)), which in principle provides the highest output voltage of full cells and thus highest energy density. However, Li dendrite can be formed during Li plating/stripping that gives rise to several fatal obstacles shown in **Figure 1.2**, including the cell short circuit indued by penetration of the Li dendrite through the separator, aggravated adverse reactions between the Li metal and electrolyte at the interface, evolution of dead Li from dendrites that causes low coulombic efficiency of Li plating/stripping, increased polarization due to non-homogeneous and porous dendritic morphology and the consequent large volume change.[8] The wide use of non-aqueous flammable electrolyte also increases the public concerns of fire accident once the cell shorts. Although intense academic efforts have been devoted to suppressing Li dendrite formation, the commercialization of LIBs based on the Li metal anode is still of in uncertainty.

"Beyond Li-ion" battery technologies are promising to achieve high energy density, high safety and low cost for electric mobility and grid storage.[9] These technologies include metal-sulfur batteries, metal-O_2/air batteries, sodium ion batteries, all-solid-state Li/Na batteries and multivalent metal batteries. Among these, divalent metal batteries (Zn, Mg and Ca) show great potential due to their high abundance, high volumetric capacity and potentially high safety. Their history, current status and challenges for commercialization will be discussed in detail in the following section.

1.3 Divalent Metal batteries

The limited availability and dendrite growth of the lithium metal anode hinder its application in commercial LIBs as an energy storage solution for grid applications and as major power sources for transportation. However, this does not prevent the concept of using the pure metal anode from being the holy grail for achieving batteries with high energy density and low cost. Among various alternatives to the lithium metal anode, divalent metal anodes – Zn, Mg

and Ca – have attracted wide academic interest, due to their high abundance and high volumetric capacity (**Figure 1.3**).[3] Compared to very limited studies for Ca-based batteries, considerable efforts have been devoted to realizing high-performance AZMBs and MMBs that will be discussed in detail in this thesis.

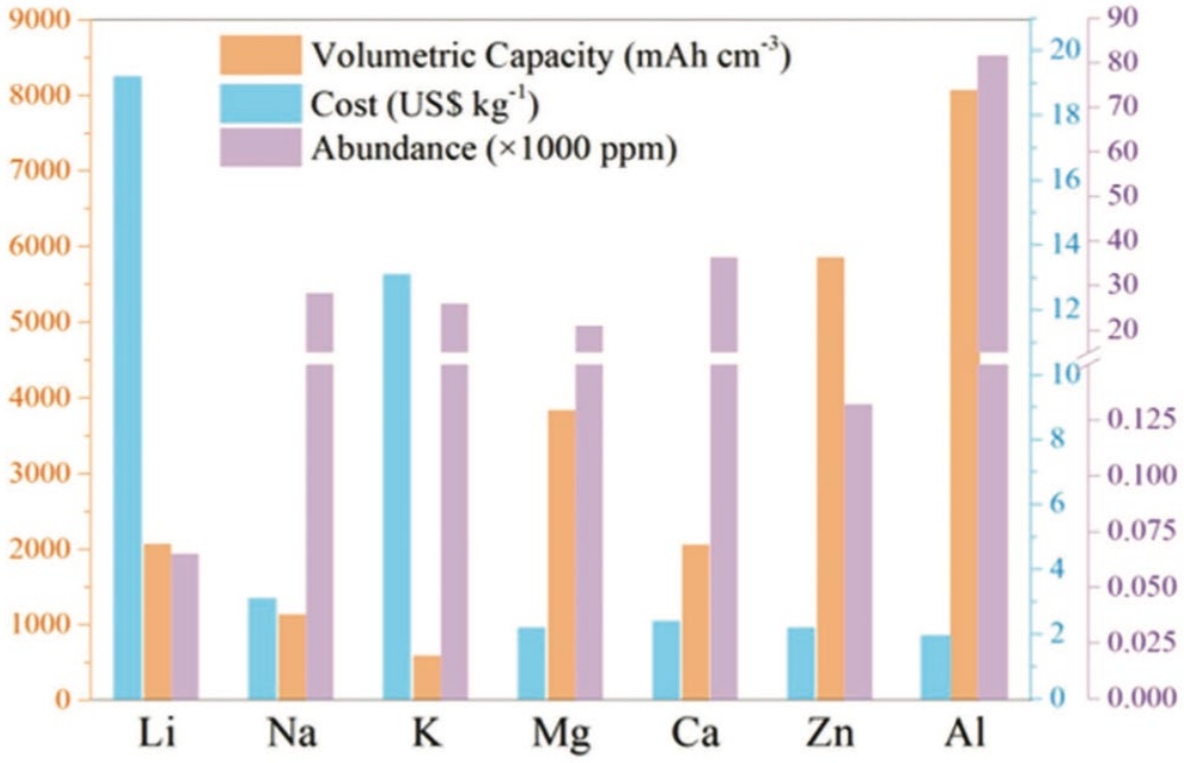

Figure 1.3. Comparison of volumetric capacity, cost and abundance parameters of candidate metal anodes for aqueous rechargeable batteries. Adapted from Ref. 3. Copyright © 2018 John Wiley & Sons, Inc.

1.3.1 Aqueous Zn Metal Batteries

Zinc-based batteries have recently attracted wide attention owing to the high theoretical volumetric capacity of the Zn anode (5,850 mAh mL^{-1}), its high compatibility in aqueous electrolyte due to its high electrodeposition potential (~-0.76V *vs.* SHE), and the advantages of low-cost, high-safety, and eco-friendly operation, resulting in their higher sustainability and affordability compared to their conventional lithium-ion analogues.[2] A search with the

keyword “zinc batteries” reveals that since 2018, more than 30,700 academic articles have been published on the subject.[10] Among these publications, approximately 60% involve aqueous electrolyte Zn batteries, as their inherent safety and potential low-cost make these batteries desirable candidates for small and large-scale stationary grid storage.

1.3.1.1 Cathode Materials for Aqueous Zn Metal Batteries

The first aqueous zinc-ion battery was reported by Shoji *et al*. in 1988, who applied a mild zinc sulfate aqueous electrolyte, MnO_2 as the cathode and the metallic Zn as the anode.[11] This discovery brought the boom of research for AZMBs. Typically, the electrochemical process of AZMBs can be illustrated by **Figure 1.4**, with zinc stripping/plating at a Zn anode and zinc-ion intercalation at a cathode.[2]

Although Zn can exhibit high capacities as anodes, their application is hindered by slow Zn^{2+} diffusion in the host materials (cathodes) resulting from a much higher polarizing character, because of the high charge to radius ratio of Zn^{2+} (2 charges to 0.74Å) compared to

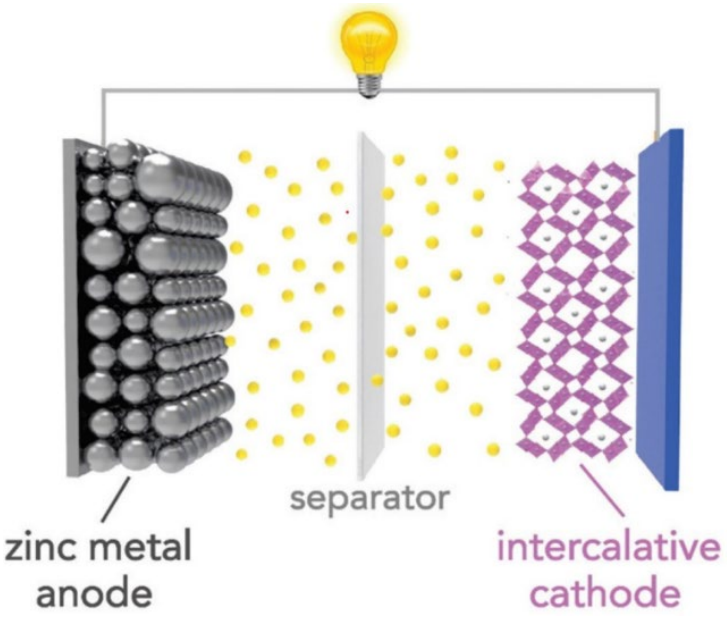

Figure 1.4 Scheme of the configuration of aqueous Zn metal battery with zinc anode and zinc-ion intercalation at cathode. Adapted from Ref. 2. Copyright © 2019 Royal Society of Chemistry.

Li^+ (1 charge to 0.76Å).[4] Thus, the exploration of new cathode materials with high ion diffusion

and good structure stability is appropriate. At present, various types of cathode materials are reported, including manganese-based compounds, vanadium-based compounds, Prussian blue analogs, and organic compounds, *etc.* In general, these cathode materials can be divided into intercalative-type and conversion-type cathodes that will be discussed below.

Most reported vanadium-based compounds belong to intercalative-type cathodes, and have been explored as electrode materials for LIBs for many years due to their abundance and multivalence. In AZMBs, these vanadium-based cathodes can deliver a high discharge capacity of over 400 mAh g^{-1} (e. g., $V_3O_7{\cdot}H_2O$[12]). In addition, V_2O_5 with a theoretical capacity of 589

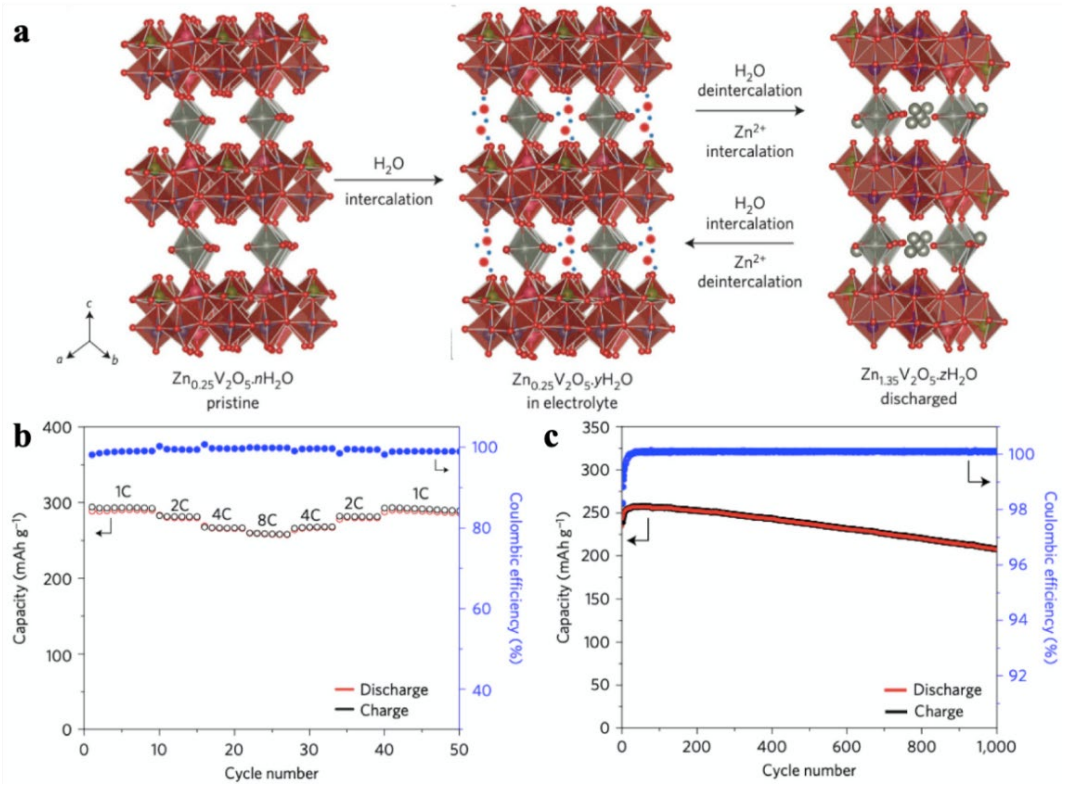

Figure 1.5 (a) Scheme of intercalation/deintercalation mechanism of $Zn_{0.25}V_2O_5{\cdot}nH_2O$. **(b)** Rate capacity at varying C and **(c)** cycling performance at 8 C of $Zn_{0.25}V_2O_5{\cdot}nH_2O$. Adapted from Ref. 13. Copyright @ 2016 Spinger Nature.

mAh g^{-1} has been investigated as an ideal cathode material for AZMBs. However, the application of V_2O_5 cathodes is seriously limited by their poor cycling stability owing to their unstable layered structure.[2] This is because of the absence of any atoms or molecules in

between layers that can act as "pillars" to hold the structural integrity during electrochemical cycling. To promote its electrochemical performance, water and metal ions are introduced into the layered structure of V_2O_5, to strengthen its structural stability during the electrochemical process. For instance, Kundu *et al*. successfully introduced water and Zn^{2+} ions into V_2O_5, to form $Zn_{0.25}V_2O_5 \cdot nH_2O$, which can transfer more than one Zn^{2+} ion per formula unit, and thus providing a high capacity up to 300 mAh g^{-1} (**Figure 1.5**).[13] Good reversibility was shown with a capacity retention of more than 80% after 1000 cycles.

Aside from V_2O_5, other vanadium oxides and related vanadates have also been widely studied. For example, Wan *et al*. reported a sodium vanadate hydrate ($NaV_3O_8 \cdot 1.5H_2O$) that exhibited a high reversible capacity of 380 mAh g^{-1} which lasted over 1000 cycles with a capacity retention of 82%.[14] These characteristics were proposed to arise from the similar pillar effect of hydrated sodium. A combination of *ex-situ* XRD, FTIR and solid-state ^1H NMR further verified that such excellent electrochemical performance benefited from the simultaneous insertion/extraction of proton and Zn^{2+}. Similar proton co-intercalation mechanism was also reported for various vanadium-based phosphates cathode materials, including VPO_4F[15] and $VOPO_4 \cdot xH_2O$[16]. In this thesis, the side effects of such unusual intercalation chemistry to practical AZMBs will be presented in detail. Some strategies that can address this issue will also be included.

Manganese dioxides are another type of materials that are widely reported as cathodes for AZMBs, and can exist in various crystallographic polymorphs that are constructed from MnO_6 octahedra linked by edges and/or corners. These polymorphs include three different tunnel-type structures (**Figure 1.6**[3]): α-MnO_2 with a tunnel size of 2 × 2 (each side of the tunnel consists of two MnO_6 octahedra), β-MnO_2 with 1 × 1 tunnel size and intergrowth γ-MnO_2 with both 1 × 1 and 1 × 2 tunnels; layered-type (δ-) MnO_2 that can be divided into birnessite-type (one layer of interlayer water molecules) and buserite-type structure (two layers of interlayer water molecules); and spinel-type (λ-) MnO_2. In contrast to vanadium-based materials, most of these MnO_2 cathodes undergo conversion reactions during electrochemical processes in AZMBs. Take α-MnO_2 for example, at least three different electrochemical charge storage

mechanisms have been reported: (i) proton-intercalation induced conversion to MnOOH or distorted MnO_2; (ii) Zn^{2+}-intercalation induced conversion to $ZnMn_2O_4$; (iii) and the disproportionation of reduced α-MnO_2 to soluble Mn^{2+} in the electrolyte.[17] All these different mechanisms suggest the instability of α-MnO_2 and some extents of conversion during the electrochemical discharge process. Strategies of adding a calculated amount of manganese salt

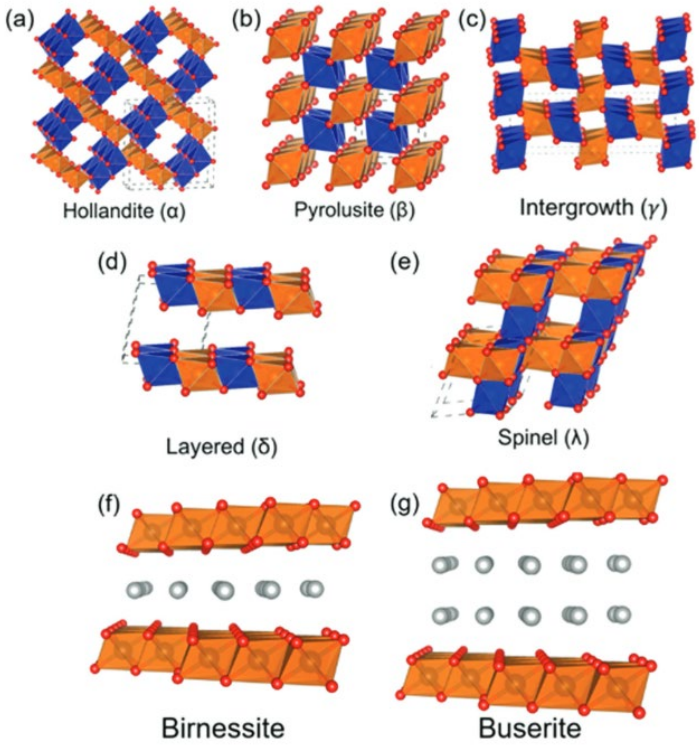

Figure 1.6 (a-g) Various polymorphs of MnO_2**.** Adapted from Ref. 3. Copyright © 2018 John Wiley & Sons, Inc.

($MnSO_4$) to shift the equilibrium of MnO_2(s)/Mn^{2+} (aq) can hinder the dissolution of Mn^{2+}, thus enhance the capacity to 285 mAh g^{-1} and the cyclic stability to 5000 cycles with a capacity retention of 92%.[18] Without such addition of $MnSO_4$, α-MnO_2 exhibits a capacity of 210 mAh g^{-1} and low stability with only100 cycles at 6 C, which mainly ascribed to the dissolution of Mn^{2+} caused by Jahn-Teller distortion. It should be noted that a conversion reaction mechanism involving Zn^{2+} and H^+ was proposed for the high capacity of α-MnO_2 in this study. However, such conversion chemistry means the existence of continuous structure transformation of the

active materials during cycling, which creates stress and strain that may cause the detachment of electrode from the current collectors. Aside from α-MnO_2, other Mn-based polymorphs including β-MnO_2, γ-MnO_2, δ-MnO_2, Mn_2O_3, $ZnMn_2O_4$, Mn_3O_4, are also reported as cathode materials for AZMBs.[19] Although most of these studies claim that Zn^{2+} insertion/extraction is the major electrochemistry during cycling, latest investigations suggest that proton intercalation is a more favorable chemistry in these oxide-based cathode systems, accompanying with structural degradation or phase transformation.

Other cathode materials that are investigated as Zn^{2+} host in AZMBs include Prussian blue analogs (PBAs) and layered sulfides that dominant Zn^{2+} (de) intercalation chemistry is reported.[17] For organic polymer cathode materials, both Zn^{2+}/proton co-intercalation and anion storage behavior are reported in dilute aqueous electrolytes.[20,21]

1.3.1.2 Anode and Electrolyte for Aqueous Zn Metal Batteries

Although many cathode materials for AZMBs exhibit higher specific capacity and superior cycling stability than those reported for LIBs, including aforementioned MnO_2[18] and $Zn_{0.25}V_2O_5 \cdot nH_2O$[13], the poor reversibility of the Zn metal anode has impeded commercialization of AZMBs. Owing to the high activity of H_2O, triggering of the hydrogen evolution reaction (HER) during Zn deposition leads to a local alkaline environment in common aqueous electrolytes (for example, 2 M $ZnSO_4$).[22] This induces the formation of high surface area zinc layered double hydroxides (LDHs) such as $Zn_4SO_4(OH)_6 \cdot xH_2O$, and zinc hydroxide on the Zn surface, resulting in a non-homogenous Zn surface that leads to low coulombic efficiency (CE) of Zn plating/stripping, aggravated dendrite formation and accelerated battery failure.[22–24]

To overcome these challenges and improve the reversibility of Zn, various intriguing strategies have been employed, including building three-dimensional (3D) Zn hosts or employing Zn/substrate surface modification. A 3D metal-organic framework (ZIF-8) exhibits a high Zn plating/stripping CE of 99% for 200 cycles at a range of current densities and

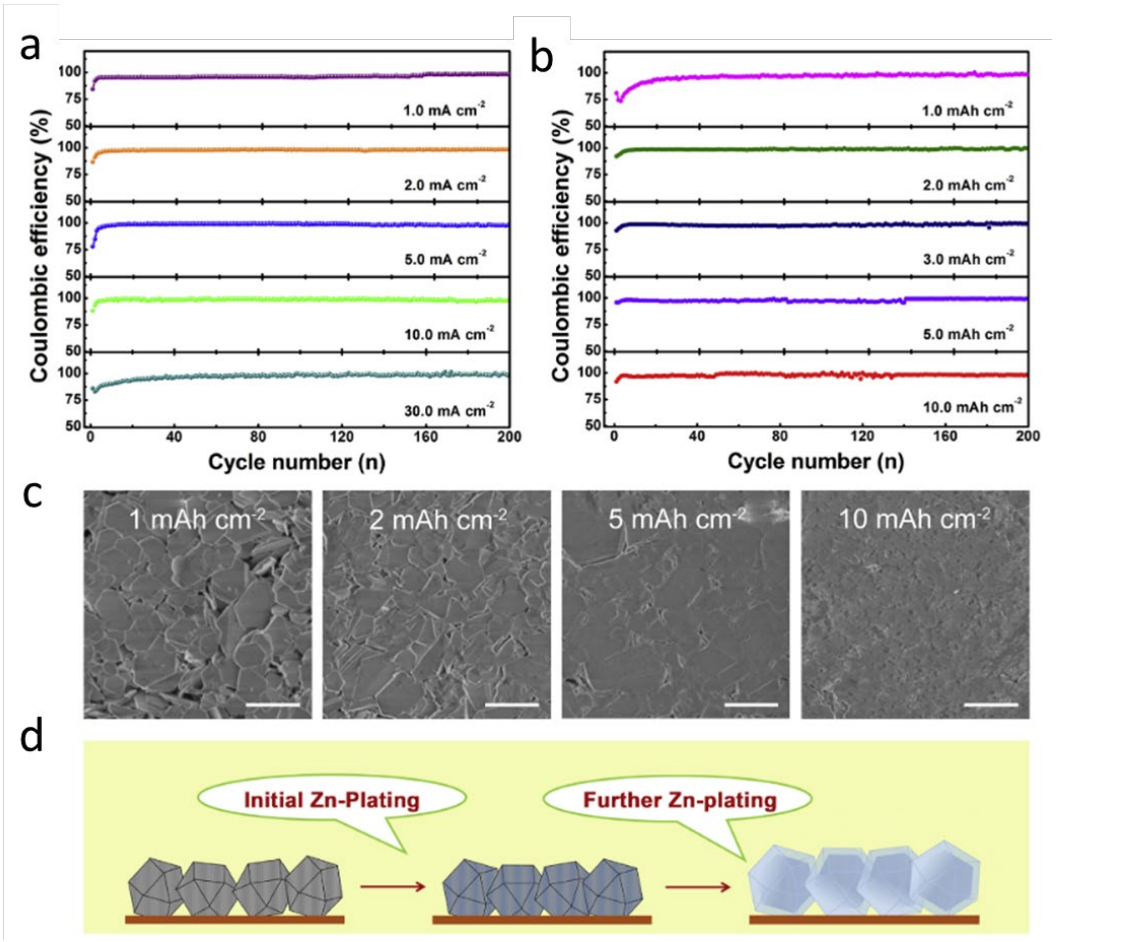

Figure 1.7 (a) Coulombic efficiency of Zn deposition on ZIF-8 electrode at different current densities. **(b)** Coulombic efficiency of Zn deposition on ZIF-8 electrode at different capacities. **(c)** SEM images of Zn deposits at different capacities. Scale bars, 2 mm. **(d)** Schematic illustration of the Zn plating. Adapted from Ref. 25. Copyright @ 2019 Elsevier Inc.

capacities (**Figure 1.7**),[25] although scalability of ZIF synthesis is a consideration for large-scale AZMBs. Archer *et al*. reported an epitaxial mechanism to regulate Zn nucleation and growth. Owing to the low lattice mismatch between Zn and graphene, remarkable performance

based on dendrite-free Zn plating/stripping on a graphene substrate was achieved via "locked orientation".[26] A similar approach was extended to electrolyte-dispersed C_3N_4 colloidal particles which improve Zn electrodeposition to achieve a CE of 99.8%.[27] Electrolyte engineering via tuning the interaction of cation, anion and solvent, is another effective approach to enhance Zn reversibility and stability. Wang's group reported a neutral 21 m LiTFSI + 1 m $Zn(TFSI)_2$ water-in-salt electrolyte (WiSE) in which H_2O molecules are strongly crowded by Li^+ ions,[28] thus exhibiting reduced H_2O activity and a high CE of 99.7%. Nonetheless, very significant polarization (around 0.3 V at 0.2 mA cm^{-2}) and high cost of the salt are potential limitations to WiSE systems.

Recently, ZnF_2-rich solid-electrolyte interfaces (SEI) formed *in-situ* on Zn metal were proposed to enhance Zn reversibility. Wang *et al.* reported a metal-organic framework layer filled with a $Zn(TFSI)_2$-tris(2,2,2-trifluoroethyl)-phosphate organic electrolyte.[29] Zn anodes coated with this layer show an average CE of 99.1% for 350 cycles in 1 M $Zn(TFSI)_2$ aqueous electrolyte, where a ZnF_2-rich SEI *in-situ* formed on Zn surface was proposed to enhance the Zn reversibility. Wang's group further explored the effect of trimethylethylammonium trifluoromethanesulfonate ($Me_3EtNOTf$) as an additive with 4 m $Zn(OTf)_2$, reporting an average CE of 99.8% for 1000 cycles.[30] A ZnF_2-SEI formed *in-situ* on the Zn surface was proposed to explain such good performance, operating at a current density of 0.5 mA.cm^{-2}. Inspired by the promising properties of a ZnF_2 rich-SEI, Passerini *et al.* designed an artificial porous ZnF_2 layer on Zn with a thickness of ~1 μm that effectively suppressed dendrite growth.[31] Their modeling results remarkably showed that Zn^{2+} could diffuse through bulk ZnF_2 as a result of Zn^{2+}-interstitial defect formation. Zn^{2+}-ion migration via the channels embedded in this fluoride layer may also play a role. Hybrid solvents with minimal water content are also proposed to suppress water activity and enhance Zn reversibility. Very recently, Yang *et al*. reported a hydrous organic electrolyte prepared by dissolving hydrated $Zn(BF_4)_2$ in ethylene glycol. [32]This electrolyte enables the formation of a dense ~ 3 μm ZnF_2 passivation layer that exhibits a relatively high CE (99.4%) for Zn plating/stripping. Despite the high Zn reversibility owing to the ZnF_2-rich SEI, the low areal capacity (0.5 mAh cm^{-2}) achieved in these studies is less than that of practical Li-ion batteries (at least 3 mAh cm^{-2}).[33]

1.3.1.3 Challenges and Practical Considerations for Aqueous Zn Metal Batteries

Despite tremendous effort and growing enthusiasm worldwide, however, the commercialization ofAZMBs is still plagued by several obstacles including (**Figure 1.8**):

(1) Unrealistically High C-Rates and Low Areal Capacities. In LIBs**,** the C-rate is a measure of the current density at which a battery is discharged relative to its theoretical (or maximum) capacity; a 1C rate means that the discharge current will discharge the battery in one hour. The same terminology is used in the AZMB field. **Figure 1.9** summarizes the published long-term cycling performances of various cathodes at both high rates (> 5 C) and low rates (0.5 - 2 C), and Zn anode studies regarding cumulative capacity at different current densities

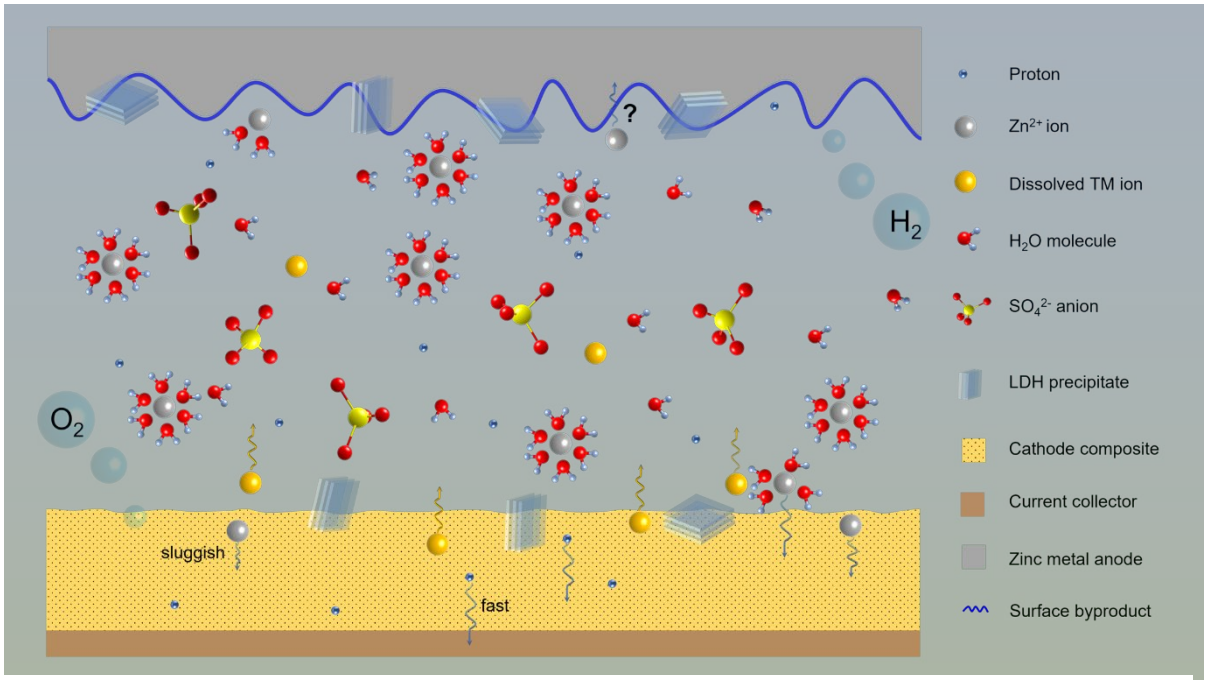

Figure 1.8 The commonly reported dilute $ZnSO_4$ electrolyte system is chosen as the platform, illustrating challenges of transition metal (TM) dissolution from the cathode, H_2 and O_2 evolution processes, layered double hydroxide (LDH) precipitation, co-proton intercalation in the cathode, inhomogeneous Zn deposition (dendrite formation), and limitations of thick SEI formation at the anode.

(0.5 - 40 mA cm^{-2}) based on “reservoir free” galvanostatic asymmetric-cell protocols (for example, Zn||Cu or Zn||Ti).

In terms of cathode stability, one can easily identify the large gap between low-rate and high-rate cycling performance, including in cells based on widely studied manganese oxides, vanadium oxides, and metal disulfides. Most of these cathode materials were reported to show

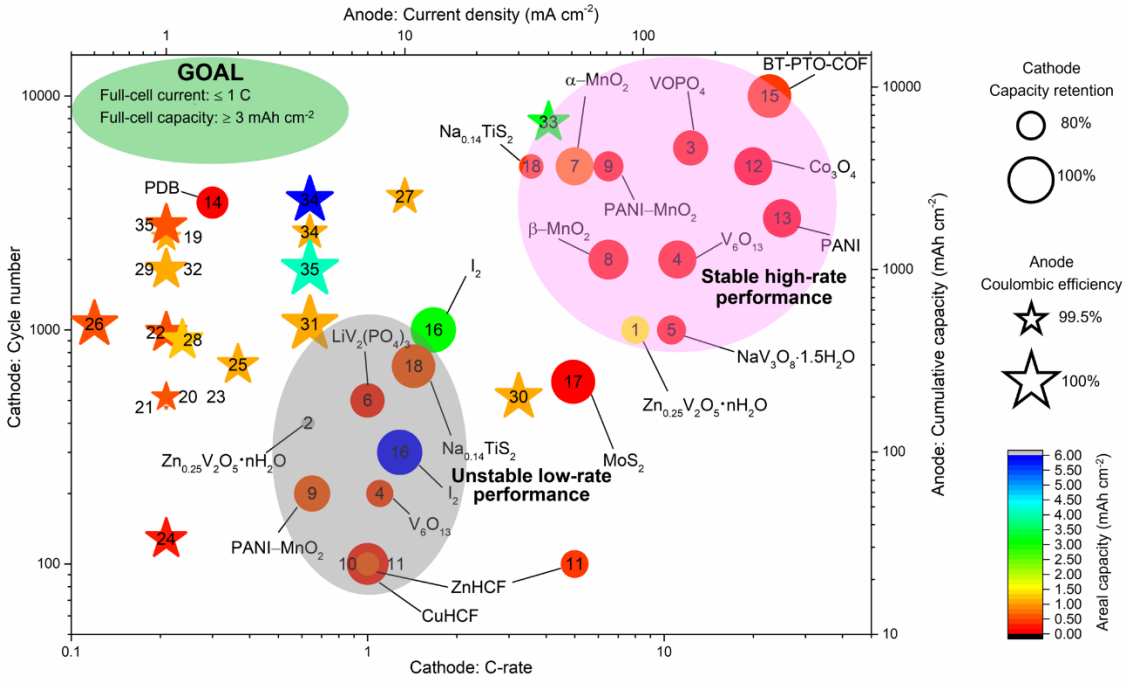

Figure 1.9 The summary of cathode and anode performance in AZMBs. The published cathode data was analyzed in terms of C-rate (bottom x axis), areal capacity (heatmap), cycle number (left y axis) and capacity retention (diameter of circle). C-rate and areal capacity values are either provided in the literature or calculated based on the reported highest discharge capacity and mass loading of active materials, respectively. Many references are excluded owing to lack of information on mass loading. The published anode data were evaluated based on asymmetric cells in terms of current density (top x axis), areal capacity (heatmap), cumulative capacity (right y axis), and coulombic efficiency (size of star). Cumulative capacity is calculated based on the areal capacity and the reported cycle numbers of Zn plating/stripping. Adapted from Ref. 10. Copyright @ 2022 Elsevier Inc.

very promising long-term cycling stability at high rates from 5 C – 30 C, but poor cycling performance at low rates from 0.5 C – 2 C. At a similar percentage of capacity retention, the cycle life achieved in these two scenarios can vary by as much as 10-fold. The source of these differences are at presently unknown. It may be speculated, for example, that the

electrochemical/chemical degradation of cathode active materials is much less severe at high rates, as they spend less time at the potential extremes. Proton (de)intercalation likely dominates in the bulk at ultra-fast rates, giving rise to "false" high Zn^{2+} capacity. Very fast cycling rates may also contribute to better performance at the Zn anode. Irrespective of the source, however, it means that AZMBs that are unable to undergo stable cycling at the moderate rates used for stationary grid storage (0.25 C – 2 C) are of limited practical interest.[34]

A more serious concern is that often the high C-rate performance is reported in cells with areal capacities less than 0.5 mAh cm^{-2}. These values are not only quite far below typical values (*e.g.*, 3 mAh cm^{-2}) used for practical LIBs, but the apparent performance benefits achieved cannot be extrapolated to higher areal capacity electrodes. Specifically, higher capacities require thick electrodes, and this triggers many other scientific challenges, including sluggish mass transport, high voltage polarization, contact loss with current collectors, and crack formation during cycling. Thus, we suggest that follow-up studies of such cells with practical areal capacity and at reasonable rates are warranted.

(2) Dissolution of cathode active materials. Most cathode studies for AZMBs in the past five years involving manganese-based and vanadium-based materials suffer from the dissolution of active materials, resulting in reduced cycle life owing to loss of active material. A promising direction focuses on Mn^{2+}-salts as electrolyte additives to suppress dissolution of manganese-based cathodes.[18] This approach has been shown to work at high rates (e.g., 92% capacity retention for 5000 cycles at 5C) but has not yet been evaluated at the more modest rates demanded in many applications.

(3) Zn^{2+} *vs.* proton intercalation and the precipitation of layered double hydroxides (LDHs). Compared with organic solvents in nonaqueous electrolytes, water – as the major solvent for aqueous Zn electrolytes – leads to merits of high ionic conductivity (1 – 100 mS cm^{-1}), inflammability, low interfacial resistance, and high salt solubility. Nonetheless, water also causes many undesired side reactions, including proton co-intercalation and the simultaneous precipitation of layered double hydroxides (LDHs; for example, $Zn_4SO_4(OH)_6{\cdot}xH_2O$) on both inorganic[35] and organic[20] cathode interfaces on discharge. Proton intercalation has also been considered as the origin of ultra high-rate capability of many

cathode materials, as Zn^{2+} diffusion in intercalation hosts may be too sluggish.[36] The insulating LDHs also increase interfacial resistance and gradually detach off the cathode surface leading to short cycle life (especially at lower rates). Therefore, understanding the interplay of Zn^{2+} *vs.* proton intercalation in specific cathodes and discovering new inorganic/organic cathode materials with excellent Zn-ion diffusivity and dominant Zn^{2+} (de)intercalation properties are necessary.

(4) Challenges ascribed to narrow electrolyte stability window. The thermodynamic electrochemical stability window of water is 1.23 V and depends on electrolyte pH.[2] The oxygen evolution reaction (OER) and hydrogen evolution reaction (HER) occur at higher and lower voltages, respectively due to overpotentials. These reactions decompose the aqueous electrolyte solvent. The risk of OER also significantly limits the choice of cathode materials, resulting in the low-voltage output (< 2 V) of current AZMBs. Thus, new fundamental approaches are required to enhance the anodic stability of aqueous Zn electrolytes and to identify suitable high-voltage cathode materials. The existence of progressive HER during Zn deposition also triggers a local alkaline environment, inducing the formation of LDHs and $Zn(OH)_2$ on the Zn surface as mentioned. These surface byproducts lead to low coulombic efficiency and a rough Zn surface, aggravating dendrite formation and decreasing the cycle life of batteries. Recently, much effort has been devoted to suppressing HER and achieving highly reversible/stable Zn anodes. Building *in/ex-situ* surface electrolyte interphases (SEI) – such as those involving ZnF_2[30]- appears to be an effective strategy; nonetheless, the understanding of Zn-ion diffusion through such interphases remains unclear and needs follow-up scrutiny from a mechanistic point of view.

(5) Impractical Low-Utilization of Zn Anodes. The often low areal capacity (< 0.5 mAh cm^{-2}) of cathode materials reported in current AZMBs highlights the low utilization of Zn anodes in these studies. As the theoretical areal capacity of commonly used Zn foil with a thickness of 250 μm or 100 μm is ~1462 mAh cm^{-2} or ~585 mAh cm^{-2} (based on the theoretical volumetric capacity of ~5855 Ah L^{-1}), the Zn utilization in each discharge or charge process is less than 0.1%. Thus, nearly 100% coulombic efficiency and very promising specific energy density based only on cathode loading were achieved in most such studies. However, such conditions are not applicable to practical stationary batteries. In order to evaluate the cycling performance of AZMBs in a more realistic way, it is important to report both specific and

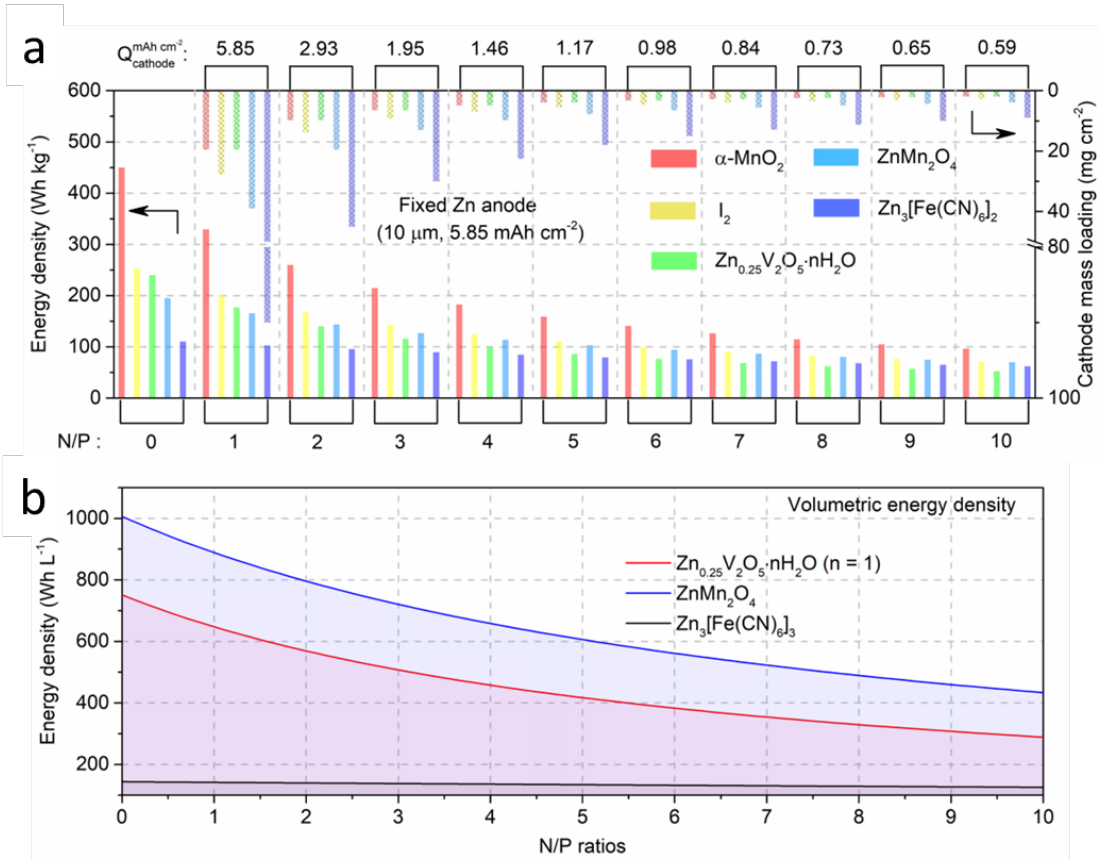

Figure 1.10 (a) Specific energy density (left y axis) as a function of N/P ratios (bottom x axis). The required cathode areal capacity and mass loading at different N/P ratios was further calculated for reference (top x and right y axis). **(b)** Volumetric energy density as a function of N/P ratios.

volumetric energy density with increased Zn utilization, or controlled capacity ratios between negative and positive electrodes (N/P ratios).[27] The following equation gives a plausible estimation of energy densities of AZMBs based on both cathode and anode volumes ($E_{cathode+anode}$) when considering a reasonable N/P ratio:

$$E_{cathode+anode} = \frac{Q_{Zn} \times Q_{cathode}}{Q_{Zn} + Q_{cathode} \times \left(\frac{N}{P}\right)} \times \bar{V} \quad (1)$$

where the Q_{Zn} and $Q_{cathode}$ are the theoretical specific or volumetric capacity of Zn and cathode materials, respectively. $\overline{V}$ is the average voltage output of batteries.

According to equation (1), the critical impact of N/P ratios on both energy densities can be easily seen in **Figure 1.10**. Considering the same cathode (**Figure 1.10a**), its specific energy density at a N/P ratio of one (corresponding to 100% Zn utilization) is nearly twice than that of a N/P ratio of four (corresponding to 25% Zn utilization). Using a more rigorous protocol with a N/P ratio of zero - a called anode-less cell configuration - the energy density is around 450 Wh kg^{-1} based on a typical manganese oxide cathode[18] (specific capacity of ~300 mAh g^{-1}, average voltage of ~ 1.5 V). In terms of volumetric energy densities, taking $Zn_{0.25}V_2O_5{\cdot}nH_2O$ (n=1)[13] as an example (**Figure 10b**), its energy density can be as high as 760 Wh L^{-1} in an anode-free cell. Therefore, screening the intermediate-rate cycle life of a cathode material at reasonable N/P ratios lower than 3 to fully evaluate its strengths and limitations is important for practical grid storage.

1.3.2 Non-Aqueous Mg Metal Batteries

Similar to AZMBs, MMBs use Mg metal foil as the anode with desirable electrochemical properties. These include a high volumetric specific capacity of 3833 mAh mL^{-1}, low standard electrode potential of -2.37 V (vs. SHE), and the less tendency of dendrite growth on electrochemical plating process compared to Li or Zn.[37,38] The low standard electrode potential of Mg guarantees the potential of building high-energy density MMBs, however, unfortunately limits the applied electrolyte in the nonaqueous regime. Aiming for using Mg metal as anode, most studies in MMBs focus on the exploration of new cathode materials and electrolytes that can sustain reversible Mg plating/stripping process.

The first reported prototype Mg battery by Aurbach et al. illustrates a Mg metal anode with a Chevrel phase Mo_6S_8 cathode in a Mg organohaloaluminate type electrolyte,[39] delivering a specific capacity of ~ 75 mAh g^{-1} at an average voltage of 1.2 V (**Figure 1.11**). This work opens up the exploration of a variety of other cathodes and electrolytes for MMBs.

1.3.2.1 Cathode Materials for Mg Metal Batteries

Early exploration of Mg cathode materials starts from the simple transition metal oxide (eg. V_2O_5[40] or MnO_2[41] in different polymorphs), which showed high capacities and operating

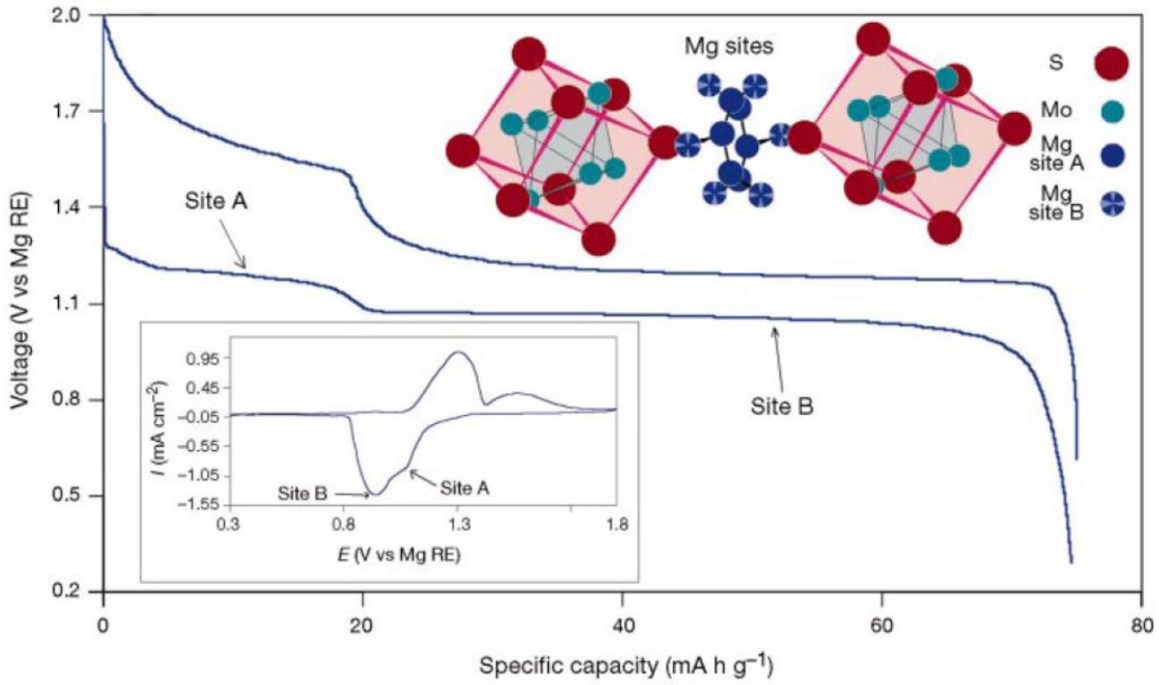

Figure 1.11 Electrochemistry of Mo_6S_8 positive electrode tested with a Mg negative electrode and 0.25 M $Mg(AlCl_2BuEt)_2$ in THF electrolyte . Adapted from Ref. 39. Copyright @ 2000 Spinger Nature.

voltages in LIBs as positive electrodes. However, the doubled charges of Mg^{2+} compared to Li^+ results in much slower Mg^{2+} diffusion in these solid materials, showing much poorer electrochemical performance. Strategies including nano-sizing materials or involving solvent molecules in crystal structures improve the kinetics to some extent,[42] the exhibited performance of these cathode materials is still very limited.

Compared to the limited success achieved with oxides, sulfide-based cathode materials have been extensively studied since the discovery of fast Mg^{2+} solid state diffusion in Chevrel phase structure.[39] This is because the softer and more covalent sulfide lattice allows faster Mg^{2+} mobility compared to that in the strong ionic oxide lattice. In Chevrel compounds, the crystal structure usually consists of multiple Mo_6T_8 blocks that stack together (**Figure 1.12**)[43]. Each block includes a molybdenum atom sitting in an octahedral site inside a cube of T atoms. The

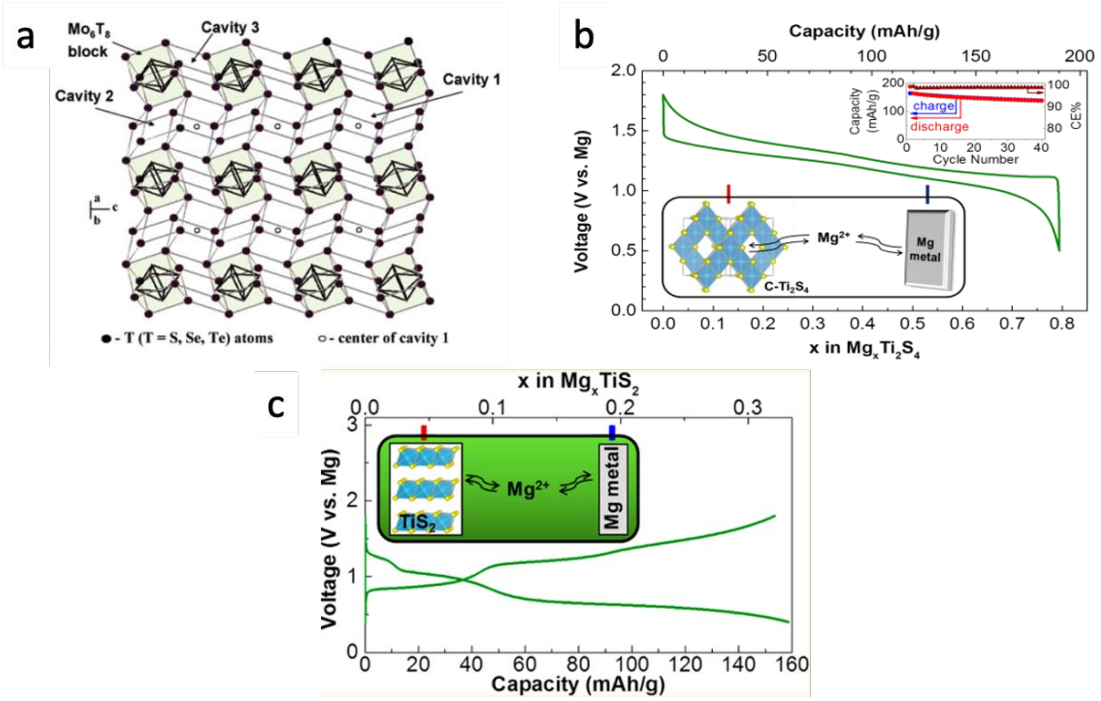

Figure 1.12 (a) Crystal structure of the Chevrel phase showing the Mo_6T_8 blocks and three cavities available for ion insertion. Adapted from Ref. 43 Copyright @ 2006 American Chemical Society. **(b** and **c)** Electrochemistry of "soft-anion" **(b)** thiospinel Ti_2S_4 and **(c)** layered TiS_2 positive electrodes with Mg negative electrodes and all-phenyl complex electrolyte. Adapted from Ref. 44 Copyright @ 2016 Royal Society of Chemsitry, and Ref. 45 Copyright @ 2016 American Chemical Society.

stacking of these blocks creates plenty of near empty sites with cavities that can facilitate fast Mg^{2+} insertion/extraction. Besides Chevrel-type Mo_6S_8, other sulfide cathodes were reported for MMBs, including thiospinel[44] and layered transitional metal sulfides,[45] where the soft Mg^{2+}-S bonding was proposed to enhance the solid-state diffusion of Mg^{2+} in these inorganic hosts. However, these reported sulfides typically exhibit low discharge voltage slightly above

1 V vs. Mg^{2+}/Mg, leading to the low specific energy density that is incomparable to LIBs and far below the requirement of practical batteries.

To develop MMBs with high energy density, a series of high voltage cathodes were studied, where oxides spinel compounds were extensively explored recently. The spinel structure has a general formula of AB_2X_4 in which X anions are located in a cubic close packed lattice and cations A and B occupy tetrahedral and octahedral sites, respectively (**Figure 1.13**).[46] The computation studies revealed that the energy barriers for Mg^{2+} diffusion of spinel-

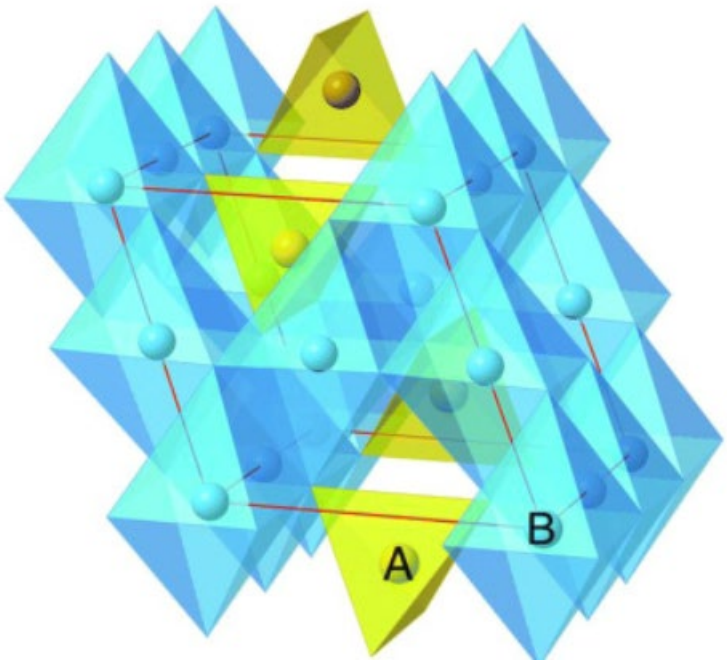

Figure 1.13. The spinel crystal structure where the 'A' atoms occupy the tetrahedral sites, and the 'B' atoms occupy the octahedral site. Adapted from Ref. 46. Copyright © 2015 Royal Society of Chemistry.

type M_2O_4 (M = Mn, Cr, Ni and Co) are in the range of 600 ~ 800 meV,[46,47] which unfortunately are too high for Mg^{2+} ions to diffuse at room temperature, compared to around 500~600 meV of thiospinels.[48] As a consequence, these oxide spinels normally require only nano-sizing treatment to shorten the Mg^{2+} diffusion length so that some limited Mg^{2+} intercalation/de-intercalation behaviors can be achieved.[49] Nonetheless, most of these studies

were conducted with electrolytes that are not compatible with Mg anode, posing more concerns of their practicability in true MMBs.

In recent years, organic compounds also have attracted much attention as cathode materials for MMBs. Different from the valence change in transition metal atoms of inorgace cathodes during Mg^{2+} (de) intercalation, the electrochemical redox reaction of organic cathodes relies on the charge in charge state of electroactive organic groups,[50] where the sluggish Mg^{2+} diffusion can be obviated to some extent. Therefore, organic cathode material typically shows much better charge-discharge kinetics. In addition, the abundance and diversity of organic materials lead to their flexible structure with high tunability, providing great opportunity to design high-capacity and high-rate organic cathodes. Among many studied organic cathodes, pyrene-4,5,9,10-tetraone (PTO) is reported as one of most promising materials (**Figure 1.14**).[51] The charge/discharge process of PTO is a heterogeneous enolization chemistry involving carbonyl reduction (C=O↔C–O−), where two Mg^{2+} storage can theoretically provide a high specific capacity of 408 mAh g^{-1}. In addition, this cathode is reported with ultrafast kinetics that can be cycled at a 50 C rate with over 200 mAh g^{-1} capacity retained. However, due to the low electronic conductivity, these organic materials tend to require high content of carbon when fabricating the cathode that can significantly decrease the energy density at cell level. In addition, the half-discharged PTO (Mg_1PTO) completely dissolves into ether-type solvents that causes additional concerns of its practicability, although graphene oxide membrane was proposed to mitigate this issue to some extent.

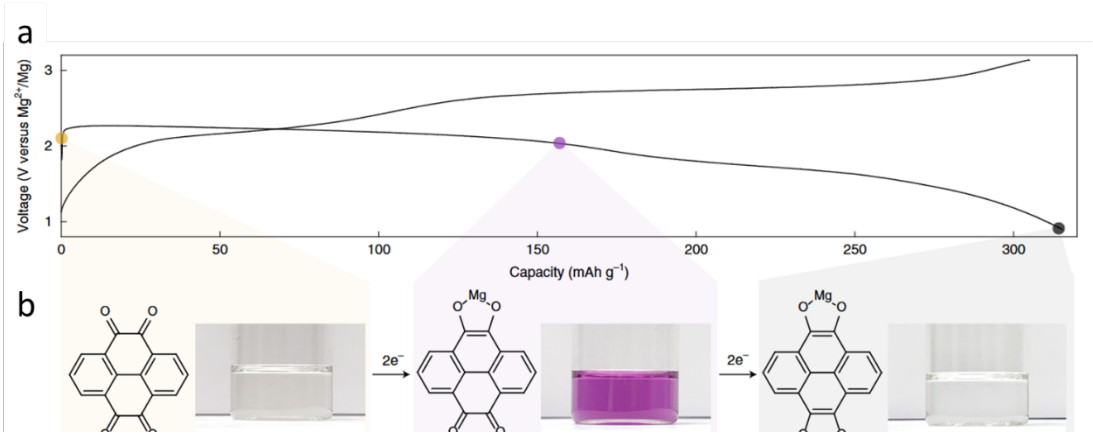

Figure 1.14 (a) The voltage profile of a Mg–PTO cell. **(b)** Reductive enolization of PTO to Mg_1PTO and Mg_2PTO. The accompanying photographs of DME solutions of the electrodes at the corresponding states indicate the solubilities and colors of the intermediates. Adapted from Ref. 51. Copyright @ 2018 Springer Nature.

1.3.2.2 Anode and Electrolyte for Mg Metal Batteries

Grignard solution – with a general formula R-Mg-X with X as halogen and R as an organic group (alkyl or aryl) – is the first electrolyte reported to achieve reversible plating/stripping of Mg,[52] however, suffers from the very low anodic stability and ionic conductivities that cannot support any practical cathode materials. Introducing Lewis acids into Grignard solution was later found as an effective approach to improve the anodic stability without sacrifice of reversible Mg plating/stripping, where 0.25 M Mg organohaloaluminate complex $Mg(AlCl_2EtBu)_2$ (butyl ethyl complex, BEC) in THF was final determined to show optimum performance with near 100% CE of Mg plating/stripping and >2.1 V (vs. Mg^{2+}/Mg) anodic stability (**Figure 1.15**).[53] Further electrolyte modification on the replacement of alkyl group with phenyl leads to the all-phenyl complex (APC) electrolyte with a higher anodic stability of 3.3 V (vs Mg^{2+}/Mg). In all these early electrolyte studies, chlorine was found to be the only feasible choice for the inorganic ligand to achieve reversible Mg plating/stripping.[54] Other ligands including fluorine or CN either passivate Mg anode or reduce the solution anodic stability window. However, these complex chlorine-based electrolytes are highly corrosive to current collectors or battery casings. More importantly, the presence of chlorine still limits the

anodic stability which is insufficient to achieve high energy density MMBs. These motivations inspire the intense academic effort to design chlorine-free electrolyte that is compatible with Mg plating/stripping and anodic stable at a high voltage of 3.5 V (vs. Mg^{2+}/Mg).

Early efforts of designing halide-free Mg electrolyte started from the first report of $Mg(BH_4)_2/LiBH_4$ hybrid electrolyte that shows 94% CE of magnesium plating/stripping.[55] The electrolyte was reported with a low oxidation stability of only 1.7 V, nonetheless, it lays the

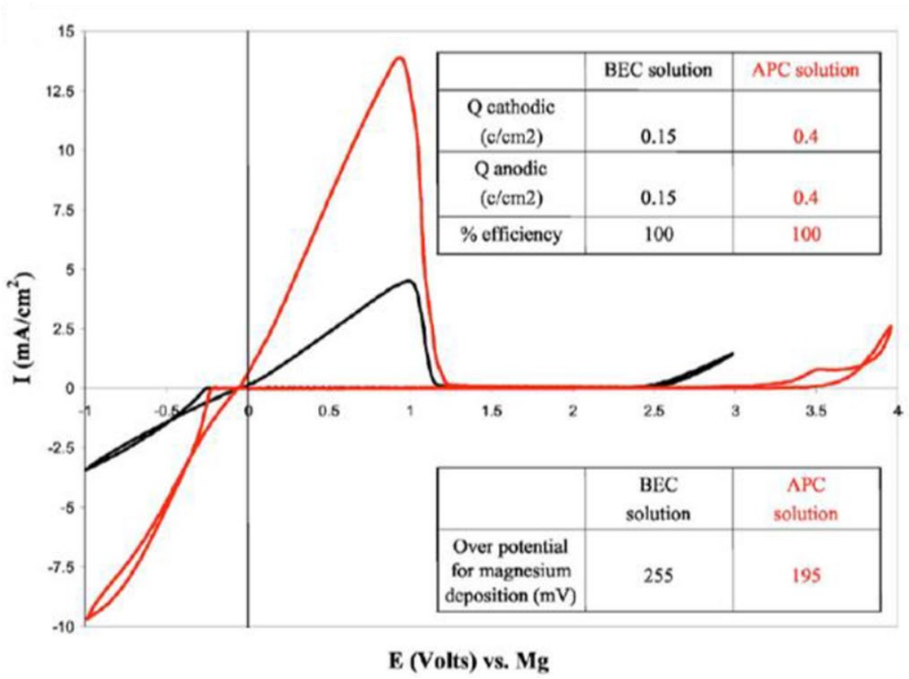

Figure 1.15 Cyclic voltammograms of 0.25 M BEC and 0.4 M APC electrolytes measured with Pt electrodes at 25 mV s^{-1}. Adapted from Ref. 53. Copyright @ 2007 The Electrochemical Society.

foundation for designing halide-free single-salt electrolyte that is compatible with magnesium plating/stripping. A follow-up $Mg(CB_{11}H_{12})_2$ salt was synthesised with a better oxidative stability of > 3.5 V in single ether solvent (G3 or G4) with 99% CE[56]. A bi-solvent blend was then tailored for this salt to boost the kinetics for magnesium plating/stripping.[51] Other unconventional boron/aluminium-clustered salts reported so far show over 99% CE and > 3.5 V anodic stability.[57–59] However, the most reported CE of magnesium plating/stripping in these electrolytes were based on CV measurements or galvanostatically at low currents and areal capacities. Achieving reversible plating/stripping with significant quantities of magnesium,

which can be sustained on long-term cycling, is still a great challenge. More serious concerns are commercial unavailability of these salts due to the expensiveness of precursors and complexity of synthetic/purifying routes,[38,60] which are unfriendly to stimulate wide research or commercialization of MMBs.

Conventional magnesium bis(trifluoromethanesulfonimide) ($Mg(TFSI)_2$) or magnesium trifluoromethanesulfonate ($Mg(OTf)_2$)-based electrolyte has over 3.5 V anodic stability but very poor compatibility with Mg anode due to strong ion pairing, which can only be improved by adding chlorides as the second salt in earlier studies.[60,61] Recently, there is considerable interest in additive engineering on $Mg(TFSI)_2$-based single salt electrolyte. Impressive studies of using highly polar additives were conducted to enable efficient magnesium plating/stripping at 98~99.5% CE with at 0.1 mA cm^{-2} and 0.1 mAh cm^{-2}.[62,63] In contrast, less attention were devoted on $Mg(OTf)_2$ due to its near zero solubility in ethers (for example, diethylene glycol dimethyl ether (G2)), which are the only polar aprotic solvents that are fully compatible with magnesium metal.[38] Although similar highly polar additives can increase $Mg(OTf)_2$ solubility to some extent,[64,65] the reported reversibility of Mg plating/stripping is insufficient to support practical rechargeable batteries, where an over 99.9% cycling efficiency of metal anodes is required at a minimum areal capacity of 3 mAh cm^{-2}.[66,67] Therefore, none of reported Mg electrolyte can meet the requirements for practical MMBs, in terms of low cost, easy-accessibility, high anodic stability, high CE for Mg plating/stripping at reasonable areal capacity.

1.4 Summary

LIBs based on intercalative graphite anode dominate the energy storage markets of portable electronic devices and electrical vehicles. However, the uncertainty of employing lithium metal anode and the ever-increasing shortage/price of lithium cause concerns of safety and affordability of LIBs. Under this context, alternative electrochemical energy storage techniques including AZMBs and MMBs are intensively studied, where Zn and Mg metal anode with high abundance and high volumetric capacity can be directly used.

One of greatest merits of AZMBs is the use of aqueous electrolyte. The resulting high affordability, inflammability and environmental-friendly make them excellent candidates for large-scale grid or mini-grid storage. Although numerous publications and academic efforts have been devoted into this new rising area, the aforementioned challenges still plague the commercialization of AZMBs. Some successful and cheerful results were achieved with conventional aqueous electrolytes in the lab; however, more serious underlying obstacles are identified when translating these attempts into practical conditions. Due to the high activity of H_2O in conventional aqueous electrolyte, H_2O-involved side reactions at both cathode and anode lead to the quick failure of batteries at practical current densities and areal capacities, including Zn dendrite, LDHs formation and cathode dissolution. Therefore, it is of vital importance to develop novel, next-generation aqueous Zn electrolyte that can fundamentally mitigate or eliminate these undesired reactions, and finally achieve desirable AZMBs that can function at practical conditions.

Earlier studies of Mg-ion electrolytes focus on the highly efficient chlorine-based or organborate/aluminate-based electrolytes. Nonetheless, the former suffers from the low anodic stability and severe corrosion to battery casing/current collector, while the latter is commercially unavailable due to the very expensive precursor, complex synthesis/purification procedure. MMBs with both types of electrolytes are unable to compete the state-of-art LIBs in terms of energy density and affordability. Therefore, it is essential to focus on the discovery and design of new Mg-ion electrolyte that fulfills the requirements of high anodic stability, low corrosion and high compatibility with Mg metal anode.

With the discovery of new Zn or Mg electrolytes, it is also important to develop a comprehensive understanding of electrolyte network of the cation solvation structure and ion-ion/solvent interaction. These directly influence the interfacial (de) solvation process at the electrode/electrolyte interface. Due the divalent nature of Zn and Mg, the interfacial chemistry at both cathode and anode surface is far more important than that in LIBs, which can directly determine the kinetics of Zn^{2+}/Mg^{2+} diffusion and thus electrochemical redox activity. Therefore, disclosing the electrolyte network and building its connection to the interfacial

chemistry at electrolyte/electrolyte interface will be the core in developing efficient electrolytes for practical AZMBs and MMBs.

1.5 Scope of the Thesis

This thesis presents a comprehensive investigation on the synthesis, characterization, electrochemical performance of newly designed Zn and Mg electrolytes, understanding the electrolyte network, Zn^{2+}/Mg^{2+} solvation structure and their influence on electrode/electrolyte interface. All these investigations were aimed to evaluate the newly discovered concepts at practical conditions to fasten the developments of commercial AZMBs and MMBs.

Chapter 1 gives a general introduction of related research reported in the past in AZMBs and MMBs. Parts of this chapter have been published as: Li, C., Jin, S., Archer, L. A., Nazar, L. F. Towards practical aqueous zinc-ion batteries for electrochemical energy storage. *Joule* **2022** 6, 1727–1742, Copyright © 2022 Elsevier Inc., reproduced with permission from Elsevier.

Chapter 2 describes the research experimental methods and characterization techniques that are employed in this thesis.

Chapter 3 introduces a novel electrolyte additive, N,N-dimethylformamidium trifluoromethanesulfonate (denoted as DOTf), for an electrolyte based on aqueous 2 M $ZnSO_4$. Its dissociation in water to neutral ion-pairs (the superacid HOTf + DMF) leads to the formation of a fluoride-free, Zn^{2+}-conducting nanostructured SEI on the Zn surface upon cycling in an electrochemical cell. The unique interfacial chemistry is understood by using a comprehensive combination of X-ray photoelectron spectroscopy (XPS), operando surface-enhanced infrared absorption spectroscopy (SEIRAS) and cryo-transmission electron microscopy (TEM) studies. We demonstrate the SEI enables water exclusion at the interface, leading to diminished LDH formation. Along with a nanoscale Zn nucleation and growth process, this additive promotes a highly dense and dendrite-free Zn plating morphology. The electrochemistry of Zn||Cu asymmetric cells demonstrates the high reversibility and stability of Zn anode at both a lab-level capacity of 0.5 mAh cm^{-2} and practical-level capacity of 4 mAh cm^{-2}. The work has been published as: Li, C. et al. Highly Reversible Zn Anode with A

Practical Areal Capacity Enabled by A Sustainable Electrolyte and Superacid Interfacial Chemistry. *Joule* **2022**, 6, 1103-1120, Copyright © 2022 Elsevier Inc., reproduced with permission from Elsevier.

Chapter 4 demonstrates that solvation-structure engineering of aqueous Zn electrolytes is an effective method to suppress H+ intercalation and realize dominant Zn^{2+} intercalation. To establish proof-of-concept, we chose $LiV_2(PO_4)_3$ (LVP) as the platform for the cathode and compared its electrochemistry in two previously reported electrolytes, 4 m (molality, mol/kg) $Zn(OTf)_2$ and 29 m $ZnCl_2$ "water-in-salt" electrolytes (WiSE), as well as a newly designed hybrid electrolyte developed by incorporating polyethylene glycol 400 (PEG 400) and water as a co-solvent with $Zn(OTf)_2$ as the salt. Importantly, we explore the H-bonding network, free water fraction, Zn^{2+}-solvation structure and their roles in the Zn^{2+} vs. H^+ intercalation in all three electrolyte systems, using experimental and computational methods to understand why the PEG-based hybrid electrolyte exhibits the least H+ intercalation and the most dominant Zn2+ intercalation. The work has been published as: Li, C., Kingsbury, R., Zhou, L., Shyamsunder, A., Persson, K. A., Nazar, L. F. Tuning the Solvation Structure in Aqueous Zinc Batteries to Maximize Zn-Ion Intercalation and Optimize Dendrite-Free Zinc Plating. *ACS Energy Lett.* **2022**, 7, 533-540, Copyright © 2022 American Chemical Society, reproduced with permission from American Chemical Society.

Chapter 5 elucidates the Zn^{2+} vs. proton intercalation mechanism of a metal oxide cathode ($Zn_{0.25}V_2O_5{\cdot}nH_2O$ (ZVO)) in various electrolytes by a combination of ex-situ/operando techniques. A strategy of using sulfolane-based hybrid eutectic electrolyte is shown to effectively suppress deleterious proton intercalation and cathode dissolution. This is ascribed to a strong hydrogen-bonded network of sulfolane-water that alleviates water activity. In addition, a fully hydrated Zn^{2+} solvation structure is revealed and induces facile interfacial charge transfer at the Zn metal surface. Highly stable and reversible Zn plating/stripping is demonstrated in both Zn||Cu and Zn||Zn cells. Benefiting from both stabilized electrodes in the hybrid eutectic electrolyte, we report the first practical high-areal-capacity (4 mAh cm-2) Zn anode-free cell that can run over 100 cycles at 0.15C with ~ 85% capacity retention. The work has been published as: C. Li, R. Kingsbury, A. S. Thind, A. Shyamsunder, T. T. Fister, R. F.

Klie, K. A. Persson, L. F. Nazar. Enabling Selective Zinc-Ion Intercalation by a Eutectic Electrolyte for Practical Anodeless Zinc Batteries. *Nat. Commun.* **2023**, 14, 3067. Copyright © 2023 Springer Nature, reproduced with permission from Springer Nature.

Chapter 6 introduces an inorganic 3A zeolite-based membrane into MMBs to stabilize the Mg anode for the first time and achieve its excellent performance at high current densities. To establish proof of concept, we chose a 0.25 M magnesium hexafluoroisoproxy borate ($Mg(B(Ohfip)_4)_2$)/G2 electrolyte as a platform for study. We identified that the short lifetime of Mg plating/stripping originates from the high activity of free G2 solvent molecules that reduce on the Mg/electrolyte interface to form a thick surface layer of decomposition by-products. This induces inhomogeneous Mg deposition and rapid cell failure. By using a low-cost zeolite film based on 3Å molecular sieves as a protective interface on the Mg anode, G2 decomposition is effectively suppressed, generating a smooth Mg plating morphology and a thinner solid electrolyte interphase (SEI). This is ascribed to the significantly alleviated free-G2 fraction within this interface revealed by Fourier-transform infrared (FTIR) spectroscopy. The protected Mg anode thus achieves a 750-fold extended lifetime in Mg||Mg symmetric cells (over 6000 hours) at a current density of 0.3 mA cm^{-2} and an areal capacity of 0.3 mAh cm^{-2}. Two chemically-different Mg^{2+} environments were revealed by ^{25}Mg magic angle spinning nuclear magnetic resonance (MAS NMR) spectroscopy, responsible for two Mg^{2+} migration pathways through the zeolite membrane. A prototype full cell based on a Mo_3S_4 cathode exhibits excellent capacity retention of 91% over 200 cycles. We also demonstrate the system is very stable at a high operation voltage of > 3.5 V vs. Mg^{2+}/Mg with polyaniline (PANI) as the cathode. By simultaneously suppressing the shuttling of dissolved PANI monomers with the zeolite membrane, a high energy density up to 320 Wh kg_{PANI}^{-1} and power density of 1320 W kg_{PANI}^{-1} are achieved. The work has been published as: C. Li, A. Shyamsunder, B. Key, Z. Yu, L. F. Nazar. Stabilizing Magnesium Plating by a Low-Cost Inorganic Surface Membrane for High-Voltage and High-Power Mg Batteries. *Joule* **2023**, 7, 2798-2813, Copyright © 2023 Elsevier Inc., reproduced with permission from Elsevier.

Chapter 7 designs a new co-ethereal phosphate electrolyte (CEPE) system that enables fast and highly stable Mg^{2+}/Mg redox activity at the anode and facile anion storage chemistry

at the cathode using commercial $Mg(TFSI)_2$ as salt. A family of methyl phosphates ($((CH_3)_3(CH_2)_nPO_4$, n = 0 - 4) with high dielectric constants and donor numbers were selected as electrolyte additives to interrupt [Mg^{2+}-$TFSI^-$] CIPs (**Scheme 1b**). This results in suppressed $TFSI^-$ reduction, which limits the thickness of the passivation layer and greatly lowers the voltage hysteresis for Mg plating/stripping. To further improve the Mg anode reversibility and stability, different ethers were chosen as co-solvents to tune the Mg^{2+} solvation sheath, thus facilitating desolvation and nanoscale Mg nucleation/growth (**Scheme 1c**). By combining advanced spectroscopy techniques, molecular dynamics (MD) simulations, and density-functional-theory (DFT) calculations, the Mg^{2+} solvation structure and its interaction with anions or solvents are disclosed in depth. The optimized CEPE electrolytes sustain highly reversible Mg plating/stripping behavior at a range of current densities. We demonstrate ultra-stable Mg plating/stripping for over 7000 hours (9.7 months) at a practical current density of 2 mA cm^{-2} and an areal capacity of 2 mAh cm^{-2}. Importantly, the 4 V anodic stability of these electrolytes enables polyaniline||Mg full cells to run up to 3.5 V for over 400 cycles at a fast 2C rate with excellent capacity retention. This work has been published as: C. Li, R. D. Guha, A. Shyamsunder, K. A. Persson, L. F. Nazar. A weakly ion pairing electrolyte designed for high voltage magnesium batteries. *Energy & Environ. Sci.* **2024**, 17, 190-204

The final chapter summarizes the work of the entire thesis and proposes potential further directions of electrolyte design of AZMBs and MMBs.

Chapter 2 Methods and Techniques

2.1 Electrolytes and Electrode Preparation

The aqueous Zn electrolytes studied in Chapter 3-6 are prepared by mixing as-purchased Zn salts in weighted amounts in either pure deionized water or mixed hybrid solvents. The mixtures were then stirred until a clear solution was obtained, which was directly used as electrolytes for further physical or electrochemical characterization. All aqueous Zn electrolytes preparation was conducted in ambient conditions.

Non-aqueous Mg electrolyte is very sensitive to moisture. All Mg salts were pre-dried in a vacuum Buchi at around 150 °C for at least three days. The as-purchased nonaqueous solvents were dried using 3A molecular sieves twice to remove the residual moisture in the solvent. To prepare Mg electrolyte, weighted amounts of pre-dried Mg salts were dissolved in solvents under vigorous stirring until a clear solution is obtained. All non-aqueous Mg electrolytes were prepared inside the glovebox.

AZMBs and MMBs studied in this thesis directly use polished Zn or Mg metal as the anode, which was pouched into proper sizes before being assembled into the cells. The cathodes were either prepared by doctor blading the active materials, polyvinylidenefluoride (PVDF) and carbon black with controlled ratio onto the metal foil or carbon paper; or fabricating the mixture of active materials, polytetrafluoroethylene (PTFE) and carbon black into a free-standing membrane. After drying at 60 °C or 100 °C overnight, these cathodes were pouched into small disks that were used for cell assembly.

2.2 Powder X-Ray Diffraction Techniques

X-ray diffraction (XRD) is a commonly used technique to identify phase composition. XRD analysis is based on the Bragg's law, as shown in **Equation 2.1**:

$$n\lambda = 2d \cdot \sin\theta \quad \textbf{Equation 2.1}$$

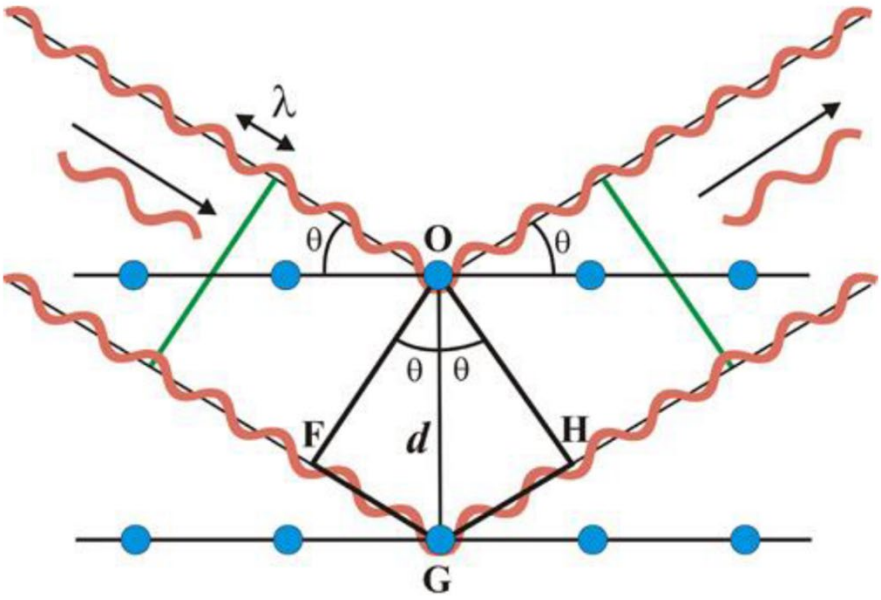

Figure 2.1 Schematic of Bragg's law. Adapted from Ref. 68.

where λ is the wavelength of the X-ray, d is the distance between crystallographic planes in the crystal structures, and θ is the angle between the incident X-ray beam and the parallel planes, as shown in **Figure 2.1**.[68] When two parallel X-ray beams are diffracted by two neighboring parallel planes with a distance of d, the beam going into a deeper plane travels an extra distance of $2d \sin \theta$. When the Bragg's law is satisfied, the two parallel beams will be in phase when they eventually reach the X-ray detector and reflected by the observable intensity of reflected X-rays. Therefore, d, assigned to plane index, can be directly correlated with θ which is known experimentally. As powder sample contains millions of single crystals that are oriented differently, a series of the θ detected in powder XRD experiments will give a whole intensity pattern including all plane indices that satisfied the Bragg's Law. This pattern can be used to compare with a comprehensive database to identify the phase component and crystal structures of target samples.

In this thesis, all powder XRD experiments were conducted using a PANalytical Empyrean diffractometer using Cu-Kα radiation. In the *operando* XRD experiments in **Chapter 5**, the diffraction patterns were collected continuously when the cell was in

galvanostatic cycling. By collecting a series of XRD patterns, the evolution of crystalline phases during electrochemical charge/discharge can be explored. The *operando* experiments were performed using a home-made Swagelok-type cell with a glassy-carbon window for X-ray penetration.

2.3 Electron Microscopy

Advanced electron microscopy studies can provide high-resolution images of specimens, for example, surface morphology of electrodeposited metal anodes. For typical scanning electron microscopy (SEM), a high-energy (0.2~40 keV) focused electron beam generated by an accelerating voltage (5~20 kV) hits the specimen surface, generating a range of electrons and X-rays (**Figure 2.2**)[69] which are detected by the specialized detectors. The collected electrons are further processed to generate high-resolution images. In addition, the

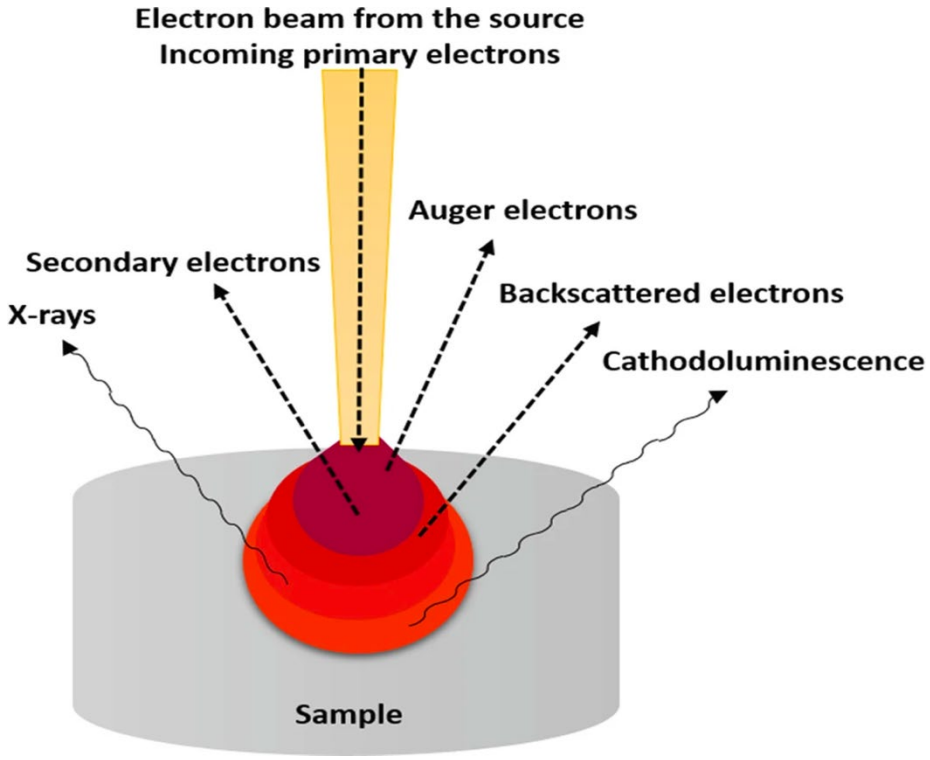

Figure 2.2 Schematic diagram of different types of interaction between the incident electron beam and specimen. Adapted from Ref. 69. Copyright @ 2018 Springer Nature.

emitting characteristic X-rays with different energies can also be detected to identify the elements existed in the specimen, called energy dispersive X-ray spectroscopy (EDX). For a transmission electron microscopy (TEM) or scanning transmission electron microscopy (STEM) study, the higher accelerating voltages of 100~400 kV will be used, allowing much better image resolution even to the atomic level.

In this thesis, the SEM morphological and elemental analysis of the materials was examined with Zeiss Ultra Plus field emission SEM equipped with an EDX. STEM images and electron energy loss spectroscopy (EELS) in **Chapter 5** were conducted by Dr. Arashdeep Singh Thind at the University of Illinois Chicago using a JEOL JEM-ARM200CF microscope operating at 200 kV. TEM images and electron energy loss spectroscopy (EELS) in **Chapter 7** were performed by the Canadian Centre for Electron Microscopy using a Spectra Ultra 30-300kV TEM (Thermo Fisher Scientific) equipped with a Cs probe and image aberration correctors that was operated at 200 kV. An attached Ultra-X EDS detector was used to map specimens and collect EELS data.

2.4 X-Ray Photoelectron Spectroscopy

X-ray photoelectron spectroscopy is a sensitive technique to characterize the oxidation states of elements at the surface of the specimen. The detecting limit is normally from the top 1~10 nm of the materials. During a typical XPS experiment, the sample was irradiated with a beam of X-rays and electrons at ground state are excited and emitted from the original orbitals into the vacuum. The electron energy transition during this process can be described as **Equation 2.2**,

$$E_{binding} = h\nu - E_{kinetic} - \phi \qquad \textbf{Equation 2.2}$$

where $E_{binding}$, $E_{kinetic}$, $h\nu$ and ϕ represent the binding energy of the electron that is ejected and correlated to oxidation states of specific elements, the kinetic energy of the photoelectron after emission, the X-ray energy, and the work function specific to the spectrometer that is irrespective of the sample. The XPS spectra were obtained by probing the kinetic energy and the number of photoelectrons to calculate the binding energy based on known hv of incident

X-rays. Thus, the information of elements can be extracted based on the obtained binding energy.

In this thesis, XPS experiments were conducted on a Thermo Scientific K-Alpha XPS instrument. CasaXPS software was used to conduct XPS data analysis, where the C 1s peak of 284.8 eV was used to calibrate the binding energies. Spectral fitting was based on Gaussian–Lorentzian functions and a Shirley-type background.

2.5 X-Ray Absorption Spectroscopy

X-ray absorption spectroscopy (XAS) is a widely used technique for determining the local geometric and/or electronic structure of matter. In a typical XAS experiment, a series of X-rays with different energies are illustrated on a specimen. The core electrons in this specimen would absorb the X-rays and get excited to an unoccupied orbital, leaving a hole in the original orbital. Such an empty hole is a highly unstable state, and electron from higher energy level can be relaxed and filled in this hole with the fluorescence of X-rays. Both absorbed and fluorescence X-rays can reveal the orbital energies.

A typical XAS spectra includes three main region: (1) the absorption threshold determined by the transition to the lowest unoccupied states; (2) the X-ray absorption near-edge structure (XANES) with the kinetic energies of photoelectron ranging from 10 to 150 eV above the chemical potential, and usually studies the oxidation state and bonding environments of the elements; (3) the extended X-ray absorption fine structure (EXAFS) at high kinetic energy range of the photoelectron, which gives details for local structures of elements. XAS is a bulk technique that can be used to study both solid or liquid samples.

In **Chapter 5** of this thesis, the XAS is mainly used to explore the solvation structure of Zn^{2+} in different aqueous electrolytes. The experiments were conducted in transmission mode using a zinc metal foil reference (9659 eV) by Dr. Timothy T. Fister in Argonne National Laboratory.

2.6 Fourier Transformed Infrared and Raman Spectroscopies

Fourier transformed infrared (FTIR) and Raman spectroscopy are both based on interaction of photons with the vibrational, rotational or other low-frequency modes of a molecule. Raman spectroscopy measures inelastic scattering of photons, while infrared measures the absorption of infrared photons. Both techniques are frequently used to explore the chemical bonding/ environment of a molecule. Samples in all forms of solid, liquid or gas can all be measured.

In this thesis, liquid FTIR were carried out on a Bruker Tensor 27 system equipped with attenuated total reflection (ATR). Liquid Raman spectra were collected using a 532 nm laser (Raman HORIBA HR800). Spectra were obtained using 3-5 accumulations with a total acquisition time ranging from 10-20 minutes under a 10x objective lens.

2.7 Thermogravimetric Analysis

Thermogravimetric analysis (TGA) is often coupled with differential scanning calorimetry (DSC), to measure the evolution of physical (melting, freezing, etc.) and chemical (endothermic and exothermic reaction) properties of a sample as a function of temperature. In a typical TG experiment, temperature is changed in a linear manner, the corresponding mass change and thermal flow from the sample can be recorded to compare with a reference (usually an empty sample holder). In this way, the change in sample mass can be correlated with the specific temperatures that causes the thermal decomposition, reduction/oxidation or phase transition of a sample.

In this thesis, the TGA in **Chapter 4** is used to determine the carbon content in the synthesized materials. The experiment was conducted in the air at a heating rate of 10 °C min^{-1} on a TA Instruments SDT Q500. In **Chapter 5**, the freezing points of a series of hybrid aqueous Zn electrolytes were determined by differential scanning calorimetry (DSC), which was performed on Netzsch STA 449 F3 Jupiter from −100 to 25 °C at a ramp rate of 10 °C min^{-1}.

2.8 Electrochemical Techniques

2.8.1 Galvanostatic Charge/Discharge

In a typical galvanostatic charge/discharge experiment, a constant current is applied to a cell until reaching a cut-off voltage or a limited amount of electricity. During charge, a positive current is applied. During discharge, a negative current is applied.

Galvanostatic cycling is the most widely used testing mode to evaluate the specific capacity, rate capability, cycling stability of a cell, where either cathode, anode, electrolyte or separator can be sample of interest. In the case of cathode materials, passing a constant current through it can lead to the oxidation/reduction of active materials in cathodes, along with corresponding cation de/insertion process. These changes in the chemical state of cathodes are also reflected in the corresponding voltage response. Theoretical, a linear increase/decrease in voltage with respect to capacity corresponds to a solid solution de/intercalation process, while a flat plateau indicates a two-phase reaction. At the end of charge/discharge where the capacity limit exists, a dramatical increase/decrease in voltage can be observed. The current applied in galvanostatically cycling is usually defined by "C-rate". 1C rate means charging/discharging the cell in one hour with full capacity being charged/discharged. The full capacity usually refers to the theoretical specific capacity (Q) of the active materials, which can be calculated from:

$$Q = nF / 3.6\, M_{am}\ (\text{mAh g}^{-1}) \qquad \textbf{Equation 2.3}$$

where F is the Faraday's constant, M_{am} is the molar mass of the active material, n is the number of electrons transferred in charge/discharge.

In this thesis, the cell cycling was carried out using a two electrode configuration, consisting of a cathode, an anode and separators saturated with electrolyte in between. The measurements were carried out using VMP3 potentiostat/galvanostat station (Bio-Logic Science Instruments) at a specific C-rate and proper voltage window.

2.8.2 Linear Sweep Voltammetry

Linear Sweep Voltammetry (LSV) is a technique that is frequently used to measure the oxidative/reductive stability of electrolytes. In a typical LSV measurement, the cell is applied by a swept potential at a constant scan rate. High current response can be recorded at potentials where the electrolyte oxidation/reduction starts. These potentials are determined as the oxidative/reductive limits for electrolytes. Cells with these electrolytes must be cycled within these limits to prevent electrolyte decomposition. In this thesis, a VMP3 potentiostat/galvanostat station (Bio-Logic) was employed for LSV studies at a sweep rate of 1-5 mV s^{-1}, using three-electrode PFA-based Swagelok-type cells with Zn or Mg as the reference electrode, and various metal foil (Ti or Al) as both working and counter electrodes.

2.8.3 Electrochemical Impedance Spectroscopy

Electrochemical impedance spectroscopy (EIS) is a widely used technique to diagnose the resistance of an electrochemical system by recording the current response to an applied potential at varying frequencies. In a typical EIS measurement, the impedance is usually investigated when the electrochemical cell is applied by an AC voltage of 1-10 mV with frequencies ranging from 1M Hz to 10 mHz.

Nyquist plot is the most used spectra to present impedance data. In a typical Nyquist plot, each impedance data at different frequencies is plotted as the negative of the imaginary part of impedance with respect to the real part. Symmetric axes (same axis scale) should always be used for the Nyquist plot in order to convey the information presented by the shape of the plot.

In this thesis, EIS measurements on Mg or Zn symmetric cells were carried out on VMP3 potentiostat/galvanostat station (Bio-Logic Science Instruments). For EIS measurements, the DC voltage was maintained at open-circuit voltage and an AC voltage of 5 or 10 mV in amplitude was applied with a frequency of 1M Hz - 100 mHz.

Chapter 3 Highly Reversible Zn Anode with A Practical Areal Capacity Enabled by a Sustainable Electrolyte and Superacid Interfacial Chemistry

3.1 Introduction

Aqueous zinc-metal batteries are plagued by poor Zn reversibility owing to zinc dendrites and layered double hydroxides (LDH) formation. The aforementioned strategies to enhance Zn reversibitliy and reversibility are mostly at the low areal capacity (0.5 mAh cm^{-2}) which is less than that of practical Li-ion batteries (at least 3 mAh cm^{-2}).

In this chapter, I introduced a novel electrolyte additive, N,N-dimethylformamidium trifluoromethanesulfonate (denoted as DOTf), for an electrolyte based on aqueous 2 M $ZnSO_4$. Its dissociation in water to neutral ion-pairs (the superacid HOTf + DMF) leads to the formation of a fluoride-free, Zn^{2+}-conducting nanostructured SEI on the Zn surface upon cycling in an electrochemical cell. The unique interfacial chemistry is understood by using a comprehensive combination of X-ray photoelectron spectroscopy (XPS), *operando* surface-enhanced infrared absorption spectroscopy (SEIRAS) and cryo-transmission electron microscopy (TEM) studies. We demonstrate the SEI enables water exclusion at the interface, leading to diminished LDH formation. Along with a nanoscale Zn nucleation and growth process, this additive promotes a highly dense and dendrite-free Zn plating morphology. The electrochemistry of Zn||Cu asymmetric cells shows highly stable and reversible Zn plating/stripping at both a lab-level capacity of 0.5 mAh cm^{-2} and practical-level capacity of 4 mAh cm^{-2}. More importantly, this electrolyte is highly compatible with Zn||$Zn_{0.25}V_2O_5{\cdot}nH_2O$ full cells at a low negative: positive (N:P) electrode ratio of 2.5, exhibiting a capacity retention of ~ 83% after 1000 cycles. By limiting the depth of discharge, an enhanced life of more than 2000 cycles can be achieved with less proton intercalation.

I proposed the idea, planned the experiments, performed all electrochemical measurements and wrote the original manuscript. Abhinandan Shyamsunder performed the NMR measurements. Alexis Grace Hoane and Dr. Andrew A. Gewirth carried out the SEIRAS. Chun Yuen Kwok helped with XPS experiments and data analysis. Dr. Daniel M. Long, Dr. Paul G. Kotula and Dr. Kevin R. Zavadil conducted TEM measurements.

3.2 Experimental Approaches

3.2.1 Synthesis of $Zn_{0.25}V_2O_5{\cdot}nH_2O$ Nanobelts

$Zn_{0.25}V_2O_5{\cdot}nH_2O$ nanobelts were synthesized by a previously reported microwave hydrothermal method.[13] Typically, 2 mmol V_2O_5 (99.6%; Sigma-Aldrich) and 1.3 mmol $Zn(CH_3COO)_2{\cdot}2H_2O$ (99%; Sigma-Aldrich) were dispersed in 50 ml water/acetone (volume ratio: 15:1) solution. The mixture was transferred to a sealed Teflon vessel and kept at 180 °C for 90 minutes at a heating rate of 18 °C min^{-1} in an Anton Parr microwave (Synthos 300). The final $Zn_{0.25}V_2O_5{\cdot}nH_2O$ nanobelts were obtained by filtration, washing with deionized water and isopropanol and drying in a 60 °C oven for 24 h.

3.2.2 Electrochemical Measurements

The $Zn_{0.25}V_2O_5{\cdot}nH_2O$ cathodes were prepared by doctor blading the mixture of active materials, conductive carbon Super P and polyvinylidene difluoride (PVDF) in a weight ratio of 7:2:1 in N-methyl-2-pyrrolidone (NMP; anhydrous, 99.5%; Sigma-Aldrich) on carbon paper (thickness: 170 μm). After drying at a 60 °C oven overnight, the electrodes were punched into small coins (diameter: 10 mm). The mass loading of $Zn_{0.25}V_2O_5{\cdot}nH_2O$ was 4.0 ± 0.5 mg cm^{-2}. The full cells were assembled in PFA-based Swagelok-type cells, using the commercial Whatman glass fiber as separators and Cu foil (thickness: 9 μm; diameter: 11 mm) with pre-deposited Zn (about 3 mAh cm^{-2} for both 0.5 V and 0.7 V voltage cutoffs) as the counter and reference electrodes with controlled N:P ratios. The Zn||Cu asymmetric and Zn||Zn symmetric cells were assembled with Zn metal foil (99.9%; Sigma-Aldrich; thickness: 250 μm; diameter: 10 mm) as the electrodes. The amount of electrolyte in each cell is 100 μL. The galvanostatic cycling were carried out on a VMP3 potentiostat/galvanostat station (Bio-logic) at room temperature.

2 M $ZnSO_4$ was prepared by dissolving 10 mmol $ZnSO_4{\cdot}H_2O$ (> 99%; Sigma-Aldrich) into 5 ml deionized water. 2 M $ZnSO_4$ - 50 mM DOTf electrolyte was obtained by adding 0.25

mmol dimethylformamidium trifluoromethanesulfonate (97%; Sigma-Aldrich) into 5 ml 2 M $ZnSO_4$.

3.2.3 Materials Characterization

Powder X-ray diffraction (XRD) studies were carried out on an X-ray diffractometer using Cu-Kα radiation (PANalytical Empyrean) equipped with a PIXcel bidimensional detector. Scanning electron microscopy (SEM) images and energy-dispersive X-ray spectroscopy (EDX) were collected by a Zeiss Ultra field emission SEM instrument equipped with an EDX detector. XPS analysis was conducted on a Thermo Scientific K-Alpha XPS instrument. The binding energies were calibrated using the C 1s peak at 284.8 eV. All spectra were fitted with Gaussian-Lorentzian functions and a Shirley-type background using CasaXPS software. The S 2p doublet peaks were fit using equal full width at half maximum (FWHM), with a 2:1 area ratio and splitting of 1.16 eV between the S 2p 3/2 and S 2p 1/2. The spot size for photoelectron collection was a 400 μm x 200 μm ellipse, and the grid for sputtering was a 1600 μm x 800 μm rectangle, with an Ar^+ etching rate estimated to be ~1.0 nm min^{-1}. NMR experiments were carried out on a Bruker Avance 300 MHZ instrument at ambient temperature. All samples were dissolved in D_2O which served as an internal lock and were loaded into 5 mm tubes (800 μl). ^1H NMR experiments were carried at 300 MHz and ^{13}C NMR experiments were carried at 75 MHz. Heteronuclear Single Quantum Coherence (HSQC) experiments were carried out to correlate the chemical shift of protons (F2 axis) to the ^{13}C chemical shift (F1 axis) of their directly attached carbons. All electrodes that were characterized were collected from the cell, rinsed thoroughly with deionized water and ethanol and dried at 80 °C *in vacuo* overnight. Attenuated total reflectance surface-enhanced infrared absorption spectroscopy (ATR-SEIRAS) was carried out by using a Nicolet Magna-IR 550 spectrometer with a home-built spectro-electrochemical cell that was previously described. *In situ* spectra were collected using the roughened 20 nm Au as the working electrode and a Zn wire as counter and reference electrode. Zn was galvanostatically plated 4 mA cm^{-2} for 30 minutes for both electrolytes and stripped at 4 mA cm^{-2} for 30 minutes for the 2 M $ZnSO_4$ – 100 mM DOTf electrolyte and 28 minutes for the 2M $ZnSO_4$ electrolyte. The reference

spectrum was collected immediately prior to Zn plating and immediately prior to Zn stripping, which was subtracted for all subsequent spectra. A Helios NanoLab 600 FIB/SEM was used to deposit a protective, infiltrating carbon capping layer onto the Zn deposit surface prior to cooling for cryogenic FIB milling, lift-out, and final thinning in a Scios 2 FIB/SEM. The resulting cross-section lamella was stored in liquid nitrogen and loaded into a Gatan 626 cryo holder for cryogenic-STEM, EDS, EELS characterization in an FEI Titan G2 operated at 200 kV. The sulfur K intensity was calibrated using a ZnS standard.

3.3 Highly Reversible Zn Plating/Stripping

The Zn plating/stripping behavior was examined in Zn||Cu asymmetric cells at 1 mA cm^{-2} and 0.5 mAh cm^{-2} - a frequently reported CE test condition for Zn anodes.[24,29,32,70,71] As shown in **Figure 3.1** and **3.2a**, the CE in 2 M $ZnSO_4$ - 50 mM DOTf quickly increases to 99% in the initial 20 cycles and finally stabilizes at > 99.8% for 3500 cycles (**Figure 3.3**). To the

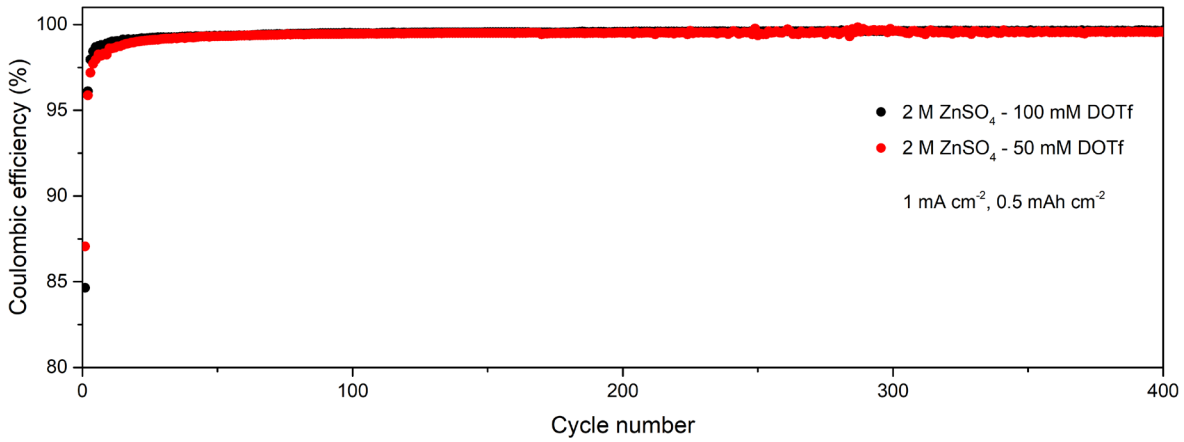

Figure 3.1 CE of Zn Cu asymmetric cells in 2 M $ZnSO_4$ electrolyte s with different concentration of DOTf at 1 mA cm^{-2} and 0.5 mAh cm^{-2} The initial CE decreases as the concentration of DOTf increases from 50 mM to 100 mM. However, the average CE in both electrolytes for a total 400 cycles is ~99.4%. Hence, the final concentration of DOTf was selected as 50 mM in this work.

best of our knowledge, this is the longest cycle life and highest cumulative capacity achieved under these conditions of current density and areal capacity. This results in a high average CE value of 99.7% for a total cumulative capacity of 1750 mAh cm^{-2}. In the 2 M $ZnSO_4$ baseline

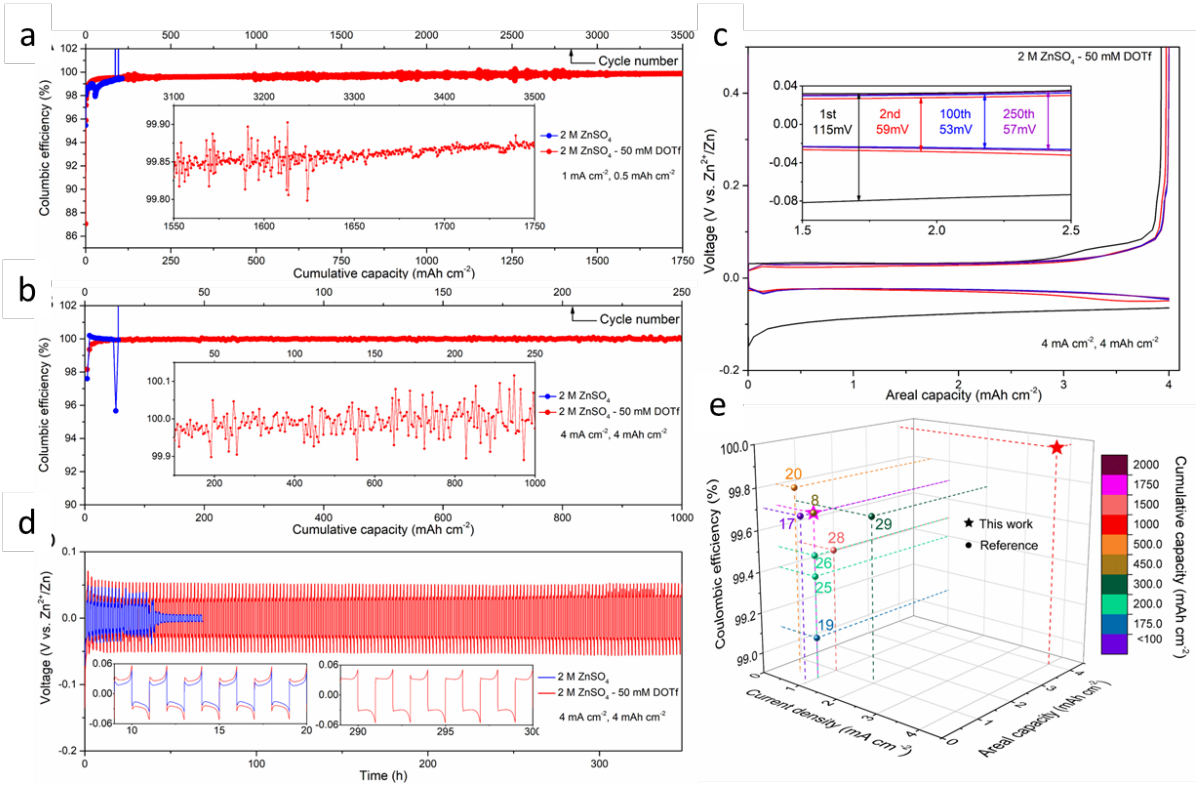

Figure 3.2 (a, b) CE evolution on cycling Zn||Cu asymmetric cells under different conditions: (A) 1 mA cm^{-2} and 0.5 mAh cm^{-2}, (B) 4 mA cm^{-2} and 4 mAh cm^{-2}. Slight variation (± 0.1%) in CE is to be expected. (c) Voltage profiles of the Zn||Cu cell in 2 M ZnSO4 - 50 mM DOTf at 4 mA cm^{-2} and 4 mAh cm^{-2}. (d) Galvanostatic Zn stripping/plating in Zn||Zn symmetric cells at 4 mA cm^{-2} and 4 mAh cm^{-2}. (e) Comparison between the Zn plating/stripping performance of asymmetric cells in this work and that reported based on four critical parameters: Coulombic efficiency, current density, areal capacity and cumulative capacity. Only electrolytes that have demonstrated an average CE of >99% for at least 200 cycles are selected.

electrolyte (**Figure 3.2a**), the Zn||Cu cell shows a fluctuating CE and fails after 214 cycles. More importantly, at practical conditions of 4 mA cm^{-2} and 4 mAh cm^{-2}, the CE in the modified electrolyte reaches over 99.9% within 10 cycles and is preserved for 250 cycles (**Figure 3.2b**). This accounts for an unprecedented high average CE of 99.97% for a total 1000 mAh cm^{-2} cumulative capacity. The cumulative irreversible capacity is only around 0.3 mAh cm^{-2}, which can originated from the HER during Zn plating. The voltage profiles in **Figure 3.2c** validate the highly reversible Zn plating/stripping at such high current density and capacity in the

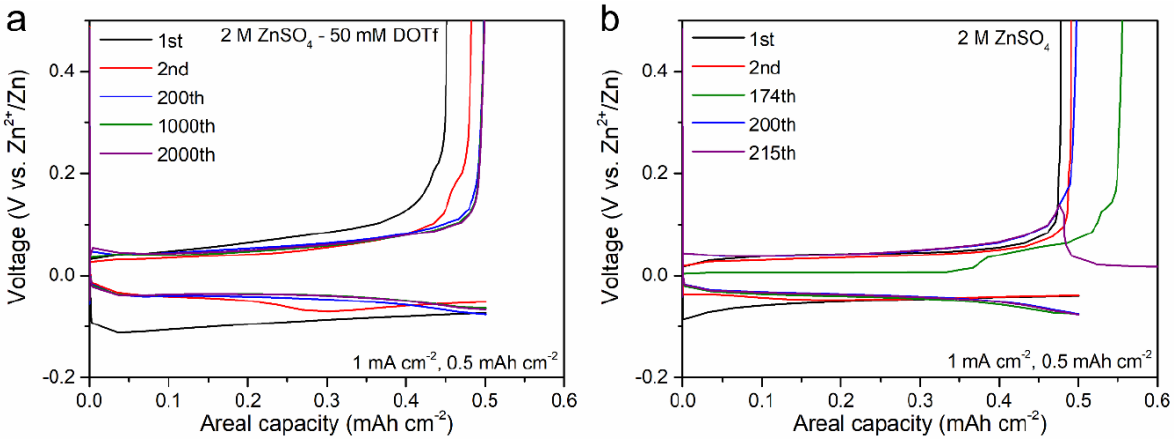

Figure 3.3 . Voltage profiles of Zn||Cu asymmetric cells in different electrolytes at 1 mA cm^{-2} and 0.5 mAh cm^{-2}. **(a)** 2 M $ZnSO_4$-50 mM DOTf ; **(b)** 2 M $ZnSO_4$.

presence of DOTf, as confirmed by the small and stable overpotential of ~28 mV after the initial cycle. In addition, at even more aggressive conditions of 10 mA cm^{-2} and 10 mAh cm^{-2},

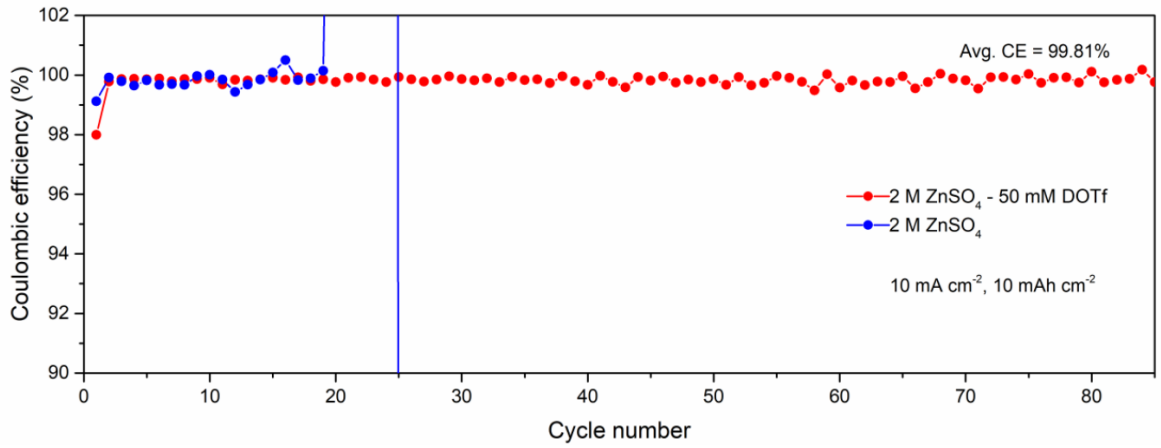

Figure 3.4. CE of Zn||Cu asymmetric cells in different electrolytes at 10 mA $cm^{-2}$and 10 mAh cm^{-2}.

a high average CE of 99.8% can still be achieved (**Figure 3.4**). **Figure 3.2d** displays the excellent stability of a Zn||Zn symmetric cell with 2 M $ZnSO_4$ - 50 mM DOTf, showing steady cycling at 4 mA cm^{-2} and 4 mAh cm^{-2} for nearly 350 hours. This is approximately one order of magnitude longer than that without DOTf, where the cell shorts and quickly fails. We ascribe the slightly higher cell polarization in the presence of the additive (~ 5 mV) to *in-situ* formation of a passivating SEI, as reported elsewhere[30] and discussed below. We note that the "soft

shorts" [72]widely reported in symmetric cell testing are not observed here, as confirmed by the stable and non-zero charge transfer resistance throughout the cycling (**Figure 3.5**).

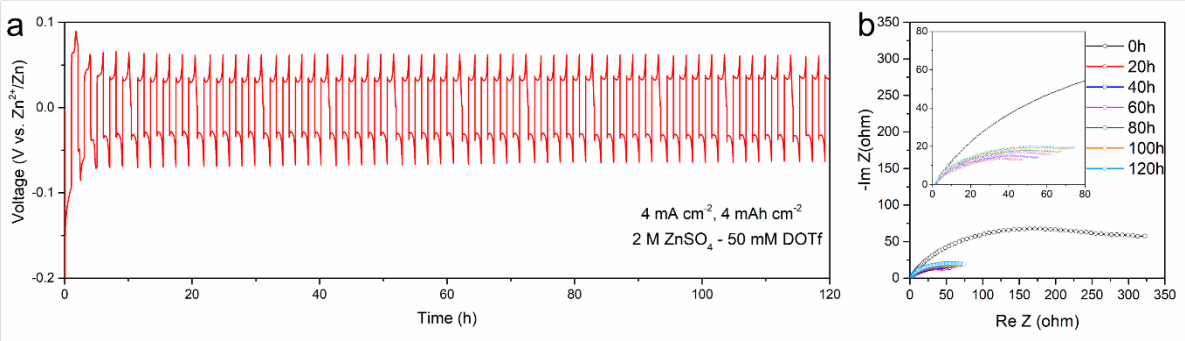

Figure 3.5. Impedance studies of the Zn symmetric cell. **(a)** Voltage profiles of Zn||Zn symmetric cell with the addition of 50 mM DOTf at 4 mA cm^{-2} and 4 mAh cm^{-2} and corresponding **(b)** Nyquist plots at 0h, 20h, 40h, 60h, 80h, 100h and 120h. EIS was conducted after each 10-hour Zn plating/stripping cycle. The stable and non-zero resistance during Zn plating/stripping indicates the absence of soft shorts.

Four important parameters: Zn plating/stripping CE, current density, areal capacity of each plating and stripping, as well as the total cumulative capacity were selected to compare our modified electrolyte to other reported Zn electrolytes.[24,28–30,70,71,73,74] As shown in **Figure 3.2e**, while the metrics exhibited in this work are comparable to, or better than other electrolytes at similar lab-level conditions (in our case, 1 mA cm^{-2} and 0.5 mAh cm^{-2}), we also demonstrate excellent performance under practical conditions (4 mA cm^{-2} and 4 mAh cm^{-2}) with a high CE of 99.97%. It is critical to screen Zn reversibility at both high and low current densities to fully investigate its commercial viability.[66,75] Such promising enhancement of Zn plating/stripping performance can also be extended to other electrolyte systems. (**Figure 3.6**).

3.4 Dendrite-free Zn Plating Morphology

Cu electrodes with plated Zn, retrieved from the asymmetric cells after the 10^{th} plating at 4 mA cm^{-2} and 4 mAh cm^{-2} were analysed by scanning electron microscopy (SEM). Zn plated in 2 M $ZnSO_4$ - 50 mM DOTf shows a smooth and compact layer, formed by merged homogeneous Zn particles with dimensions of ~250 nm (**Figure 3.7a-b**) whereas porous and

dendritic Zn was observed in 2 M $ZnSO_4$ (**Figure 3.7e-f**), consistent with the rapid battery failure in both Zn||Cu and Zn||Zn cells. The cross-sectional view of deposited Zn shows a spongy morphology with a thickness of ~ 13 μm in 2 M $ZnSO_4$ (**Figure 3.7g-h**), whereas a thin ~ 6 μm layer is observed in the modified electrolyte (**Figure 3.7c-d**). This is nearly six times denser than the reported Zn deposition layer with a fluorinated SEI,[30] based on calculation of the Zn capacity and thickness described in Cao et al.[30] Similar morphologies in both electrolytes were also confirmed at 1 mA cm^{-2} and 0.5 mAh cm^{-2} (**Figure 3.8**).

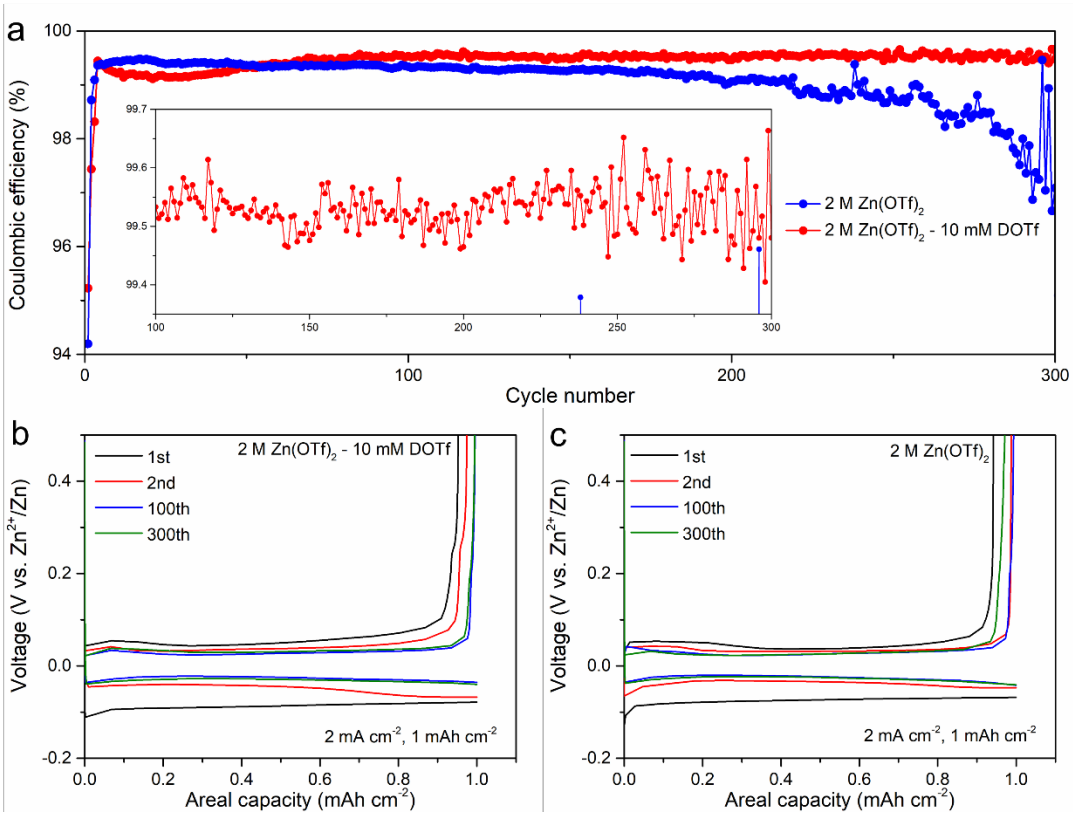

Figure 3.6 The Zn plating/stripping electrochemistry of Zn||Cu asymmetric cells at a current density of 2 mA cm^{-2} and areal capacity of 1 mAh cm^{-2}. **(a)** CE evolution as a function of cycle numbers in different electrolytes; Voltage profiles in **(b)** 2 M $Zn(OTf)_2$ - 10 mM DOTf and **(c)** 2 M $Zn(OTf)_2$.

These results show the effectiveness of the DOTf additive to suppress dendrite growth. A combination of nuclear magnetic resonance (NMR) spectroscopy and X-ray photoelectron

spectroscopy (XPS) studies described below indicate that this can be ascribed to a unique Zn^{2+}-conducting SEI formed on the Zn surface.

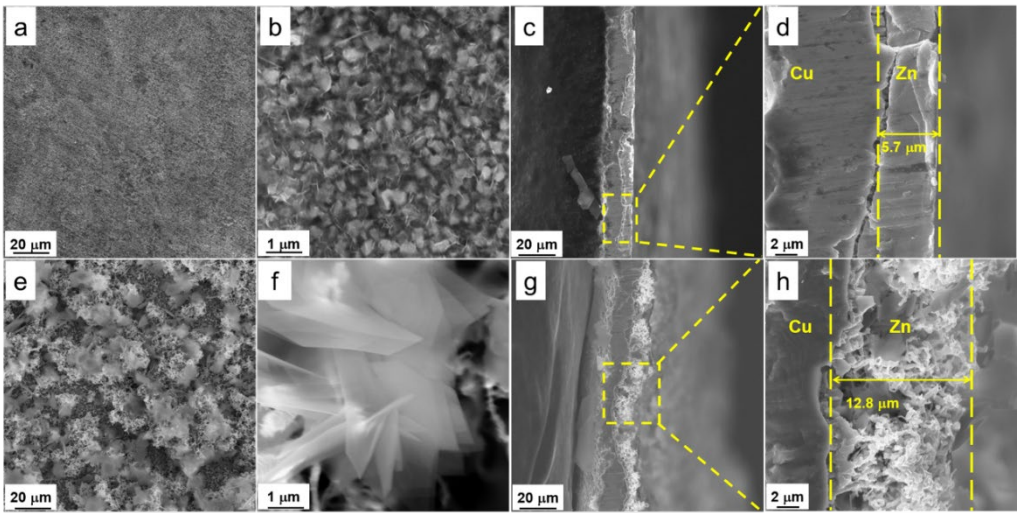

Figure 3.8 Morphologies of plated Zn on Cu after 10 cycles at 4 mA cm^{-2} and 4 mAh cm^{-2}. **(a–d)** SEM images of plated Zn in 2 M $ZnSO_4$-50 mM DOTf: **(a** and **b)** top view and **(c** and **d)** cross-sectional view. **(e–h)** SEM images of plated Zn in 2 M $ZnSO_4$: **(e** and **f)** top view and **(g** and **h)** cross-sectional view. Images shown and indicated thicknesses are representative of the average deposition layers

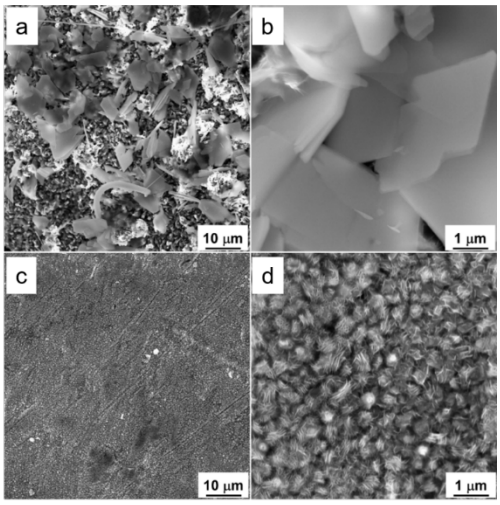

Figure 3.7 SEM images of plated Zn in **(a-b)** 2 M $ZnSO_4$ and **(c-d)** 2 M $ZnSO_4$ – 50 mM DOTf at 1 mA cm^{-2} and 0.5 mAh cm^{-2}.

3.5 Forming the Zn^{2+}-conducting SEI

The ^{1}H NMR spectrum of the 2 M $ZnSO_4$ - 50 mM DOTf solution (**Figure 3.9**) shows characteristic peaks of N,N-dimethylformamide (DMF) at δ= 2.42 ppm, 2.57 ppm and 7.49 ppm, along with two additional peaks at δ= 2.28 ppm and 7.85 ppm which are not observed in the spectrum of 2 M $ZnSO_4$ - 50 mM DMF. Upon adding 50 mM triflic acid (HOTf) into a 2 M $ZnSO_4$ - 50 mM DMF solution, the two additional peaks appear and lead to an identical

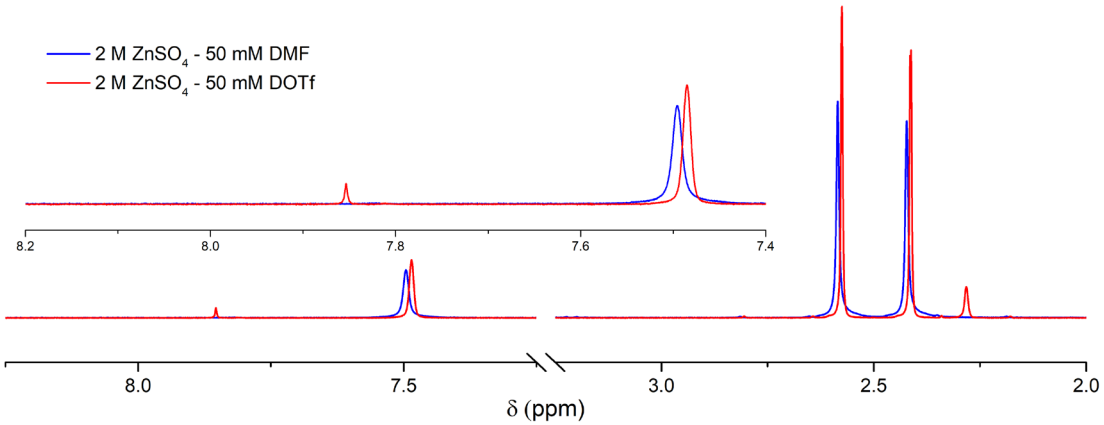

Figure 3.9 ^{1}H-NMR spectrum of the modified electrolyte and 2 M $ZnSO_4$ - 50 mM DMF

pattern (**Figure 3.10a**). These results indicate that DOTf exists as its "neutral ion pair" in water ($[DMF]^{+}[OTf]^{-} \rightarrow$ DMF and HOTf), a phenomenon known for other formamidium ionic liquids.[76,77] The presence of the super-acid HOTf explains the unusually low initial pH of 2 M $ZnSO_4$ - 50 mM DOTf (pH ≈ 1.6). Similar excellent Zn plating/stripping performance was observed using 2 M $ZnSO_4$ - 50 mM DMF - 50 mM HOTf as the electrolyte, (**Figure 3.11**), further corroborating the existence of neutral ion pairs in aqueous solution.

^{1}H-^{13}C Heteronuclear Single Quantum Coherence (HSQC) experiments were carried out to further characterise the additional peaks obtained in the modified electrolyte. As shown in **Figure 3.10b**, three different protons (**a**, **b** and **c**) correlate with three carbons at around δ=164.8 ppm, 36.9 ppm and 31.4 ppm, characteristic of DMF. The highest frequency proton

a' (δ=7.83 ppm) shows a distinguishable correlation with the carbon at δ=166.1 ppm. These point at the possible presence of formic acid which was confirmed through spiking the

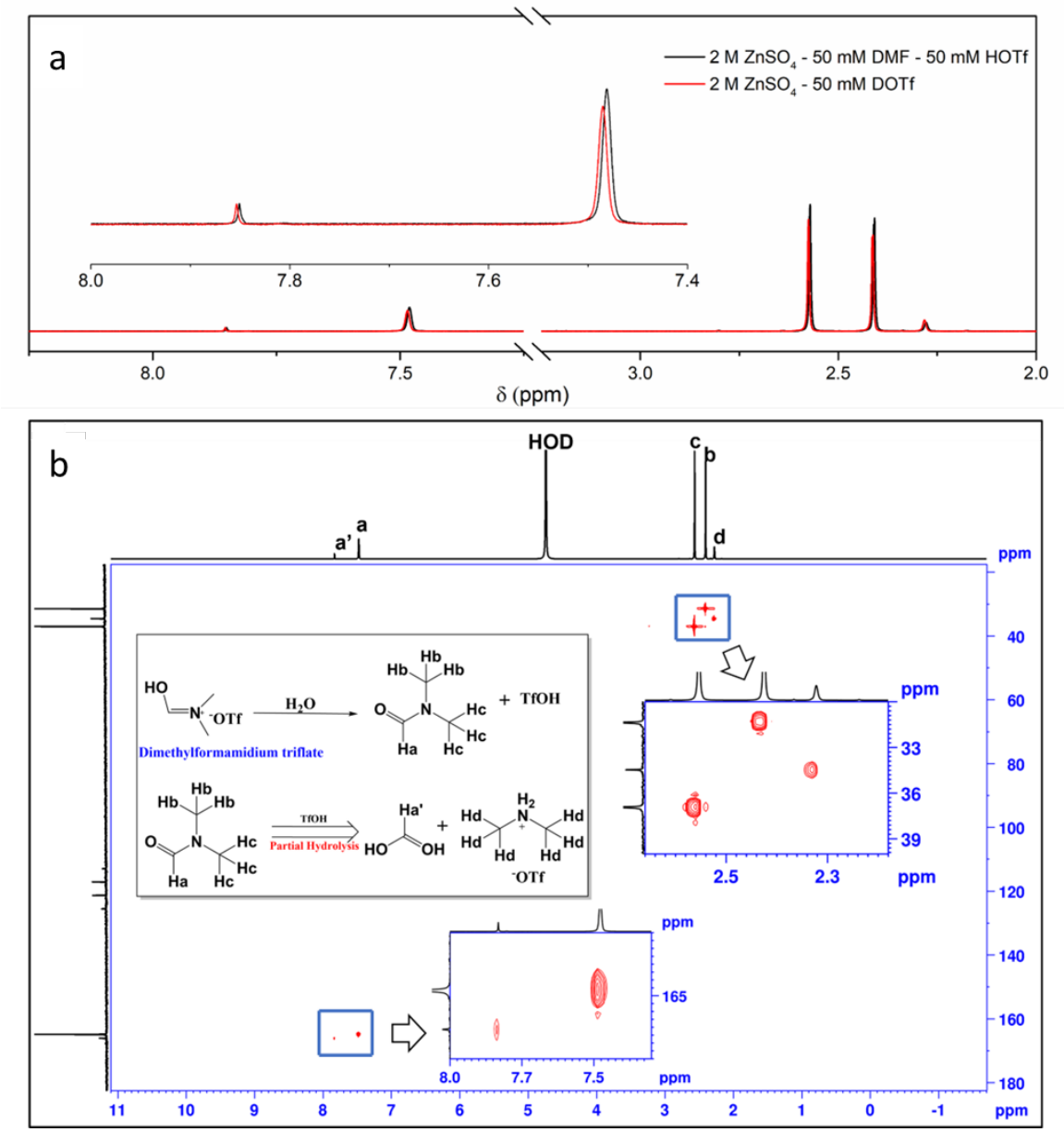

Figure 3.10 NMR studies for the 2 M $ZnSO_4$-50 mM DOTf electrolyte**. (a)** Comparison of the 1H-NMR spectra of 2 M $ZnSO_4$ with 50 mM DOTf and 50 mM DMF-HOTf. **(b)** The HSQC 2D spectrum of the DOTf modified electrolyte. The 1H and 13C patterns are shown on the horizontal axis and the vertical axis, respectively.

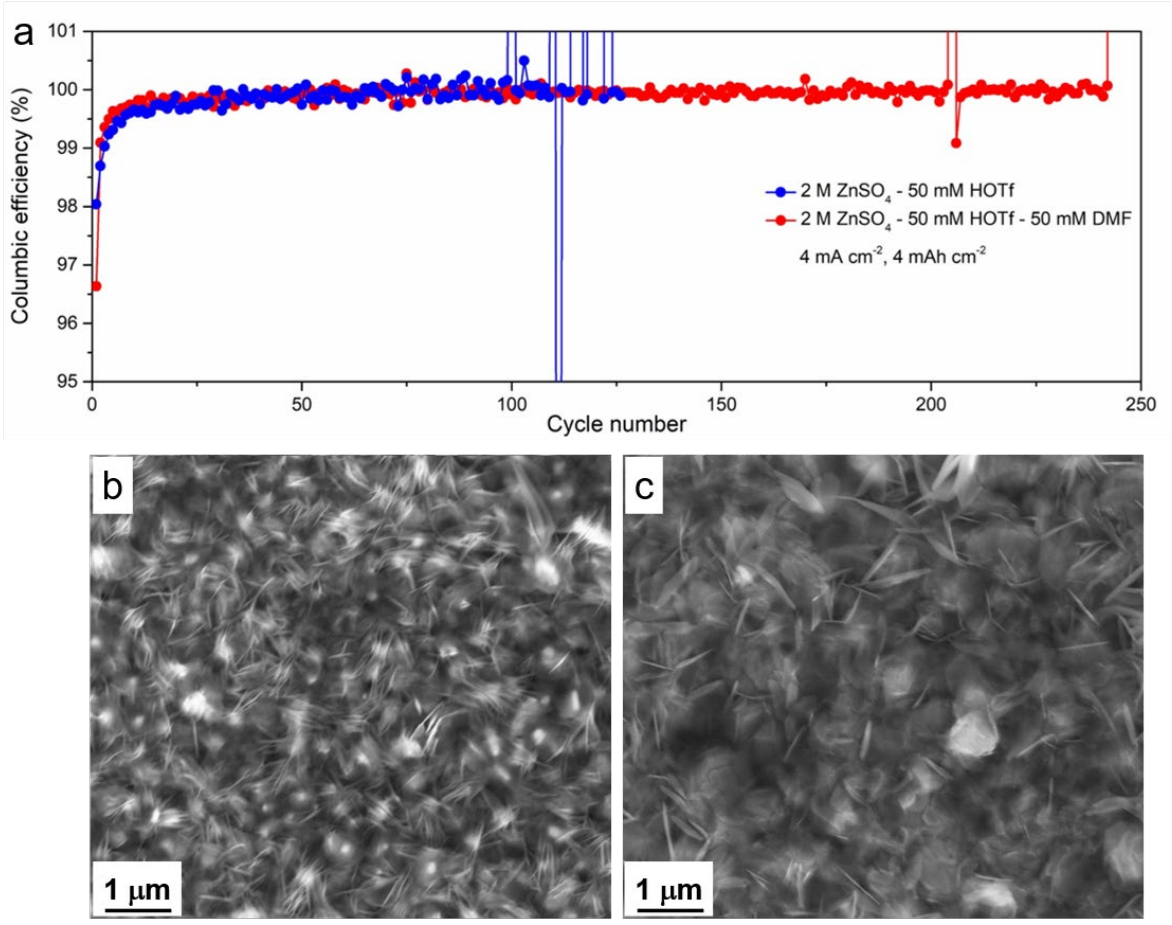

Figure 3.11 The Zn plating/stripping chemistry of different electrolytes at a current density of 4 mA cm-2 and areal capacity of 4 mAh cm-2. **(a)** CE evolution as a function of cycle number in different electrolytes. Surface morphologies of the 10th plated Zn on Cu in **(b)** 2 M $ZnSO_4$ – 50 mM HOTf and **(c)** 2 M $ZnSO_4$ - 50 mM HOTf - 50 mM DMF. The longer cycling life and slightly denser surface morphology in 2 M $ZnSO_4$ - 50 mM HOTf - 50 mM DMF show that DMF plays a key role in improving the Zn stability.

solution with its excess (**Figure 3.12**). The formation of formic acid from DMF (a result of acid hydrolysis reaction),[78] helped us to identify the proton **d** (δ=2.28 ppm) as protonated dimethylamine. While characteristic ion solvent coordination results in a more de-shielded solvent environment,[79] our results (**Figure 3.13**) depict the opposite behaviour. All the DMF peaks are significantly shifted to lower frequency indicative of possible formation of poly-

metal clusters in solution that could shield the solvent environment.[80] These complex molecular species along with the "amine" products obtained through hydrolysis could potentially assist the formation of a Zn^{2+}-conducting SEI layer on the Zn surface during the electrochemical process.

To delve more into the nature of the SEI, XPS was carried out on the topmost surface

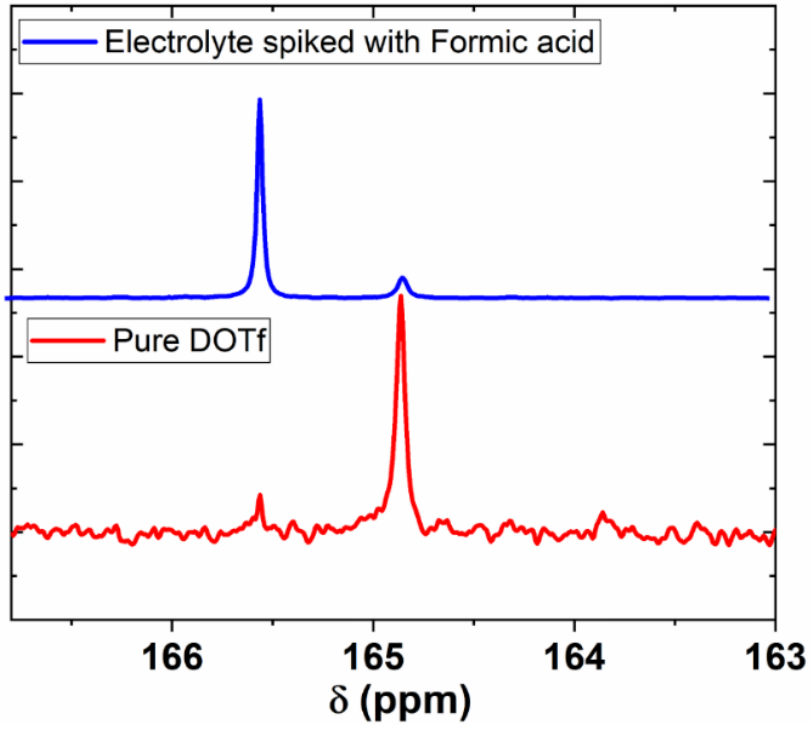

Figure 3.12 ^{13}C-NMR spectra of 200 mM DOTf before (red curve) and after spiking with HCOOH (blue curve). The peak at δ= 165.5 ppm corresponds to the carbonyl hydrogen of HCOOH, while the peak at δ= 164.8 ppm corresponds to the carbonyl hydrogen of DMF.

of the plated Zn, and at a depth of ~2 nm and ~10 nm underlying the surface by removing the upper material *via* 2 min and 10 min Ar^+ sputtering, respectively. The XPS spectra of plated Zn in 2 M $ZnSO_4$ - 50 mM DOTf are shown in **Figure 3.14**. All binding energies were calibrated by using the C 1s peak (at 284.8 eV) as the reference. The N 1s spectra shows a

stable amine-related component (at 399.4 eV) at different depths. This amine signal – which is absent in the additive-free electrolyte - can be ascribed to either dimethylamine bonded to

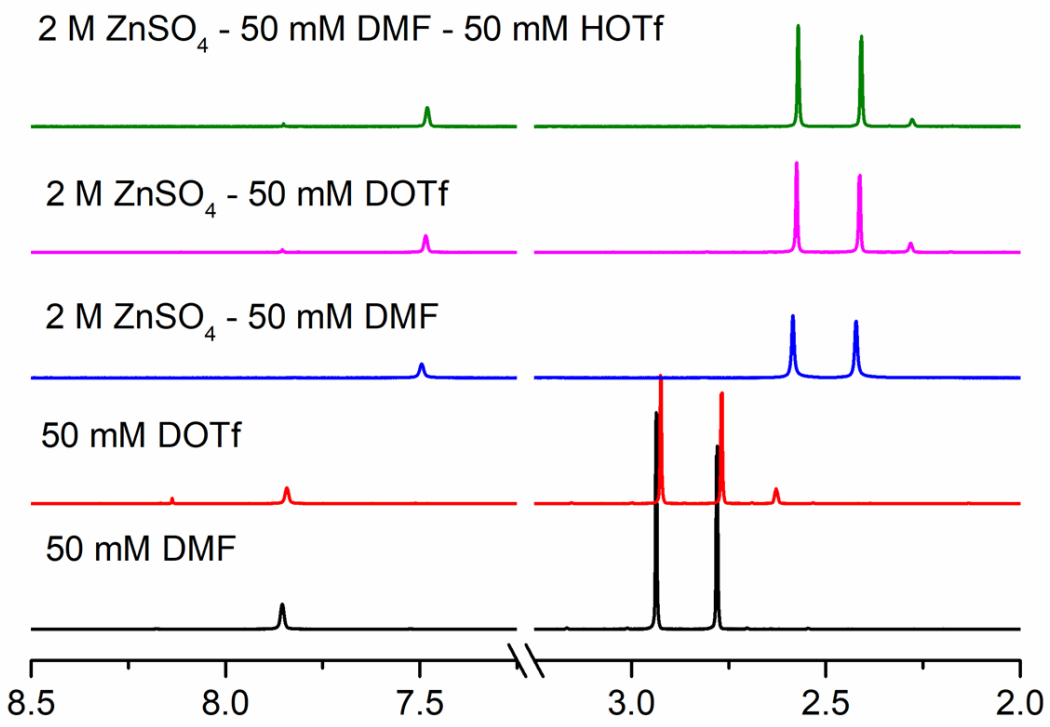

Figure 3.13 ^{1}H-NMR spectra of aqueous solutions as labelled.

Zn^{2+}, or trimethylamine produced by the electrochemical reduction of DMF.[81] The O 1s spectrum of the topmost surface exhibits two major components: SO_4^{2-} (at 532.1 eV, 91%) and $ZnO/Zn(OH)_2$ (at 530.4 eV, 9%). The sulfate signal can be ascribed to the precipitation of Zn salt in the electrolyte.[71,82] The S 2p spectrum also confirms the existence of $ZnSO_4$ (at 169.4 eV, 92%) along with minor ZnS species (at 162.1 eV, 8%). At a depth of ~2 nm (sputtering for 2 min) the $ZnSO_4$ content reduces to ~ 77% in both O 1s and S 2p spectra. Meanwhile, both $ZnO/Zn(OH)_2$ and ZnS fractions increase to ~ 23%. Upon further sputtering to a depth of ~ 10 nm, the $ZnSO_4$ signal is further reduced in intensity while both $ZnO/Zn(OH)_2$ and ZnS increase

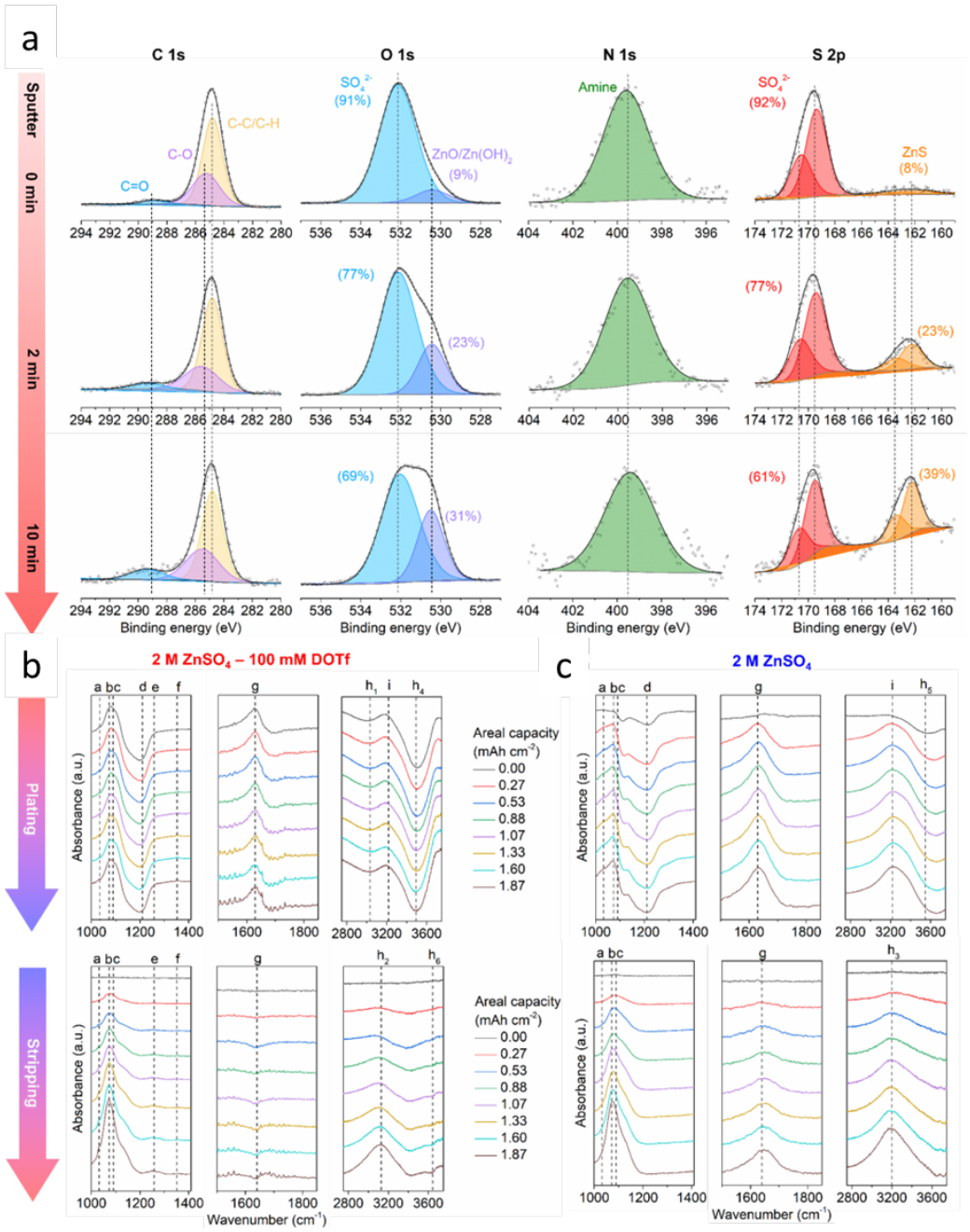

Figure 3.14 (a) XPS spectra for 1st plated Zn on Cu in 2 M $ZnSO_4$-50 mM DOTf at 4 mA cm^{-2} and 4 mAh cm^{-2}. **(b** and **c)** Operando SEIRAS of both plating and stripping process on Au in **(b)** 2 M $ZnSO_4$-100 mM DOTf and **(c)** 2 M $ZnSO_4$ at 4 mA cm^{-2} for 30 min.

to reach over 30% of their respective (O 1s, S 2p) signal. The ZnS component probably

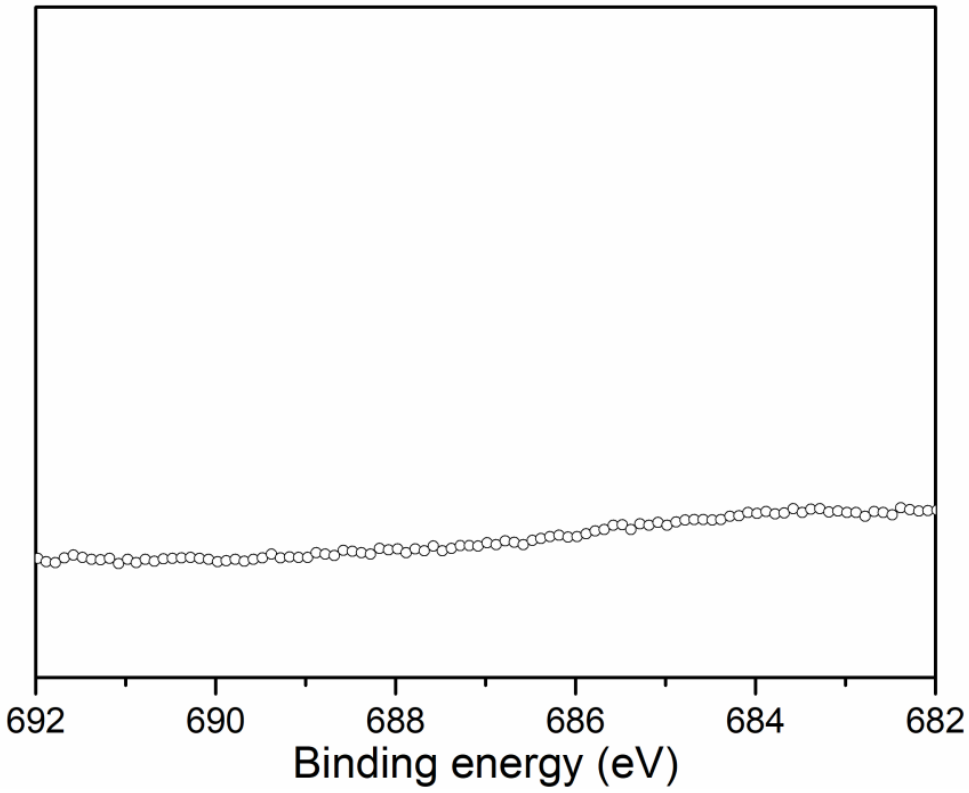

Figure 3.15 F1s XPS spectrum of 1st Plated Zn on Cu in 2 M $ZnSO_4$ - 50 mM DOTf

originates from the reduction of SO_4^{2-} rather than the OTf^- anion owing to the lack of fluorine-related species in the F 1s XPS spectrum (**Figure 3.15**). This conclusion is supported by the lack of a significant ZnS signal in the XPS obtained from deposits grown in a 2 M $Zn(ClO_4)_2$ - 50 mM DOTf electrolyte and where poor Zn reversibility is observed (**Figure 3.16**). It is likely that SO_4^{2-} is reduced to ZnS by the H_2 formed by the chemical reaction between Zn and HOTf in the initial cycles (**Figure 3.17**), as ZnS is also observed on Zn metal soaked in the modified electrolyte (**Figure 3.18**). In addition, no ZnS is observed after soaking Zn in 50 mM DOTf without $ZnSO_4$ and for electrochemically deposited Zn in the baseline electrolyte further

confirming that SO_4^{2-} anion and the chemically formed H_2 are key to the formation of ZnS (**Figure 3.19**).

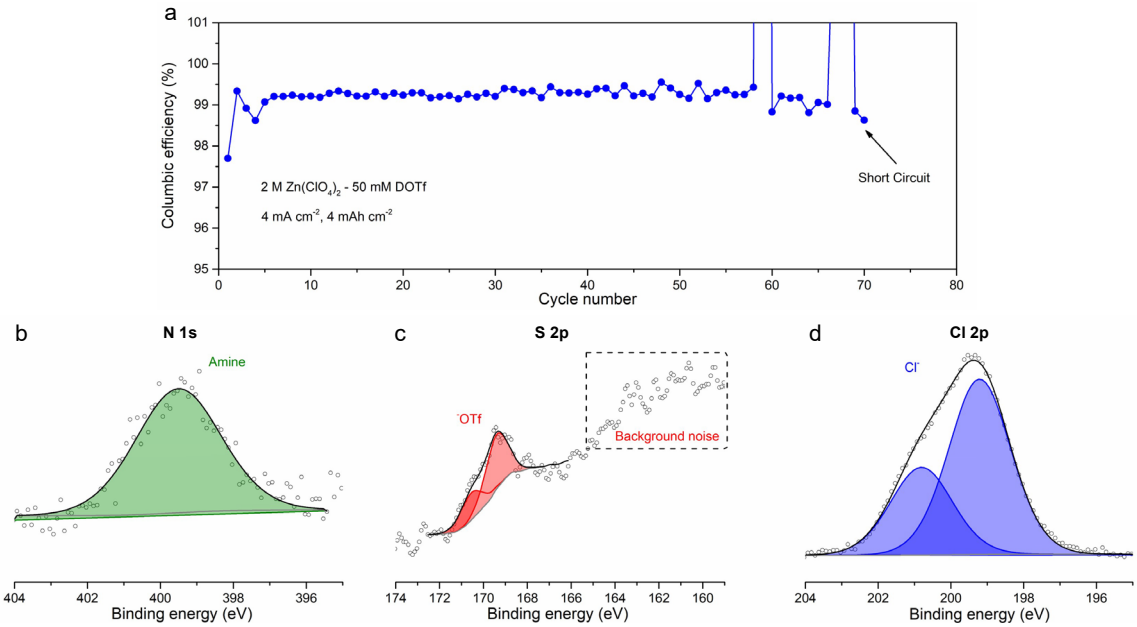

Figure 3.16 Electrochemistry of 2 M $Zn(ClO_4)_2$ - 50 mM DOTf at 4 mA cm_{-2} and 4 mAh cm_{-2}. **(a)** CE evolution of Zn||Cu cell as a function of cycle number. XPS for 1st plated Zn: **(b)** N 1s, **(c)** S 2p and **(d)** Cl 2p. The sulfide region is obscured by the background noise, suggesting either an insignificant amount of (or no) ZnS is formed on the Zn surface.

X-ray diffraction (XRD) analysis reveals that no deleterious LDH forms on plated Zn in the modified electrolyte, whereas well-defined peaks of LDH are observed for the electrode cycled in the baseline electrolyte (**Figure 3.20**). Details of the interfacial chemistry were further studied by surface-enhanced infrared absorption spectroscopy (SEIRAS). In these experiments, a reference spectrum was collected immediately prior to Zn plating and immediately prior to Zn stripping and was subtracted from all subsequent spectra. Although free SO_4^{2-} (band **d**) is displaced from the Au surface during plating owing to the negative surface polarization (**Figure 3.14b-c**), significant amounts of SO_4^{2-} association with Zn^{2+} leads

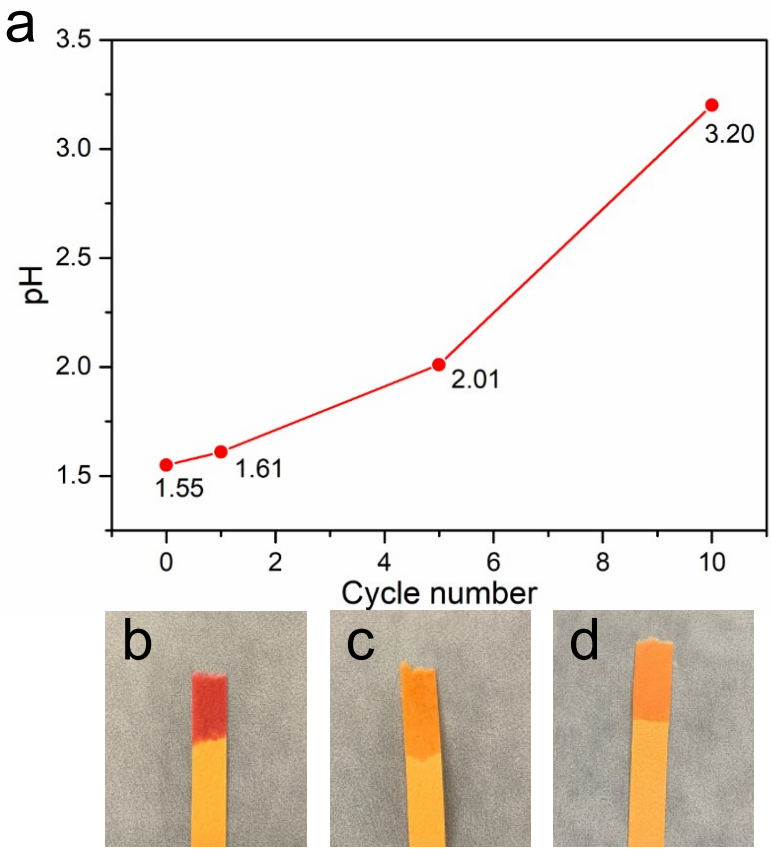

Figure 3.17 pH evolution of 2 M $ZnSO_4$ - 50 mM DOTf during Zn plating/stripping. **(a)** pH changes as a function of cycle number in a beaker cell with 5 ml electrolyte and 16 cm^{-2} Cu and Zn electrode at 4 mA cm^{-2} and 4 mAh cm^{-2}. Images of the pH paper contacted with glass fibre separators **(b)** after initial soaking with 100 uL electrolyte, **(c)** after soaking with the electrolyte after the first cycle and **(d)** after soaking with the electrolyte at the 10th cycle at a current density of 4 mA cm^{-2} and areal capacity of 4 mAh cm^{-2}. The pH increases to 4~5 after the first plating/stripping and stabilization in this range after subsequent cycles indicates that the SEI mainly forms during the initial cycles.

to the presence of $ZnSO_4$ (band **b**) at the interface in both electrolytes. However, in the presence of DOTf, the local acidic environment limits the formation of LDH, possibly allowing for the formation of other products such as ZnS. This acidity also results in lower peak intensities of bands **a, c** and **i** that correspond to $Zn(OH)_2$. In addition, changes to the OTf^- (band **e**) presence at the interface were observed. While peak **e** is obscured by the larger peak **d** during plating, there is a negative-going shoulder of peak **d** at band **e**, indicating that OTf^- is likely leaving the

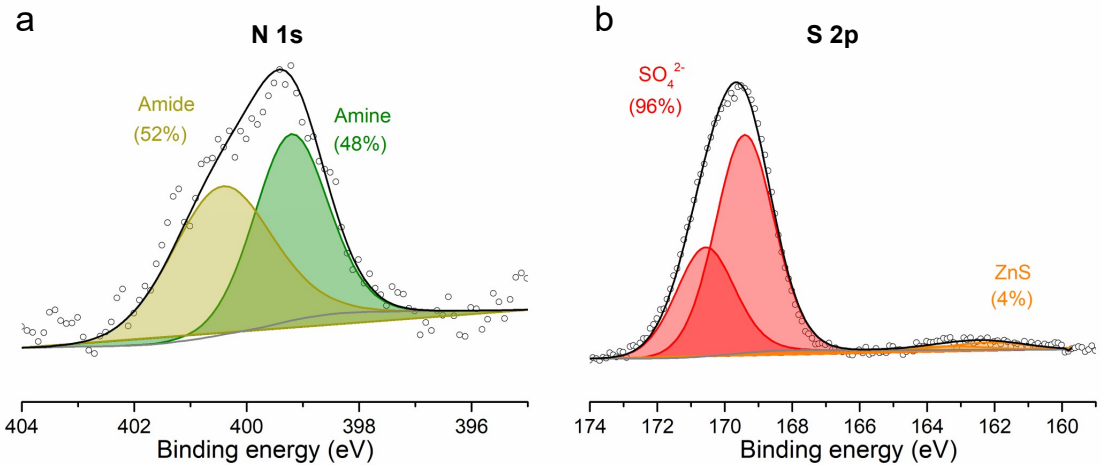

Figure 3.19 . XPS spectra of bare Zn metal soaked in 2 M $ZnSO_4$ - 50 mM DOTf. **(a)** N 1s spectrum. **(b)** S 2p spectrum.

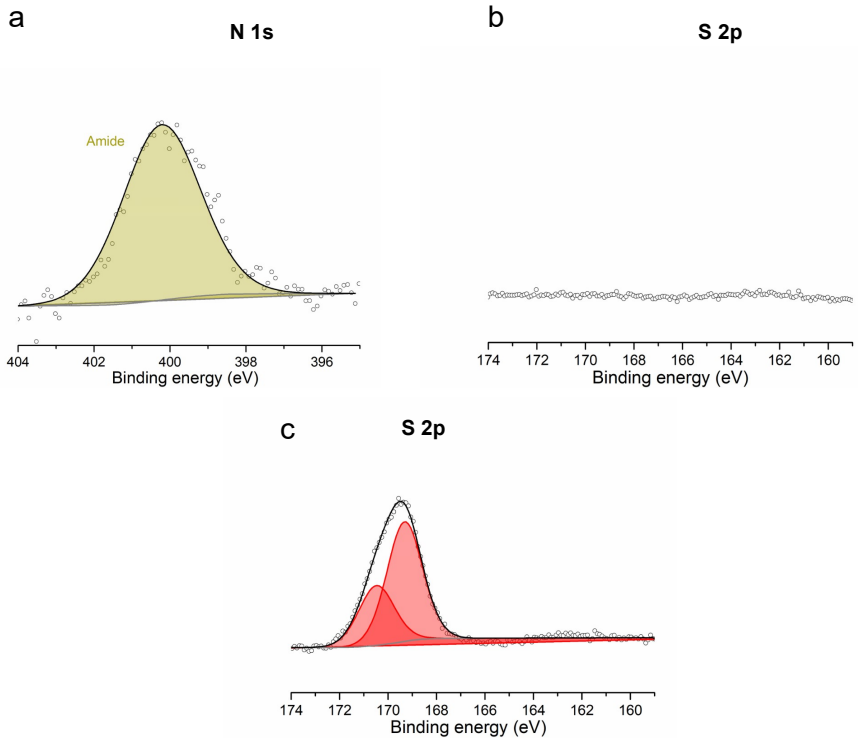

Figure 3.18 XPS spectra of **(a-b)** bare Zn soaked in 50 mM DOTf: **(a)** N 1s **(b)** S 2p; and **(c)** S 2p spectrum of 1st plated Zn layer on Cu in 2 M $ZnSO_4$ at a current density of 4 mA cm^{-2} and areal capacity of 4 mAh cm^{-2}.

interface. During stripping, there is a clear positive-going peak **e**, which indicates that OTf^- is

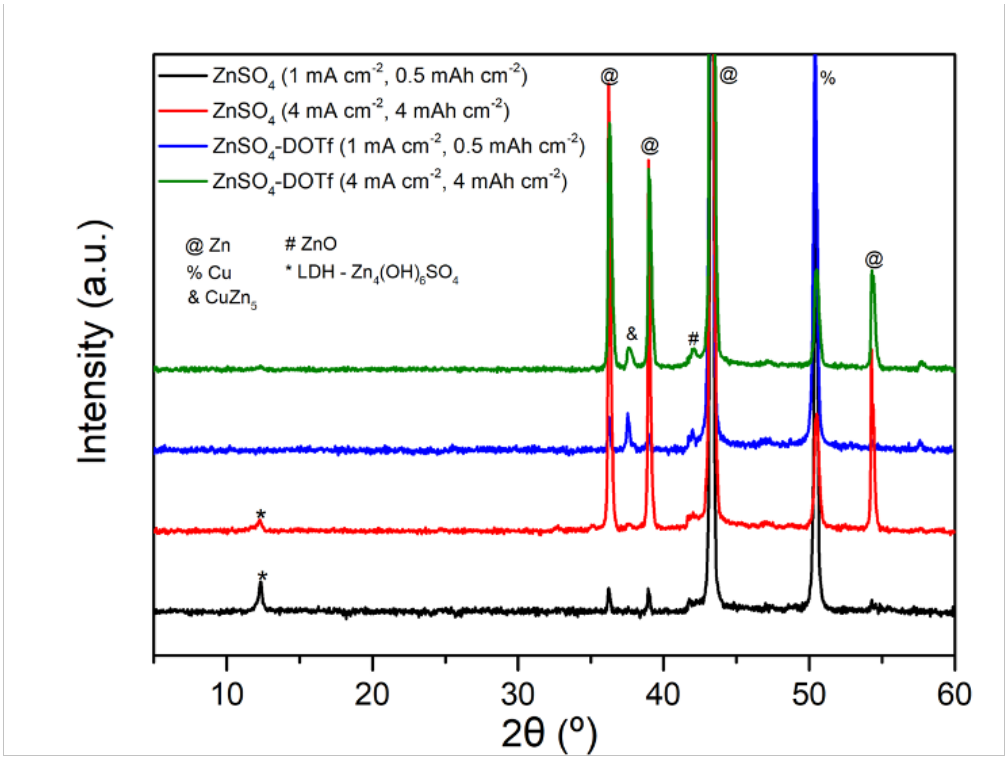

Figure 3.20 XRD of plated Zn on Cu after 10 cycles in different electrolytes under different cycling conditions.

drawn to the surface. The presence of formate (band **f**) at the interface was also identified in both stripping and plating. More importantly, in 2 M $ZnSO_4$ - 100 mM DOTf, much less H_2O approaches the interface during plating compared to that in 2 M $ZnSO_4$, as verified by different intensities of peak **g** which corresponds to the H_2O bending mode. In the case of 2 M $ZnSO_4$ - 100 mM DOTf during plating, each spectrum following reference subtraction exhibits negative-going peaks $\mathbf{h_1}$ and $\mathbf{h_4}$ assigned to H_2O O-H stretching modes, indicating changing H_2O modes at the interface. For 2M $ZnSO_4$ a similar trend is observed with the decrease of peak $\mathbf{h_5}$, although this decrease is somewhat obscured by the stronger positive-going peak **i**. During stripping, peak $\mathbf{h_6}$ appears at a much higher energy, indicating an interrupted hydrogen bonding network of H_2O at the interface. These changes suggest the presence of a H_2O-deficient interface in the presence of DOTf, thus suppressing LDH formation and enhancing Zn reversibility. During stripping, an increase in similar H_2O stretching modes ($\mathbf{h_2}$ and $\mathbf{h_3}$) is

observed in both electrolytes, which probably results from the increasing concentration of Zn^{2+} at the interface that influences the interaction between H_2O and Zn^{2+}.

Structural and chemical mapping of the interphase produced with the DOTf additive was conducted using cryogenic ion milling and cryo-transmission electron microscopy. Low temperature milling reduced the mechanical distortion observed with room temperature milling of the Zn deposit, allowing for more uniform, thinner Zn cross-sections and higher fidelity imaging. A representative dark field image at the surface of a first cycle Zn deposit (4 mA cm^{-2}, 4 mAh cm^{-2}) formed with DOTf is shown in **Figure 3.21a**. The interphase appears as a bright contrast, conformal layer at the electrolyte exposed facets of the Zn grains and underneath a nanosheet structure, viewed edge on here, forms with the

DOTf additive. We find the interphase is a porous layer ranging in thickness from 10 nm to less than 5 nm, where pores are seen as dark regions in the high angle annular dark field (HAADF) image of **Figure 3.21b**. We propose these nanopores are created *in-situ* by the initiation of superacid (HOTf) reduction at the Zn surface to release minute quantities of H_2 as described above. These H_2 also reduces SO_4^{2-} to form ZnS. Nanoporosity is critical as it provides the cation access to a sufficiently thin portion of the nanostructured interphase enabling cation transport, thus producing the dense Zn deposits shown to form in the presence of DOTf. The interphase appears compositionally similar to the nanosheets as a mixture of ZnO and ZnS, with as much as 5% sulfide present, as determined by multivariate analysis of energy dispersive X-ray spectroscopic (EDS) imaging data (**Figure 3.21c-d**).[83] The presence of oxide in the interphase is confirmed from lattice spacings characteristic of wurtzite ZnO observed in high resolution scanning transmission electron microscopy (STEM). We are not able to similarly differentiate the chemical state of S using diffraction or electron energy loss spectroscopy (EELS) due to low concentration and possibly a lack of crystallinity of the ZnS phase. Regardless, the presence of S within the interphase is consistent with the XPS derived composition of the interphase highlighting the DOTf additive's role in forming a nanometric, porous SEI responsible for facilitating Zn cation transport.

In short, these results clearly demonstrate that a uniform nanostructured SEI forms on the Zn surface in 2 M $ZnSO_4$ - 50 mM DOTf electrolyte owing to the unusual surface

chemistry. Reduced water activity can be anticipated within this SEI layer as result of altered Zn^{2+} solvation structures in these pores, as observed in artificial porous protective layers on Zn anodes (for example, zeolitic membranes[84]). Such a porous SEI layer allows Zn^{2+} to diffuse but prevents the formation of LDHs on the Zn anode, and effectively enhances the reversibility and stability of Zn plating/stripping.

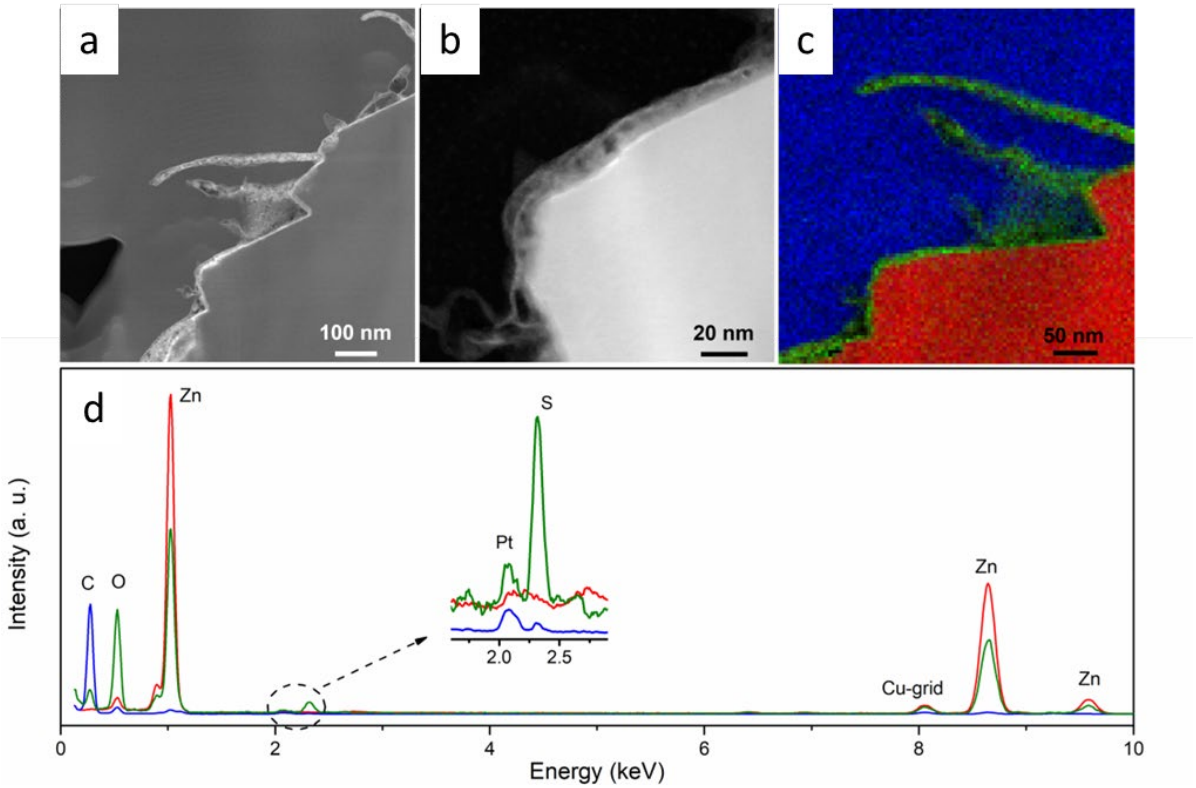

Figure 3.21 Structural and compositional mapping of the SEI formed in 2 M $ZnSO_4$-50 mM DOTf (**a** and **b**) Dark-field and HAADF images showing the conformal and porous structure of the SEI. (**c** and **d**) EDS-based spectral imaging of the SEI with the corresponding multivariate spectral components: Zn deposit, red; interphase and nanosheets, green; carbon cap, blue.

3.6 Nanoscale Zn Nucleation and Growth

The aforementioned SEI also manipulates the initial Zn nucleation and subsequent growth behavior, leading to dendrite-free Zn electrodeposition. The process of nucleation and

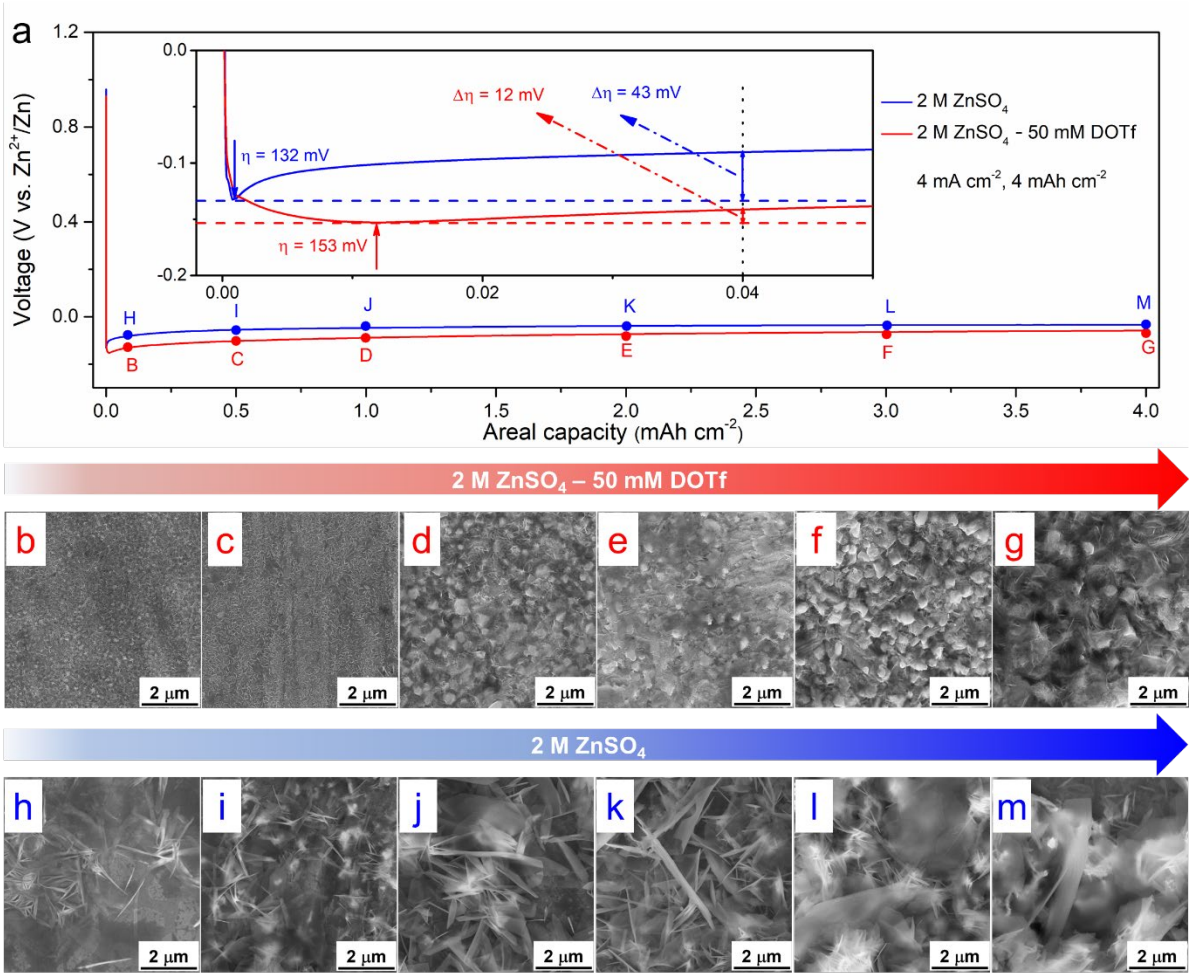

Figure 3.22 Nanoscale nucleation and growth of plated Zn. **(a)** The first plating voltage profiles of Zn||Cu cells at 4 mA cm^{-2} and 4 mAh cm^{-2} with a magnified view of initial nucleation process. **(b–m)** Ex situ SEM images of plated Zn on Cu in 2 M $ZnSO_4$-50 mM DOTf **(b–g)** and 2 M $ZnSO_4$ **(h–m)** after: **(b** and **h)** 0.1 mAh cm^{-2}, **(c** and **i)** 0.5 mAh cm^{-2}, **(d** and **j)** 1.0 mAh cm^{-2}, **(e** and **k)** 2.0 mAh cm^{-2}, **(f** and **l)** 3.0 mAh cm^{-2}, and **(g** and **m)** 4.0 mAh cm^{-2}.

growth is correlated with the evolution of the voltage profile, which allows us to distinguish the overpotentials related to these processes during Zn electrodeposition. **Figure 3.22a** shows

the characteristic voltage profiles of the first Zn plating process in different electrolytes. In the baseline electrolyte, a sharp nucleation overpotential (η) is observed of about 132 mV, whereas in in 2 M $ZnSO_4$ - 50 mM DOTf, η is not at all well defined and is slightly larger (153 mV). This is ascribed to higher impedance at the DOTf-Zn interface due to the presence of the SEI layer that promotes homogeneous deposition of more, smaller and denser Zn nuclei.[85] The SEM image of plated Zn with a capacity of 0.1 mAh cm^{-2} further confirms the uniform and nanoscale Zn deposits in the modified electrolyte (**Figure 3.22b**), whereas sparse needle-shape Zn nuclei about ~ 2 μm in length are observed in 2 M $ZnSO_4$ (**Figure 3.22h**). In addition, the difference in the growth overpotential with respect to the nucleation overpotential (Δη) is 12 mV in the DOTf electrolyte, which is approximately one quarter of that without DOTf. Thus, it is more favorable for Zn to deposit as smaller crystals than large dendrites.[85,86] The

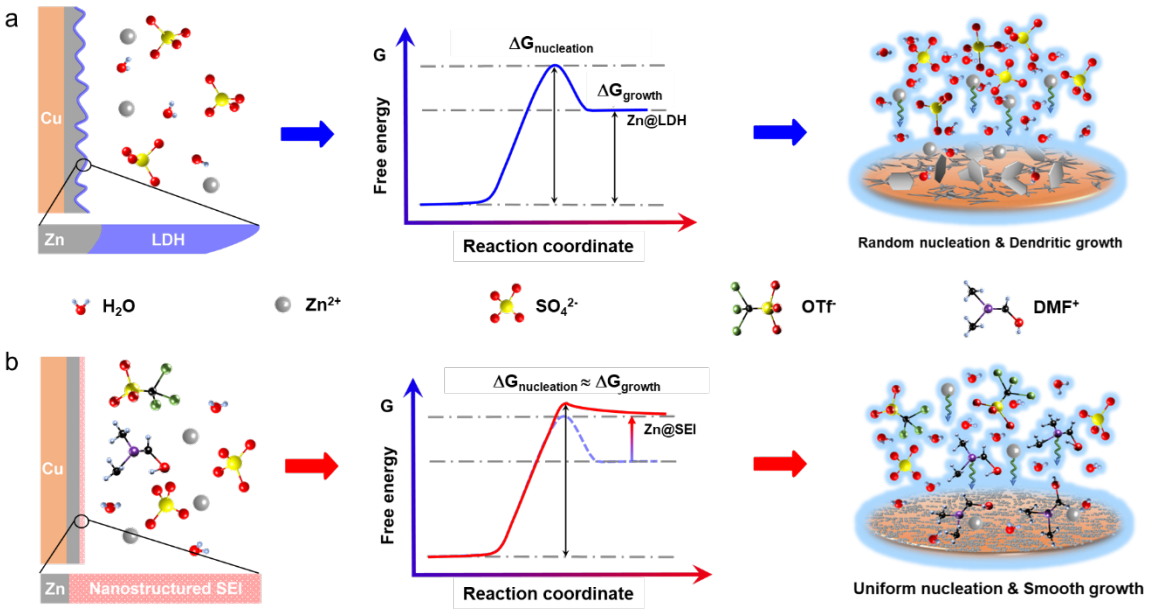

Figure 3.23 Illustration of SEI formation and its role in tuning Zn nucleation and growth in **(a)** 2 M $ZnSO_4$ electrolyte with LDH formation, and **(b)** 2 M $ZnSO_4$-50 mM DOTf electrolyte with SEI formation.

morphological evolution of Zn growth was further investigated by *ex-situ* SEM. Fixed amounts of Zn from 0.1 - 4.0 mAh cm^{-2} were galvanostatically deposited on Cu at 4 mA cm^{-2}. In 2 M $ZnSO_4$ - 50 mM DOTf, nanoscale Zn nuclei grows as small ~ 250 nm crystallites, which merge

into dense and compact Zn deposition layers (**Figure 3.19b-g**), while random Zn dendrites gradually form in the baseline electrolyte (**Figure 3.19h-m**).

The proposed effect of the SEI on Zn nucleation and growth is shown in **Figure 3.23**. In the baseline electrolyte, porous LDH deposits on the Zn surface owing to the progressive HER and consequently local alkaline environment during Zn electrodeposition (**Figure 3.23a**). Such an inhomogeneous surface leads to a large energy difference between the Gibbs energy for Zn nucleation ($\Delta G_{nucleation}$) and growth (ΔG_{growth}). Therefore, Zn^{2+} prefers to deposit on the existing Zn nuclei to form large Zn flakes or dendrites. In contrast, the homogeneous nanostructured SEI in the modified electrolyte raises the ΔG_{growth} to the same level of $\Delta G_{nucleation}$ (**Figure 3.23b**). This significantly reduces the size of the Zn crystallites, and results in uniform dendrite-free Zn deposition.

3.7 Electrochemistry of Zn||$Zn_{0.25}V_2O_5{\cdot}nH_2O$ Full cells

The electrochemistry of 2 M $ZnSO_4$ - 50 mM DOTf electrolyte was tested in full cells, (**Figure 3.24**) using $Zn_{0.25}V_2O_5{\cdot}nH_2O$ as a representative positive electrode to examine compatibility with the stabilized Zn anode (**Figure 3.25** and **3.26**).[13] The rate performance of Zn||$Zn_{0.25}V_2O_5{\cdot}nH_2O$ full cells in 2 M $ZnSO_4$ - 50 mM DOTf electrolyte shows a specific discharge capacity of 326 mAh g^{-1} at 0.3 A g^{-1} (1C rate) and 217 mAh g^{-1} at 2.4 A g^{-1} (**Figure 3.24a-b**), which is slightly higher than that in the absence of DOTf. This shows good compatibility between $Zn_{0.25}V_2O_5{\cdot}nH_2O$ cathode and the modified electrolyte, yielding an average discharge voltage of ~ 0.7 V and energy densities of 228 Wh kg_{zvo}^{-1} or 714 Wh L_{zvo}^{-1} (based on the theoretical density of ZVO of 3.13 g cm^{-3}) at 0.3 A g^{-1}. Long-term Zn reversibility of the full cell was further evaluated in both electrolytes at a current density of 1.5 A g^{-1} (5C rate) with a controlled anode/cathode (N:P) capacity ratio of 2.5 (**3.24c-e**). The estimated volumetric energy density in the modified electrolyte based on both cathode and anode is ~ 400 Wh L^{-1} (the thickness of deposited Zn is estimated as ~5 μm based on **Figure 3.7d**). In the baseline electrolyte, a sharp voltage drop at the end of discharge gradually appears with dramatic capacity loss with continued cycling (**Figure 3.24e**), which is mainly ascribed to the

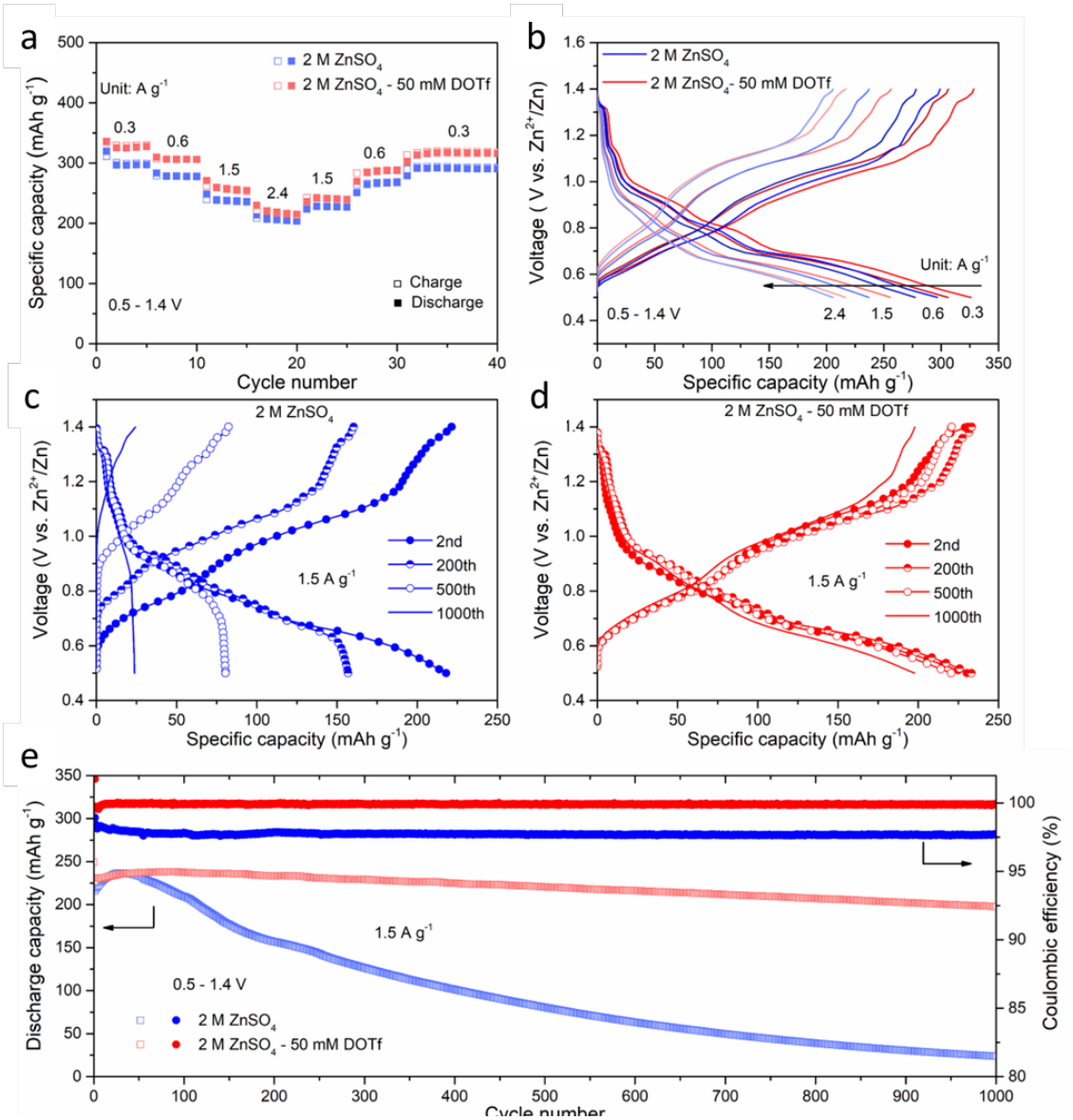

Figure 3.24 Electrochemistry of Zn||$Zn_{0.25}V_2O_5 \cdot nH_2O$ full cells between 0.5 and 1.4 V. **(a** and **b)** Rate performance of full cells in different electrolytes: (a) specific capacity as a function of cycle numbers and **(b)** corresponding charge-discharge curves at different current densities. **(c** and **d)** The voltage profiles of full cells **(c)** in 2 M $ZnSO_4$ and **(d)** 2 M $ZnSO_4$-50 mM DOTf at 5 C (N:P ≈ 2.5). **(e)** Long-term stability of full cells in different electrolytes at 1.5 A g^{-1} (N:P ≈ 2.5). The Zn anode was deposited on Cu foil.

failure of the Zn anode. However, in the modified electrolyte, the high Zn reversibility enables

stable charge/discharge of the Zn|| $Zn_{0.25}V_2O_5 \cdot nH_2O$ cell (**Figure 3.24d**) at the controlled N:P

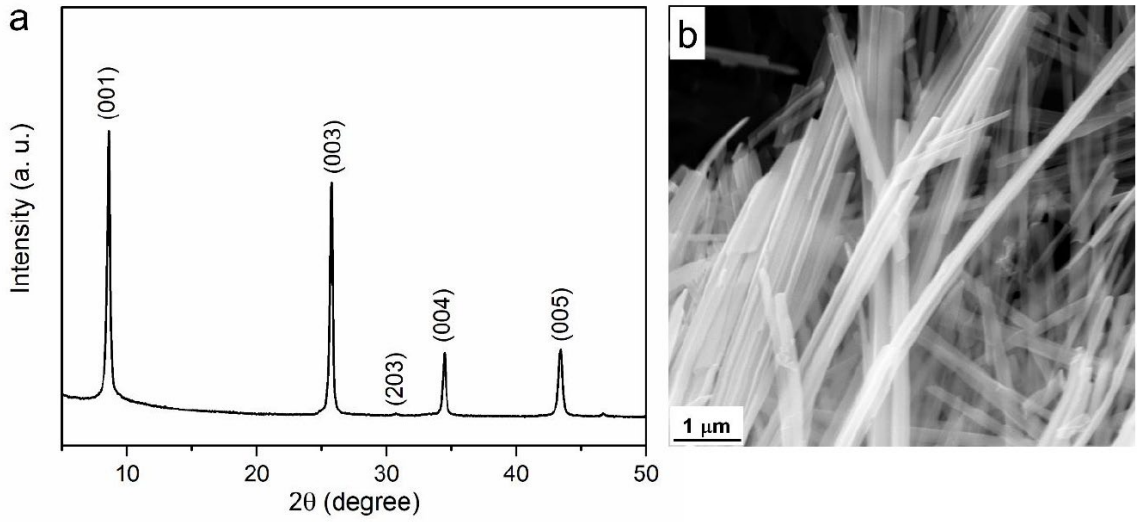

Figure 3.25 Characterization of $Zn_{0.25}V_2O_5 \cdot nH_2O$ nanobelts.**(a)** XRD pattern and **(b)** SEM morphology of $Zn_{0.25}V_2O_5 \cdot nH_2O$

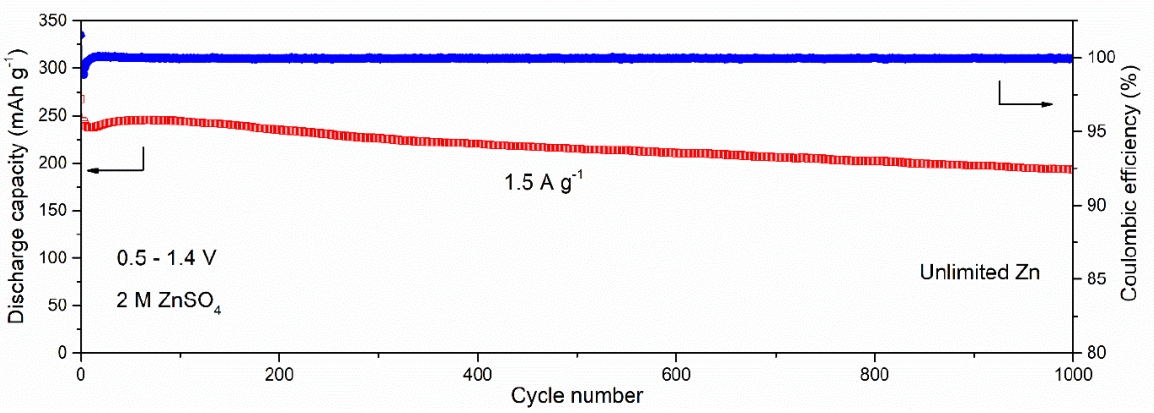

Figure 3.26 Long-term cycling of Zn||$Zn_{0.25}V_2O_5 \cdot nH_2O$ full cell in 2 M $ZnSO_4$ in the voltage range of 0.5 V -1.4V at 5 C with unlimited Zn. The cell retains ~ 78.8% of its initial highest capacity after 1000 cycles, no less than the previous reported value.This confirms the high cycling stability of $Zn_{0.25}V_2O_5 \cdot nH_2O$ cathode and enables us to further explore the Zn reversibility in the modified electrolyte in full cells.

ratio. As shown in **Figure 3.24e**, in the presence of the DOTf additive, this full cell still

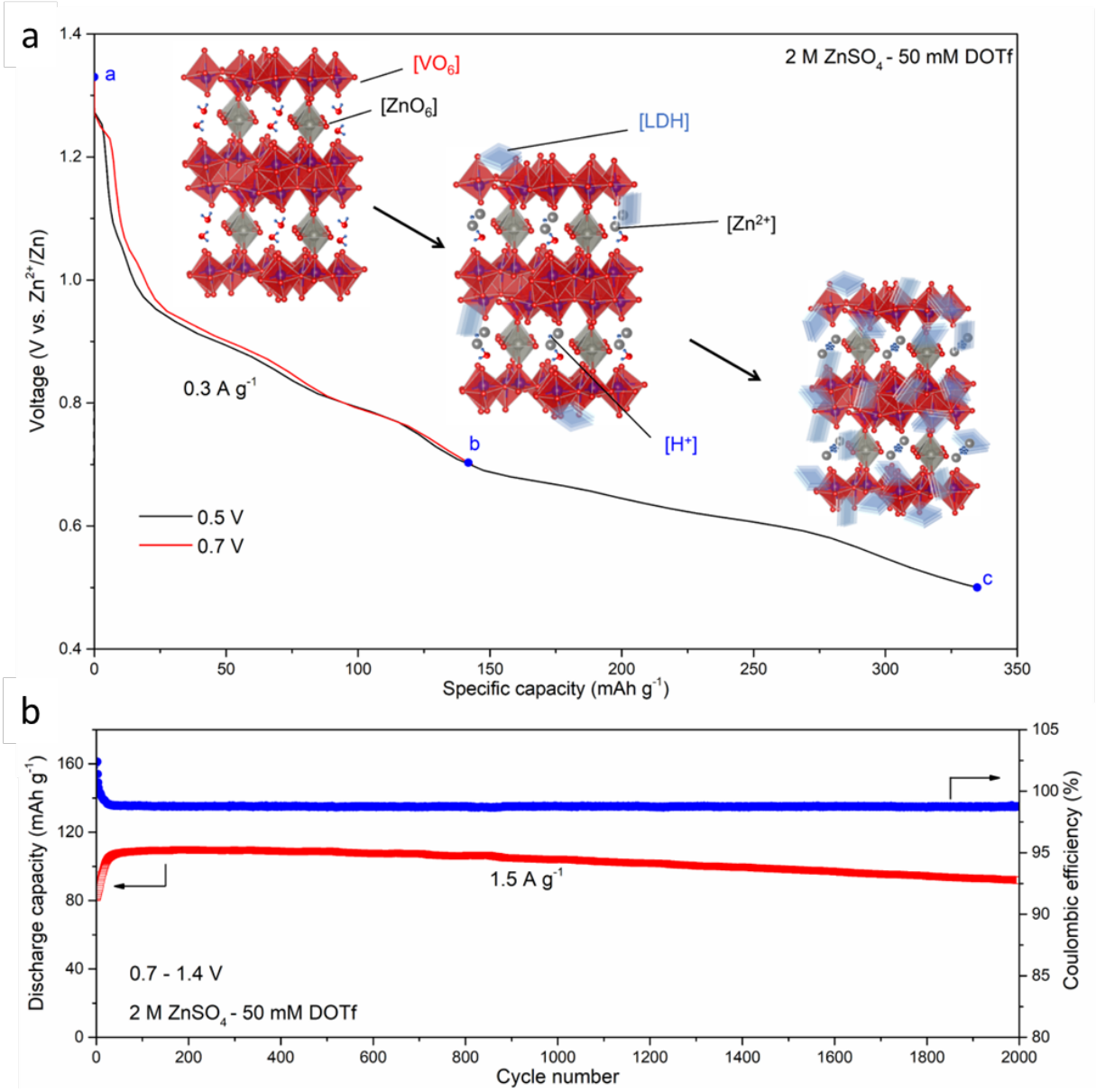

Figure 3.27 H^+/Zn^{2+} Intercalation of Zn||$Zn_{0.25}V_2O_5 \cdot nH_2O$ full cells in 2 M $ZnSO_4$ 50 mM DOTf. **(a)** The first voltage profiles of full cells at different discharge states and corresponding schematic illustration of H^+/Zn^{2+} intercalation into the lattice (a, b, and c indicate the open circuit voltage, 0.7 and 0.5 V). **(b)** Long-term stability of the full cell between 0.7 and 1.4 V at 1.5 A g^{-1} (N:P ≈ 5.2, the areal capacity of deposited Zn on Cu is the same as that in 0.5–1.4 V).

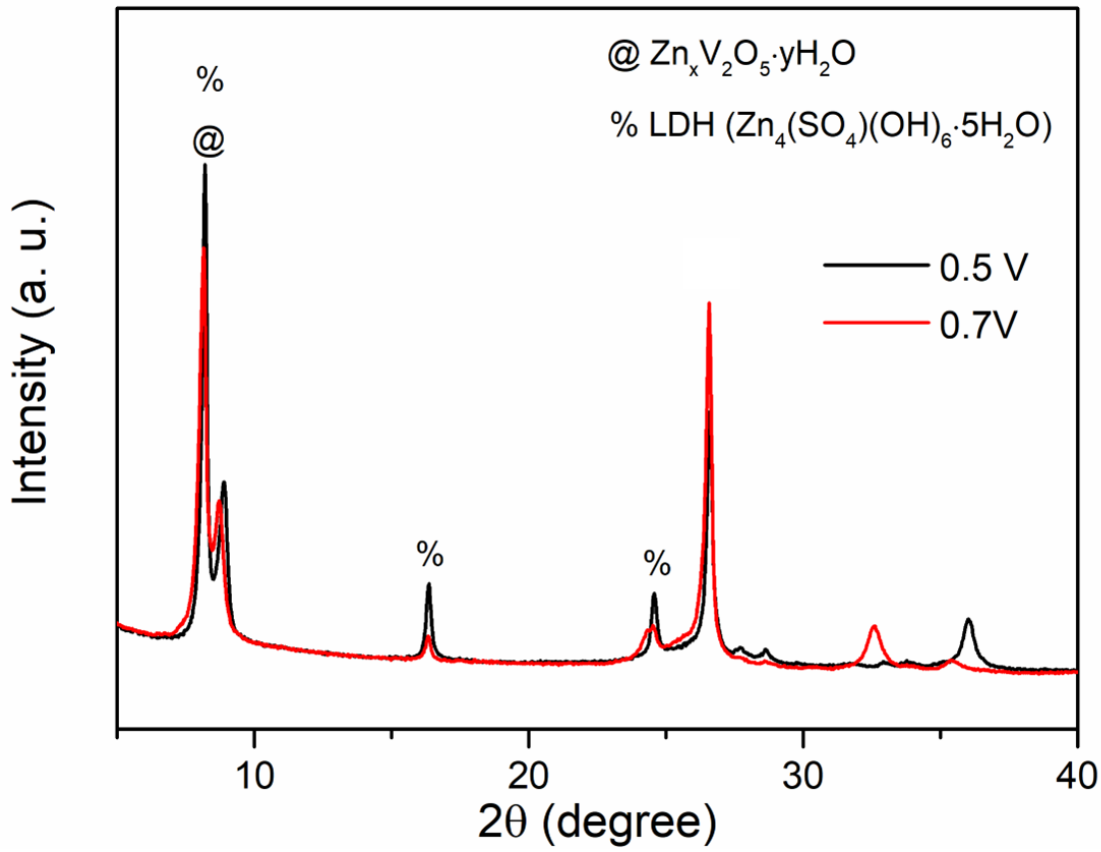

Figure 3.28 Comparison of the XRD patterns of $Zn_{0.25}V_2O_5{\cdot}nH_2O$ electrodes discharged to different lower cutoff voltages in 2 M $ZnSO_4$ - 50 mM DOTf.

maintains ~ 197.6 mAh g^{-1} after 1000 cycles, exhibiting a capacity retention of ~83% with an average CE of 99.9%. In contrast, the capacity in 2 M $ZnSO_4$ electrolyte quickly drops to ~ 24 mAh g^{-1} owing to the poor Zn reversibility with a lower average CE of 97.7 %.

Proton intercalation has been reported to be deleterious to the long-term cycling of various metal oxides in AZMBs as it results in the formation of LDHs.[17,36,87,88] Similar to the anode side, LDHs also deposit on the cathode owing to the local alkaline environment after protons intercalate into the cathode host as shown schematically in **Figure 3.27a**. However, the thin, flaky LDHs tend to spontaneously detach from the cathode side, causing irreversible capacity loss and poor long-term cycling stability.[17,88] XRD analysis on $Zn_{0.25}V_2O_5{\cdot}nH_2O$ cathodes collected at different discharge states shows that LDH mainly forms in the low

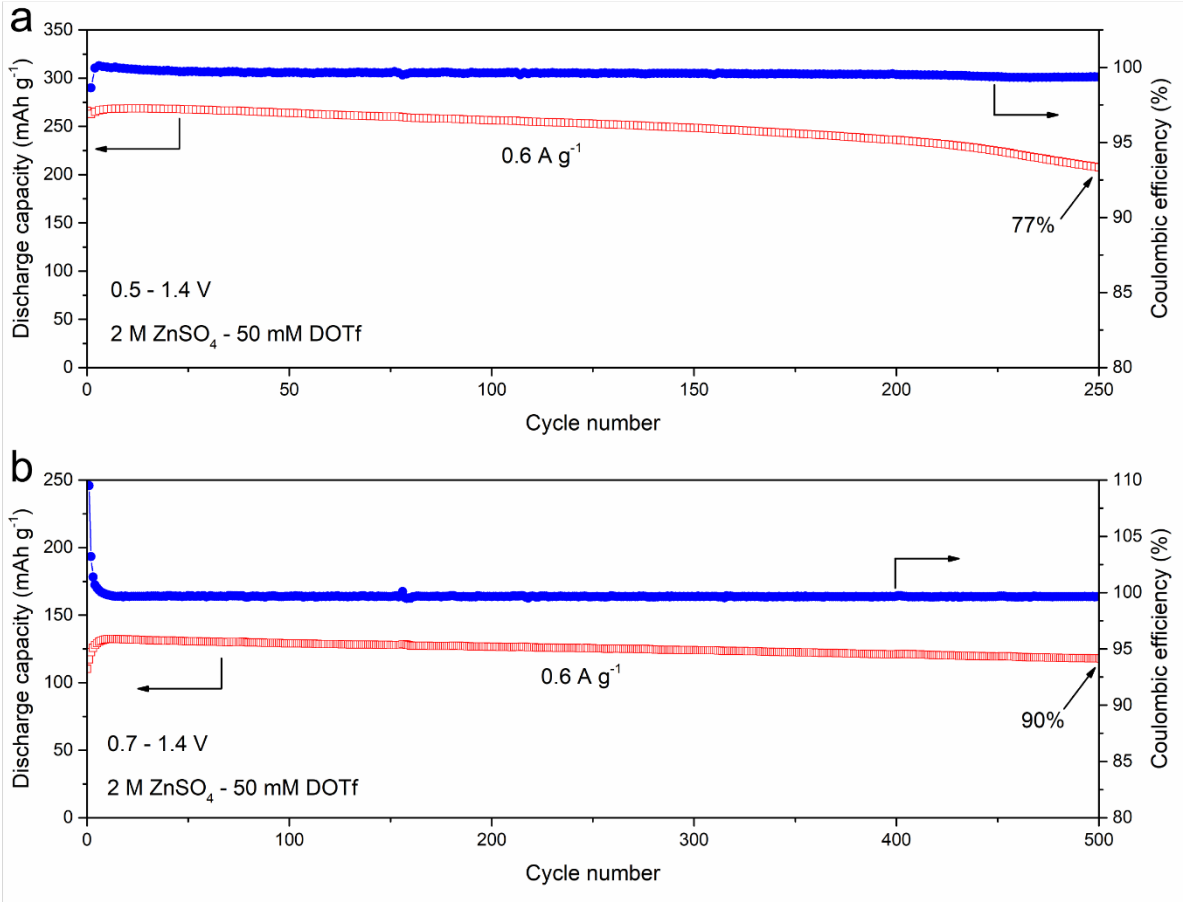

Figure 3.29 Cycling stability of ZVO in 2 M $ZnSO_4$ – 50 mM DOTf at 0.6 A g^{-1} (2C rate) with a lower cut-off voltage of **(a)** 0.5 V (N:P = 2.5) and **(b)** 0.7 V (N:P = 5.2).

voltage range from 0.7 V to 0.5 V (**Figure 3.28**). The discharge curves of $Zn_{0.25}V_2O_5{\cdot}nH_2O$ cathodes are shown in **Figure 3.27a**. Up to the initial discharge state of 0.7 V, Zn^{2+} gradually intercalates into the lattice with a small portion of proton intercalation and concomitant formation of LDH on the cathode surface. Below 0.7 V, proton intercalation and LDH formation dominate the discharge process and account for the most of electrochemical capacity, consistent with previous reports.[13,89] This allows us to further enhance the stability of Zn||$Zn_{0.25}V_2O_5{\cdot}nH_2O$ full cells by modifying the lower cut-off voltage from 0.5 V to 0.7 V based on a similar strategy.[90] **Figure 3.27b** shows this full cell still maintains ~84% of its initial highest capacity after even 2000 cycles at the same Zn capacity with an average CE of 99.3%

(N:P ratio increases to ~5.2 owing to the lowered cathode capacity), which is twice the cycle life at 0.5 V. We note this promising stability is obtained at a moderate current density of 5C, while many literature reports utilize very high rates (> 10C) to favor stability.[25,30] At a 2C rate (0.6 A g^{-1}), ZVO also exhibits good cycling stability at the lower cut-off voltage of 0.7 V, with a capacity retention of ~ 90% after 500 cycles (**Figure 3.29**). The enhanced cycling stability can be attributed to the alleviated proton intercalation, where the capacity loss owing to the detachment of LDH particles is significantly reduced.

3.8 Conclusions

In this work, we introduce DOTf as a novel low-concentration electrolyte additive for aqueous Zn metal batteries. The use of this electrolyte leads to dendrite-free and highly reversible Zn plating/stripping for more than 3500 hours in Zn||Cu cells. More importantly, ~100% average CE of Zn plating/stripping is achieved under a practical cycling condition of a high current density of 4 mA cm^{-2} and a high areal capacity of 4 mAh cm^{-2} for more than 250 cycles. The superior Zn stability and reversibility are ascribed to robust nanostructured SEI layers leading to the suppression of detrimental LDHs and a nanoscale nucleation-growth process during Zn electrodeposition. The origin of this Zn^{2+}-conducting SEI is speculated to be a result of the water assisted dissociation of DOTf into neutral ion pairs. Zn||$Zn_{0.25}V_2O_5 \cdot nH_2O$ full cells (N:P ratio of 2.5 and 5.2) based on this electrolyte exhibit excellent cycling performance with different depth of proton intercalation. Our findings and understanding of this novel electrolyte additive could potentially accelerate the commercialization of practical aqueous Zn metal batteries.

Chapter 4 Tuning the Solvation Structure in Aqueous Zinc Batteries to Maximize Zn-Ion Intercalation and Optimize Dendrite Free Zinc Plating

4.1 Introduction

Much work has focussed on developing cathode materials for AZMBs including MnO_2,[18] $Zn_{0.25}V_2O_5{\cdot}nH_2O$,[13] along with many others. However, recent studies have found that the high electrochemical capacity of these metal oxides is not solely due to Zn^{2+} insertion/extraction, but largely relies on H^+ (de)intercalation.[17,87–89,91,92] Proton intercalation results in the formation of layered double-hydroxide salts (LDH, for example, $Zn_4SO_4(OH)_6{\cdot}5H_2O$) on the surface of metal oxides, which aids the reversible and stable operation of metal oxides due to its unique buffering mechanism.[17] On the other hand, the LDH forms an insulating layer on the oxide surface that detaches from the electrode over time, leading to loss of active material. Proton intercalation has now been generally accepted as a common phenomenon for metal oxides in AZMBs.

Studies involving polyanion compounds similarly showed that either H^+ (or Na^+) insertion occurs along with Zn^{2+} intercalation.[15,16,93] For example, by analysing the differential capacity curves (dQ/dV) of layered $VOPO_4{\cdot}xH_2O$ cathode in different electrolytes,[16] Sun *et al.* found that H^+ intercalation played a dominant role in an electrolyte comprised of 5 m $ZnCl_2$/0.8 m H_3PO_4. Not surprisingly, on increasing the concentration of $ZnCl_2$ to 10 - 13 m, Zn^{2+} was suggested to dominate the intercalation process based on the higher peak intensity of the Zn contribution in the dQ/dV curve. The factors responsible for Zn^{2+} vs. H^+ intercalation (aside from concentration) were not investigated in this study, however. Monoclinic $LiV_2(PO_4)_3$ was reported to be a superior host for AZMBs, and can be cycled at an exceptionally high rate of 60 C.[94] As the high charge density of Zn^{2+} would likely result in limits to solid-state diffusion at this current density and significant structural distortion in monoclinic $V_2(PO_4)_3$,[95] a fundamentally different mechanism based on H^+ intercalation rather than exclusive Zn^{2+} insertion has been proposed to account for this high-rate performance. [88]Recently, an approach to favor Zn^{2+} intercalation was reported for a VPO_4F host lattice based on a hybrid electrolyte (water + propylene carbonate); however proton intercalation still could not be fully suppressed.

A multiphase mixture with overall composition of $Zn_{0.3}H_yVPO_4F$ was formed on discharge, but the implicit existence of a more highly zincated phase could not be quantified.[15]

In this chapter, I demonstrate that solvation-structure engineering of aqueous Zn electrolytes (AZEs) is an effective method to suppress H^+ intercalation and realize dominant Zn^{2+} intercalation. To establish proof-of-concept, we chose $LiV_2(PO_4)_3$ (LVP) as the platform for the cathode and compared its electrochemistry in two previously reported electrolytes, 4 m (molality, mol/kg) $Zn(OTf)_2$ and 29 m $ZnCl_2$ "water-in-salt" electrolytes (WiSE), as well as a newly designed hybrid electrolyte developed by incorporating polyethylene glycol 400 (PEG 400) and water as a co-solvent with $Zn(OTf)_2$ as the salt. Importantly, we explore the H-bonding network, free water fraction, Zn^{2+}-solvation structure and their roles in the Zn^{2+} vs. H^+ intercalation in all three electrolyte systems, using experimental and computational methods to understand why the PEG-based hybrid electrolyte exhibits the least H^+ intercalation and the most dominant Zn^{2+} intercalation.

I proposed the idea, planned the experiments, synthesized the materials and performed all electrochemical measurements and wrote the original manuscript. Dr. Ryan Kingsbury and Kristin A. Persson performed molecular dynamics simulations.

4.2 Experimental Approaches

4.2.1 Sol-gel Synthesis of $Li_3V_2(PO_4)_3$

$Li_3V_2(PO_4)_3$ (L_3VP) was synthesized by a simple sol-gel approach reported before.[96] Typically, 3 mmol vanadium (V) oxide (Sigma-Aldrich) and 9 mmol oxalic acid dihydrate (Sigma-Aldrich) were first dissolved in 50 mL deionized water and stirred at room temperature until a clear green solution was formed. Then 9 mmol ammonium dihydrogen phosphate (Sigma-Aldrich) and 4.59 mmol lithium carbonate (Sigma-Aldrich) were added into the above solution, following by vigorous stirring for 1h. Finally, Ketjenblack (KB) carbon was added to the solution and the mixture was stirred at 70°C overnight until a gel formed. The gel was transferred to an oven and dried at 80 °C overnight. The obtained solid sample was ground in a mortar for 15 minutes and then pelletized at 2 tons in a die with a diameter of 13 mm. The

pellets were transferred to an alumina crucible and heated in a tube furnace at 350 °C for 4 h and 800 °C for 8 h at a heating rate of 5 °C min^{-1} under a constant Ar gas flow. The obtained L_3VP powder was used as a precursor to synthesize $LiV_2(PO_4)_3$ (LVP).

4.2.2 Material Characterizations

Powder X-ray diffraction (XRD) patterns were collected on an X-ray diffractometer using Cu-Kα radiation (PANalytical Empyrean) that was equipped with a PIXcel bidimensional detector. For short scans, XRD patterns were collected using a flat-stage model in Bragg-Brentano geometry. For long scans, the powder samples were loaded in sealed glass capillary tubes and the data were recorded in Debye-Scherr geometry. Scanning electron microscopy (SEM) images and energy-dispersive X-ray spectroscopy (EDX) were performed a Zeiss Ultra field emission SEM instrument attached with an EDX detector. Thermogravimetric analysis (TGA) was obtained in air at a heating rate of 10 °C min^{-1} on a TA Instruments SDT Q500. Fourier transformed infrared spectroscopy (FTIR) was carried out on a Bruker Tensory 27 system equipped with attenuated total reflection (ATR). The ionic conductivity of aqueous electrolytes was measured via an Orion Star A325 pH/ Conductivity Meter (Thermo) at 22 °C.

4.2.3 Electrochemical Measurements

The Li_3VP cathodes were prepared by doctor blading a homogeneous ink of 90 wt% as-prepared powder materials and 10 wt% polyvinylidene difluoride (PVDF) onto titanium foil. The slurry was dried at 60 °C overnight before being punched into small coins with a diameter of 11 mm. The mass loading for the active materials was about 3 mg cm^{-2}. Galvanostatic cycling measurements (VMP3, Biologic) were performed in PFA-based Swagelok-type cells, assembled with metallic zinc foil (Sigma-Aldrich) as both the counter and reference electrodes. Linear sweep voltammetry (LSV) was carried based on three-electrode cells with Zn as reference electrodes, Ti as both working and counter electrodes.

Galvanostatic intermittent titration technique (GITT) measurements were carried using a current pulse of 20 min at C/40 followed by a 4 h rest. The average ion diffusion coefficients

in LVP were calculated from GITT data by the following formula first reported by Weppner and Huggins:[97]

$$D = (4/\pi\tau) * [n_M V_M/S]^2 [\Delta E_s/\Delta E_t]^2$$

where τ is the current pulse duration (20 min) of a single step of GITT experiment; n_M and V_M are the moles and molar volume of the active material, respectively; S is taken as the geometric area of the electrode for simplicity, which is the typically used in such calculations; ΔE_S and ΔE_t are the change in the steady state voltage and overall cell voltage in one current pulse, respectively.

LVP electrodes were prepared by an electrochemical oxidation method. Typically, the Li_3VP || Zn cells were charged to 1.85 V vs. Zn^{2+}/Zn in 4 m $Zn(OTf)_2$, during which two Li^+ were extracted and Li_3VP was oxidized to LVP. The cathodes were disassembled from the cells, rinsed with deionized water and ethanol for five times, then dried *in vacuo* at 80 °C overnight for later characterization. To collect long-scan XRD patterns of LVP for Rietveld analysis, LVP was carefully removed from the Ti foil, ground and loaded in a sealed glass capillary tube.

4 m Zn $(OTf)_2$ (m: molality, mol/kg) was prepared by dissolving 20 mmol $Zn(OTf)_2$ into 5 mL deionized water. For 29 m $ZnCl_2$ WiSE, 29 mmol $ZnCl_2$ was dissolved into1 mL deionized water. 70PEG was prepared by dissolving 2 mmol $Zn(OTf)_2$ into 0.7 g PEG 400 and 0.3 g deionized water.

4.3 Electrochemistry of LVP in Dilute Electrolyte and WiSE.

The synthesized $Li_3V_2(PO_4)_3$ (Li_3VP) - carbon composite consists of approximately 1 μm aggregate crystallites that are enclosed by conductive carbon (**Figure 4.1).** ≈ 8.75% carbon content was confirmed by thermogravimetric analysis (TGA), as shown in **Figure 4.2**. $LiV_2(PO_4)_3$ (LVP) electrodes were prepared by charging Li_3VP electrodes to 1.85 V (vs. Zn^{2+}/Zn) in 4 m $Zn(OTf)_2$, where two Li^+ per formula unit of Li_3VP was successfully extracted.

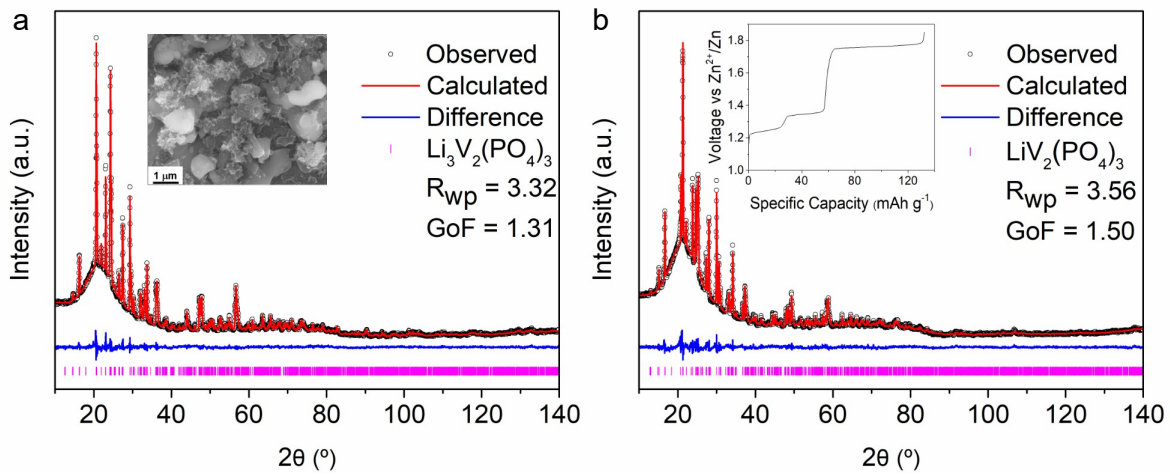

Figure 4.1 (a) Rietveld refinement of XRD patterns of sol-gel prepared $Li_3V_2(PO_4)_3$ (inset shows the SEM image of pristine Li_3VP powder) and **(b)** electrochemically oxidized $LiV_2(PO_4)_3$ (inset shows the corresponding charge-discharge curve in 4 m $Zn(OTf)_2$ at C/20).

Rietveld refinement of the powder X-ray diffraction (XRD) pattern indicates that all LVP reflections are well indexed to a monoclinic LVP phase with a space group of $P2_1/c$.

A unit cell volume contraction of 7.3% upon two Li^+-ion extraction is in close accord with the reported value (**Table 4.1, 2**).[98]

Table 4.1 Atomic coordinates, occupation factor and isotropic displacement parameter of $Li_3V_2(PO_4)_3$ obtained from powder XRD data. Li atoms were ignored in all refinements, as the accurate information of their positions and occupancy cannot be refined by X-ray measurements. The occupancies of non-alkaline atoms were fixed as 1 during the refinements.

R_{wp} = 3.32, GoF = 1.31						
$Li_3V_2(PO_4)_3$, space group = $P2_1/c$, a = 8.615(2) Å, b = 8.5991(4) Å, c = 14.738(6) Å, β = 125.180(5) ° ; Volume = 892.4(2) Å^3						
Atom	**Wyck. Site**	**x**	**y**	**z**	**Occ.**	**U_{iso} (Å^2)**
V1	4e	0.1360(8)	0.5264(5)	0.3892(4)	1.000	0.029(3)
V2	4e	0.3601(8)	0.5387(5)	0.1083(4)	1.000	0.021(3)

P1	4e	0.0466(9)	0.2496(9)	0.0073(6)	1.000	0.018(3)
P2	4e	0.4566(9)	0.3992(9)	0.3499(6)	1.000	0.027(3)
P3	4e	0.7499(9)	0.3837(8)	0.14448(6)	1.000	0.025(3)
O1	4e	0.015(2)	0.183(2)	0.0952(9)	1.000	0.012(5)
O2	4e	0.033(2)	0.371(2)	0.4228(9)	1.000	0.013(5)
O3	4e	0.086(2)	-0.002(2)	0.2774(9)	1.000	0.011(5)
O4	4e	0.109(2)	0.630(2)	0.0681(9)	1.000	0.026(5)
O5	4e	0.176(2)	0.711(2)	0.316(2)	1.000	0.021(5)
O6	4e	0.234(2)	0.325(2)	0.068(2)	1.000	0.029(6)
O7	4e	0.289(3)	0.390(2)	0.355(2)	1.000	0.036(6)
O8	4e	0.368(2)	0.549(2)	0.542(2)	1.000	0.044(6)
O9	4e	0.478(2)	0.230(2)	0.310(2)	1.000	0.038(6)
O10	4e	0.587(2)	0.016(2)	0.2366(9)	1.000	0.006(4)
O11	4e	0.590(2)	0.400(2)	0.1715(9)	1.000	0.002(4)
O12	4e	0.687(2)	0.413(2)	0.0293(9)	1.000	0.007(4)

Table 4.2 Atomic coordinates, occupation factor and isotropic displacement parameter of $LiV_2(PO_4)_3$ obtained from powder XRD data. Li atoms were ignored in all refinements, as the accurate information of their positions and occupancy cannot be refined by X-ray measurements**.** The occupancies of non-alkaline atoms were fixed as 1 during the refinements.

R_{wp} = 3.56, GoF = 1.50						
$LiV_2(PO_4)_3$, space group = $P2_1/c$, a = 8.307(4) Å, b = 8.5330(8) Å, c = 14.28(2) Å, β = 125.189(9)° ; Volume = 827.3(3)Å^3						
Atom	**Wyck. Site**	**x**	**y**	**z**	**Occ.**	**U_{iso} (Å^2)**
V1	4e	0.131(2)	0.5285(9)	0.3816(7)	1.000	0.038(4)

V2	4e	0.356(2)	0.5367(8)	0.1135(6)	1.000	0.031(4)
P1	4e	0.039(2)	0.246(2)	0.004(2)	1.000	0.037(4)
P2	4e	0.462(2)	0.390(2)	0.3565(8)	1.000	0.035(5)
P3	4e	0.757(2)	0.383(2)	0.1448(9)	1.000	0.032(4)
O1	4e	0.017(3)	0.185(2)	0.097(2)	1.000	0.005(5)
O2	4e	0.003(3)	0.379(3)	0.416(2)	1.000	0.044(8)
O3	4e	0.064(3)	-0.021(3)	0.261(2)	1.000	0.024(7)
O4	4e	0.127(3)	0.628(2)	0.068(2)	1.000	0.011(7)
O5	4e	0.219(3)	0.695(3)	0.326(2)	1.000	0.048(9)
O6	4e	0.225(4)	0.316(3)	0.067(2)	1.000	0.046(9)
O7	4e	0.302(3)	0.398(3)	0.374(2)	1.000	0.030(9)
O8	4e	0.334(3)	0.548(2)	0.537(2)	1.000	0.019(7)
O9	4e	0.496(3)	0.228(2)	0.315(2)	1.000	0.009(6)
O10	4e	0.591(3)	0.011(3)	0.236(3)	1.000	0.043(9)
O11	4e	0.598(3)	0.410(3)	0.168(2)	1.000	0.013(7)
O12	4e	0.679(3)	0.432(2)	0.021(2)	1.000	0.004(6)

The electrochemistry of LVP in 4 m $Zn(OTf)_2$ was compared to 29 m $ZnCl_2$ WiSE electrolytes at a 1 C rate (discharge/charge of 1 Zn^{2+} in one hour). Very different electrochemical behavior was observed. As shown in **Figure 4.3a**, in 4 m $Zn(OTf)_2$ a new discharge plateau below 0.5 V accompanies the increase in capacity and becomes more dominant as the cycle number rises, suggesting a phase conversion process (**Figure 4.3b**). The new lower-voltage plateau was also identified by Wang et al in a spray-dried LVP cathode,[93] but its origin was not disclosed. It should be noted that this low-voltage discharge plateau (~0.5 V vs Zn) is also seen in VO_x-based cathode materials, indicating H^+ intercalation and the formation of LDHs. In contrast, no lower-voltage plateau was observed in $ZnCl_2$ WiSE, only a minor activation-like process (**Figure 4.3c, d**). Strikingly different from the high maximum

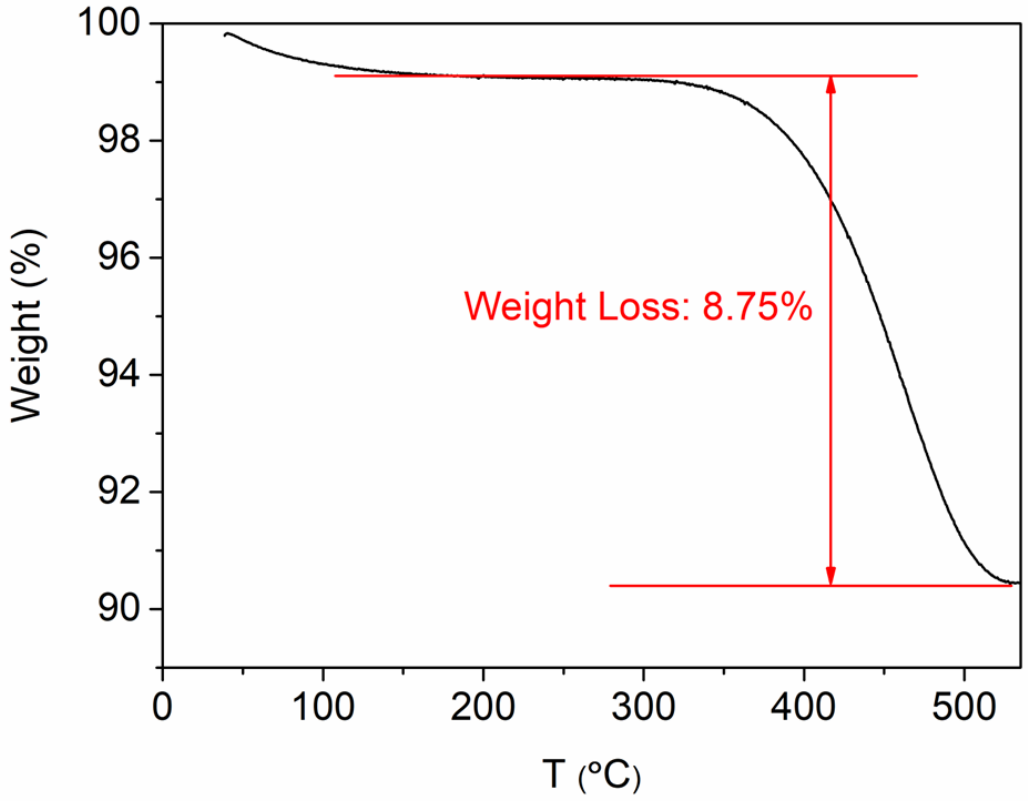

Figure 4.2 TGA of sol-gel synthesized $Li_3V_2(PO_4)_3$

capacity of 200 mAh g^{-1} exhibited in 4 m $Zn(OTf)_2$, a more realistic discharge capacity of about 90 mAh g^{-1} was recorded at the 60th cycle in $ZnCl_2$ WiSE after the initial activation process. LVP also shows poor cycling stability in 4 m $Zn(OTf)_2$ with only 61% capacity retained after cycling at 1 C for 200 cycles (**Figure 4.3b**), whereas very good cycling stability with a high capacity retention of about 88% in $ZnCl_2$ WiSE was observed at the same rate for 500 cycles (**Figure 4.3d**). Such contrasting electrochemistry is also exhibited at higher current densities, as shown in **Figure 4.4**.

4.4 Structure and Morphology Evolution of LVP

The abnormal electrochemistry observed in 4 m $Zn(OTf)_2$ can be attributed to the decomposition of LVP and the formation of hydrated vanadium oxides (VO_x) phases based on

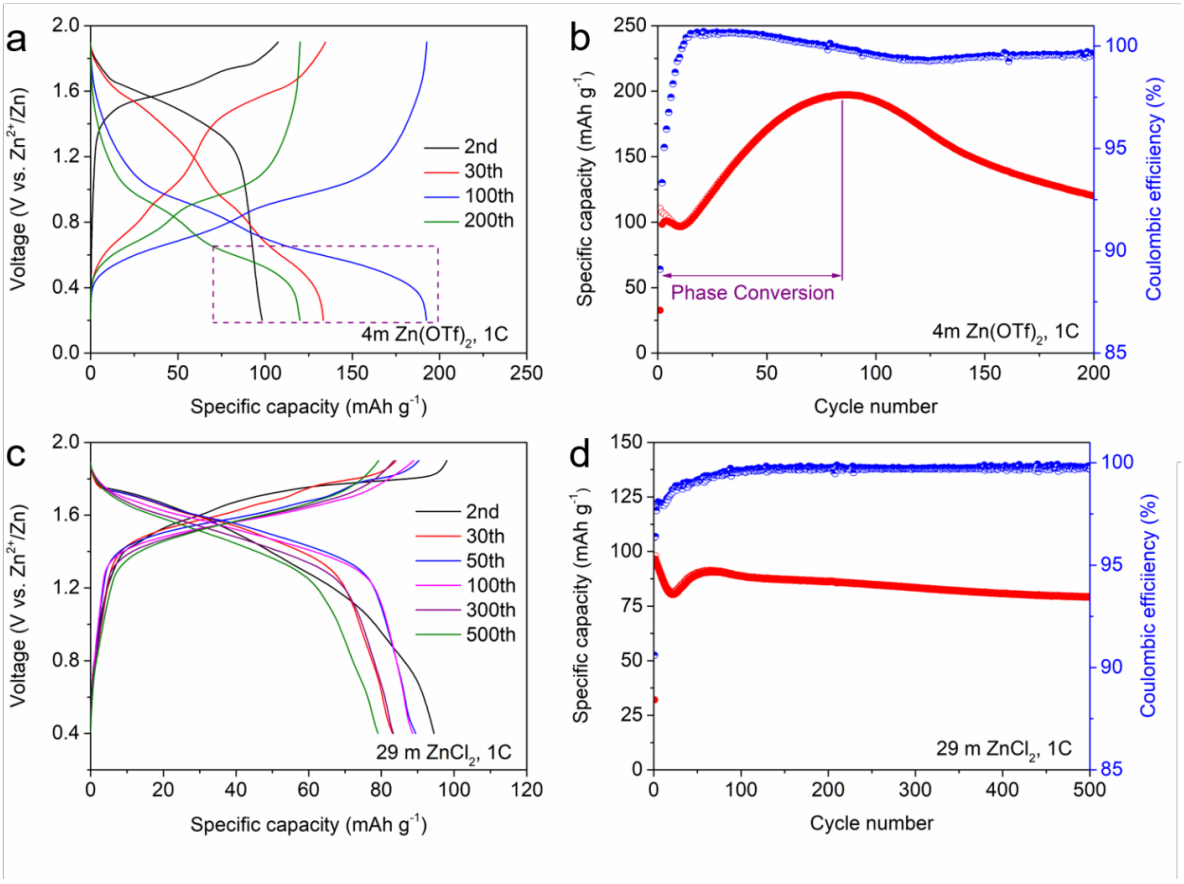

Figure 4.3 Charge–discharge curves of LVP during different cycles and corresponding capacity retention at 1 C (= 136 mA g^{-1}) in (a, b) 4 m $Zn(OTf)_2$ and (c, d) 29 m $ZnCl_2$ WiSE.

our X-ray diffraction (XRD) studies. The XRD patterns in **Figure 4.5a** show that monoclinic LVP gradually disappears in 4 m $Zn(OTf)_2$ as the cycle number increases. Simultaneously, two new reflections assigned to hydrated VO_x phases appear, and finally become the major components of the active material (**Figure 4.6**). The morphology of the LVP electrodes during this phase conversion process was determined by SEM (**Figure 4.5b**). The well-crystallized particles gradually decompose and exhibit severe loss of crystallinity on cycling. EDX mapping also reveals a gradually decreasing P:V ratio (**Figure 4.7a**), further supporting the formation of hydrated VO_x phases. In contrast, the structure of LVP was better maintained in $ZnCl_2$ WiSE as cycling progressed (**Figure 4.5a**), although two small new peaks corresponding to hydrated VO_x appear over a period of 20 cycles. **Figure 4.5b** and **4.7b** shows that the

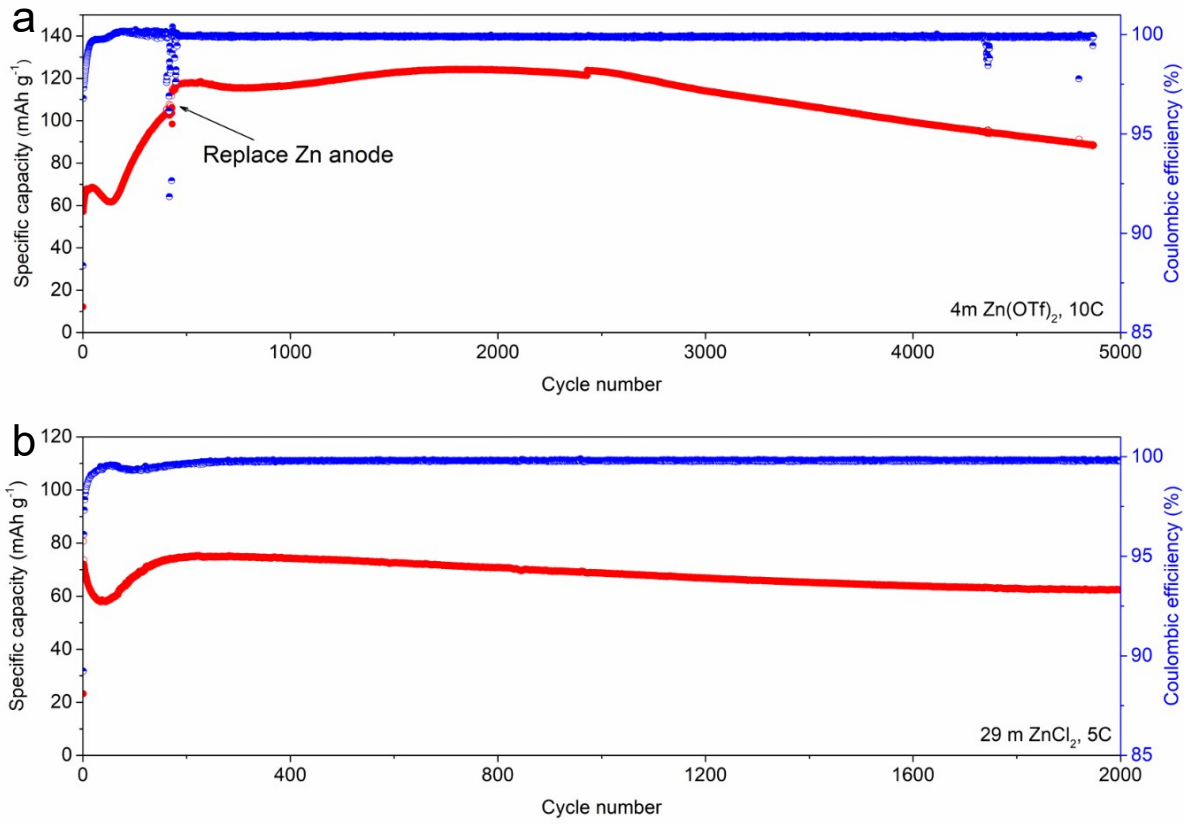

Figure 4.4 Charge-discharge capacity of LVP as a function of cycle number in a) 4 m $Zn(OTf)_2$ at a rate of 10 C and b) 29 m $ZnCl_2$ at a rate of 5 C.

morphology and P:V ratio of LVP electrodes only change slightly in $ZnCl_2$ WiSE, where clear and distinguishable crystalline particles are preserved upon cycling.

To explore whether hydrated VO_x phases result from vanadium dissolution of LVP or H^+ uptake, LVP electrodes were soaked in 4 m $Zn(OTf)_2$, $ZnCl_2$ WiSE, and with the addition of 0.2 m H_3PO_4 to both electrolytes. **Figure 4.5c** shows the XRD patterns of LVP electrodes that were soaked in the above four electrolytes for 24 hours. The intensity and position of the LVP reflections remain unchanged in 4 m $Zn(OTf)_2$, indicating insignificant vanadium

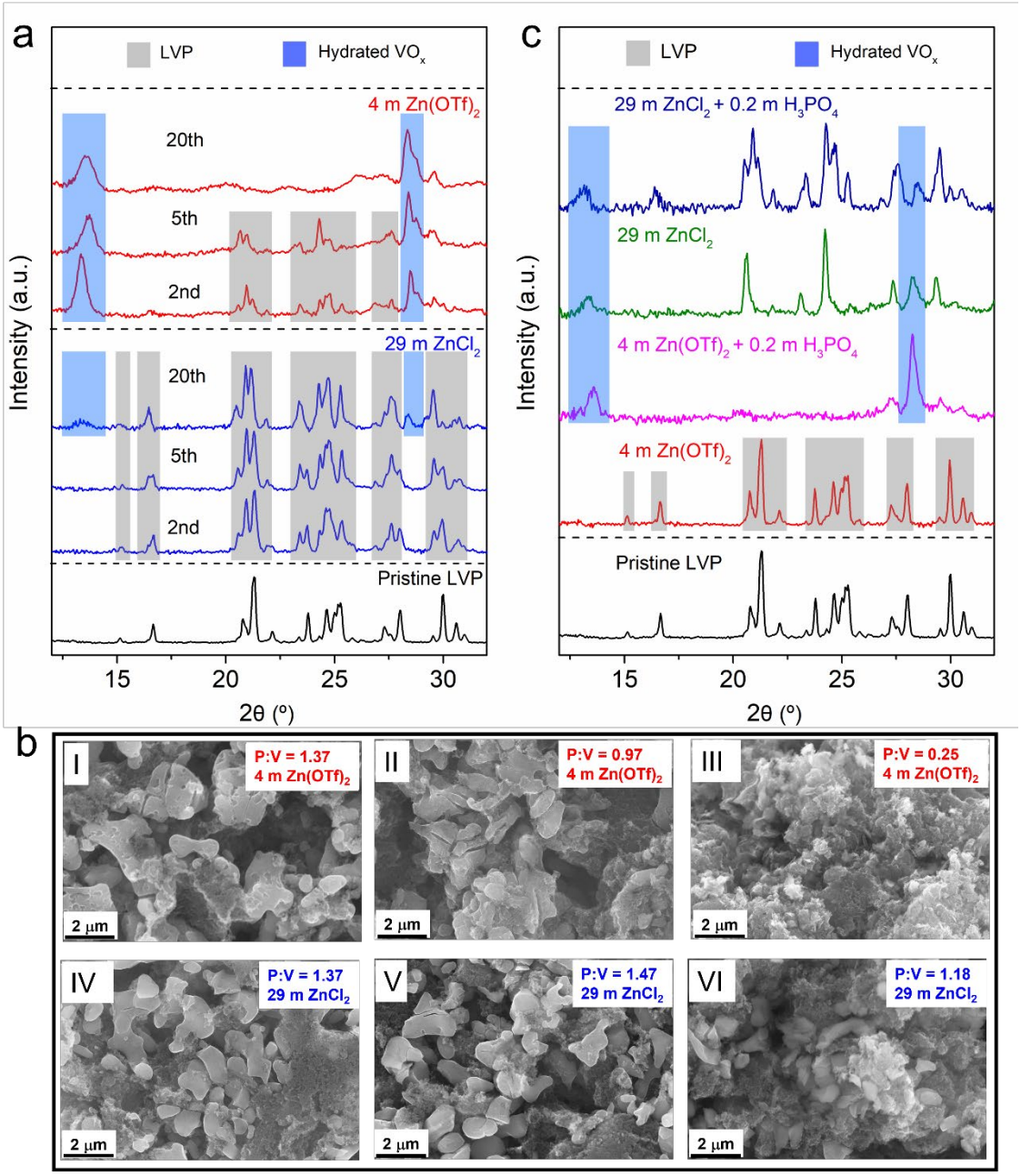

Figure 4.5 (a) XRD patterns of fully charged LVP electrodes at C/5 after different cycles and **(b)** corresponding SEM images and P:V ratios collected by EDX at the 2nd (I, IV), 5th (II, V), and 20th (III, VI) cycle. **(c)** XRD patterns of LVP electrodes soaked in various electrolytes for 24 h.

dissolution. However, a major change in the XRD pattern was observed for the electrode soaked in $ZnCl_2$ WiSE for 24 hours, probably caused by ion-exchange of Li^+ for Zn^{2+} owing

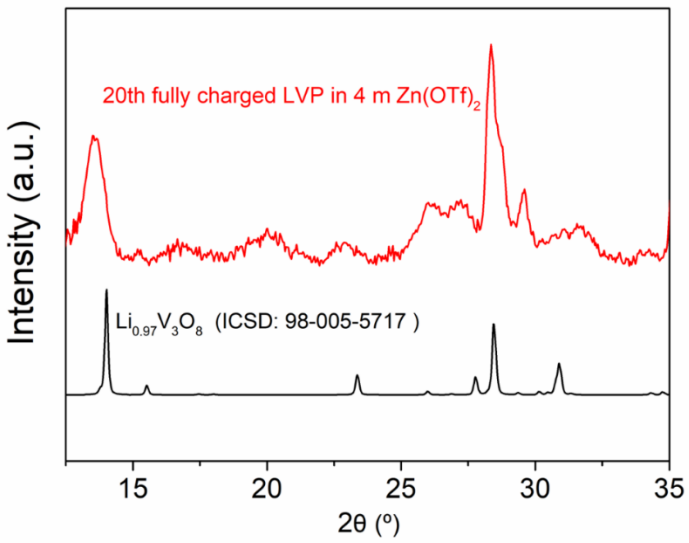

Figure 4.7 XRD patterns of fully charged LVP on the 20th cycle. The difference between this pattern and reference $Li_{0.97}V_3O_8$ can be ascribed to the formation of multiple VO_x phases with various amounts of H_2O between the layers.

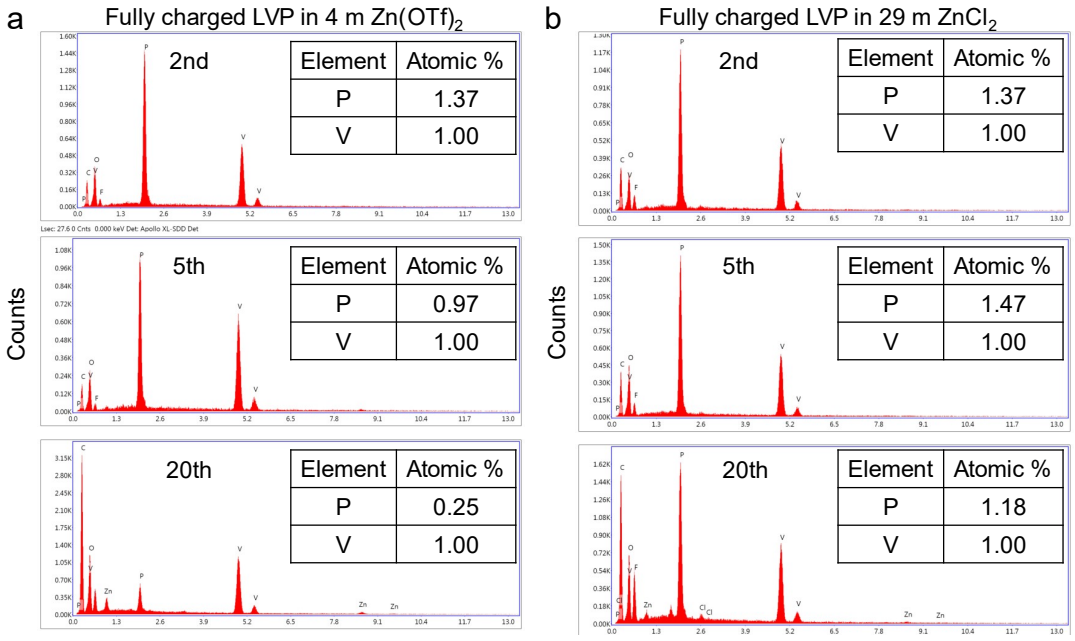

Figure 4.6 EDX of fully charged LVP electrodes at C/5 during different cycles in **(a)** 4 m $Zn(OTf)_2$ and **(b)** 29 m $ZnCl_2$.

to their similar ionic radius and the ultra-high Zn concentration. With the addition of 0.2 m

H_3PO_4, this ion exchange process is partially suppressed. While the LVP phase completely

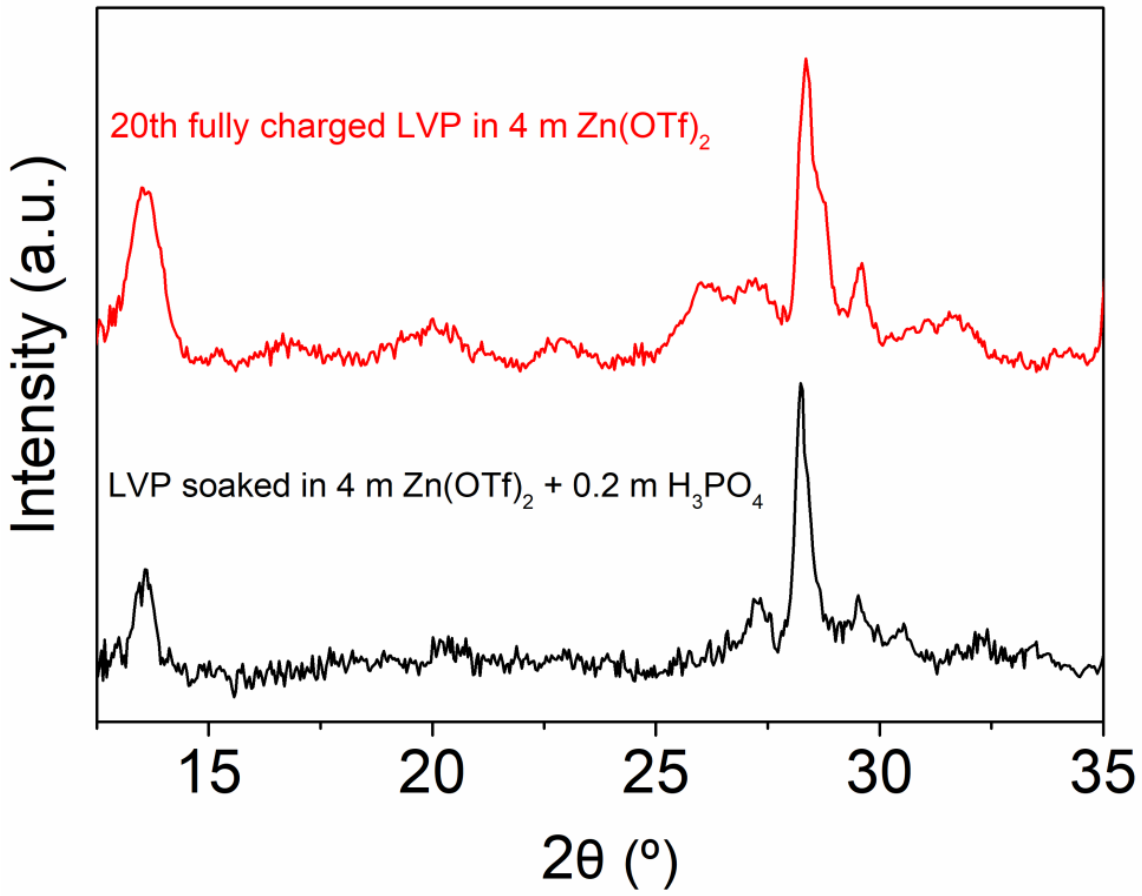

Figure 4.8 XRD patterns of **(a)** fully charged LVP on the 20th charge and **(b)** pristine LVP soaked in 4 m $Zn(OTf)_2$ + 0.2 m H_3PO_4 for 24 hours

disappears in 4 m $Zn(OTf)_2$ + 0.2 m H_3PO_4, two new distinct peaks of hydrated VO_x appear. This pattern is almost the same as fully charged LVP after 20 cycles at C/5 in 4 m $Zn(OTf)_2$ (**Figure 4.8**), suggesting H^+ uptake is responsible for generating these hydrated VO_x phases.

4.5 Dominant Zn^{2+} (de) intercalation of LVP in WiSE

Dominant Zn^{2+} intercalation of LVP in $ZnCl_2$ WiSE was confirmed by Rietveld refinement of the XRD pattern of fully discharged LVP (at a C/40 rate). As shown in **Figure 4.9a** and **Table S4.3**, two independent phases with different amounts of intercalated Zn^{2+}

coexist: 59 wt% of a Zn-rich phase ($Zn_{0.81}LiV_2(PO_4)_3$) and 41 wt% of a Zn-deficient phase

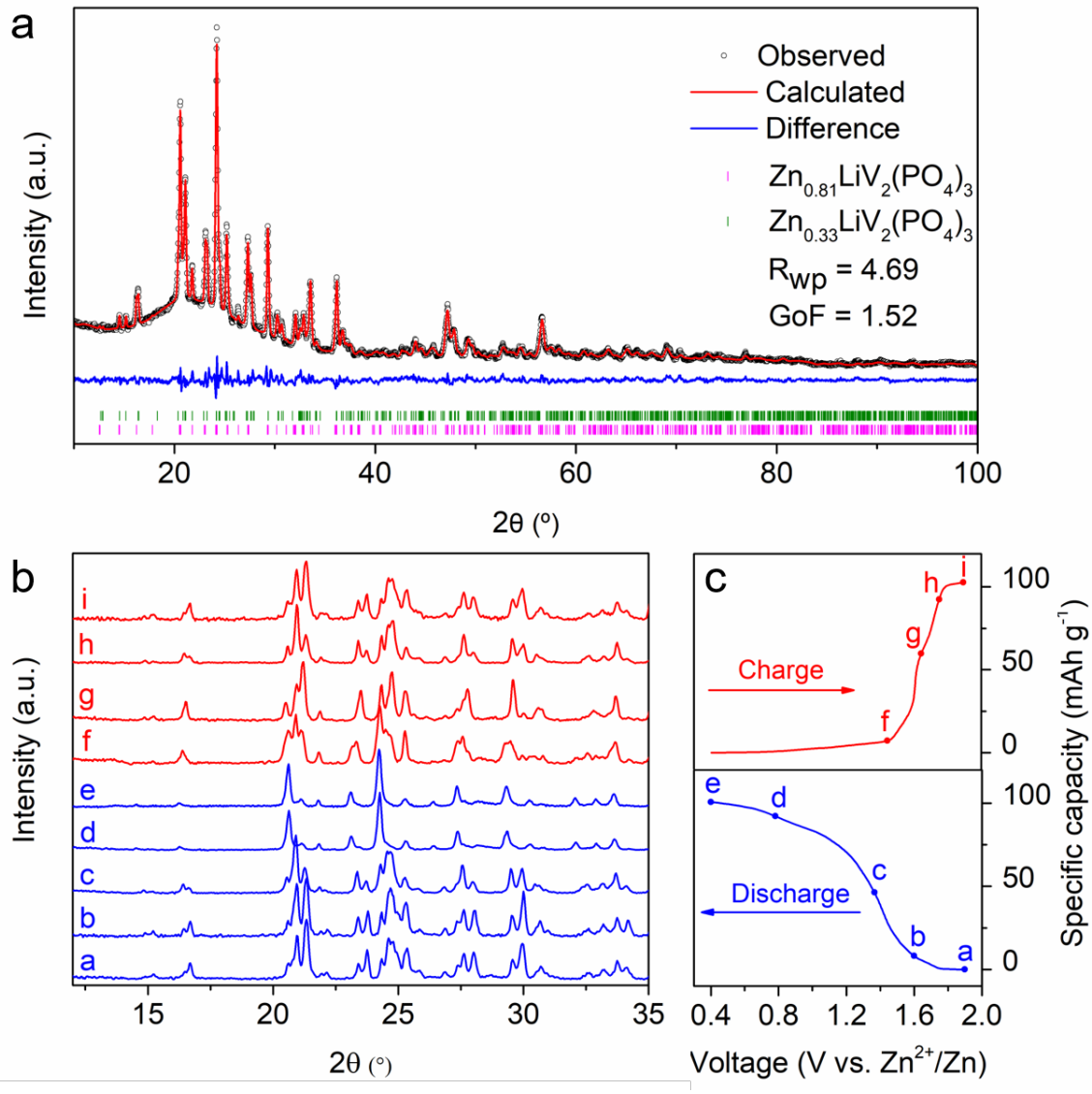

Figure 4.9 (a) Rietveld fit result of the 2nd fully discharged LVP electrode in 29 m $ZnCl_2$ at C/40. **(b)** Ex situ XRD patterns of LVP during the 2nd cycle and (c) corresponding charge–discharge curve in 29 m $ZnCl_2$ at C/5.

($Zn_{0.33}LiV_2(PO_4)_3$). The average fraction of inserted Zn^{2+} was 0.61 per formula unit, corresponding to an electrochemical capacity of 81 mAh g^{-1}. While EDX also shows that around 0.60 Zn^{2+} has intercalated into the lattice (**Figure 4.10a**), the actual discharge capacity

is 115 mAh g^{-1} (≈ 0.85 Zn^{2+}, **Figure 4.10b**). The difference of 34 mAh g^{-1} we ascribe to H^+ co-intercalation. Thus, over 70% of the capacity can be attributed to Zn^{2+} intercalation in the LVP lattice. This value is much higher than that reported (< 30%) for V_3O_7,[17] $Ca_{0.34}V_2O_5{\cdot}1.16H_2O$[89] and VPO_4F[99]. The (de)intercalation of Zn^{2+} into LVP was also confirmed by an *ex-situ* XRD study conducted at C/5 on the 2nd cycle (**Figure 4.9b, c**). With the increasing fraction of intercalated Zn^{2+}, peaks continuously merge and shift to lower angle. During Zn^{2+} *de*intercalation, exactly the converse process was observed, with gradual peak separation and shift to higher angles. This demonstrates the good structural reversibility of LVP as a host for Zn^{2+} insertion/extraction.

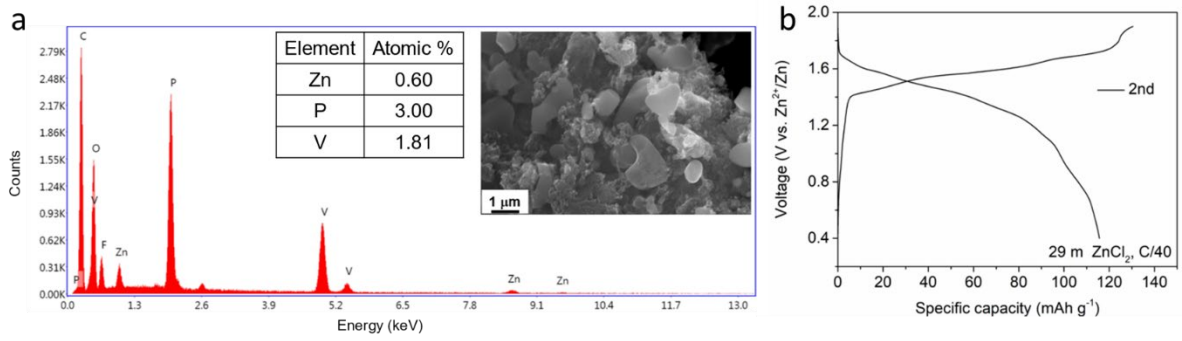

Figure 4.10 (a) EDX of fully discharged LVP electrodes on the 2nd discharge at C/40 in 29 m $ZnCl_2$ and **(b)** corresponding charge-discharge curve.

Table 4.3 Atomic coordinates, occupation factor and isotropic displacement parameter of fully discharged $LiV_2(PO_4)_3$ in 29 m $ZnCl_2$ at C/40. Li atoms were ignored in all refinements, as the accurate information of their positions and occupancy cannot be refined by X-ray measurements. The occupancies of non-alkaline atoms were fixed as 1 during the refinements.

R_{wp} = 4.69, GoF = 1.52						
$Zn_{0.81}LiV_2(PO_4)_3$, space group = $P2_1/c$, a = 8.569(8) Å, b = 8.6324(7) Å, c = 14.850(21) Å, β = 125.229(20)° ; Volume = 897.44(10)Å^3; 58.77(56) wt%						
Atom	**Wyck. Site**	**x**	**y**	**z**	**Occ.**	**U_{iso} (Å^2)**

Zn1	4e	0.063(6)	0.511(6)	0.233(3)	0.217(12)	0.013
Zn2	4e	0.209(6)	0.178(4)	0.246(3)	0.312(8)	0.074
Zn3	4e	0.422(8)	0.223(5)	0.179(5)	0.280(10)	0.065
V1	4e	0.133(3)	0.517(2)	0.383(2)	1.000	0.037
V2	4e	0.357(3)	0.536(2)	0.1067(9)	1.000	0.013
P1	4e	0.040(3)	0.266(4)	0.003(3)	1.000	0.029
P2	4e	0.456(4)	0.373(3)	0.362(3)	1.000	0.069
P3	4e	0.762(4)	0.400(3)	0.169(2)	1.000	0.050
O1	4e	0.018(7)	0.149(5)	0.045(4)	1.000	0.038
O2	4e	0.026(7)	0.350(6)	0.427(4)	1.000	0.033
O3	4e	0.125(6)	-0.021(5)	0.270(4)	1.000	0.023
O4	4e	0.126(6)	0.603(5)	0.066(4)	1.000	0.030
O5	4e	0.137(8)	0.668(6)	0.313(5)	1.000	0.110
O6	4e	0.245(7)	0.309(5)	0.114(4)	1.000	0.053
O7	4e	0.267(7)	0.375(5)	0.348(4)	1.000	0.047
O8	4e	0.358(5)	0.532(5)	0.527(3)	1.000	0.011
O9	4e	0.476(9)	0.237(6)	0.312(6)	1.000	0.056
O10	4e	0.588(9)	-0.005(6)	0.225(4)	1.000	0.072
O11	4e	0.571(6)	0.372(5)	0.150(4)	1.000	0.013
O12	4e	0.663(7)	0.450(5)	0.053(4)	1.000	0.018

$Zn_{0.33}LiV_2(PO_4)_3$, space group = $P2_1/c$, a = 8.481(7) Å, b = 8.6818(9) Å, c = 14.350(16) Å, β = 125.925(15)° ; Volume = 855.68(13)Å^3; 41.23(56) wt%

Atom	**Wyck. Site**	**x**	**y**	**z**	**Occ.**	**U_{iso} (Å^2)**
Zn1	4e	0.303(17)	0.815(11)	0.995(11)	0.135(10)	0.037
Zn2	4e	0.155(8)	0.061(9)	0.257(5)	0.135(10)	0.087

Zn3	4e	0.455(11)	0.340(8)	0.145(8)	0.056(8)	0.085
V1	4e	0.123(2)	0.533(2)	0.375(2)	1.000	0.037
V2	4e	0.375(2)	0.552(2)	0.103(1)	1.000	0.008
P1	4e	0.028(5)	0.241(4)	-0.007(4)	1.000	0.069
P2	4e	0.484(4)	0.399(3)	0.356(3)	1.000	0.087
P3	4e	0.744(4)	0.384(3)	0.153(3)	1.000	0.035
O1	4e	0.006(6)	0.153(6)	0.065(4)	1.000	0.041
O2	4e	0.077(9)	0.372(7)0.	0.405(6)	1.000	0.132
O3	4e	0.090(7)	-0.075(6)	0.278(4)	1.000	0.038
O4	4e	0.150(6)	0.623(5)	0.081(4)	1.000	0.045
O5	4e	0.143(7)	0.678(6)	0.329(4)	1.000	0.059
O6	4e	0.208(8)	0.312(5)	0.050(4)	1.000	0.031
O7	4e	0.303(7)	0.378(6)	0.362(5)	1.000	0.047
O8	4e	0.340(7)	0.493(5)	0.543(4)	1.000	0.067
O9	4e	0.458(7)	0.210(6)	0.308(4)	1.000	0.054
O10	4e	0.604(6)	-0.065(6)	0.235(4)	1.000	0.031
O11	4e	0.620(6)	0.395(5)	0.143(4)	1.000	0.033
O12	4e	0.689(5)	0.455(4)	0.012(3)	1.000	0.001

4.6 Designing Hybrid Aqueous Zn Electrolyte to Maximize Zn^{2+} Intercalation

The electrochemistry observed for LVP in 4 m $Zn(OTf)_2$ can be ascribed to the decomposition of active materials induced by H^+ intercalation, which likely produces hydrated vanadium oxides as discussed above. This H^+ intercalation process can be largely suppressed by using $ZnCl_2$ WiSE, resulting in dominant and reversible Zn^{2+}-(de)intercalation electrochemistry. Suppression of H^+ intercalation is due to an interrupted H_2O hydrogen

bonding network and the existence of only a small fraction of free water molecules in $ZnCl_2$-WiSE as we show below via molecular dynamics (MD) simulations. A systematic study on a similar $ZnCl_2$-WiSE has been carried out by Ji *et al.*[92,100] FTIR spectroscopy revealed a decreased O-H symmetric stretch (3200 cm^{-1}) and an increased asymmetric stretch (3400 cm^{-1}) on increasing the concentration of $ZnCl_2$ from 5 m to 30 m, suggestive of a strong Zn^{2+}-water interaction that triggers interruption of H_2O hydrogen bonding network. Furthermore, their MD simulations show that the number of uncoordinated free water molecules in the electrolyte significantly decreases from 10 m $ZnCl_2$ to 30 m $ZnCl_2$.[100]

Nonetheless, while $ZnCl_2$ is low-cost, it is also corrosive at high concentrations. As an alternative approach to reducing H_2O activity, we designed a novel hybrid AZE by using a high concentration of polyethylene glycol 400 (PEG 400) as a crowding agent to form a PEG/H_2O co-solvent. Increased PEG content in 2 m $Zn(OTf)_2$ (≈ 2.2 M) lowers the

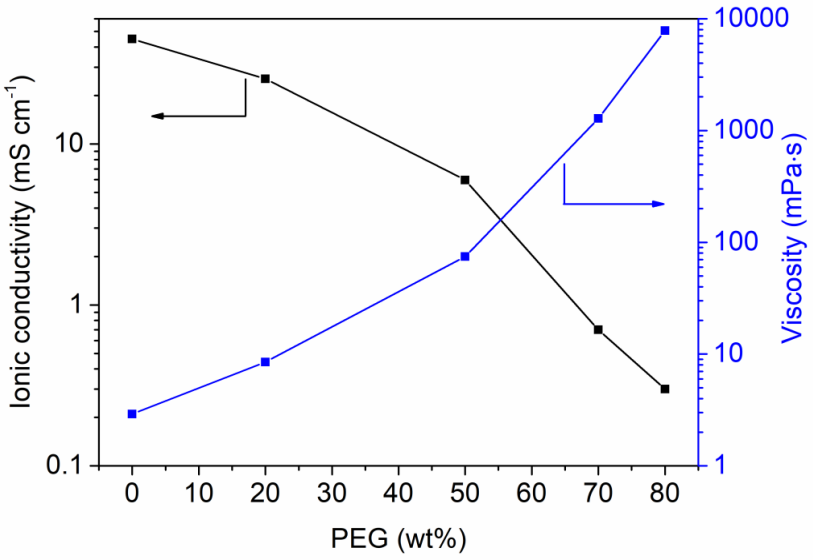

Figure 4.11 Electrolyte ionic conductivity and viscosity of 2 m $Zn(OTf)_2$ with different weight ratios of PEG.

conductivity and increases the viscosity as expected (**Figure 4.11**). Nonetheless, σ_i is still 0.7 mS cm^{-1} even at 70 wt% PEG (denoted as 70PEG), comparable to that of $ZnCl_2$-WiSE. FTIR spectra suggests a strengthened O-H bond owing to the strong H-bonding network between

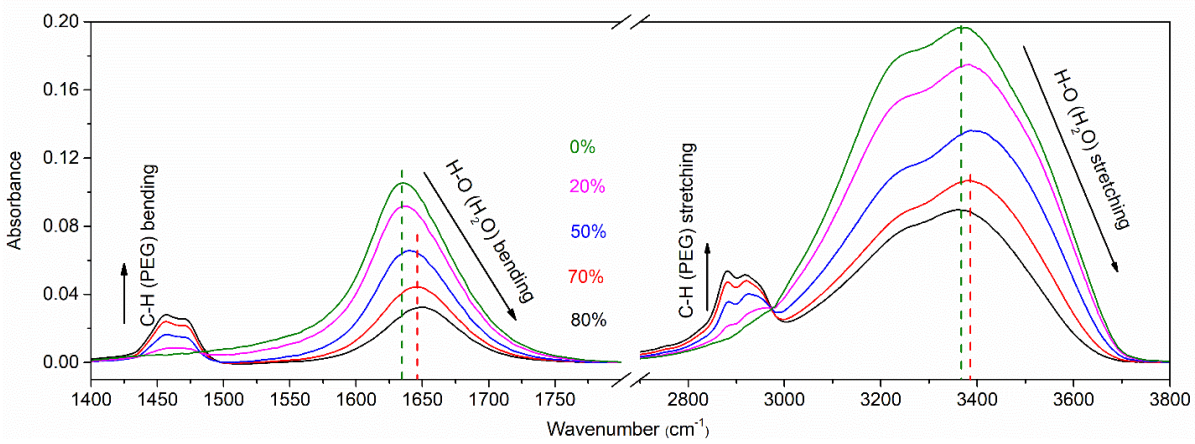

Figure 4.12 FTIR spectra of 2 m $Zn(OTf)_2$ hybrid electrolytes with various weight ratios of PEG in PEG/water co-solvent

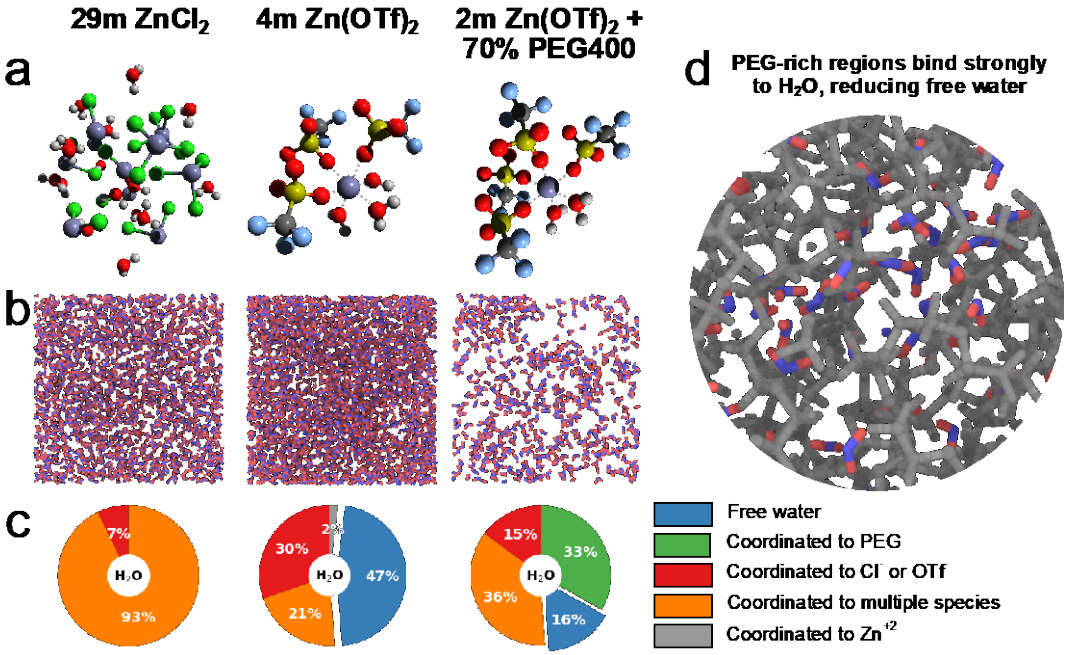

Figure 4.13 Electrolyte structure in 29 m $ZnCl_2$, 4 m $Zn(OTf)_2$, and 70PEG electrolytes. **(a)** Typical Zn^{2+} solvation structures. 29 m $ZnCl_2$ WiSE resembles a disordered crystal due to the relative scarcity of water molecules. Zn^{2+} is most commonly coordinated to 3 OTf^- and 3 H_2O in 4m $Zn(OTf)_2$, whereas in 70PEG the solvation shell typically comprises 4 OTf^- and 2 H_2O. **(b)** Simulation snapshots showing only the water molecules. **(c)** Distribution of water populations**. (d)** Water molecules absorbed into the PEG-rich region of the 70PEG electrolyte.

PEG and H_2O (**Figure 4.12**), which is anticipated to be less favorable to cleavage at the cathode

interface in an electrochemical cell.

We propose that H^+ intercalation at the cathode interface can be effectively suppressed owing to this decreased H_2O activity. Indeed, analysis of the Zn^{2+} solvation structure obtained from MD simulations of the bulk electrolyte shows that the Zn^{2+}- H_2O coordination number in 70PEG (2.3) is lower than in 4 m $Zn(OTf)_2$ (3.3, **Figure 4.13a** and **4.14**), reducing the amount of water available to react at the cathode surface. The Zn^{2+}-H_2O coordination distance is similar in all three electrolytes (**Figure 4.15**), indicating that the strong Zn^{2+}-H_2O interactions previously observed in $ZnCl_2$ WiSE are operative in 70PEG as well.

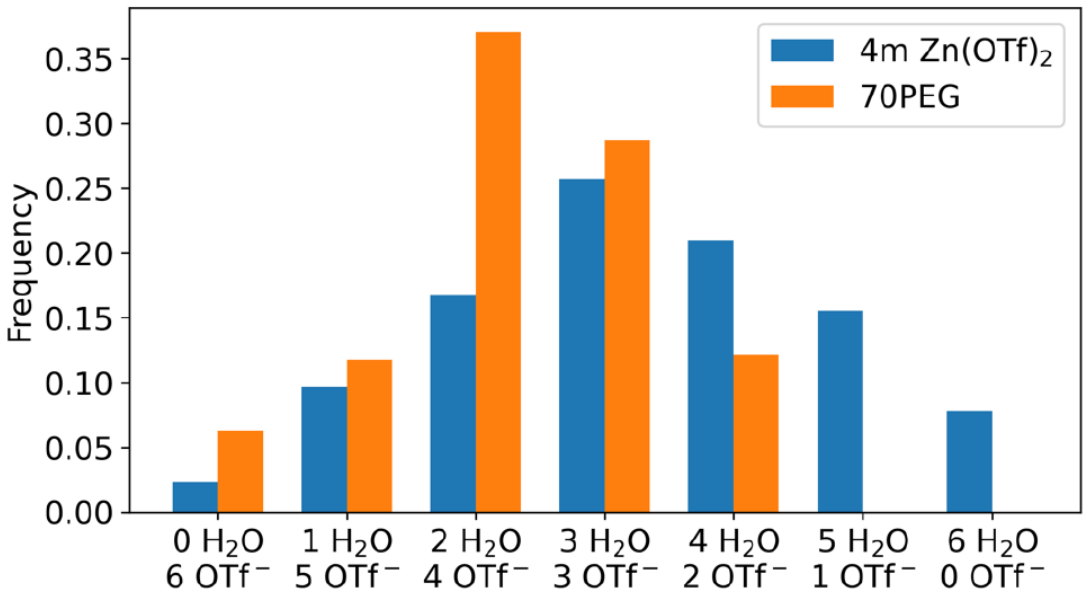

Figure 4.14 Frequency of occurrence of different solvation environments around Zn^{2+}, as obtained from MD simulations. The Zn^{2+} coordination number was always found to be six, but the number of water and triflate molecules (indicated by the x axis labels) varied, shifting from more waterrich shells in 4 m $Zn(OTf)_2$ to more OTf^- rich shells in 70PEG.

Further analysis of our simulations reveals that the fraction of free water is only 16% in 70PEG, compared to 47% in 4 m $Zn(OTf)_2$ and 0% in $ZnCl_2$-WISE (**Figure 4.13c**), presumably resulting in very low water activity. Examination of the structure of the 70PEG shows that PEG400 molecules aggregate to form PEG-rich regions which absorb water but

exclude ions (**Figure 4.13b-d**). This finding is consistent with experimental studies, which

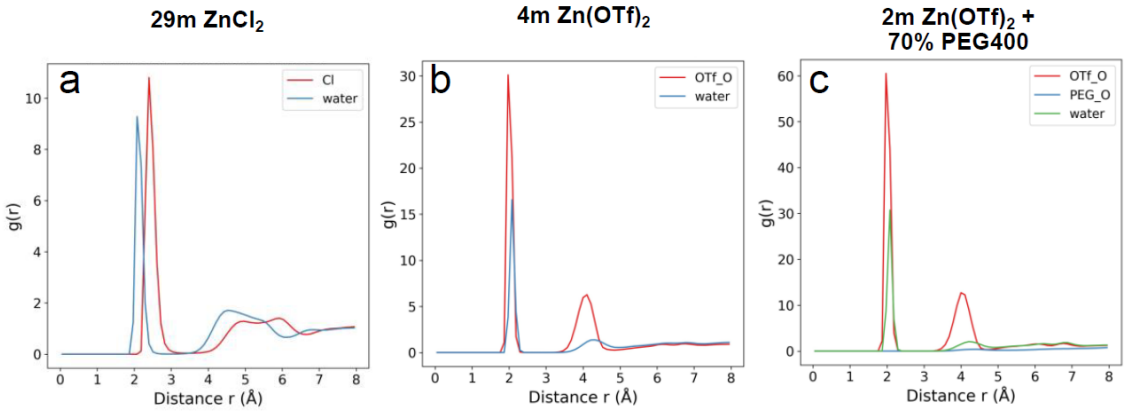

Figure 4.15 Radial distribution functions for H_2O, Cl^-, OTf^- and PEG coordination to Zn^{2+} obtained from MD simulations.

have shown that PEG aggregates in aqueous solution, forming internally-hydrated helical structures that result from the balance of hydrophobic and hydrophilic moieties on the molecule.[101] In 70PEG, this internal hydration reduces the free water content and hinders H_2O molecules from transporting to the cathode interface. Thus, we attribute the reduced H^+ intercalation in $ZnCl_2$-WISE and 70PEG to the low availability and reactivity of water molecules.

Proof of concept was realized by evaluating Zn plating/stripping behavior for the hybrid AZE in Ti || Zn asymmetric cells, where a very high coulombic efficiency of around 99.7% is achieved for 70PEG at a current density of 1 mA cm^{-2} (1 mAh cm^{-2} capacity), as shown in **Figure 4.16a, b**. In contrast, 0PEG cells suffer from serious dendrite formation under the same operating conditions and failed after three cycles (**Figure 4.17**). A Zn || Zn symmetric cell with 70PEG also functions steadily with a capacity of 1 mAh cm^{-2} over more than 1800 hours (> 450 cycles), with a denser and more oriented Zn deposition morphology (**Figure 4.18, 19**). Such dendrite-free Zn plating/stripping is consistent with previous work based on a very low weight ratio of PEG or PEO (<1 wt%) in water, where the adsorption of PEG polymer on the electrode surface was proposed to result in more uniform Zn deposition. In addition, an

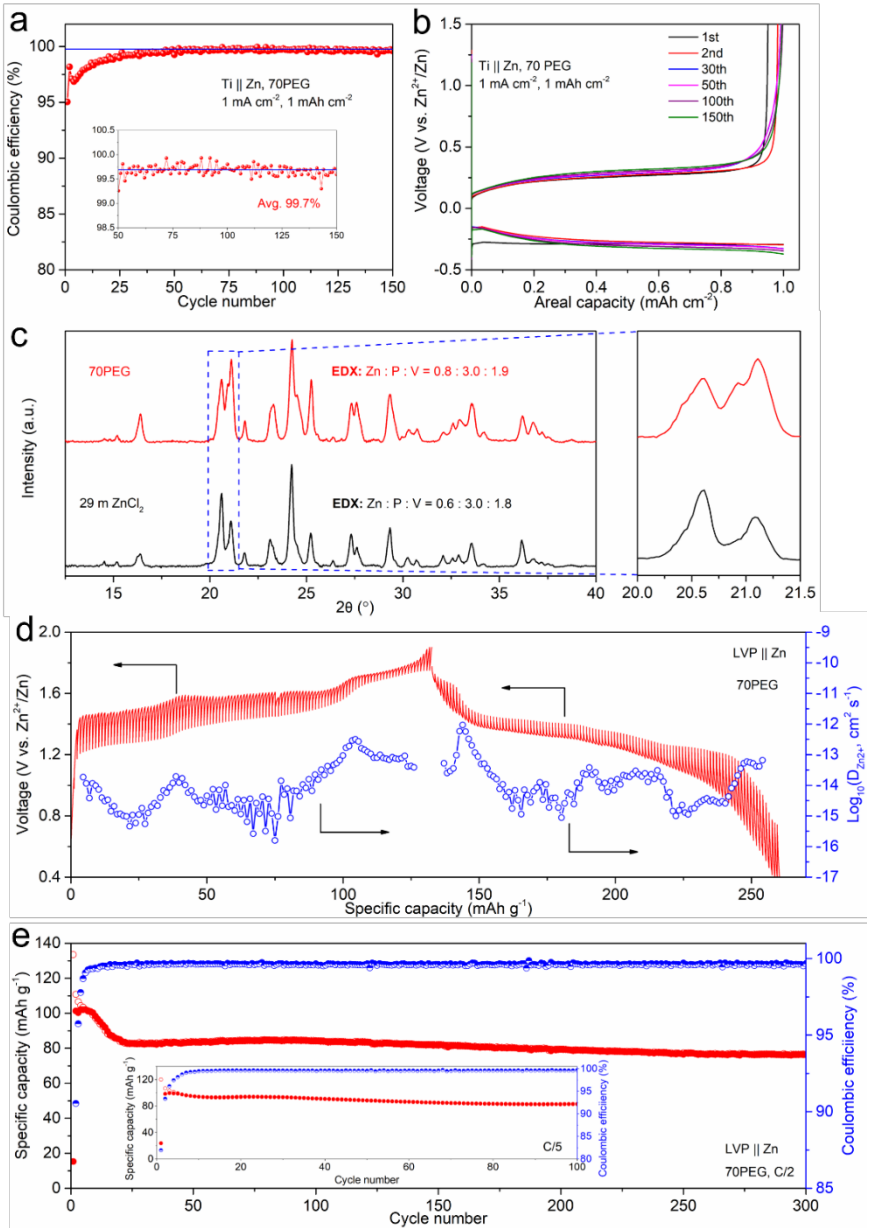

Figure 4.16 (a) CE evolution over 150 cycles in 70PEG of Ti||Zn asymmetric cell at 1 mA cm^{-2} for 1 mAh cm^{-2} (Inset = magnified view from 50th to 150th cycles) and **(b)** corresponding charge–discharge curves. **(c)** XRD patterns of 2nd fully discharged LVP electrodes in 29 m $ZnCl_2$ and 70PEG at C/40 with corresponding EDX ratios of Zn, P and V. **(d)** GITT profiles and resulting diffusion coefficient data for LVP in 70PEG at C/40; cells were first discharged prior to charge. **(e)** Capacity retention of LVP in 70PEG at C/2 and C/5 (inset).

expanded electrochemical stability window of 2.75 V in 70PEG from 2.32 V in 0PEG can be

obtained owing to the reduced water activity (**Figure 4.20**).

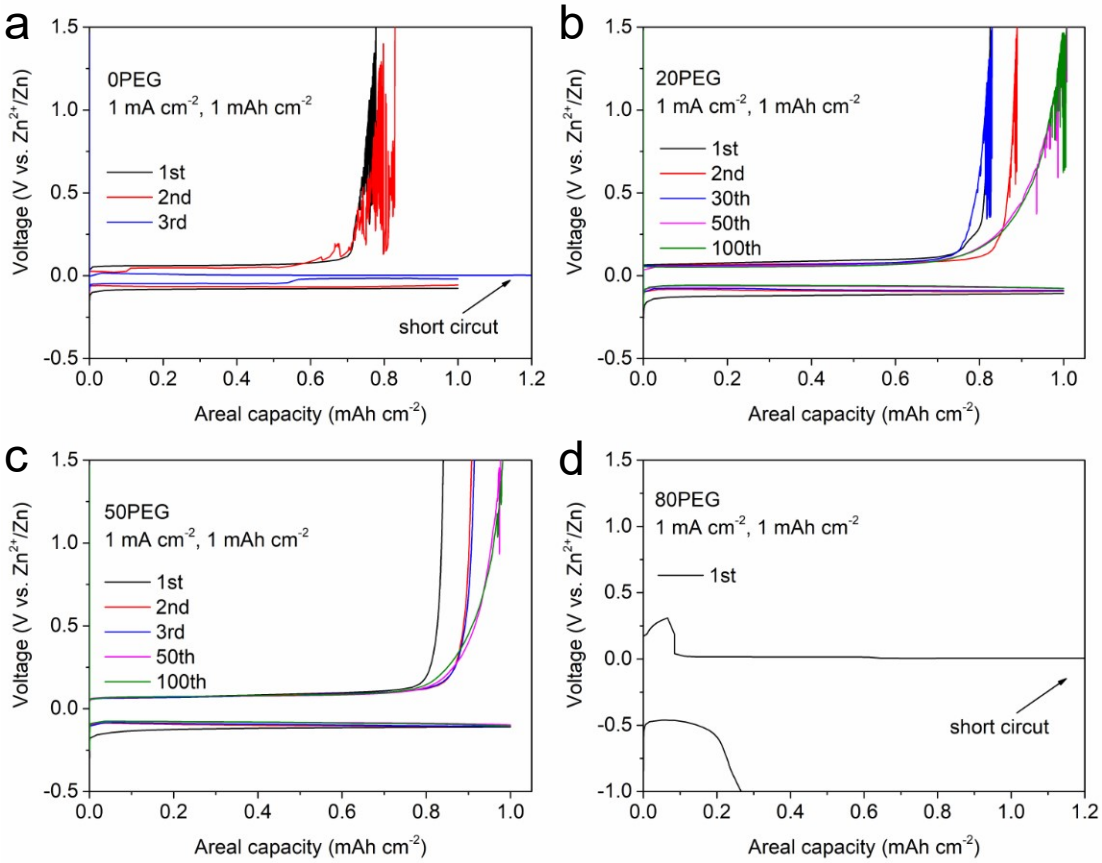

Figure 4.17 Charge-discharge curves of Ti || Zn asymmetric cells at 1 mA cm^{-2} for 1 mAh cm^{-2} in **(a)** 0PEG, **(b)** 20PEG, **(c)** 50PEG and **(d)** 80PEG.

The 70PEG electrolyte is as efficient for suppressing H^+ intercalation as $ZnCl_2$ WiSE in LVP || Zn full cells (**Figure 4.16c-d**). Compared to the 2nd discharge capacity of 115 mAh g^{-1} (≈ 0.85 Zn^{2+}) in $ZnCl_2$ WiSE, a similar capacity of 112 mAh g^{-1} (≈ 0.82 Zn^{2+}) is obtained at C/40 in 70PEG (**Figure 4.21**). Analysis of the electrode by EDX shows a composition of 0.83 Zn^{2+} per formula unit, suggesting almost all the capacity is contributed by Zn^{2+} intercalation (compared with only 70% in $ZnCl_2$ WiSE). XRD patterns of these two discharged samples are quite similar (**Figure 4.16c**), however, the presence of at least three zincated phases lead to a poor Rietveld fit owing to the significant overlap of peaks in these similar

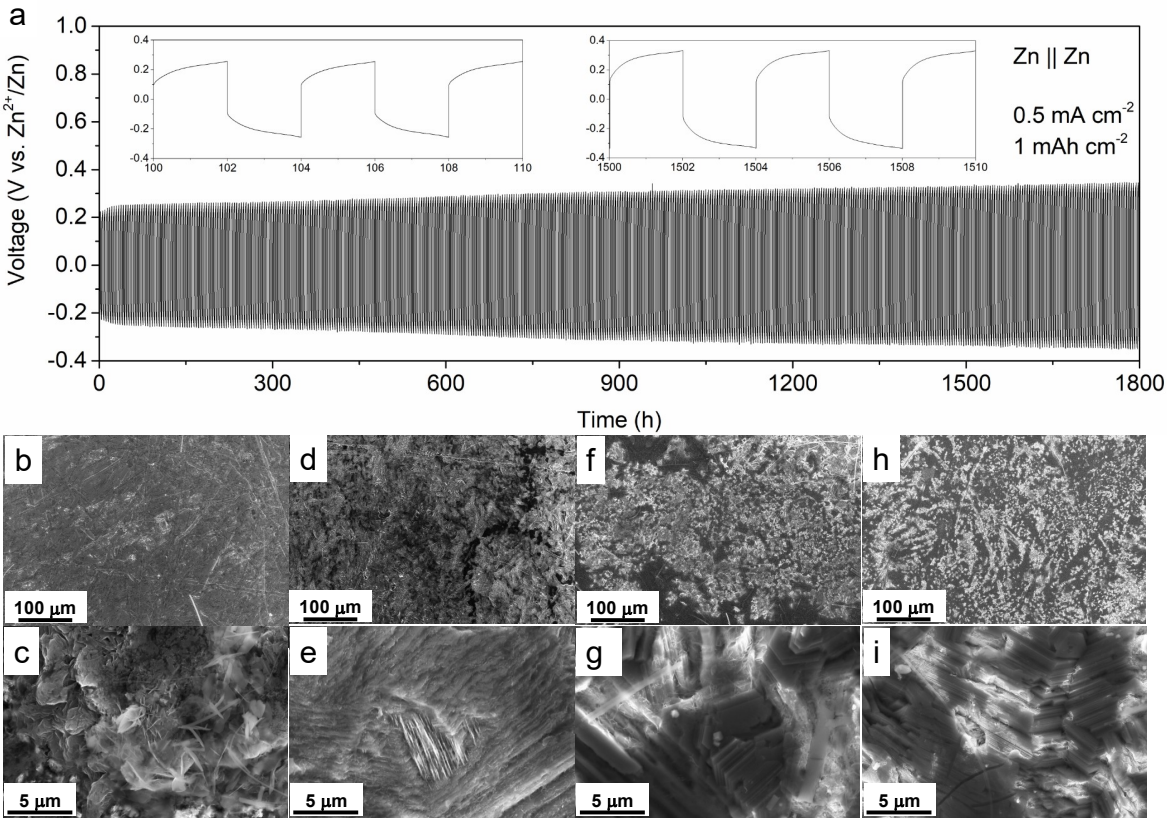

Figure 4.18 (a) Voltage profiles of Zn stripping/plating in a Zn || Zn symmetric cell at 0.5 mA cm^{-2} for 1 mAh cm^{-2}; SEM images of Zn in a Zn || Zn symmetric cell after 10 stripping/plating at 1 mA cm^{-2} for 1 mAh cm^{-2} in **(b, c)** 0PEG, **(d, e)** 20PEG, **(f, g)** 50PEG and **(h, i)** 70PEG.

structures. GITT studies in LVP/70PEG (**Figure 4.16d**) yielded an average diffusion coefficient of ~10^{-13} - 10^{-16} cm^2 s^{-1} that is about 10^2-10^3 lower than previously reported,[94] presumably owing to the lack of significant contribution from H^+ ion diffusion. Protons are anticipated to be much more mobile due to their small ionic radius and monovalent property. However, direct comparison with LVP/4 m $Zn(OTf)_2$ could not be obtained due to severe phase transformation resulting from very high degrees of proton intercalation at such a low rate of C/40, where endless discharging was observed (**Figure 4.22**). Long-term Zn^{2+} cycling behavior of LVP in PEG was also evaluated at higher rates (**Figure 4.16e**). After an initial activation process, LVP can be cycled steadily with capacity retention of 83.5% after 100

cycles at C/5 and 74.5% after 300 cycles at C/2. Compared to the evolution of the charge/discharge curve profiles upon cycling cells in 4 m $Zn(OTf)_2$, only a slight change can be observed in 70PEG (**Figure 4.23**). The absence of a voltage plateau below 0.5 V also indicates the suppression of H^+ intercalation.

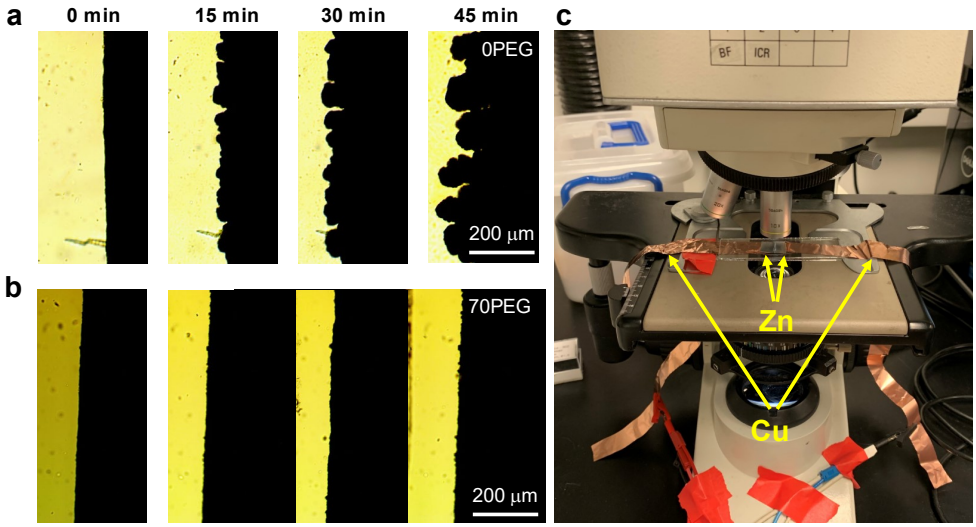

Figure 4.20 In-situ optical microscopy studies of Zn plating in Zn||Zn symmetric cells in **(a)** 0PEG and **(b)** 70PEG at a current density of 5 mA cm^{-2} (based on the cross-sectional area of Zn foil electrode); **(c)** picture of the transparent cell in the optical microscope.

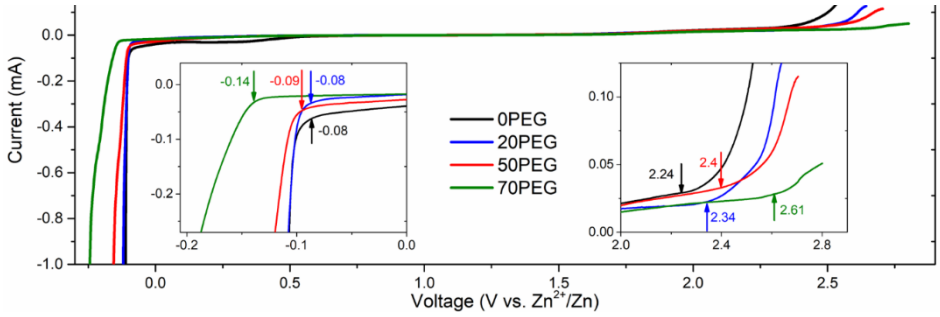

Figure 4.19 LSV curves of different electrolytes at a scan rate of 1 mV s^{-1} based on three electrode cells with Zn as the reference electrode and Ti as both working and counter electrode.

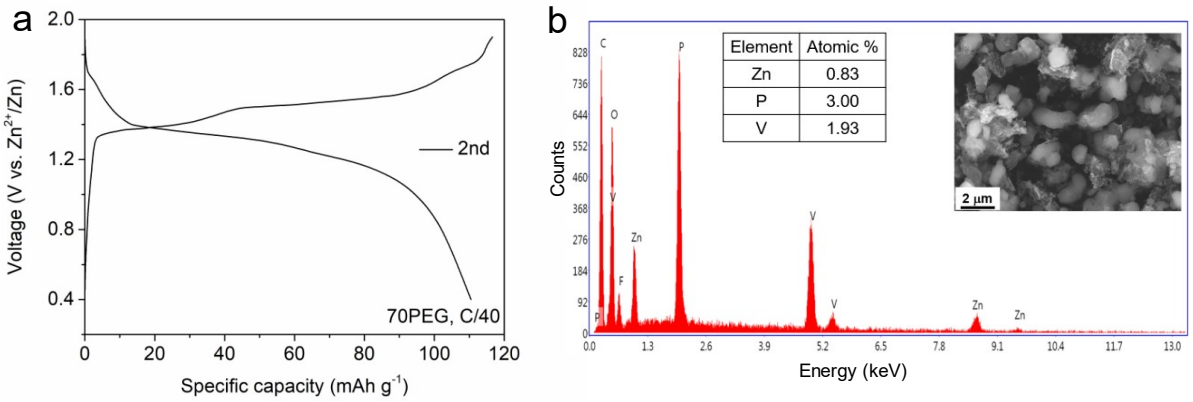

Figure 4.21 (a) Charge-discharge curves of LVP in 70PEG at C/40 and **(b)** corresponding EDX data and SEM image.

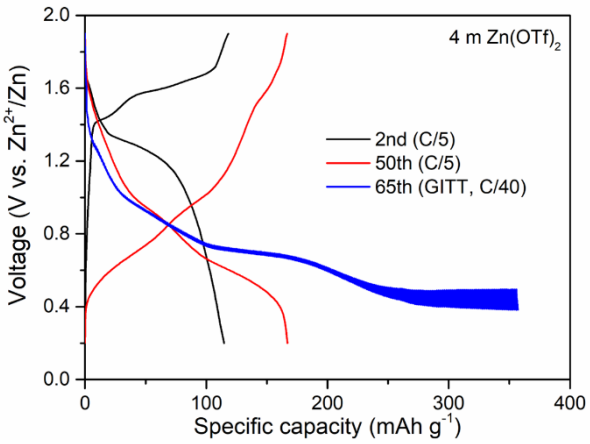

Figure 4.22 GITT profile of LVP/4 m $Zn(OTf)_2$ at C/40. The cell was first run for 64 cycles to reach maximum capacity at C/5 prior to the GITT measurement.

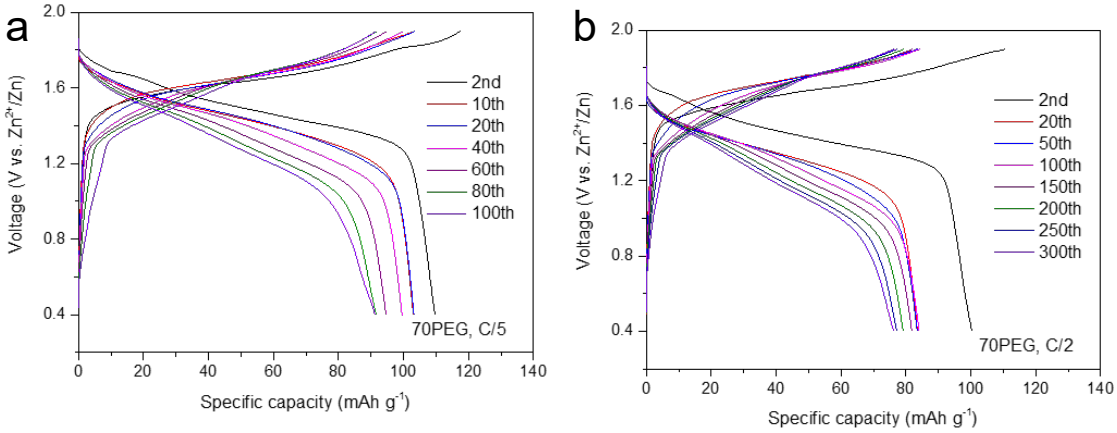

Figure 4.23 Charge-discharge curves of LVP at **(a)** C/5 rate and **(b)** C/2 rate in 70PEG

Chapter 5 Enabling Selective Zinc-Ion Intercalation by A Eutectic Electrolyte for Practical Anodeless Zinc Batteries

5.1 Introduction

In this aforementioned chapters, commercialization of ZMBs is still hindered by two major obstacles including: (1) Zn dendrite formation and its parasitic reactions with the electrolyte that lead to unsatisfactory anode reversibility;[66] and (2) unfavorable proton intercalation and consequent deleterious transition-metal dissolution of oxide cathodes at practical loadings and rates.[10,17,88] In contrast to countless studies on tackling the former, currently, very limited studies are being devoted to the issues of oxide cathodes. Proton co-intercalation is an intrinsic parasitic reaction occurring in these oxides during discharge in mildly-acidic dilute Zn electrolytes,[18,89,102] which favors high-rate cycling but compromises low-rate stability. Previous studies have demonstrated that layered double hydroxides (LDHs) always participate/dissolve on the surface of the cathode upon proton insertion/extraction, thus ensuing charge balance on the cathode/electrolyte interface. The high mobility of protons in the hydrated lattice enables the high-rate capability of ZMBs, nonetheless, the facile detachment of LDHs from the surface, accompanied by cathode dissolution, causes considerable irreversibility. Lowering water activity using aqueous-nonaqueous electrolytes has been reported to potentially suppress proton intercalation.[15] However, the efficacy of such approaches has not been verified in the more widely studied and high-capacity transitional metal oxide cathodes. More serious concerns are the low (typically ~0.3 mAh cm^{-2}) cathode loading and ~0.2% Zn anode utilization due to poor Zn reversibility that were achieved in these studies; below the benchmark for translation and scale-up for practical ZMBs.

Recently, in the design of dilute-salt aqueous electrolytes, various aqueous-nonaqueous hybrid solvents were reported for Li-ion batteries, where some water was substituted by organics including polyethylene glycol (PEG)[103] and sulfolane.[104–106] Similar concepts were then applied to ZMBs.[24,107–113] A critical similarity among these studies is the displacement of water by nonaqueous solvents in the Zn^{2+} solvation structure, thus reducing the water activity. Unfortunately, a partially hydrated Zn^{2+} solvation sheath has a greater desolvation penalty than a fully hydrated one,[12] that can result in sluggish interfacial charge transfer and high Zn

deposition overpotentials. Moreover, most studies utilized low areal capacities of the cathode (<1 mAh cm^{-2}), high C-rates (5 ~ 50C), or impractically low Zn utilization (<1 %), and did not address deleterious proton intercalation and cathode dissolution at practical level.

In this chapter, I elucidated the Zn^{2+} vs. proton intercalation mechanism of a metal oxide cathode ($Zn_{0.25}V_2O_5{\cdot}nH_2O$ (ZVO)) in various electrolytes by a combination of *ex-situ*/*operando* techniques. A strategy of using sulfolane-based hybrid eutectic electrolyte – where the strong interaction of two or three components enables different physical/chemical properties from either of single components – is shown to effectively suppress deleterious proton intercalation and cathode dissolution. This is ascribed to a strong hydrogen-bonded network of sulfolane-water that alleviates water activity. In addition, a fully hydrated Zn^{2+} solvation structure is revealed and induces facile interfacial charge transfer at the Zn metal surface. Highly stable and reversible Zn plating/stripping is demonstrated in both Zn||Cu and Zn||Zn cells. Benefiting from both stabilized electrodes in the hybrid eutectic electrolyte, we report the first practical high-areal-capacity (4 mAh cm^{-2}) Zn anode-free cell that can run over 100 cycles at 0.15C with ~ 85% capacity retention.

I proposed the idea, planned the experiments, performed all electrochemical measurements and wrote the original manuscript. Dr. Ryan Kingsbury and Dr. Kristin A. Persson performed molecular dynamics, DFT and XANES spectra simulations. Dr. Timothy T. Fister collected XANES and EXAFS spectra. Dr. Arashdeep Singh Thind and Dr. Robert F. Klie. performed STEM studies. Abhinandan Shyamsunder performed NMR measurement.

5.2 Experimental Approaches

5.2.1 Preparation of Hybrid Eutectic Electrolytes

Hybrid eutectic co-solvents were prepared by mixing 0.3, 0.5, 0.8, 1.0 g deionized water with 0.7, 0.5, 0.2 and 0 g sulfolane (99%, Sigma-Aldrich) at 25 °C. Subsequently, 2 mmol $Zn(OTf)_2$ (98%, Sigma-Aldrich) was added into the above mixtures to obtain 70SL, 50SL, 20 SL and 0SL electrolytes, respectively. For Zn-iodine full cell measurements, 0.5 m KI was added into 70SL and 0SL as the active material.

5.2.2 Preparation of $Zn_{0.25}V_2O_5 \cdot nH_2O$ (ZVO) and Activated Carbon (AC) Cathodes

The ZVO nanobelts were synthesized based on a previously reported microwave hydrothermal method.[13] High-surface area Black Pearls 2000 carbon (BP 2000) was directly used as the iodine host. The low-loading cathodes were prepared by mixing 70 wt% active material, 20 wt% conductive carbon (Super P) and 10 wt% polyvinylidene difluoride (PVDF) in N-methyl-2-pyrrolidone (NMP; anhydrous, 99.5%; Sigma-Aldrich). The mixed homogeneous slurry was cast on carbon paper (thickness: 170 μm) by doctor blading. The electrodes were punched into 10 mm discs after being dried at 60 °C overnight. The mass loading of active material was approximately 3.6 ± 0.3 mg cm^{-2}, although each cathode laminate was weighed independently. To prepare freestanding thick electrodes, 80 wt% active materials were mixed with 10 wt% conductive carbon (Ketjenblack) and 10 wt% polytetrafluoroethelene (PTFE, 60 wt% in H_2O, Sigma-Aldrich), using isopropanol (99.5%, Sigma-Aldrich) as the dispersing agent. The slurry thus obtained was quickly pressed to form freestanding electrodes. After drying at 60 °C overnight, the electrodes were cut into small pieces and pressed onto 10 mm titanium mesh.

5.2.3 Electrochemical Measurements

PFA-based Swagelok-type cells were used in this study. The Zn||Cu asymmetric cells were assembled using Cu foil (thickness: 9 μm; diameter: 11 mm) as the positive current collector, Zn metal foil (99.9%; Sigma-Aldrich; thickness: 250 μm; diameter: 10 mm) as the negative, and commercial Whatman glass fiber as the separator (diameter: 12.7 mm). In Zn||Zn symmetric cells, Zn foils were used as both positive and negative electrodes. The full cells with low-loading ZVO or activated carbon (AC) cathodes were assembled with 100 μL electrolyte, using Zn metal foil as the anode. Cu foil with pre-deposited Zn was utilized as the anode in high-loading full cells, where the amount of electrolyte was increased to 200 μL to ensure good electrode infusion. The electrochemical stability window of the hybrid eutectic electrolyte was investigated by linear sweep voltammetry (LSV) at a sweep rate of 1 mV s^{-1}, based on three-electrode cells with Zn as the reference electrode, and Ti as both working and counter

electrodes. Chronoamperometry (CA) measurements were conducted at a constant polarization of 5 mV on Zn||Zn symmetric cells. All cells were examined using a VMP3 potentiostat/galvanostat station (Bio-Logic) at 25 °C.

5.2.4 Impedance Analysis

The evolution of charge transfer resistance of two-electrode Zn||Zn symmetric cells was measured by electrochemical impedance spectroscopy (EIS) with a voltage amplitude of 5 mV in the frequency range of 1 MHz to 100 mHz. The cell was rested for 10 min to reach equilibrium before each EIS measurement. For the activation energy measurements, three-electrode cells were assembled with Zn as both working, counter and reference electrodes. Impedance was measured from 1 MHz to 1 Hz with 10 mV amplitude, at temperatures ranging from 40 °C to 70 °C. The activation energy (*Ea*) for interfacial charge transfer is extrapolated based on the Arrhenius equation (1):

$$\frac{1}{R_{CT}} = A\, e^{-\frac{Ea}{RT}} \quad (1)$$

where R_{CT} is the charge transfer resistance, R is the ideal gas constant, T is the absolute temperature and A is the frequency factor.

5.2.5 Galvanostatic Intermittent Titration Technique (GITT) Studies

GITT of ZVO in different electrolytes were performed using a current pulse of 20 min at an equivalent 0.1C rate followed by a 3-hour rest. The average ion diffusion coefficients (D) in ZVO were calculated from the GITT data by the following equation (2) first reported by Weppner and Huggins[97]:

$$D = \frac{4}{\pi\tau} \times \left(\frac{n_M V_M}{S}\right)^2 \times \left(\frac{\Delta E_s}{\Delta E_t}\right)^2 \quad (2)$$

where τ is the current pulse duration (20 min) of a single step of GITT experiment; ΔE_S and ΔE_t are the change in the steady state voltage and overall cell voltage in one current pulse, respectively; n_M and V_M are the moles and molar volume of ZVO, respectively; and the geometric area (S) of the electrode is used for simplicity and comparison with previous data.

5.2.6 Material Characterization

Powder X-ray diffraction (XRD) patterns were obtained on an X-ray diffractometer (PANalytical Empyrean) with Cu-Kα radiation and a PIXcel bidimensional detector. *Operando* XRD were performed in a home-built cell, using glassy carbon as the current collector and X-ray window. The free-standing electrodes were used in *operando* diffraction experiments, during which low-angle peaks (< 10°, 2θ) were blocked by the cell case. Fourier transform infrared spectroscopy (FTIR) was carried out on a Bruker Tensor 27 system equipped with attenuated total reflection (ATR). ^{1}H NMR experiments were carried on a Bruker Advance 300 MHZ instrument at 25 °C. The ionic conductivity and viscosity of the series of electrolytes was measured using an Orion Star A325 pH/ Conductivity Meter (Thermo) and an automated viscometer (RheoSense Inc.) at 22 °C, respectively. To collect X-ray absorption near-edge structure (XANES) and the Fourier transformation of extended X-ray absorption fine structure (EXAFS) spectra, samples were prepared by wetting multiple layers of glass fiber separator that were packaged between two glass coverslips with a fluorsilicone gasket. Dilute samples were measured in 3mm NMR tubes. In both cases, X-ray absorption was measured in transmission mode using a zinc metal foil reference (9659 eV). A Zeiss Ultra field emission SEM instrument was used to collect scanning electron microscopy (SEM) images and energy-dispersive X-ray spectroscopy (EDS) data. The *in-situ* optical microscopy was carried out using a home-made transparent electrochemical cell and an optical microscope outfitted with a digital camera. XPS experiments were conducted on a Thermo Scientific K-Alpha XPS instrument. CasaXPS software was used to conduct XPS data analysis, where the C 1s peak of 284.8 eV was used to calibrate the binding energies. Spectral fitting was based on Gaussian-Lorentzian functions and a Shirley-type background. The Ar^{+}-ion sputtering etching rate was estimated to be ~1.0 nm min^{-1}. High-resolution transmission electron microscopy (TEM) images of deposited Zn were collected on a Hitachi HF-3300. All electrodes disassembled from the cells were washed by water five times and by ethanol twice, and dried at 25 °C before each characterization. Differential scanning calorimetry (DSC) was performed on Netzsch STA 449 F3 Jupiter from -100 °C to 25 °C at a ramp rate of 10 °C min^{-}

[1]. Gas chromatography (GC) data was obtained on a multiple gas analyzer SRI MG-5 using Ar as the gas carrier.

5.2.7 Scanning Transmission Electron Microscopy (STEM)

The high-resolution imaging and spectroscopy experiments were conducted at the University of Illinois Chicago using the JEOL JEM-ARM200CF microscope operating at 200 kV. The microscope is equipped with a cold-field emission electron gun and a CEOS aberration corrector with a probe size of 0.78 Å. The pristine and discharged samples were dispersed in acetonitrile and subsequently drop cast onto a TEM grid. EDS data was acquired using the Oxford X-Max 100TLE windowless silicon drift detector. EELS experiments were carried out using a dual-range Gatan Continuum spectrometer with a dispersion of 0.3 eV per channel and an entrance aperture of 5 mm. The convergence and collection semi-angles for the spectrometer were 17.8 mrad and 53.4 mrad respectively. The zero-loss peak (ZLP) and the core-loss edges (V L, O K and Zn L edges) were acquired simultaneously with an acquisition time of 0.0001 seconds and 0.25 seconds per pixel respectively. Fourier log deconvolution was performed to remove the multiple scattering components from the core-loss edges. To improve the signal-to-noise ratio of the core-loss spectra, we have performed principal component analysis. A power law was used to model the background signal before V L and Zn L edges. The atomic-resolution HAADF images were obtained using the probe convergence angle of 25 mrad where the inner and outer diameters of the annular detector were set to 68 mrad and 174.5 mrad. To minimize electron beam damage, the atomic-resolution HAADF imaging was performed sequentially, where multiple frames (10-20 frames) were aligned and integrated to obtain atomically resolved HAADF images with a high signal-to-noise ratio. The electron dose was kept below a threshold of 400 e/Å^2 for the pristine and discharged ZVO samples during STEM experiments.

5.3 Electrolyte Network of Hybrid Eutectic Electrolytes

We chose sulfolane (SL) as the crowding agent because of its low-cost; high flash and boiling points (**Figure 5.1a**); and ability to act as a second hydrogen bond acceptor to reduce

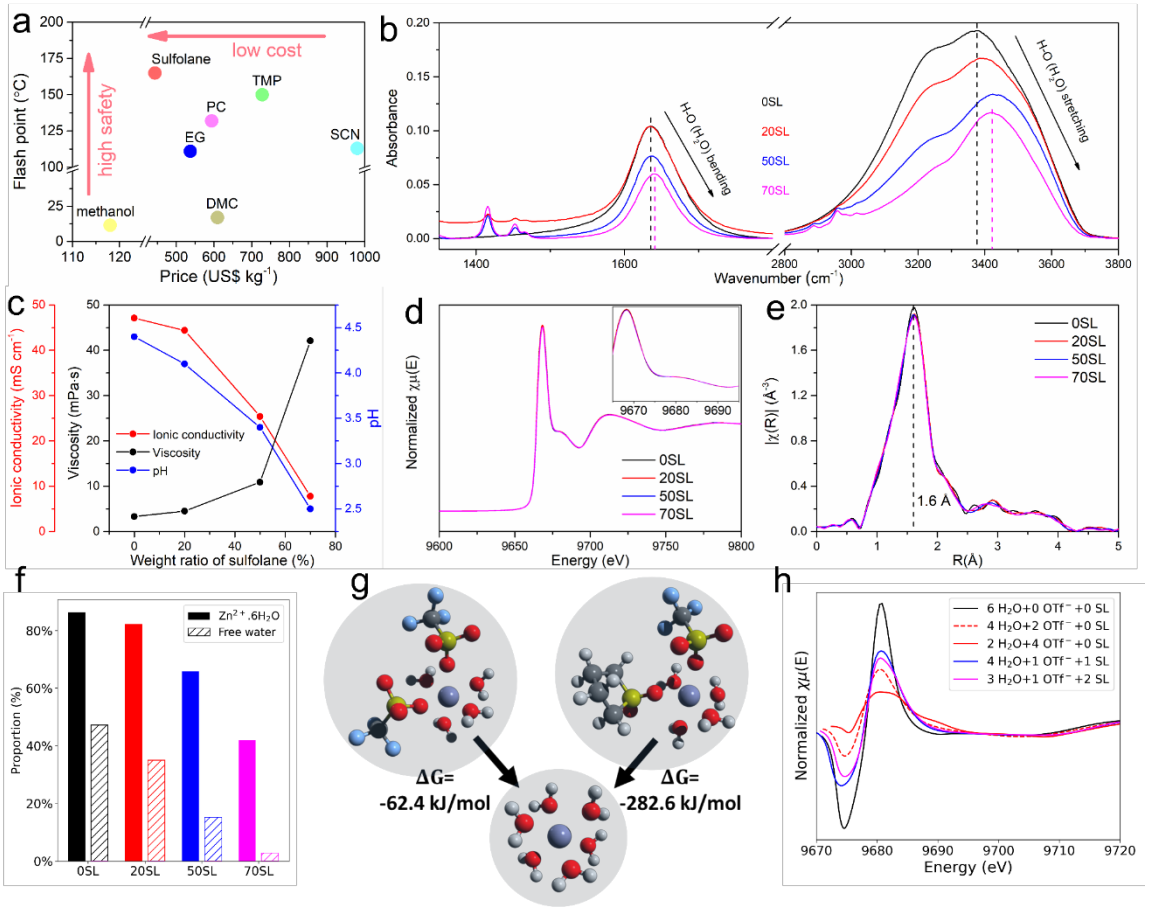

Figure 5.1 (a) Price and flash points of various nonaqueous solvents: methanol, sulfolane, ethylene glycol (EG), propylene carbonate (PC), dimethyl carbonate (DMC), trimethyl phosphate (TMP), and succinonitrile (SCN). **(b)** FTIR spectral evolution of different electrolytes. **(c)** Evolution of ionic conductivity, viscosity, and pH at various weight ratios of sulfolane. **(d, e)** XANES **(d)** and EXAFS **(e)** spectra of different electrolytes. **(f)** Proportion of fully hydrated Zn^{2+} (filled bars) and free water (hatched bars) from classical MD simulation of bulk electrolytes. **(g)** DFT-computed reaction energies to form fully hydrated Zn^{2+} from other cluster types ($Zn^{2+}{\cdot}4H_2O{\cdot}2OTf^-$, left, or $Zn^{2+}{\cdot}4H_2O{\cdot}1OTf^-{\cdot}1SL$, right). **(h)** Simulated XANES spectra associated with different solvated cluster types.

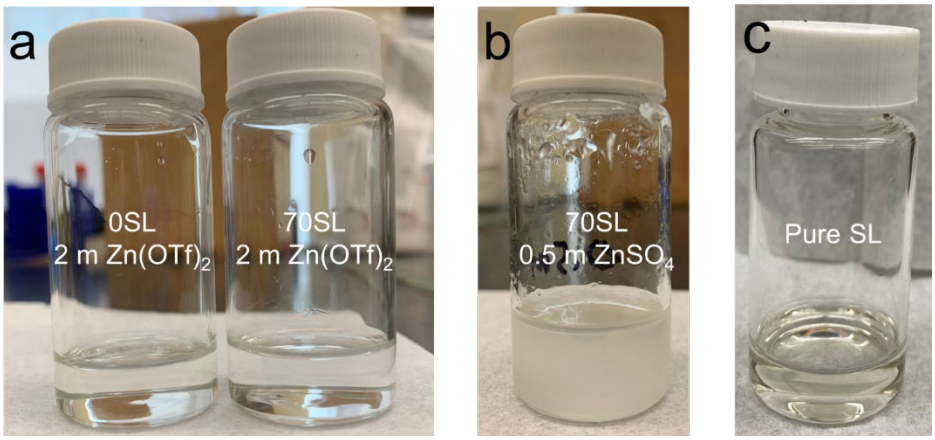

Figure 5.2 Pictures of prepared hybrid eutectic electrolyte. **(a)** 0SL/2 m $Zn(OTf)_2$ and 70SL/2 m $Zn(OTf)_2$ shows similar colorless electrolyte with all salts fully dissolved. **(b)** 70SL/0.5 m $ZnSO_4$ shows a cloudy mixture, indicating very limited solubility of $ZnSO_4$. **(c)** Pure SL shows slightly yellowish color due to the unknown industrial impurity, which could have a possible but minor effect on electrolyte properties considering its very low quantity (<1% in pure SL). All electrolytes were stirred at room temperature for at least 4 hours to fully mix solvents and salts.

water activity.[110,112] $Zn(OTf)_2$ exhibits high solubility (**Figure 5.2**), and reduced desolvation penalty owing to the bulky OTf^- anion; good compatibility with Zn,[114–116] and relatively low cost compared to other bulky-anion salts.[32] Through experimental trials, we find that 7:3 (denoted as 70SL), weight/weight, is the highest ratio of SL/water that can form the eutectic electrolyte with a low melting point of -81.6 °C (**Figure 5.3**) and adequate solubility of salts (2 m, molality) at 25 °C. The much lower melting point of eutecti electrolyte compared to water (0 °C) and sulfolane (27.5 °C) suggests the strong interaction between these two compoents that interrupts the hydrogen network of water as shwon below.

The reduced water activity of 70SL relative to 0SL was demonstrated by the blue shift of both bending and stretching modes of the O-H bond of H_2O in Fourier Transform Infrared spectra (FTIR, **Figure 5.1b**), suggesting a strengthened O-H bond due to the strong interaction between SL and H_2O. This is verified by the narrowing of the corresponding ^1H peak in the ^1H-NMR spectrum with the addition of SL as well as low volatility in an open atmosphere

(**Figure 5.4**). While increased SL/water ratios give lower ionic conductivity (σ_i) and higher viscosity **(Figure 5.1c)**, σ_i is sufficiently high (7.8 mS cm^{-1}) for 70SL.

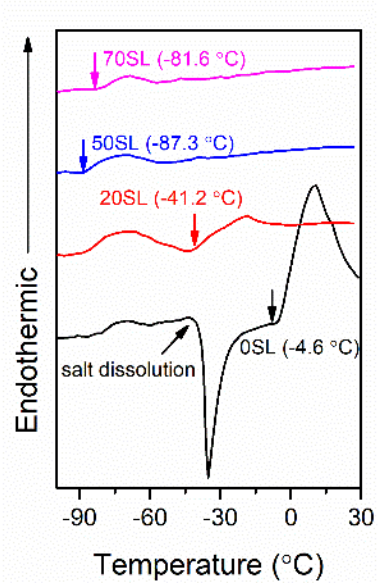

Figure 5.3 DSC curves with labeled melting points of various electrolytes. Data were collected from -100 °C to room temperature with a heating rate of 10 °C min^{-1}**.**

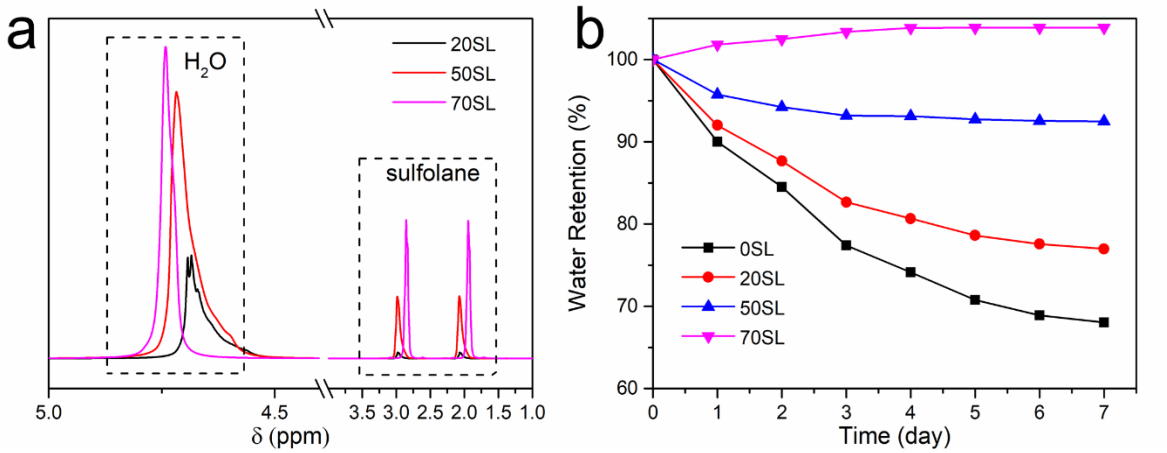

Figure 5.4 (a) ^{1}H-NMR spectra of different electrolytes. **(b)** water retention of different electrolytes as a function of time on exposure to open atmosphere.

Intriguingly, the Zn^{2+} solvation structure is not altered by SL, as shown by the exactly overlapped X-ray absorption near-edge structure (XANES) spectra (**Figure 5.1d**). Extended

X-ray absorption fine structure (EXAFS) data (**Figure 5.1e**) reveal a peak at 1.60 Å, corresponding to the Zn-O bond length in $Zn^{2+}(H_2O)_6$.[117] This was further confirmed by classical molecular dynamics (MD) simulations that show fully hydrated Zn^{2+} is the predominant solvated cluster type in 0SL, 20SL, and 50SL. Solvation shells containing triflate and/or SL become more prevalent as the SL loading increases (**Figure 5.1f**), although Zn^{2+} was 6-coordinate in all cases. The free water content also decreases with SL loading. Although the MD simulations suggest that a significant fraction of Zn^{2+} clusters in 70SL are not fully hydrated, this result should be interpreted cautiously because competition between water, triflate, and SL in Zn^{2+} solvation was found to be particularly sensitive to the charge scaling protocol employed. This reflects inherent limitations of empirical, non-polarizable water models.[118,119] Indeed, first-principles reaction energies computed from density functional theory (DFT) indicate that Zn^{2+} clusters containing triflate or SL in their primary solvation shell will spontaneously revert to fully hydrated Zn^{2+} (**Figure 5.1g**). Moreover, simulated XANES spectra of specific cluster types indicates that entry of triflate or SL into the primary Zn^{2+} solvation shell would result in features to the right of the primary K-edge peak at ~9685 eV (**Figure 5.1h**), which were not observed in the experimental spectra (**Figure 5.1d**). Taken together, the results support the view that a high proportion of fully hydrated Zn^{2+} is maintained at all SL content. Thus, facile interfacial charge transfer and a low Zn deposition overpotential can be anticipated owing to the low desolvation penalty of the $(Zn(H_2O)_6)^{2+}$ cation.[12] It should be noted that the partially hydrated solvation structures based only on MD simulations were proposed in previously reported hybrid electrolytes.[24,107–113] Nonetheless, such simulation results should be cautiously interpreted due to the complicated parameter optimization as mentioned above. We believe that a combination of conclusive experimental analysis (for example, XAS spectra), MD simulations and DFT calculations are necessary to identify the Zn^{2+} solvation sheath in hybrid electrolytes.

5.4 Zn^{2+} vs. Proton Intercalation Electrochemistry in the Metal Oxide Cathode

$Zn_{0.25}V_2O_5{\cdot}nH_2O$ (ZVO) was selected as a representative cathode to investigate Zn^{2+} vs. proton intercalation mechanism in various electrolytes. **Figure 5.5a** shows the initial

voltage profiles of ZVO||Zn full cells at 0.5C (1C = 300 mA g_{zvo}^{-1}) in three electrolytes: 2 m $ZnSO_4$, 2 m $Zn(OTf)_2$/0SL and 2 m $Zn(OTf)_2$/70SL, where the exhibited discharge capacities

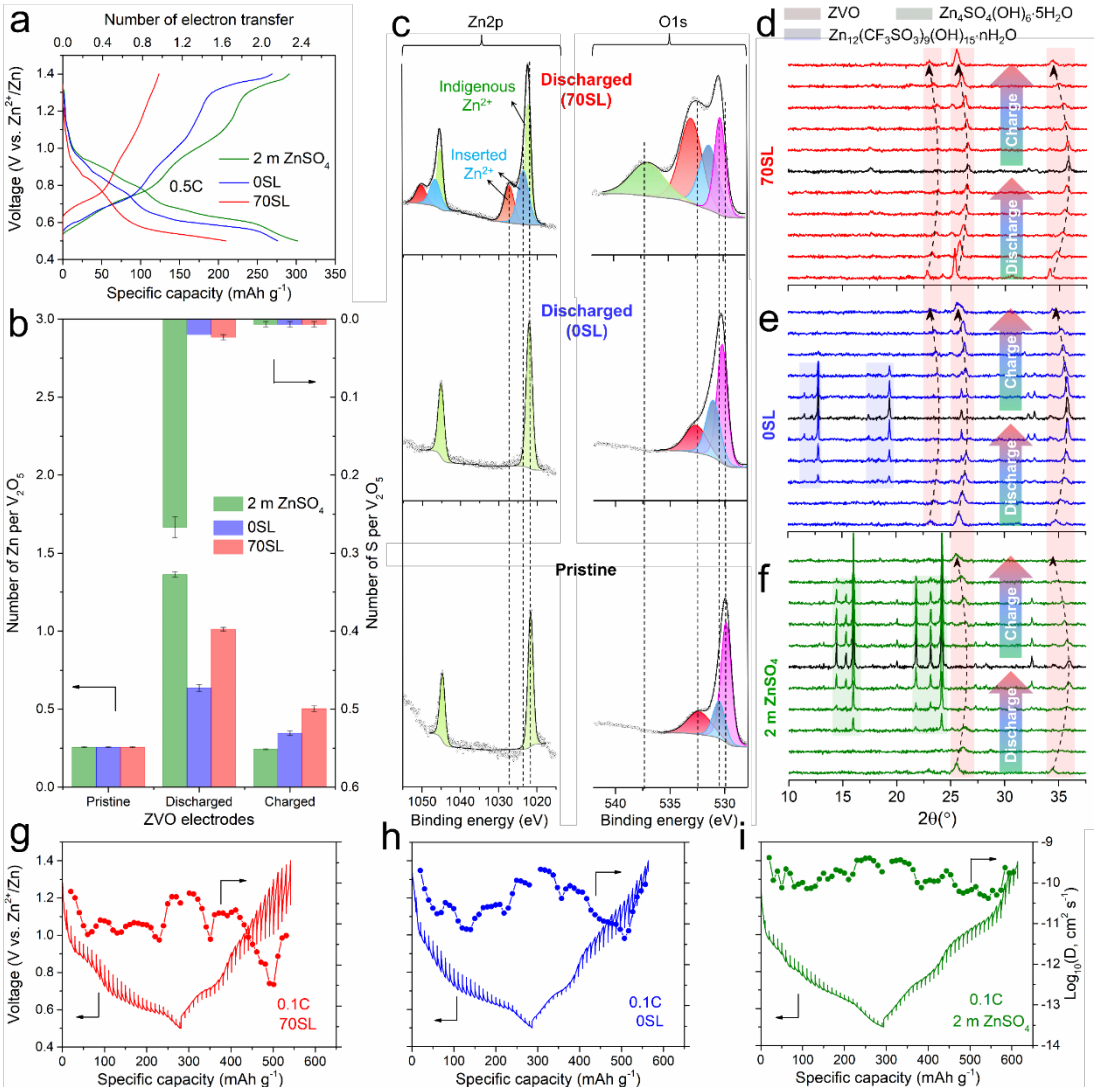

Figure 5.5 (a, b) Voltage profiles of ZVO during the first cycle **(a)** and corresponding EDS-derived elemental ratio of Zn, V, and S at different electrochemical states **(b).** The error bars are derived from the mathematical average of the EDX ratios in three different areas of each electrode. **(c)** Zn 2p and O 1s XPS spectra of pristine ZVO and discharged ZVO in 0SL and 70SL. **(d–f)** Operando XRD patterns of ZVO in 70SL **(d),** 0SL **(e),** and 2 m $ZnSO_4$ **(f). (g–i)** GITT voltage profiles of ZVO and corresponding average diffusion coefficients in 70SL **(g),** 0SL **(h),** and 2 m $ZnSO_4$ (i).

are 302 mAh g_{zvo}^{-1} (2.3 electron (e^-)), 276 mAh g_{zvo}^{-1} (2.2 e^-) and 210 mAh g_{zvo}^{-1} (1.6 e^-),

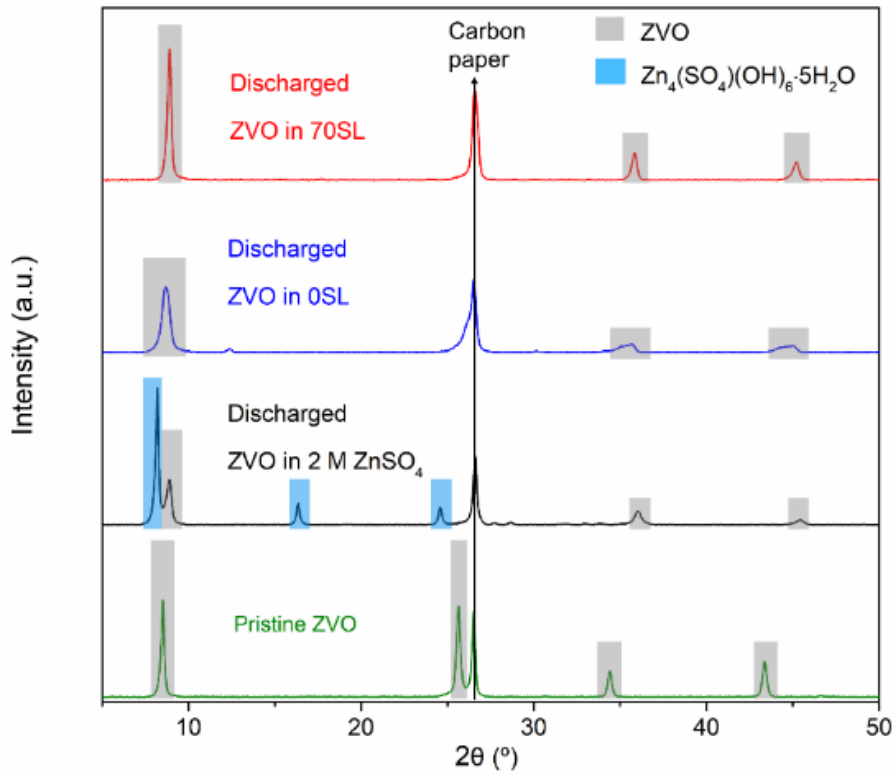

Figure 5.6 XRD patterns of the first discharge of ZVO in different electrolytes at 0.5C.

respectively. In 70SL, a higher cell polarization is observed with 60% discharge capacity recovered on subsequent charge; lower than 97% achieved in either 2 m $ZnSO_4$ and 0SL. Energy-dispersive X-ray spectroscopy (EDS) analysis reveals ~1.01 Zn^{2+} per formula unit in ZVO discharged in 70SL (**Figure 5.5b**), ie., a composition of $Zn_{1.0}V_2O_5$, and intercalation of ~ 0.76 Zn^{2+} (after accounting for ~ 0.25 indigenous Zn^{2+}). This accounts for 95% of the initial discharge capacity, as opposed to only 35% in 0SL (~0.38 Zn^{2+} intercalated, based on EDS analysis). In 2 m $ZnSO_4$, the discharged sample shows high sulfur content (**Figure 5.5b**), originating from sulfate-based LDH ($Zn_4(SO_4)(OH)_6{\cdot}5H_2O$, **Figure 5.6**). For the charged sample in 70SL, the apparent limit of ~0.47 Zn^{2+} deintercalation matches well with the ~60% capacity recovery (**Figure 5.3b**). This suggests that Zn^{2+} diffusion in ZVO is sluggish in the

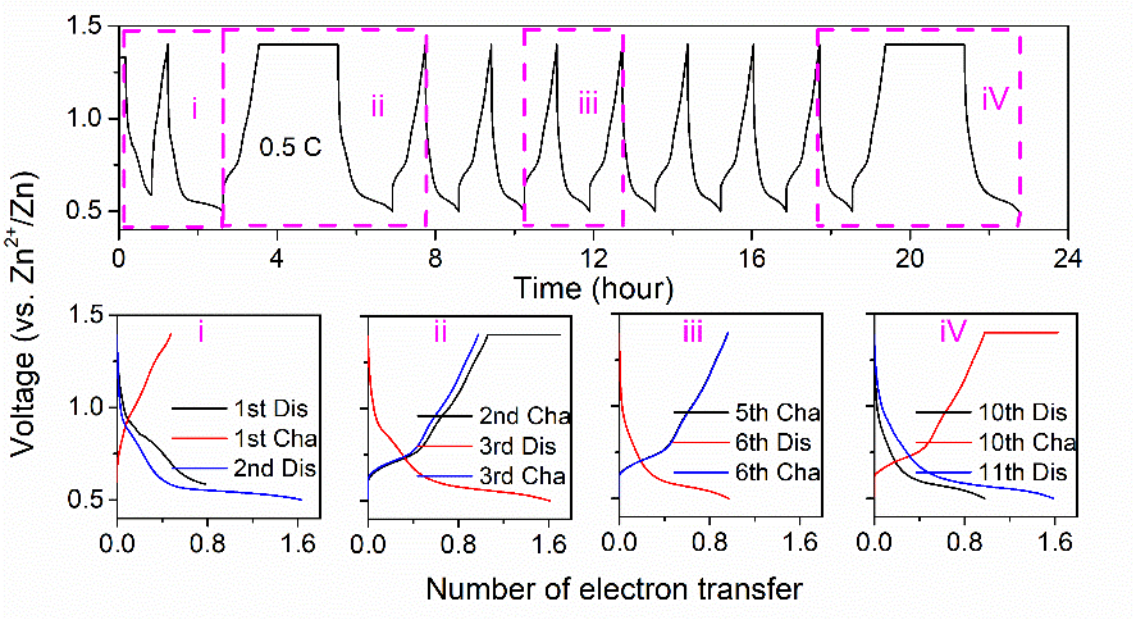

Figure 5.7 Voltage profiles of ZVO with/without holding the potential at the fully charged state in 70SL. The cell that was initially discharged to ~ 0.6 V and achieved ~ 0.8 electron transfer **(i),** however, only ~ 0.5 electron transfer was obtained on charge. In subsequent cycles, without holding the potential at 1.4 V at the end of charge **(iii),** the electron transfer for each redox process (in the voltage range of 0.5 - 1.4 V) was only ~1.0. However, after holding the potential at the fully charged state for two hours **(ii** and **iv),** a much higher electron transfer of ~1.6 was obtained on subsequent discharge. These results indicate that Zn-ion diffusion is limited in the ZVO host, especially in the charged state.

solid state, as verified by subjecting cells to a potential hold at the top of charge during cycling (**Figure 5.7**).

XPS analysis provides further proof for dominant Zn^{2+} intercalation in 70SL (**Figure 5.5c**). Compared to pristine ZVO, in the Zn2p region, two additional peaks appear at higher binding energies (1023.7 eV and 1027.4 eV) for the sample discharged in 70SL, which can be ascribed to the inserted Zn^{2+}. However, in 0SL, only the peak (1022.1 eV) corresponding to the indigenous Zn^{2+} is observed with a slight blue shift. In the O1s region of ZVO discharged in 70SL, a new distinct broad peak at 537.1 eV may indicate the concomitant bonding rearrangements of the oxygen atoms owing to the inserted Zn^{2+}, which also induces significant blue shift of the three peaks between 530-534 eV relative to that of pristine ZVO. In contrast,

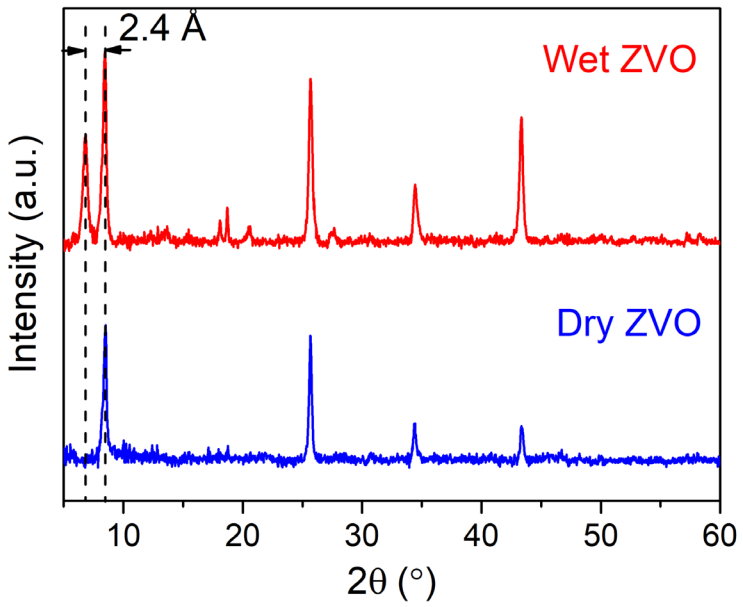

Figure 5.8 XRD patterns of dry and wet ZVO electrodes. Upon immersion in the aqueous electrolyte, the interlayer distance increases from 10.5 Å to 12.9 Å. The difference is 2.4 Å, which is in excellent accord with values of 2-2.5 Å reported for water intercalation in other layered oxides or hydroxides. [120–122]

discharged ZVO in 0SL only shows a slight blue-shift of the O1s peaks, indicating that the inserted protons have an insignificant impact on the lattice oxide. This can be ascribed to the monovalent properties of the proton and its small size, whereas the larger divalent Zn^{2+} may distort the structure by bonding with the ZVO framework, thus altering the local oxide environment.

Operando XRD measurements were further conducted to elucidate structural differences upon intercalation of Zn^{2+} vs. H^{+}. In 70SL (**Figure 5.5d**), the progressive structural evolution of ZVO can be clearly identified by the peak positions shifting to higher 2θ angles (lower d-spacing). The gentle lattice shrinkage during discharge is ascribed to the expulsion of interlayer water molecules upon Zn^{2+} insertion[13] (**Figure 5.8**). In 0SL (**Figure 5.5e**) and 2 m $ZnSO_4$ (**Figure 5.5f**), a set of strong reflections corresponding to triflate and sulfate-based LDHs appear, respectively.[17,88] These result from the local alkaline environment on the cathode interface because of dominant proton intercalation on discharge. The complete lack of LDH reflections in 70SL indicates alleviated proton intercalation and dominant Zn^{2+} intercalation.

The charge process follows the reverse evolution of discharge in all three electrolytes, showing good structural reversibility of ZVO. In addition to major proton intercalation in 0SL, significant cathode dissolution is also identified by the yellow color of the separator disassembled from the cycled cell, in contrast to no apparent dissolution in 70SL (**Figure 5.9**).

To measure Zn^{2+} diffusion kinetics in ZVO, we conducted galvanostatic intermittent

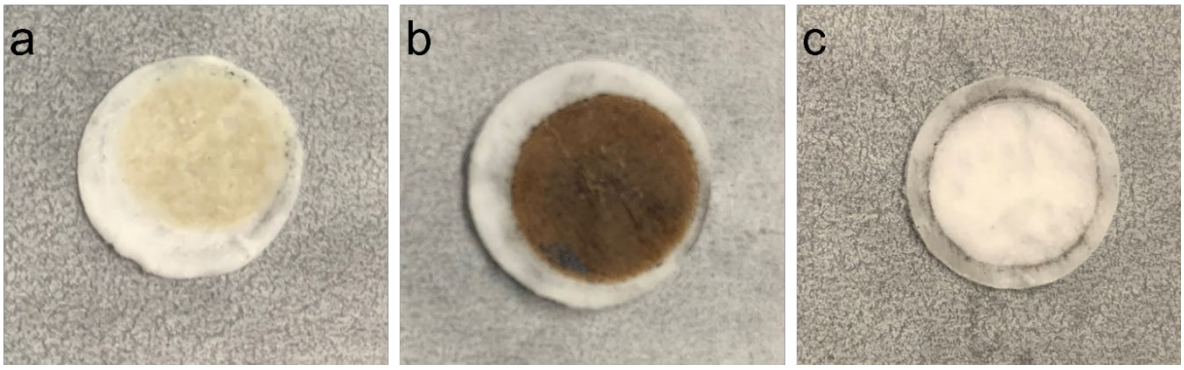

Figure 5.9 Glass fiber separators in ZVO||Zn cells after **(a)** 120 cycles at 0.5C in 0SL and **(b)** 4000 cycles at 10C in 0SL and **(c)** 350 cycles at 0.5C in 70SL.

titration technique (GITT) studies. ZVO in 70SL shows a relatively low average Zn^{2+}-ion diffusion coefficient (D_{eff}) ranging from 10^{-10} – 5×10^{-12} cm^2 s^{-1} at most states of discharge/charge (**Figure 5.5g**). A very low diffusion coefficient of ~5×10^{-13} cm^2 s^{-1} was observed at the mid-point of charge at 1.2 V, perhaps explaining the low-capacity recovery observed during the first charge. ZVO cycled in 0SL and 2 M $ZnSO_4$, however, shows more than one magnitude higher average D_{eff} (**Figure 5.5h** and **5.5i**), ranging from 5×10^{-10} –10^{-11} and 10^{-9} – 5×10^{-11} cm^2 s^{-1}, respectively. These results support the substantial co-proton intercalation of ZVO in 0SL and 2 m $ZnSO_4$, as H^+ diffusion is expected to be much faster than Zn^{2+}.

The above discussion highlights that the extremely high-rate function of ZMBs based on the oxides utilized in this work or elsewhere is likely only attainable with proton co-intercalation. Such batteries could potentially be used for high-power load leveling, but would be unable to support long-duration electricity energy storage that requires stable cycling at moderate current densities with discharge periods of near 10 hours (see below).

5.5 Evidence of Zn^{2+} Intercalation from Electron Microscopy

Scanning transmission electron microscopy (STEM) imaging combined with energy-dispersive X-ray spectroscopy (EDS) and electron energy loss spectroscopy (EELS) was used investigate the evolution of morphology, chemical distribution, electronic and crystal structures of the ZVO upon discharge in 70SL. Compared to the clean surface of pristine ZVO nanobelts in the high-angle annular dark-field (HAADF) image, the discharged sample exhibits corrosion-induced surface roughness typical of electrochemically cycled materials (**Figure 5.10a**). The EDS chemical maps show homogeneously distributed Zn, V and O elements for both pristine and discharged nanobelts (**Figure 5.10b**), with V/Zn ratios of 9.6 and 2.3, respectively. This agrees well with the intercalation of 0.7 Zn^{2+} per formula unit described above (**Figure 5.5b**).

To understand the impact of Zn^{2+} intercalation on the electronic structure of ZVO, we show a comparison of the integrated EELS spectra (a total of 10 spectra each) for the pristine and discharged ZVO samples in **Figure 5.10c**. The reduction in the V valence state upon Zn^{2+} intercalation results in a shift of the V L edge towards lower energy loss.[120,121] The pre-peak in the O K edge is the result of electronic transitions from O 1s states to O 2p states. The O 2p states are hybridized with the V 3d states, and as a result, the higher O K edge pre-peak intensity points towards a higher number of empty O 2p states hybridized with V 3d states.[122,123] Therefore, the reduced intensity of the O K edge pre-peak is a direct result of V reduction upon Zn^{2+} intercalation. While the Zn L edge is extremely noisy for the pristine ZVO sample, the discharged sample shows a Zn L edge with a much higher signal-to-noise ratio due to the increased Zn content upon intercalation. **Figure 5.10d** shows atomic-resolution HAADF

images corresponding to the various crystal structure orientations in the discharged ZVO samples.

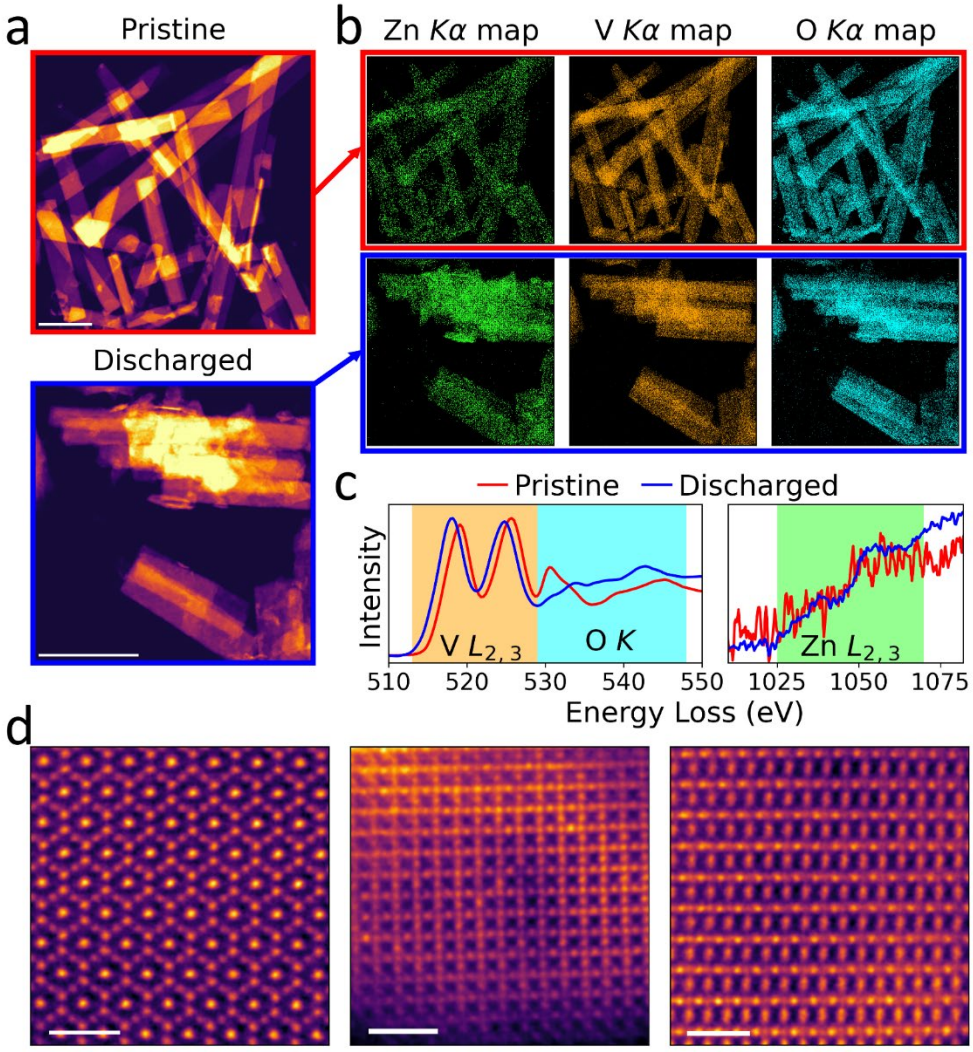

Figure 5.10 (a) STEM-HAADF images showing the nanobelt-like morphology for the pristine (top) and discharged (bottom) ZVO. **(b)** EDS chemical maps showing the distribution of Zn, V, and O across the nanobelts in the pristine and discharged ZVO samples. **(c)** Integrated EEL spectra showing the changes in the fine structure of V L, O K, and Zn L edges for the pristine and discharged ZVO samples. **(d)** Atomic-resolution HAADF images showing various crystal structure orientations for the discharged ZVO samples. The scale bars correspond to 500 and 1 nm for **(a)** and **(d)**, respectively.

5.6 Highly Reversible Zn Plating/Stripping and Solid Electrolyte Interphase (SEI) Chemistry

Practical ZMBs also require anodes with high reversibility and stability. Zn||Cu asymmetric cells evaluated in 70SL demonstrated a very high Zn plating/stripping CE of at least 99% at different current densities (**Figure 5.11a**), which is slightly higher than that in

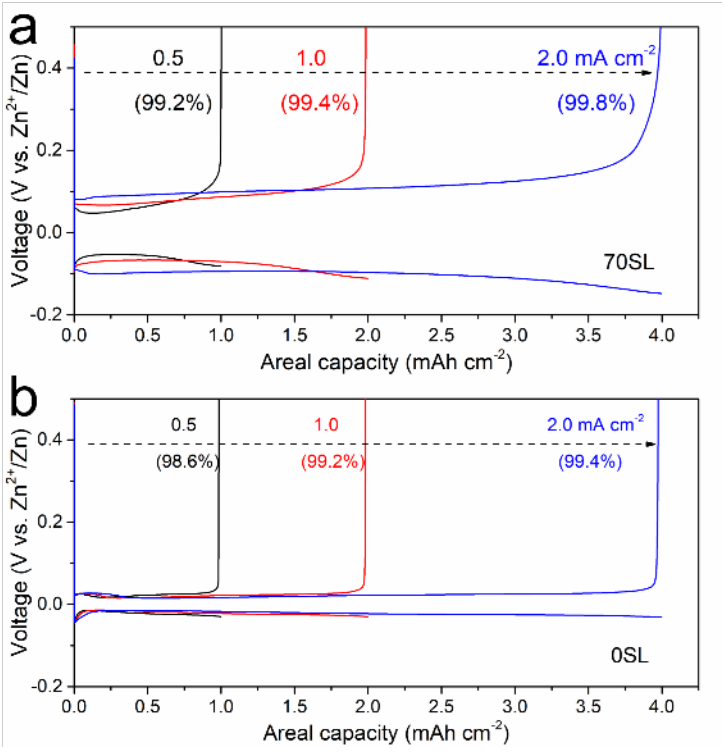

Figure 5.11 The second voltage profiles of Cu||Zn cells at different current densities in **(a)** 70SL and **(b)** 0SL.

0SL (**Figure 5.11b**). The long-term Zn plating/stripping behavior was further evaluated at 2 mA cm^{-2}. In Zn||Cu cells with a high areal capacity of 4 mAh cm^{-2}, the CE in 70SL (initially 90.4%) stabilizes at ~ 99.9% for 200 cycles (**Figure 5.12a** and **5.13**), yielding a very high average CE of 99.8% without the presence of "soft shorts" (also see full-cell cycling below)[72]. In 0SL, in contrast, a large CE fluctuation owes to extensive dendrite formation. We also note 70SL shows significantly better results than 50SL (**Figure 5.14**), which can be ascribed to the lower free water content of ~3% in 70SL *vs*. ~16% in 50SL. This proves the critical role of

SL/water ratio in these hybrid electrolytes. The excellent long-term stability of multiple Zn||Zn symmetric cells in 70SL (**Figure 5.12b** and **5.15**) is demonstrated by a cycle life of at least

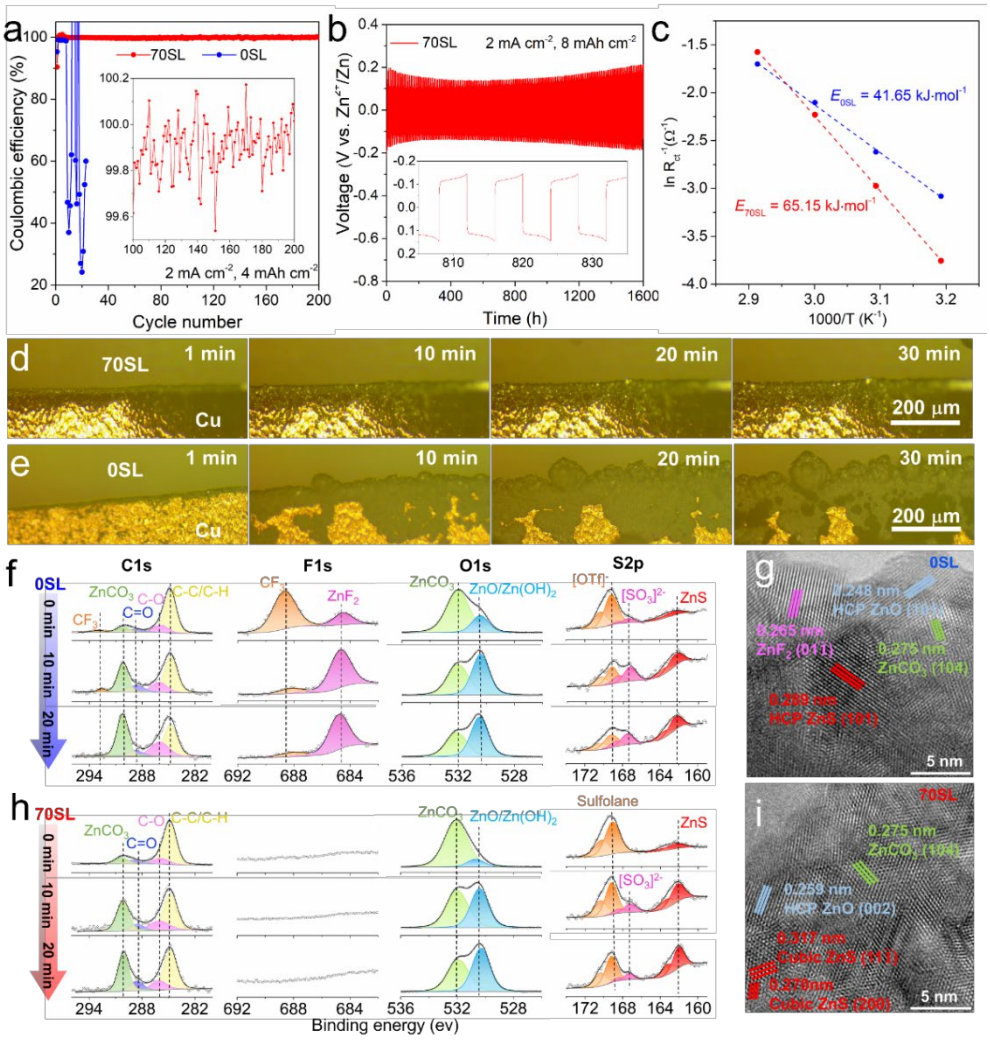

Figure 5.12 (a) Coulombic efficiency of Zn||Cu cells at 2 mA cm^{-2} with a capacity of 4 mAh cm^{-2}. **(b)** Galvanostatic Zn stripping/plating in Zn||Zn symmetric cells with 70SL at 2 mA cm^{-2} with a capacity of 8 mAh cm^{-2}. **(c)** Arrhenius plots of inverse R_{CT} (R_{CT}^{-1}) values at different temperatures (from 40 to 70 °C) for the working electrode in a three-electrode cell with Zn as working, counter, and reference electrode; **(d, e)** In In-situ optical microscopy images showing the **Zn** plating process in 70SL **(d)** and 0SL **(e)** at 5 mA cm^{-2}. **(f, h)** High-resolution depth-profiling XPS spectra of Cu electrodes with deposited Zn after 5 cycles at 2 mA cm^{-2} (4 mAh cm^{-}2) in 0SL **(f)** and 70SL **(h). (g, i)** TEM images of the interfaces on the deposited Zn surface in 0SL **(g)** and 70SL **(i).**

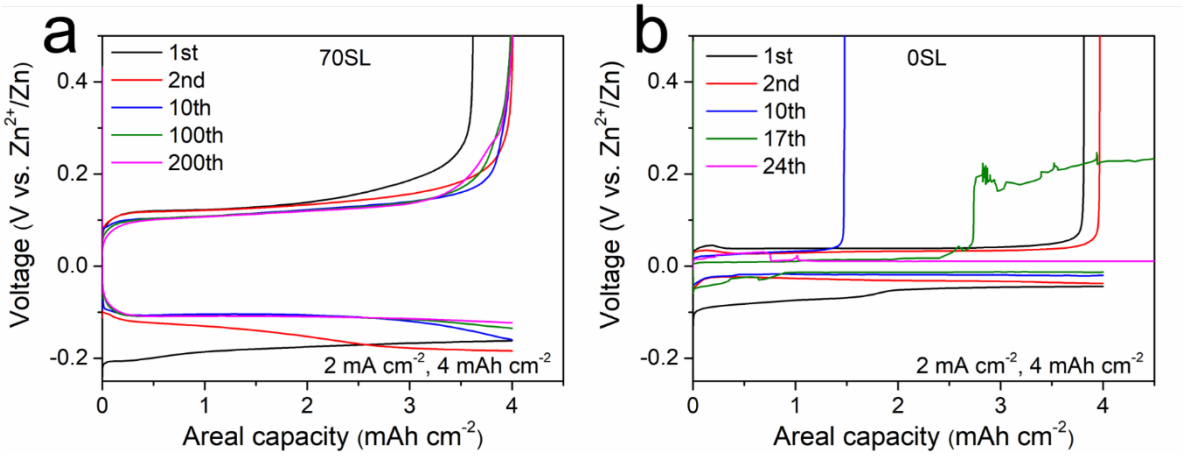

Figure 5.14 Voltage profiles of Zn stripping/plating in Zn||Cu asymmetric cells at 2 mA cm^{-2} with a capacity of 4 mAh cm^{-2}, in **(a)** 70SL and **(b)** 0SL.

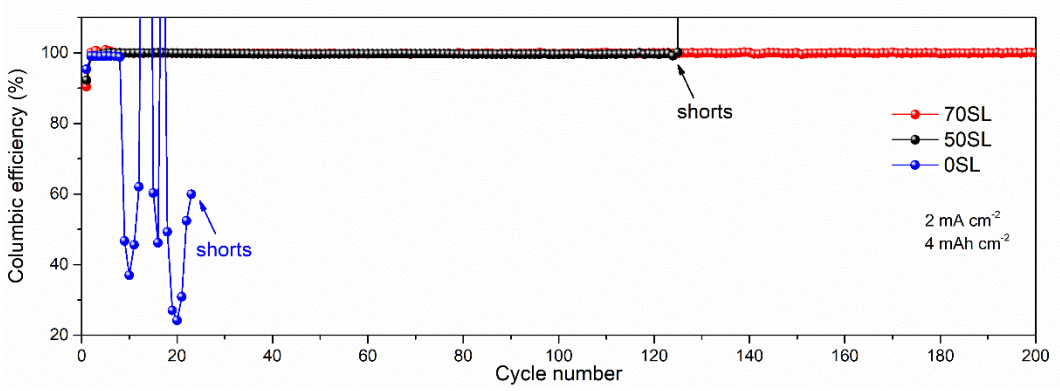

Figure 5.13 Coulombic efficiency of Zn||Cu cells at 2 mA cm^{-2} with a capacity of 4 mAh cm^{-2} in different electrolytes.

2000 hours at 4 mAh cm^{-2}, 1600 hours at 8 mAh cm^{-2} and 1000 hours at 12 mAh cm^{-2}. The lifetime is extended 20-fold compared to cells employing 0SL at 8 mAh cm^{-2}, which quickly short after only 80 hours (**Figure 5.16**). The superior Zn anode stability in 70SL is further

verified by the little change in charge transfer resistance (R_{CT}) during the Zn plating/stripping (**Figure 5.17**).

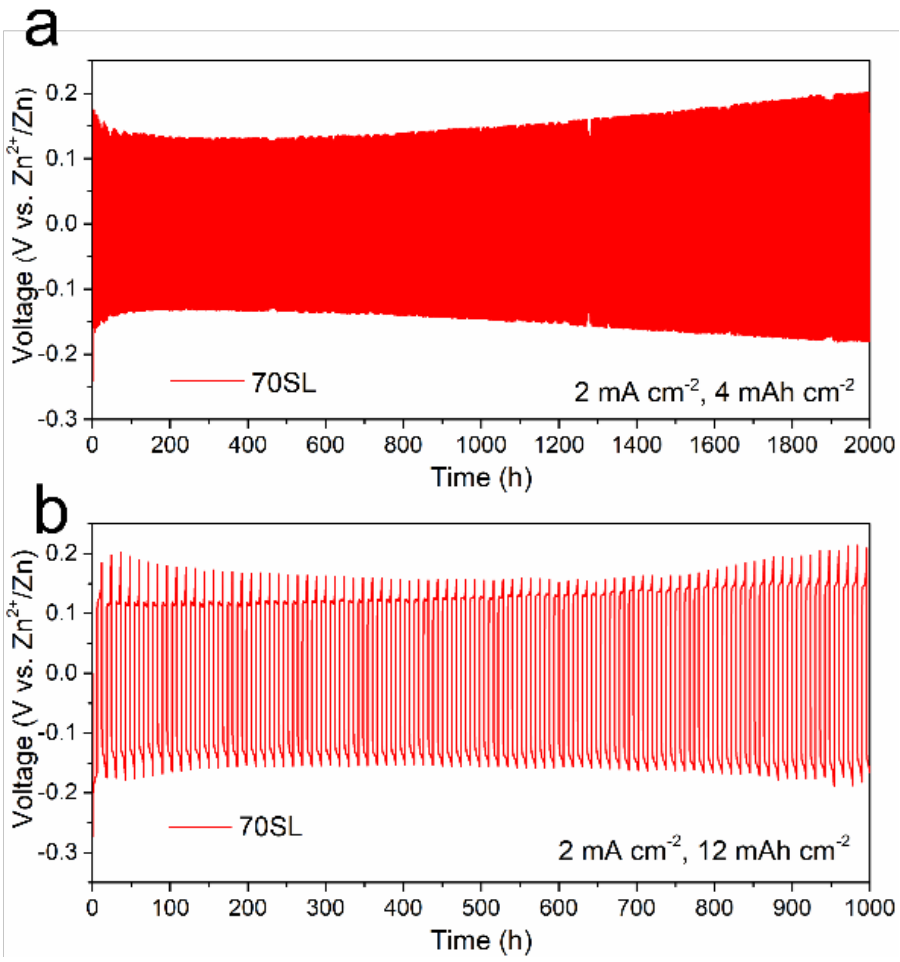

Figure 5.15 Galvanostatic Zn stripping/plating in Zn||Zn symmetric cells with 70SL at 2 mA cm^{-2} with a capacity of **(a)** 4 mAh cm^{-2} and **(b)** 12 mAh cm^{-2}.

The activation energy (E_a) for the charge transfer process $(Zn(H_2O)_6)^{2+} \leftrightarrow Zn^{2+} \leftrightarrow Zn^0$ on the Zn surface was measured by electrochemical impedance spectroscopy (EIS). As shown in **Figure 5.10c** and **5.18**, the E_a of 70SL is 65.15 kJ mol^{-1}, higher than the 41.65 kJ mol^{-1} for 0SL. As 0SL and 70SL present similar fully hydrated Zn^{2+} solvation structures and presumably a comparable desolvation energy, we ascribe the higher E_a and R_{CT} in 70SL to the slower diffusion of desolvated Zn^{2+} in the proposed sulfolane-derived SEI (see below) on the Zn

surface and a slightly lower transference number (**Figure 5.19**). We note that the E_a of 70SL is still similar to that of dilute 2 M $ZnSO_4$ (68.2 kJ mol^{-1}),[124] and more than three-fold lower than reported for 0.25 M $Zn(OTf)_2$ in acetonitrile (~223.64 kJ mol^{-1}),[12] where a water-free Zn^{2+} solvation sheath and strong Zn^{2+}-OTf^- ion pairing induce a much higher desolvation penalty.

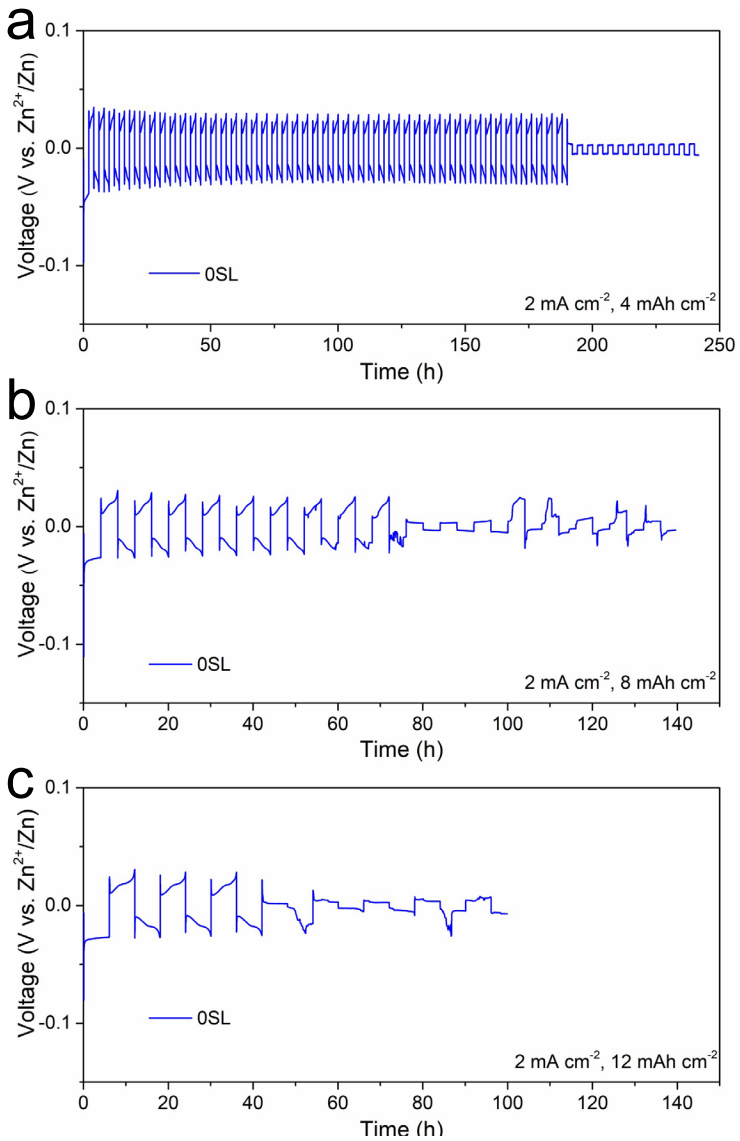

Figure 5.16 Galvanostatic Zn stripping/plating in Zn||Zn symmetric cells with 0SL at 2 mA cm^{-2} with a capacity of **(a)** 4 mAh cm^{-2}, **(b)** 8 mAh cm^{-2} and **(c)** 12 mAh cm^{-2}.

In contrast, fully hydrated $(Zn(H_2O)_6)^{2+}$ in 70SL facilitates facile interfacial desolvation owing to the shielding effect of water.[12]

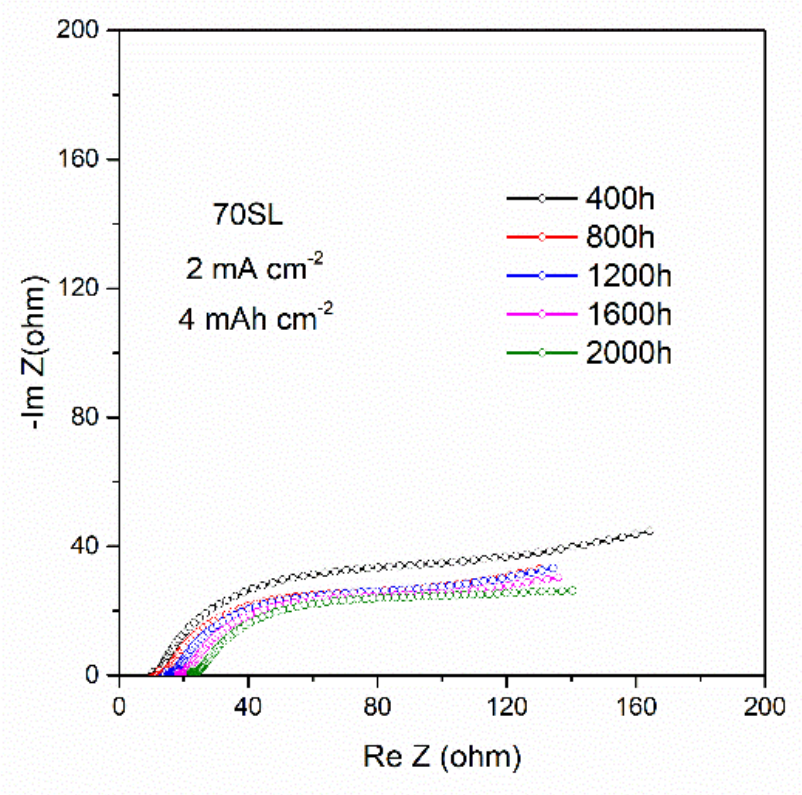

Figure 5.17 Nyquist plots of Zn || Zn symmetric cells in 70SL after cycling for different time periods as indicated.

The superior Zn stability and reversibility exhibited in 70 SL is attributed to suppressed HER kinetics (**Figure 5.20**) and improved compatibility with Zn (**Figure 5.21**). The lowered HER potential is ascribed to an *in-situ* surface SEI (see below), which prevents water from approaching the interface but allows Zn^{2+} to pass through, and suppresses the formation of Zn layered double hydroxides (LDHs, **Figure 5.22**). This alleviates dendrite formation during Zn plating, as validated by the homogeneous, smooth and dense Zn deposition morphology (**Figure 5.12d** and **5.23a-c**). In 0SL, the porous LDHs induce inhomogeneity and aggravate dendrite formation, creating spongy Zn deposits (**Figure 5.10e** and **5.23d-f**).

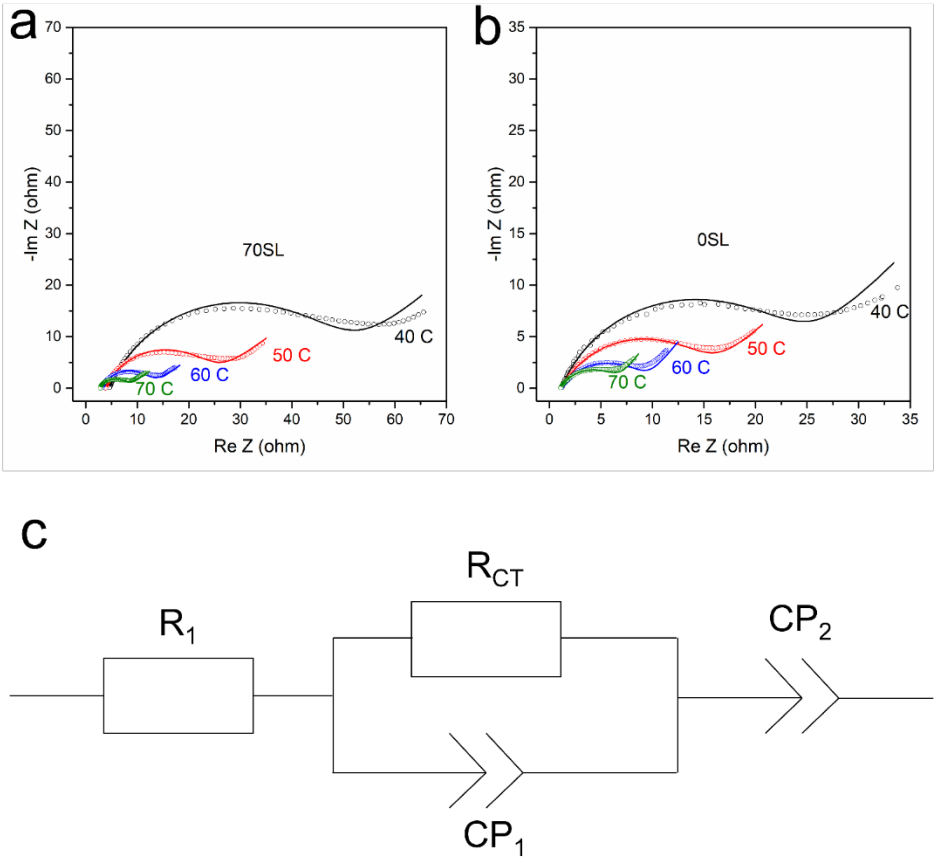

Figure 5.18 EIS fitting of charge transfer resistance in three-electrode Zn symmetric cells in **(a)** 0SL and **(b)** 70SL at various temperatures. The data were fit (shown by the line) with **(c)** the indicated equivalent circuit.

The Zn solid-electrolyte interface (SEI) chemistry was explored by depth-profiling high-resolution X-ray photoelectron spectroscopy (XPS). In the F1s region of Zn deposited in 0SL **(Figure 5.10f)**, the CF_3 species at 688.6 eV originates from OTf^-, along with the feature

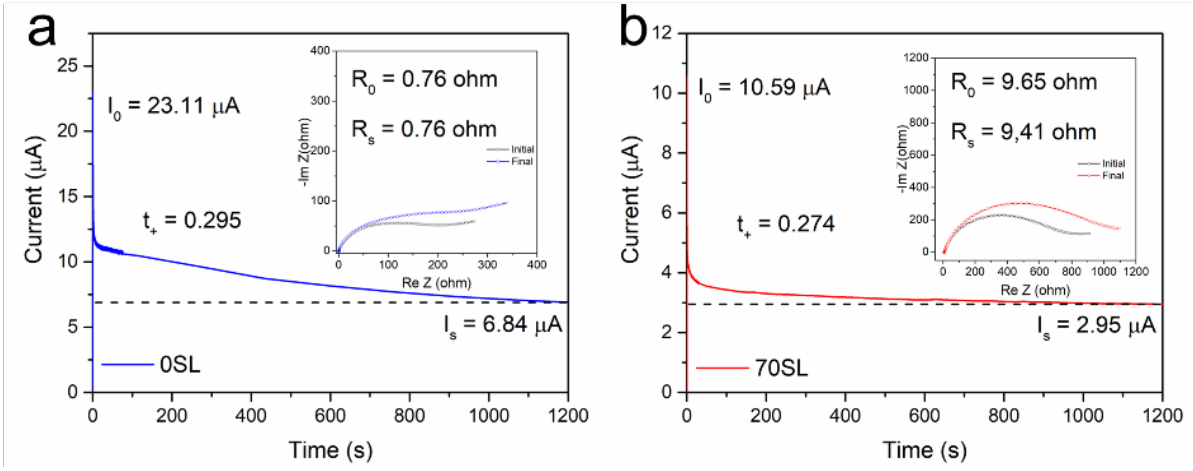

Figure 5.19 Transference number measurements using Zn//Zn symmetric cells following a constant polarization of 5 mV for 1200 s. **(a)** 0SL, **(b)** 70SL (Insets are the corresponding initial and final EIS plots). The transference number of Zn^{2+} cation (t_+) was determined by **Equation 5.1**:[30,32]

$$t_+ = \frac{I_s(\Delta V - I_0 R_0)}{I_0(\Delta V - I_s R_s)} \qquad \textbf{Equation 5.1}$$

where ΔV is the applied constant polarization voltage (5 mV), I_o and R_o are the initial current and resistance, respectively; I_s and R_s are the steady-state current and resistance, respectively.

in the C1s region at 292.8 eV. The OTf^- is incorporated in the LDH. Reduction of the OTf^- (169.2 eV) anion is signalled by a peak at 684.7 eV ascribed to ZnF_2; along with sulfites (167.3 eV) and ZnS (162.1 eV) observed in the S2p spectra. In the O 1s region, the two peaks correspond to $ZnCO_3$ (532 eV) and $ZnO/Zn(OH)_2$ (530.5 eV) as confirmed by their characteristic lattice d-spacings measured by high-resolution transmission electron microscopy (TEM; **Figure 5.10g**). In summary, Zn deposited in 0SL yields a complex interface that can be characterized as a mixture of $ZnCO_3$-$ZnO/Zn(OH)_2$ - ZnF_2 - ZnS - sulfite - LDH. While a ZnF_2-rich interface has been reported as a protective layer to realize a highly reversible Zn

anode,[30,32,125,126] nonetheless, the high-porosity LDH reduces the ability to exclude water from the Zn surface.

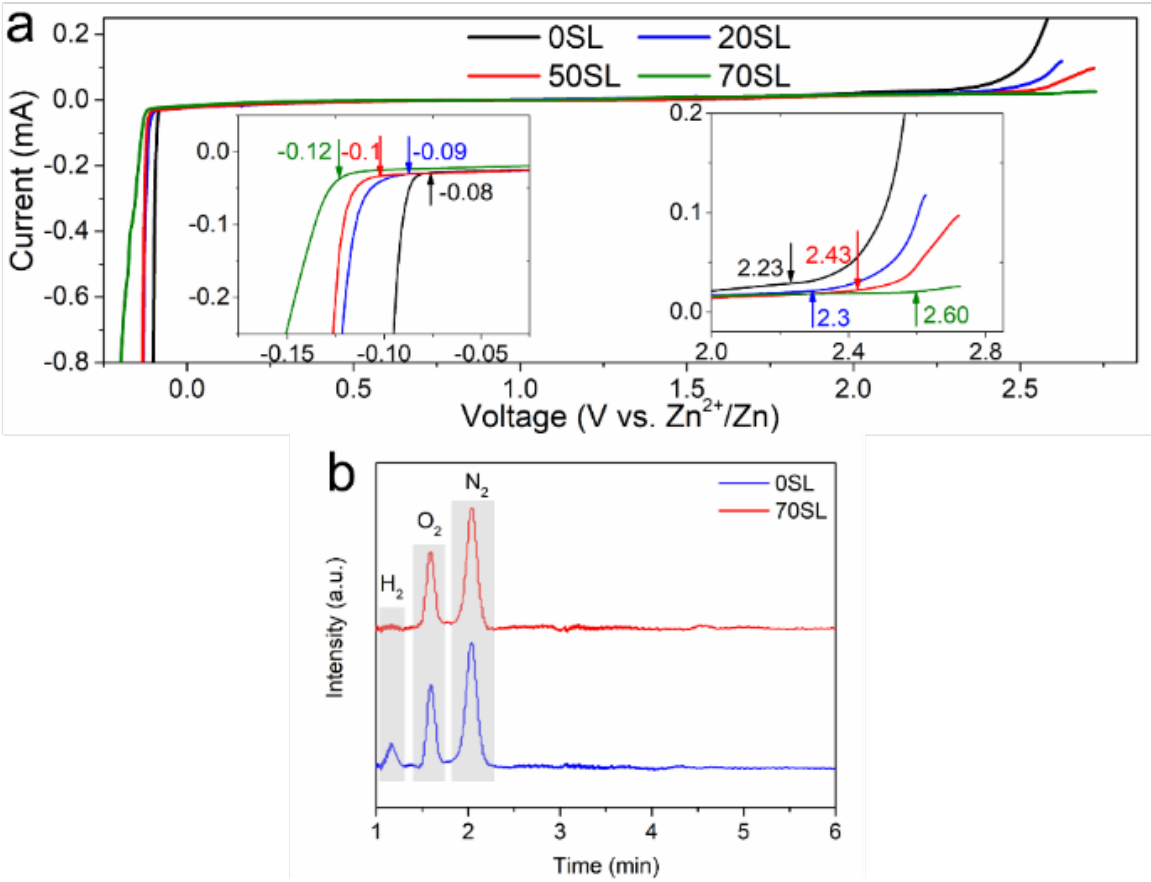

Figure 5.20 (a) Linear sweep voltammetry (LSV) curves of different electrolytes. **(b)** Gas chromatograph response for HER in different electrolytes, which was collected after plating at 4 mA cm^{-2} for 20 min in Zn||Cu asymmetric cells

The XPS spectra of the Zn deposited in 70SL are quite different (**Figure 5.10h**). In particular, no CF_3 species appear in the C1s region and no significant features were observed in the F1s region, indicating OTf^- reduction does not occur at the interface. Thus, the sulfite and ZnS peaks in the S 2p region must originate from the reduction of sulfolane rather than OTf^-. More evidence of inorganic ZnS, $ZnCO_3$ and ZnO was obtained from TEM (**Figure 5.10i**). These findings show that an *LDH/ZnF_2-free*, $ZnCO_3$-ZnO/$Zn(OH)_2$-ZnS-sulfite SEI

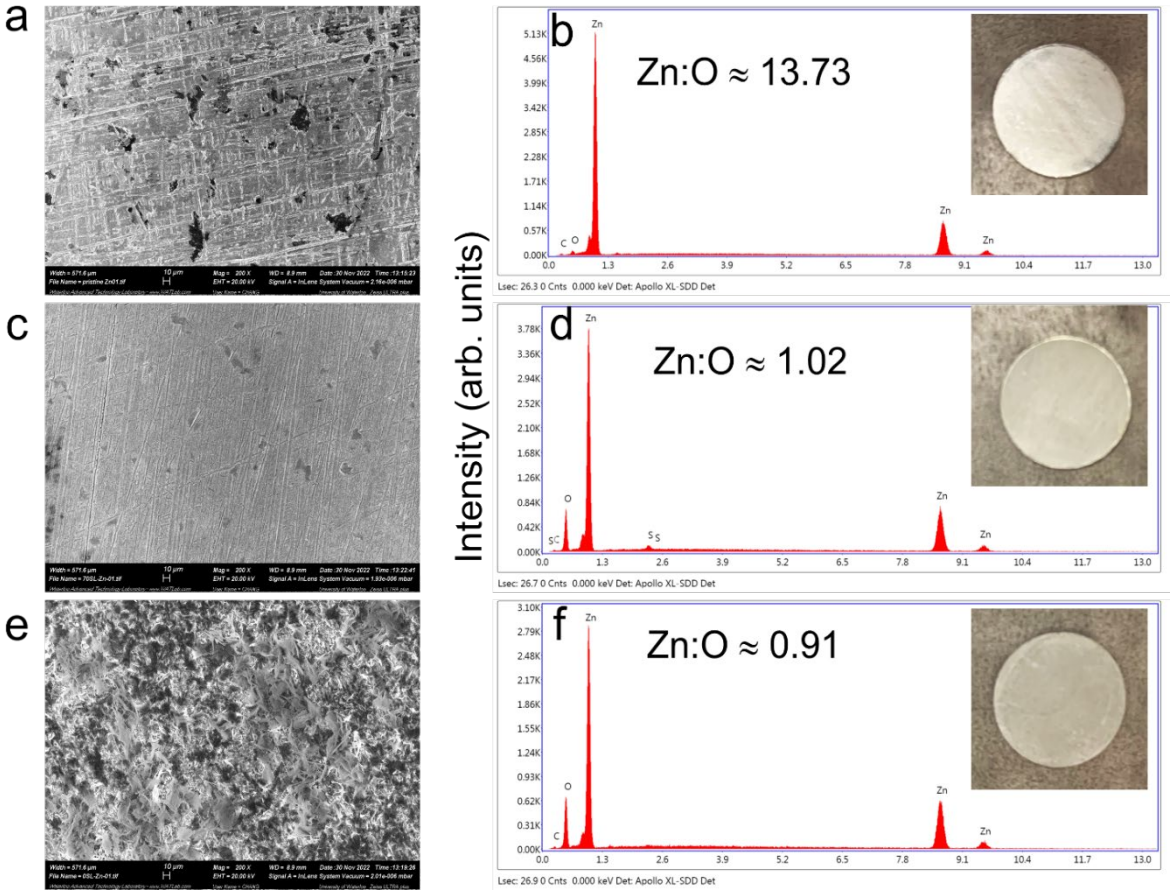

Figure 5.21 SEM images and corresponding EDX maps of **(a, b)** pristine Zn and Zn soaked in **(c, d)** 70SL and **(e, f)** 0SL for 8 days. Although the soaked Zn in both electrolytes show the formation of ZnO on the surface, Zn in 70SL shows much smoother surface and less ZnO, indicating the better compatibility due to the much lower free water in 70SL.

forms at the Zn surface. This SEI not only prevents water penetration but also suppresses the adsorption and reduction of OTf⁻ on the Zn surface, resulting in depressed kinetics of HER and deposition of LDHs, thus enhancing reversibility and stability of Zn plating/stripping.

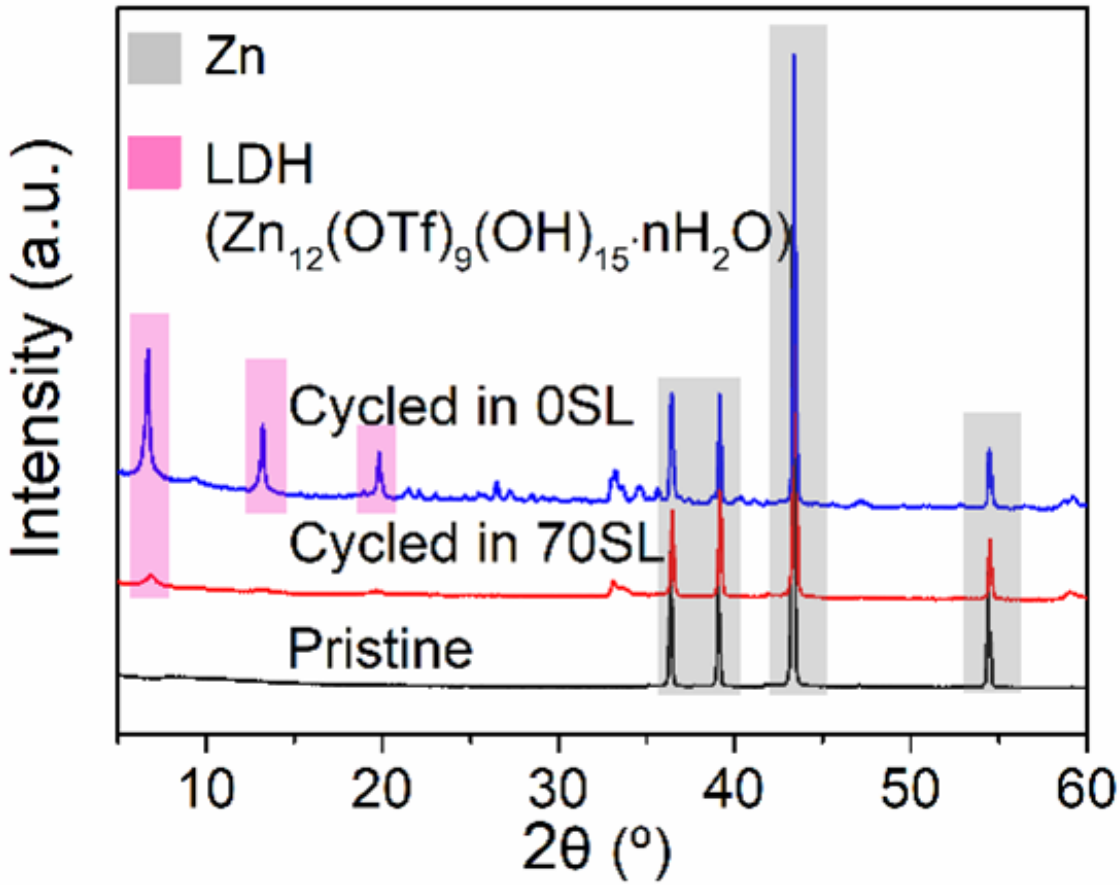

Figure 5.22 XRD of deposited Zn on a Cu substrate after 5 cycles in different electrolytes at 2 mA cm^{-2} and 4 mAh cm^{-2} in different electrolytes.

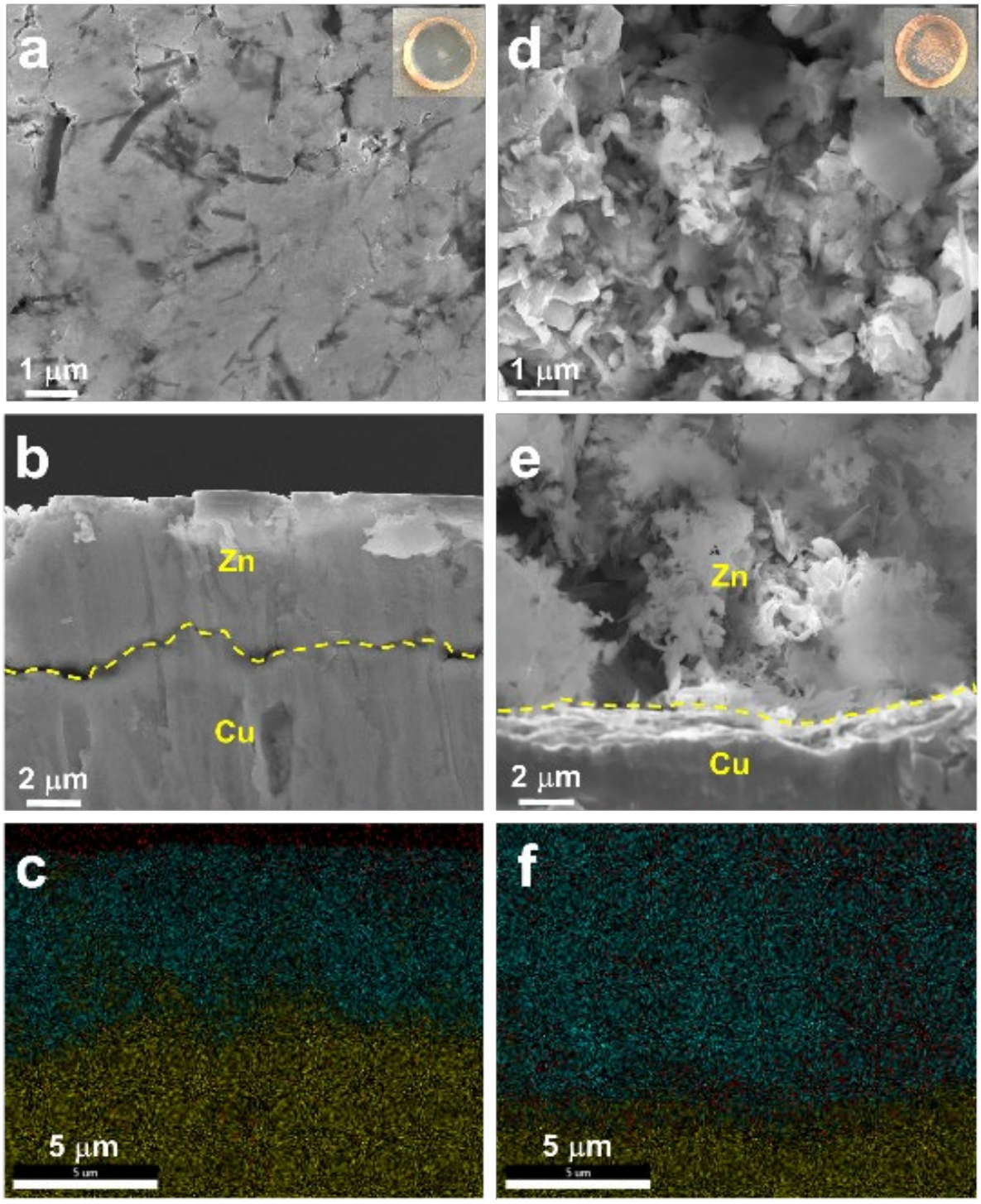

Figure 5.23 Top and cross-sectional **(a, b, d, e)** SEM images and **(e, f)** corresponding EDX mapping of deposited Zn on Cu substrate after 5 cycles in **(a-c)** 70SL and (d-f) 0SL at 2 mA cm^{-2} and 4 mAh cm^{-2}.

5.7 Long-Term Full Cell Performance under Practical Conditions

The dual-stabilized electrodes prompted us to further investigate full cell performance. In contrast to using high current rates up to 10 to 25C enabled by a high degree of proton co-intercalation,[111–113] intermediate rates (< 1C) and much higher areal capacities up to 4 mAh cm^{-2} were applied in this work (**Figure 5.24a-d**). These metrics are recognized as one of the major challenges for practical aqueous ZMBs.[10] At 0.5C and a cathode loading of ~ 1.1 mAh

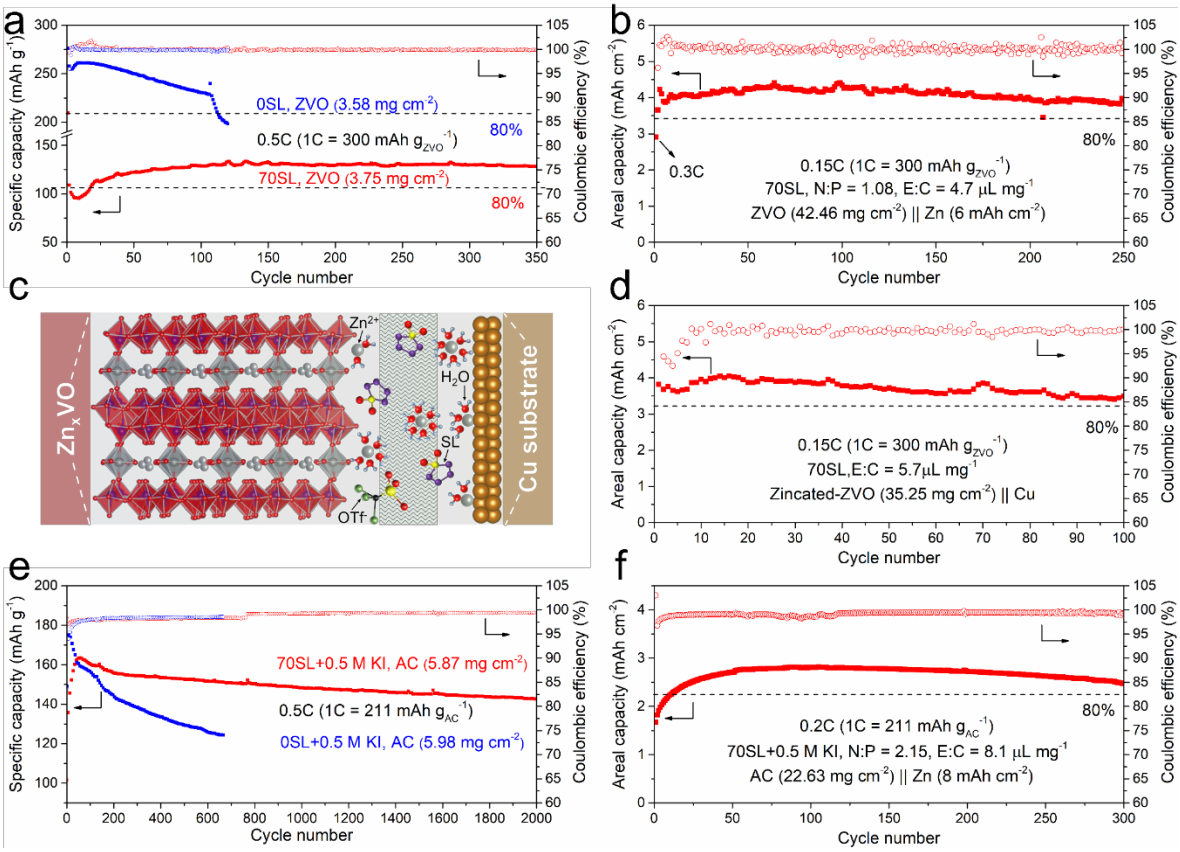

Figure 5.24 (a) Discharge capacity of ZVO as a function of cycle number in different electrolytes at 0.5 C. **(b)** Long-term cycling performance of high-loading ZVO in 70SL at 0.15 C and a controlled N/P ratio of 1.08. **(c, d)** Schematic of an anode-free $Zn_{0.25+x}VO$||Cu cell with 70SL **(c)** and corresponding cycling performance at 0.15 C **(d). (e)** Discharge capacity of activated carbon (AC) electrodes as a function of cycle numbers in different electrolytes with the addition of 0.5 m KI at 0.5 C (unexpected power shutdown at 770th cycle). **(f)** Long-term cycling performance of high-loading AC in 70SL + 0.5 m KI at 0.2 C at a controlled N/P ratio of 2.15.

cm^{-2} (based on 300 mAh g_{zvo}^{-1}, **Figure 5.24a and 5.25**) in 0SL, ZVO fades quickly with a decay rate of 0.12% per cycle before short circuiting at the 106th cycle. This contrasts with its outstanding stability at a 10C rate with a decay of 0.003% per cycle resulting in ~91% capacity retention after 3000 cycles (**Figure 5.26**), similar to previous reports.[13,113,127] This is because at high rates, the shorter time that the cathode spends at extreme potentials suppresses deterioration owing to vanadium dissolution, proton intercalation and corresponding LDH

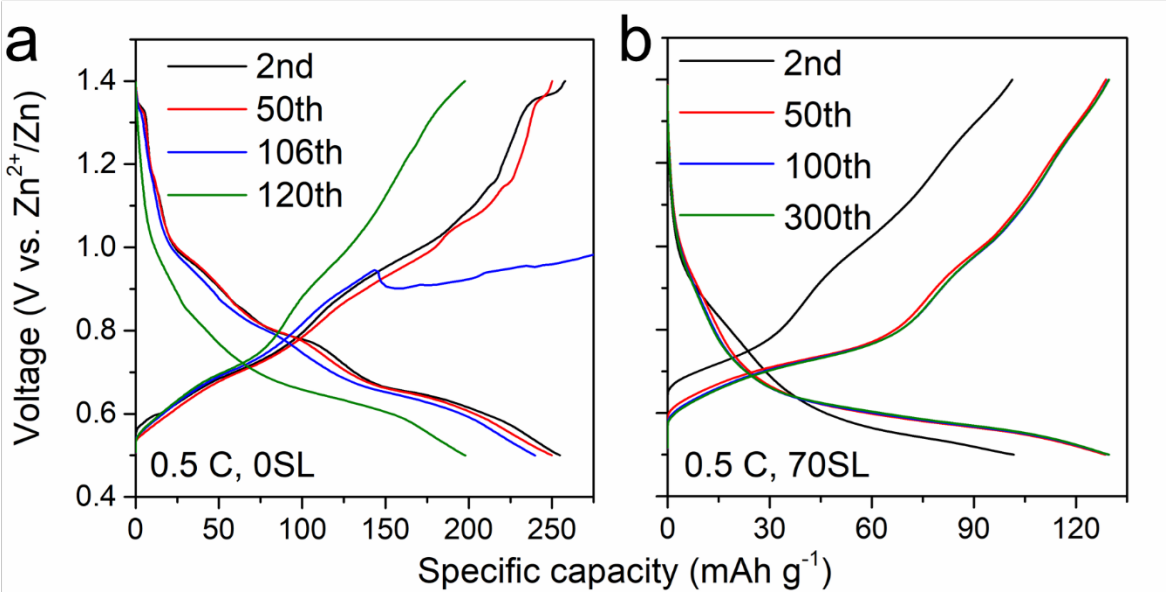

Figure 5.25 Voltage profiles of ZVO in different electrolytes at 0.5C in **(a)** 0SL and **(b)** 70SL.

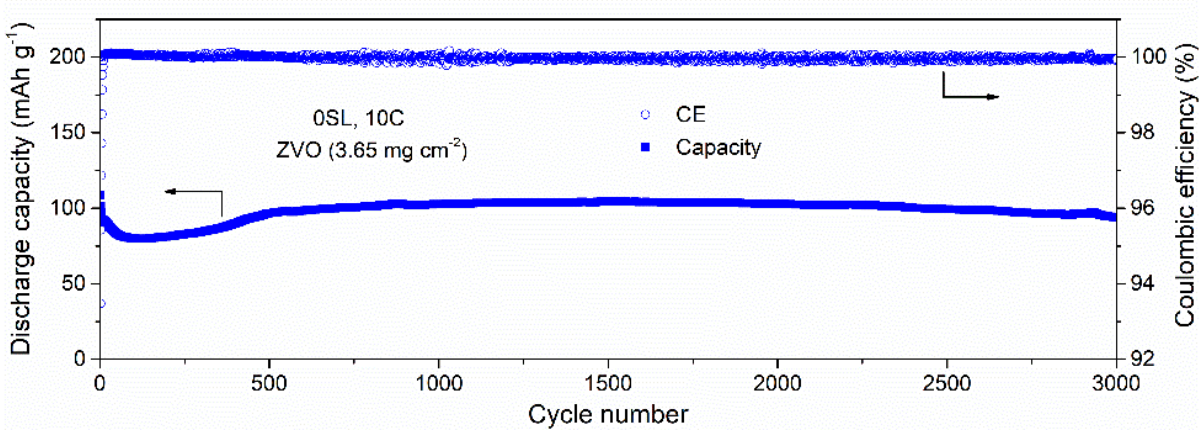

Figure 5.26 The discharge capacity of a ZVO||Zn full cell as a function of cycle number in 0SL at 10C.

formation. In 70SL, these side reactions are effectively addressed, resulting in very good cycling stability of ZVO even at a 0.5C rate with virtually no capacity decay after 350 cycles. To further address the practical requirements of ZMBs, we fabricated free-standing ZVO electrodes with a high loading of ~ 42 mg cm^{-2} and a thickness of ~580 μm (**Figure 27**). In

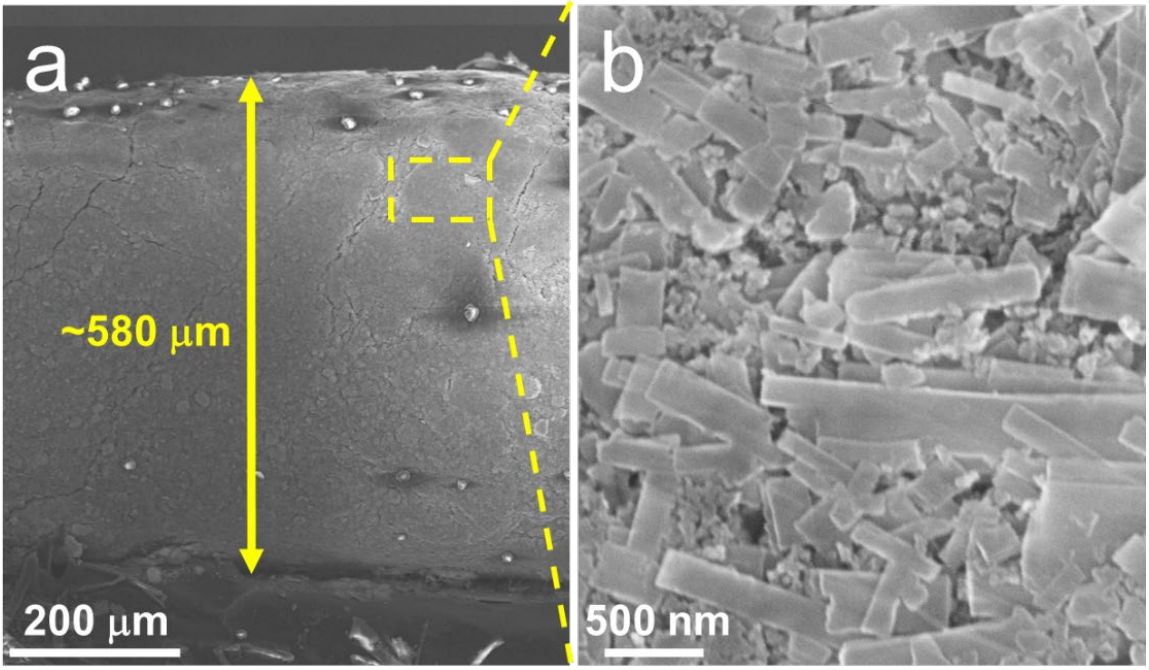

Figure 5.27 SEM images of the high-loading and freestanding ZVO cathode **(a)** and a magnified view of the indicated region **(b).**

70SL, the full cell based on this high-loading ZVO cathode provides a practical-level areal capacity of 4.4 mAh cm^{-2} at 0.15C (**Figure 5.24b** and **5.28**). The cell maintains ~ 90% capacity retention over 250 cycles at a low negative/positive ratio (N/P) of 1.08 (based on 130 mAh g_{zvo}^{-1} achieved at 0.5C in **Figure 5.24a**) and a low electrolyte volume/active material mass ratio (E/C) of 4.7 μL mg^{-1}. Importantly, an average CE of ~100% is obtained. Under even more challenging conditions, an anode-free $Zn_{0.25+x}VO$||Cu cell configuration was constructed with

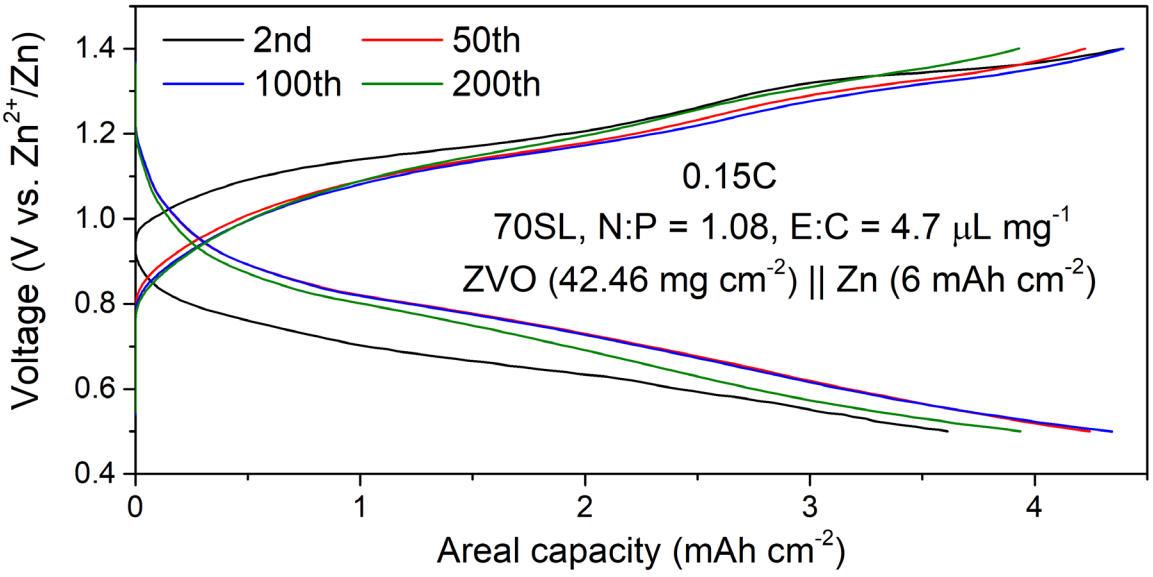

Figure 5.28 Voltage profile of high-loading ZVO in 70SL at 0.15C with a controlled N/P ratio of 1.08.

the only source of Zn being that stored in pre-zincated ZVO (**Figure 5.24c-d**). The cell exhibits an areal capacity of ~4 mAh cm^{-2} and maintains 85% of its capacity after 100 cycles at 0.15C.

We further verified the adaptability of this electrolyte design strategy by replacing ZVO with conversion-type iodine cathode, which obviate the sluggish Zn^{2+} diffusion in ZVO. In these studies, 0.5 m KI dissolved in 0SL or 70SL was the active material and high-surface area activated carbon (AC) cathode acted as the iodine host (**Figure 5.24e** and **5.29**)**.** The reversible capacity in 70SL is 164 mAh g_{AC}^{-1} at 0.5C (1C = 212 mA g_{AC}^{-1}), only slightly lower than in 0SL (175 mAh g_{AC}^{-1}), and indicating better kinetics compared to intercalative ZVO. The Zn||iodine cell with 70SL also shows excellent stability at a high rate of 10C (**Figure 5.30**). Moreover, the reduced water activity in 70SL suppresses the dissolution of I_2 and formation of the intermediate I_3^- at charged states,[128] leading to much-improved cycling stability with a capacity retention of 88% over 2000 cycles, as opposed to only 70% after 670 cycles in 0SL. A practical-level full cell with a high-loading AC cathode (**Figure 5.31**) at an N/P ratio of 2.15 (based on 164 mAh g_{AC}^{-1} achieved at 0.5C in **Figure 5.24e** and **5.32**) and E/C ratio of 8.1 μL

mg^{-1} (**Figure 5.24f**), provided an areal capacity of 2.8 mAh cm^{-2} with 88% capacity retention after 300 cycles at 0.2C.

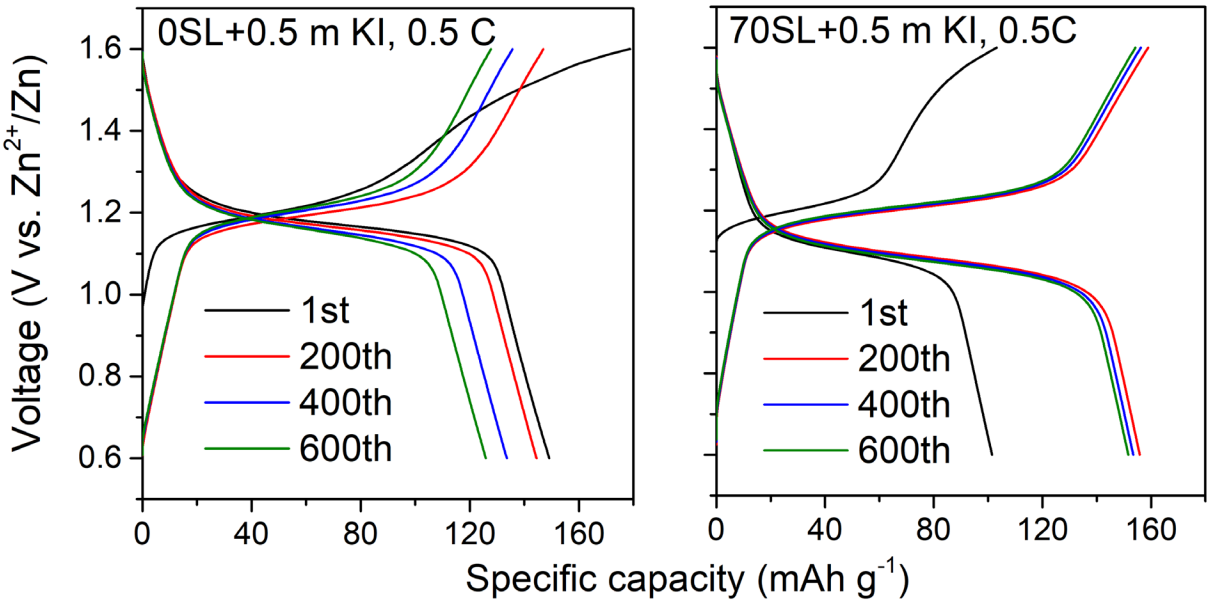

Figure 5.29 Voltage profiles of activated carbon (AC) electrodes in different electrolytes with the addition of 0.5 m KI at 0.5C

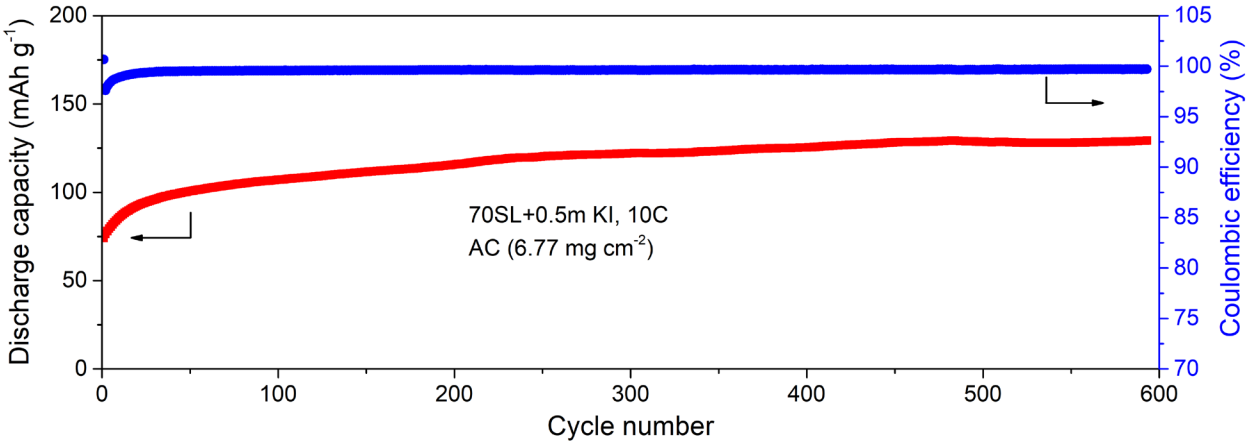

Figure 5.30 The cycling stability of AC electrodes in 70SL with the addition of 0.5 m KI at 10C

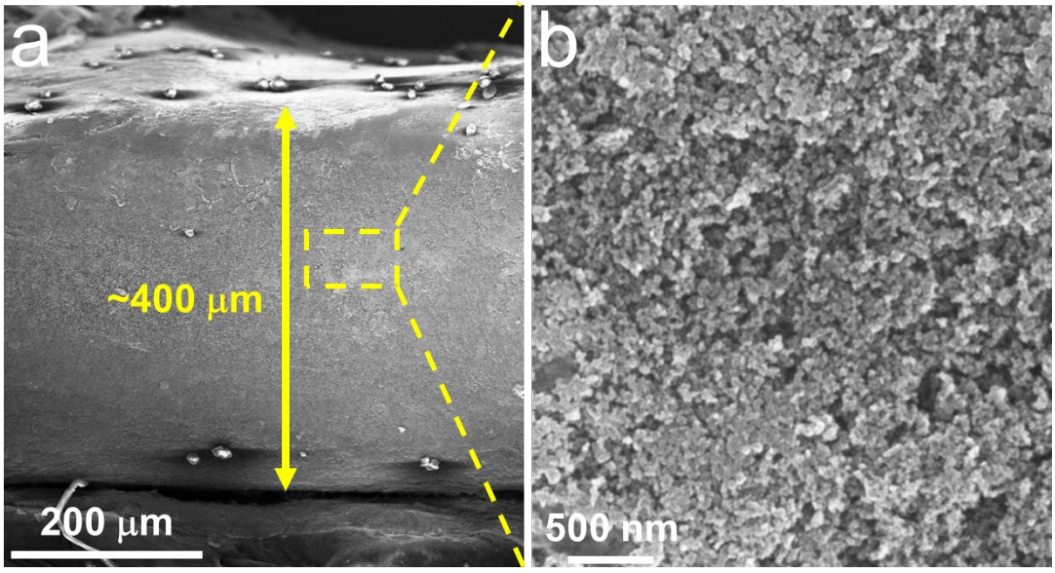

Figure 5.32 SEM images of the high-loading and freestanding activated carbon cathode **(a)** and a magnified view of the indicated region **(b).**

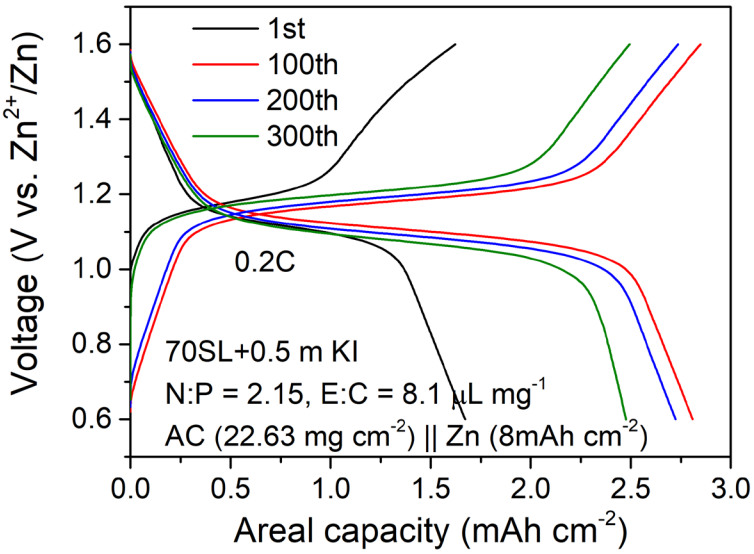

Figure 5.31 Voltage profiles of high-loading AC in 70SL with addition of 0.5 m KI at 0.2 C at a controlled N/P ratio of 2.15.

5.8 Conclusion

The competition between Zn^{2+} vs. proton intercalation in a conventional ZVO cathode is shifted to 95% Zn^{2+}-selective with a high-sulfolane/water hybrid eutectic electrolyte that alleviates deleterious proton intercalation and cathode dissolution. Dominant Zn^{2+} intercalation – disclosed by multiple physical/electrochemical characterization techniques – stabilizes the ZVO at low and moderate current densities with a high areal capacity of over 4 mAh cm^{-2}. Simultaneously, a fully hydrated Zn^{2+} solvation structure – revealed by the combination of experimental and theoretical characterization – enables a facile interfacial desolvation process at the solid/electrolyte interface. We realize highly reversible Zn plating/stripping with a 20-fold extended lifetime assisted by a sulfolane-derived SEI, and demonstrate excellent low-rate cycling stability of practical-level *anode-free* cells. Nonetheless, we do acknowledge that while dominant Zn^{2+} intercalation chemistry stabilizes the low or intermediate rate performance necessary for long duration energy storage, it inevitably diminishes ultra high-rate performance needed for high power load leveling. Solid-state Zn^{2+}-diffusion is slower than H^+ diffusion in hydrated oxides. This highlights that developing a new generation of cathode materials that are amenable to Zn desolvation/solvation (without proton co-intercalation) is likely necessary to realize high-rate function while not compromising the low-rate stability. Our work represents a practical strategy to stabilize both electrodes by tuning the hybrid electrolyte network and also provides an understanding of Zn^{2+}-(de)intercalation in conventional oxide cathodes which could expedite the commercialization of practical ZMBs.

Chapter 6 Stabilizing Magnesium Plating by a Low-Cost Inorganic Surface Membrane for High-Voltage and High-Power Mg Batteries

6.1 Introduction

The aforementioned magnesium bis(trifluoromethanesulfonimide) ($Mg(TFSI)_2$)[62,129,130] and newly invented alkoxy-borates/aluminates[51,56–59] are promising halide-free Mg salts with high oxidative stability up to 3.5 V. Unfortunately, they exhibit pronounced decomposition during repeated Mg plating/stripping that leads to poor long-term reversibility.[60,62,129,131–135] Most these Mg salts are electrochemical reductive during Mg plating and highly sensitive to the presence of moisture and impurities resulting from their synthesis procedures, which further aggravates their instability at the Mg anode.[131,136,137] In addition, the reductive instability of ether-based solvents has been widely reported as one of major factors that induces electrolyte decomposition to polymeric components (for example, C-O or C=O species), leading to the formation of unstable solid-electrolyte interface (SEI) or passivation layer on Mg surface that induces inhomogeneous Mg plating/stripping with short cycle life.[60,132,133] The strategy of using lithium hexafluoroisopropoxy borate ($LiB(Ohfip)_4$) as an electrolyte additive has been reported to achieve long-term Mg plating/stripping in a $Mg(B(Ohfip)_4)_2$/1,2-dimethoxyethane (DME) electrolyte, which is ascribed to the formation of a Li-species-containing SEI. However, the need for Li salts lows down the energy density and compromises the potential economic benefits anticipated for Mg batteries. Various artificial SEIs have also been reported to enable reversible Mg plating/stripping in $Mg(TFSI)_2$-based electrolytes by suppressing their decomposition via the formation of a passivation film on the Mg surface;[138–140] however, a very low current density of less than 0.05 mA cm^{-2} was used in these studies. Chloride-salt induced protective interface on Mg were also widely reported to enable reversible and stable Mg^{2+}/Mg redox,[141–144] nonetheless, concerns remain on the dissolution of these chloride species from Mg surface into electrolytes that may compromises the electrolyte oxidative stability. To the best of our knowledge, none of these studies reported full cell performances with an operating voltage of over 3 V. Therefore, creating a Mg^{2+}-conducting, practical and cost-effective protective interface from electrolyte decomposition remains an ongoing challenge for these high-voltage electrolytes.

In this chapter, I utilized zeolite-polymer membranes to stabilize the Mg anode for the first time and achieve excellent performance in full cells at relatively high current rates. Zeolite A is used as molecular sieves for dehydration of gases or solvents owing to its propensity to absorb water.[145] Its cubic structure consists of aluminosilicate cages that form an 11.4 Å α-cavity and much smaller β cavity, which are interconnected in three dimensions to form the microporous structure. The windows into the cavities/pores range from 3-5 Å, as dictated by the cations that sit within them (eg. K^+, Na^+, Ca^{2+}, etc.) to balance the negative charge of the aluminosilicate framework. For example, zeolite 3A - defined by a high K^+/Na^+ ratio - has windows of 3.2 Å in diameter (making it ideal for the adsorption of water) whereas zeolite 4A has windows of 3.8 Å, based on Na^+ as the only counter-cation. Zeolite 3A was recently reported to effectively create local concentrated electrolytes in the battery area.[84,146–148] For example, the oxidative activity of ethereal solvents in sodium-ion batteries was decreased based on a regulated electrolyte network;[147] incorporation of Na^+-diglyme (G2)-anion complexes in the zeolite pores; and suppressed activity of diglyme at the electrode/electrolyte interface. However, the functionality of the zeolite was not explicitly explained, while we note that diglyme is much too large to penetrate the 3.2 Å window (see below).

To establish proof of concept for our study, we chose a 0.25 M $Mg(B(Ohfip)_4)_2$/G2 electrolyte as a platform to study the solvent reduction activity during Mg plating/stripping, where the factor of salt decomposition can be alleviated. This is because bulky $B(Ohfip)_4)_2$ anion results in less contact ion pairs (CIPs) compared to conventional $TFSI^-$ anion, which facilitates fast interfacial charge transfer process with less anion reduction activity. $Mg(B(Ohfip)_4)_2$ is also a widely reported salt and can be synthesized with relatively lower cost and higher purity compared to other state-of-art salts (for example, $Mg(CB_{11}H_{12})_2$). In this study, we identify that the short lifetime of Mg plating/stripping in this electrolyte originates from the high activity of free G2 solvent molecules that reduce on the Mg/electrolyte interface

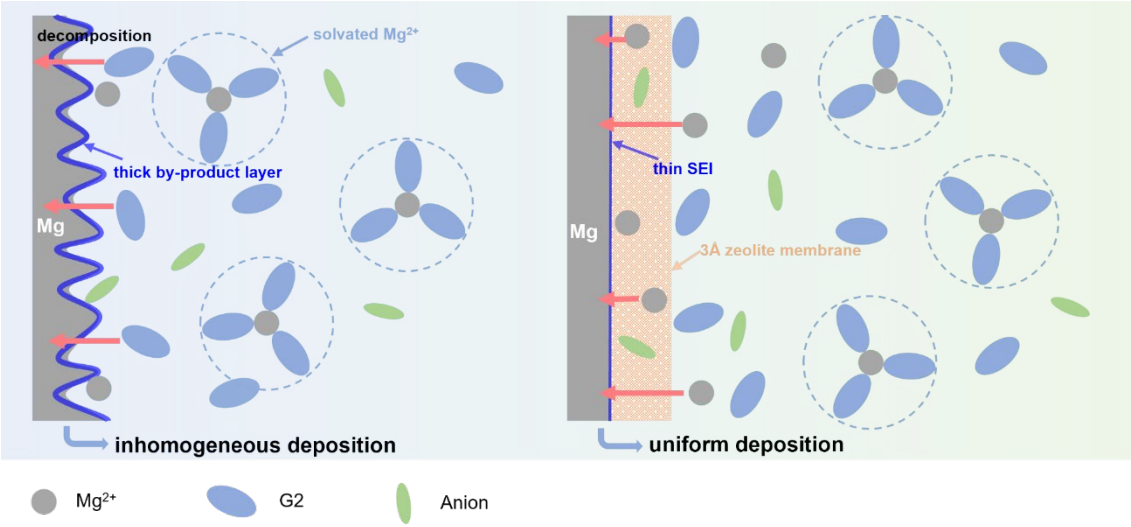

Figure 6.1 Illustration of the functionality of the zeolite membrane. Inhomogeneous Mg deposition with pronounced solvent (G2) decomposition on a bare Mg/electrolyte interface (left), and uniform Mg deposition with suppressed G2 decomposition in the presence of 3A zeolite membrane on the Mg surface (right).

to form a thick surface layer of decomposition by-products (**Figure 6.1**). This induces inhomogeneous Mg deposition and rapid cell failure. By using the low- cost zeolite film based on 3Å molecular sieves as a protective interface on the Mg anode, G2 decomposition is effectively suppressed, generating a smooth Mg plating morphology and a thinner SEI. This is ascribed to the significantly alleviated free-G2 fraction within this interface revealed by FTIR spectroscopy. The protected Mg anode thus achieves a 750-fold extended lifetime in Mg||Mg symmetric cells (over 6000 hours/7 months) at a current density of 0.3 mA cm^{-2} and an areal capacity of 0.3 mAh cm^{-2}. Two chemically-distinct Mg^{2+} environments were revealed by ^{25}Mg magic angle spinning nuclear magnetic resonance (MAS NMR) spectroscopy, that are likely involved in the Mg^{2+} migration pathways through the zeolite membrane. A prototype full cell based on a Mo_3S_4 cathode and ethereal electrolyte exhibits excellent capacity retention of 91% over 200 cycles. We furthermore demonstrate Mg batteries that are very stable at a high operation voltage of > 3.5 V vs. Mg^{2+}/Mg at a 2C rate using polyaniline (PANI) as the cathode. By simultaneously suppressing the shuttling of dissolved PANI monomers with the zeolite

membrane, a high energy density up to 320 Wh kg_{PANI}^{-1} and power density of 1320 W kg_{PANI}^{-1} are achieved.

I proposed the idea, planned the experiments, performed all electrochemical measurements and wrote the original manuscript. Abhinandan Shyamsunder synthesized the Mg salt and Mo_3S_4 materials. Dr. Baris Key conducted solid-state ^{25}Mg MAS NMR experiments. Zhuo Yu performed the TGA experiments.

6.2 Experimental Approaches

6.2.1 Synthesis of magnesium hexafluoroisopropoxide ($Mg(Ohfip)_2$).

This material was synthesized using a similar procedure to that previously reported,[149] but magnesium ethoxide (98% Sigma Aldrich) was used instead of calcium methoxide. ^1H NMR (300 MHz, CD3CN): δ = 4.85(m). ^{19}F NMR (282 MHz CD3CN): δ = -76.8.

6.2.2 Synthesis tris-hexafluoroisoproxy borate ($B(Ohfip)_3$).

Tris-hexafluoroisopropoxy borate was prepared according to a previously reported procedure,[150] and chemical analysis was in agreement with the expected composition. This borate salt was sublimed before use.

6.2.3 Synthesis of magnesium hexafluoroisoproxy borate ($Mg(B(Ohfip)_4)_2 \cdot 3DME$).

1,2-dimethoxy ethane (DME, 99% Sigma Aldrich) was first passed over a column of activated alumina, distilled over sodium, degassed and stored under molecular sieves. Magnesium hexafluoroisopropoxide ($Mg(Ohfip)_2$) and tris-hexafluoroisopropoxy borate ($B(Ohfip)_3$) were mixed in the appropriate ratio in DME at 65˚C for 6 hours. The clear solution obtained was then concentrated under dynamic vacuum at room temperature to obtain the $Mg(B(Ohfip)_4)_2 \cdot x$DME salt. The salt was then redissolved in DME and recrystallised with hexanes (Mixture of isomers 95% Sigma Aldrich) to obtain crystals of $Mg(B(Ohfip)_4)_2 \cdot 3DME$. ^1H NMR (300 MHz, CD3CN): δ = 4.76(m), 3.55(t), 3.42(s). ^{19}F NMR (282 MHz CD3CN): δ = -75.1 11B NMR (96.25 MHz, CD3CN): δ = 9.2(s).

6.2.4 Preparation of 0.25 M $Mg(B(Ohfip)_4)_2$ electrolyte solution.

The weighted $Mg(B(Ohfip)_4)_2 \cdot 3DME$ powder were dissolved into proper amount of G2 and was stirred overnight at 25 °C. The obtained clear electrolyte solution was directly used for cell assembly without any pre-conditioning process.

6.2.5 Preparation of zeolite membrane.

Three grams of 3 Å molecular sieves (Sigma Aldrich, 8-12 mesh) were ball-milled at 400 rpm for 12 hours before being dried in vacuum at 200 °C overnight. The membrane was fabricated by mixing 90 wt% zeolite power and 10 wt% polytetrafluoroethylene (PTFE, Sigma Aldrich, 60wt% in water). The mixture was ground evenly in a mortar and pressed into a freestanding thin film about 100 mm thin. After being cut into 14 mm disks, the zeolite membrane was dried in vacuum at 120°C overnight. The dried membrane was stored in an Ar-filled glovebox before electrochemical measurements.

6.2.6 Preparation of Mo_3S_4 and PANI cathodes.

Chevrel Mo_3S_4 (or Mo_6S_8) was synthesized by acid leaching from $Cu_2Mo_6S_8$ based on a previously reported procedure.[151] PANI was purchased from Fisher Scientific without any further purification. The Mo_3S_4 cathode was prepared by mixing 70 wt% active material, 20 wt% conductive carbon (Super P) and 10 wt% polyvinylidene difluoride (PVDF) in N-methyl-2-pyrrolidone (NMP; anhydrous, 99.5%; Sigma-Aldrich). The slurry was cast on carbon-coated aluminum foil (thickness: 18 μm) by doctor blading and the electrodes were punched into 10 mm discs after being dried at 60 °C for 5 hours. The discs were finally dried *in vacuo* at 120 °C overnight before being transferred into an Ar-filled glovebox. For the PANI cathode, 50 wt% PANI was mixed with 40 wt% conductive carbon (KETJENBLACK) and 10 wt% polytetrafluoroethylene (Sigma-Aldrich, 60 wt% dispersion in H_2O) in isopropanol. The free-standing PANI composite film thus obtained was dried at 60 °C overnight, and punched into small disks that were pressed onto a Ti mesh (diameter: 11 mm). These were utilized as cathodes in the full cells. The mass loading of active material was ~ 2.5 mg cm^{-2}.

6.2.7 Electrochemical measurements.

Mg foils (thickness: 100 μm) were polished by sandpaper several times before being pouched as 9/16-inch disks and using them in symmetric or full 2032 coin cells. To evaluate the effectiveness of zeolite membrane, zeolite/Mg anodes were prepared by tightly pressing the zeolite membrane onto a Mg disc with hands before cell assembly. Such a contact between zeolite membrane and Mg was held by the pressure from spring in the coin cell. All cells – using 100 μL of electrolyte incorporated in a glass fiber separator - were cycled using a VMP3 potentiostat/galvanostat station (Bio-Logic). Cyclic voltammetry (CV) of the Mo_3S_4 cathode was measured at a sweep rate of 0.1 mV s^{-1} in a voltage range of 0.2 - 2.4 V. The evolution of the charge transfer resistance of two-electrode Mg symmetric cells was measured by electrochemical impedance spectroscopy (EIS) with a voltage amplitude of 5 mV in the frequency range of 1 MHz to 100 mHz. The cell was rested for 10 min to reach equilibrium before each EIS measurement. All cells were cycled at 25 °C.

6.2.8 Materials characterization.

Fourier transform infrared spectroscopy (FTIR) was carried out on a Bruker Tensor 27 system equipped with attenuated total reflection (ATR). A Zeiss Ultra field emission SEM instrument was used to collect scanning electron microscopy (SEM) images and energy-dispersive X-ray spectroscopy (EDX) data. XPS experiments were conducted on a Thermo Scientific K-Alpha XPS instrument. CasaXPS software was used to conduct XPS data analysis, where the C 1s peak of 284.8 eV was used to calibrate the binding energies. Spectral fitting was based on Gaussian-Lorentzian functions and a Shirley-type background. Solid-state ^{25}Mg magic angle spinning (MAS) NMR experiments were performed at 11.7 T (500 MHz) on a Bruker Avance III spectrometer operating at a Larmor frequency of 30.64 MHz using a 3.2 mm MAS probe. The spectra were acquired at a spinning speed of 5 kHz using 3.2 mm rotors in direct observe (single pulse) mode and with recycle delays of 1 s. ^{25}Mg shifts were referenced to 5 M $MgCl_2$ (aq.) at 0 ppm. All electrodes disassembled from the cells were washed three times with DME and dried at room temperature *in vacuo* before each characterization.

6.3 Zeolite 3A membrane to suppress G2 activity

The fabricated flexible zeolite membrane shows a flat surface produced by ball-milled 3A molecular sieve particles that have a dimension less than 200 nm (**Figure 6.2a**). Different from previous reported defect-free metal-organic-framework (MOF)-based interfacial

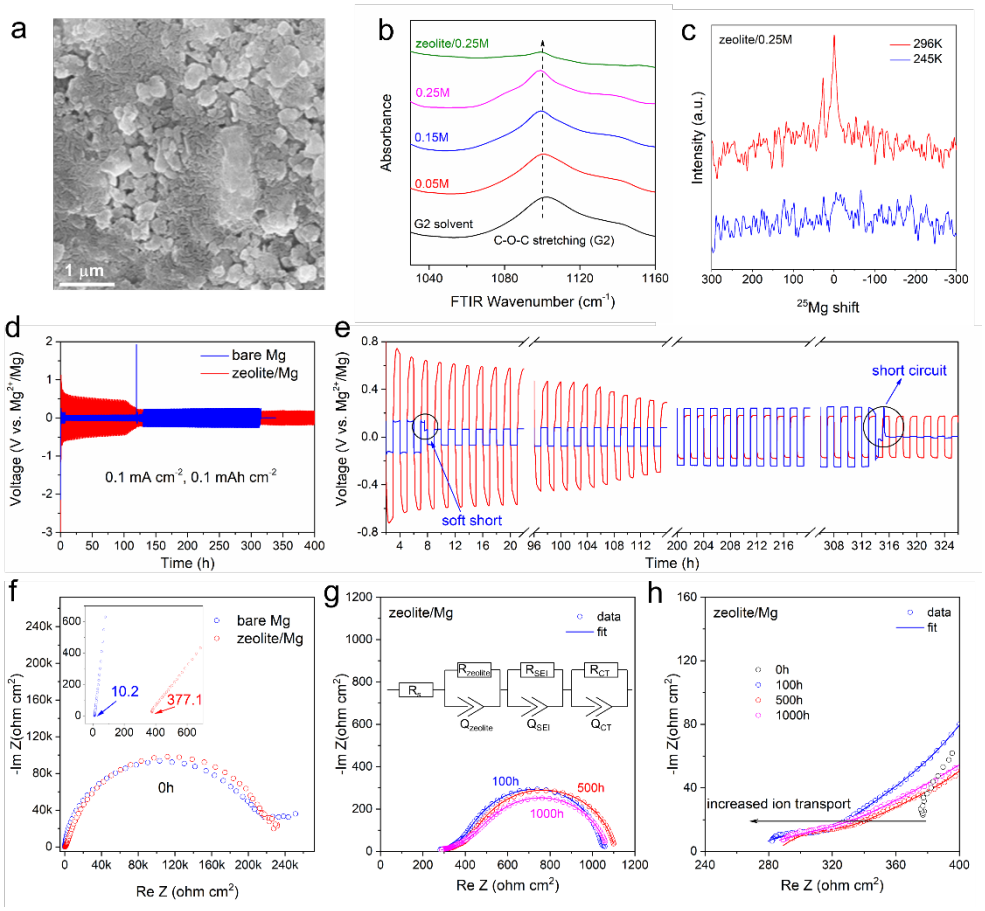

Figure 6.2 Characterization of the zeolite membrane. **(a)** SEM images of the zeolite membrane. **(b)** FTIR spectra at different concentrations of $Mg(B(Ohfip)_4)_2$/G2 electrolyte and zeolite-modified 0.25M electrolyte. **(c)** Variable temperature solid-state ^{25}Mg MAS NMR spectra of zeolite/0.25M. **(d** and **e)** Galvanostatic Mg plating/stripping of Mg||Mg symmetric cells with bare Mg and zeolite/Mg at 0.1 mA cm^{-2} (0.1 mAh cm^{-2}), and **(e)** magnified voltage curves. **(f)** Nyquist plots of symmetric cells at open circuit with zeolite/Mg and bare Mg. **(g** and **h)** Nyquist plots of symmetric cells with zeolite/Mg after plating/stripping for different hours at 0.3 mA cm^{-2} (0.3 mAh cm^{-2}): The evolution of **(g)** interfacial resistance fitted (shown by line) with the indicated equivalent circuit and **(h)** bulk ion transport.

membrane that completely blocks the electrolyte penetration, the existence of many macropores between the zeolite particles enables good absorption of the electrolyte, thus ensuring fast ion transport with a high ionic conductivity of 0.76 mS cm^{-1} (**Figure 6.3)**. After

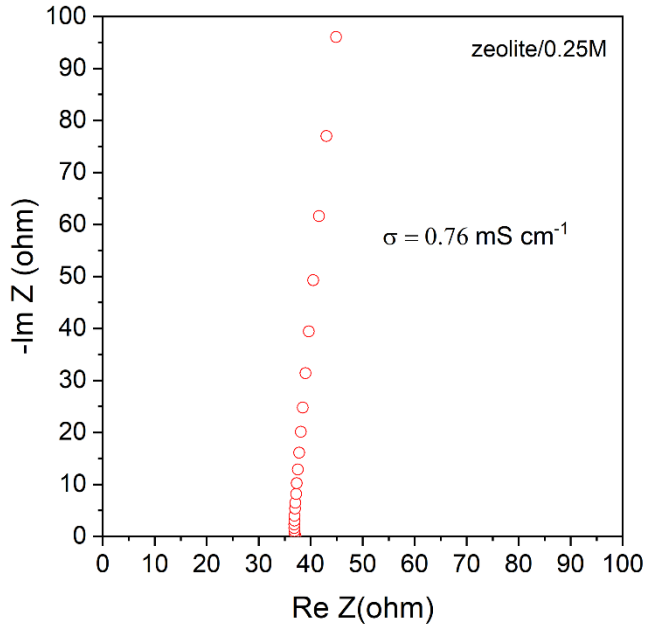

Figure 6.3 Nyquist plot of ionic conductivity measurement of zeolite/0.25M. To prepare zeolite/0.25M, zeolite membrane was soaked in 100 uL electrolyte overnight. After wiping residual surface electrolyte, stainless steel was used as current collector for EIS measurements.

soaking this zeolite membrane in 0.25 M $Mg(B(Ohfip)_4)_2$/G2 electrolyte (denoted as zeolite/0.25 M), the change in bonding environment of the G2 molecules was revealed by FTIR spectroscopy. A gradual blue shift of the CH_2 bending mode (G2) with increased salt concentration can be observed (**Figure 6.4**, from 852 cm^{-1} in pure G2, to 858 cm^{-1} in 0.25 M $Mg(B(Ohfip)_4)_2$/G2). Addition of the zeolite membrane (zeolite/0.25 M) leads to a further blue shift to 861 cm^{-1}, indicating the free G2 molecules in the electrolyte are adsorbed by the zeolite membrane. This is further verified by the change of the C-O-C stretching mode at ~1101 cm^{-1}

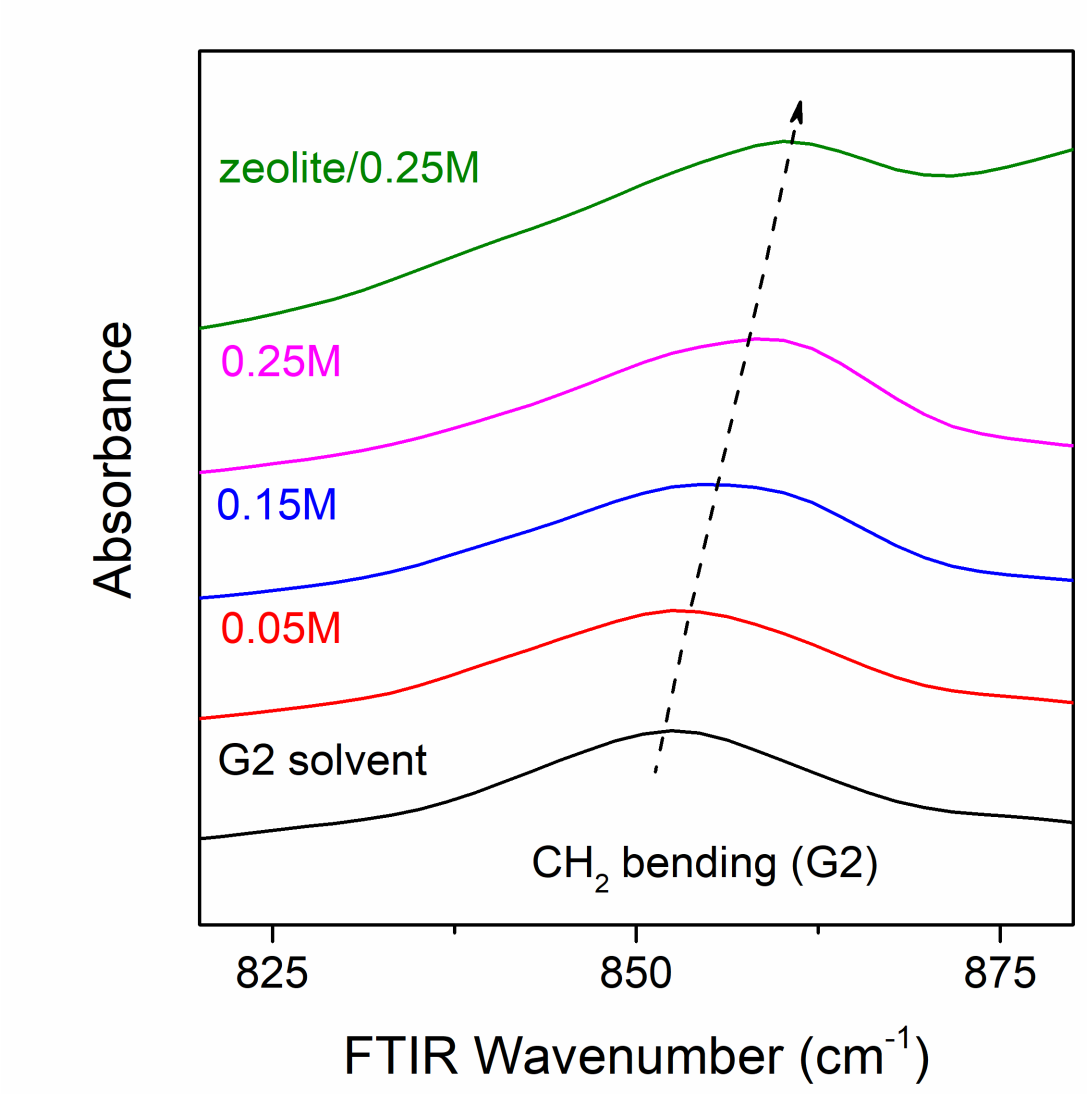

Figure 6.4 FTIR spectra of $Mg(B(Ohfip)_4)_2$/G2 electrolytes at different concentrations, and zeolite-modified 0.25M electrolyte.

(**Figure 6.2b**). The gentle decrease in its intensity as the salt concentration increases originates from G2 molecules being bound to Mg^{2+} ions.[152] The pronounced decrease of this peak in zeolite/0.25 M, however, suggests the existence of much more tightly bound (i.e., less free) G2

molecules. Therefore, we can anticipate lower decomposition of free G2 at the Mg/zeolite interface during Mg plating/stripping.

We carried out solid-state ^{25}Mg magic angle spinning (MAS) nuclear magnetic resonance (NMR) on a zeolite/PTFE film to gain insight into the Mg^{2+} environments in zeolite/0.25M (**Figure 6.2c**). As the film was dried at 120 °C prior to analysis, we expect the presence of indigenous water in the zeolite pores, which is not removed until > 300 °C. At 296 K under MAS conditions, two ^{25}Mg peaks were detected at 0.2 ppm and 27.2 ppm. These peaks were respectively assigned to Mg^{2+} coordinated to water molecules – hydrated Mg^{2+} in the zeolite structure – and Mg^{2+} coordinated to diglyme molecules (presumably Mg-O_6 octahedral units). The former assignment is close and consistent with free Mg^{2+} in 5 M $MgCl_2$ aqueous solution (see Experimental procedures), and the latter is in excellent agreement with the shift for Mg^{2+}-diglyme coordination in a xerogel (24.7 ppm).[153] These environments are represented, according to the peak integrals, by a molar ratio of 1:3 in zeolite/0.25M. At 245 K with identical parameters including the number of scans, however, no ^{25}Mg peaks but only noise was observed in the spectrum. We assume that the motional linewidth narrowing is significant at 296 K, whereas the linewidth broadening due to lack of motion for both hydrated and diglyme-coordinated Mg^{2+} at 245 K renders the broad peaks buried in the noise of the ^{25}Mg spectrum. Therefore, it is reasonable to propose significant mobility for both Mg^{2+}-coordination environments in zeolite/0.25M at room temperature at the local level, possibly giving rise to two different Mg^{2+} migration pathways (see discussion below).

The effectiveness of the zeolite membrane in stabilizing Mg plating/stripping was tested in Mg||Mg symmetric cells using 0.25 M $Mg(B(Ohfip)_4)_2$/G2 as the electrolyte. **Figure 6.2d** displays the initial 400-hour Mg plating/stripping behavior using bare Mg and zeolite-protected Mg (zeolite/Mg) at a typical current of 0.1 mA cm^{-2} with an areal capacity of 0.1 mAh cm^{-2}. In the presence of zeolite, an initial activation process is observed with a Mg plating overpotential of 0.74 V (**Figure 6.2e**). The overpotential decreases to a stable value of 0.17 V after the first 120-hour activation, which is only slightly higher than that of initially using bare Mg (~ 0.13V). The slightly higher plating overpotential can be ascribed to the insulating nature of the zeolite membrane and lower ion transport (see below), which increase the interfacial

resistance during Mg plating/stripping. However, with bare Mg, a sudden voltage drop to 0.06 V occurs after only 7 hours of plating/stripping, which is a clear indication of the occurrence of soft shorts. This results in the fluctuation of the Mg overpotential in subsequent cycling until a complete short circuit is observed after 314 hours. In contrast, cells with zeolite/Mg show stable Mg plating/stripping without any abrupt voltage change, exhibiting excellent stability.

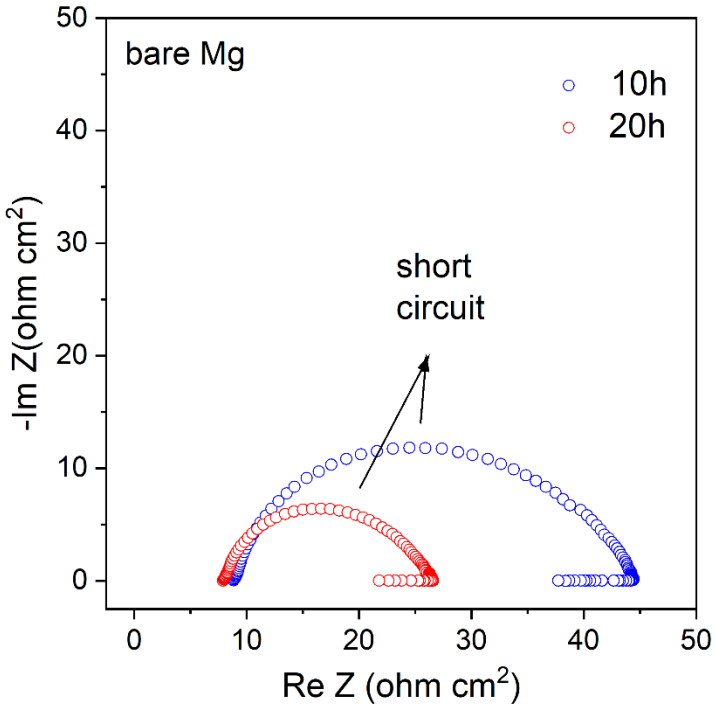

Figure 6.5 Nyquist plots of symmetric cells with bare Mg after plating/stripping at different times.

We conducted electrochemical impedance spectroscopy (EIS) studies to identify interfacial stability. **Figure 6.2f** reveals that both cells with bare Mg and zeolite/Mg show an initial large interfacial resistance that can be ascribed to the native MgO.[154] With the presence of zeolite, a much higher resistance (377.1 ohm cm^2) related to ion transport is observed compared to only 10.2 ohm cm^2 for bare Mg, which explains the initial higher overpotential for Mg plating/stripping in **Figure 6.2d**. In subsequent plating/stripping processes, the interfacial resistance for a bare Mg anode quickly decreases to near zero after only 10 hours (**Figure 6.5**), again, a clear indication of short circuits that is consistent with the sudden

decrease in plating/stripping overpotential (**Figure 6.2d-e**). With zeolite/Mg anode, however,

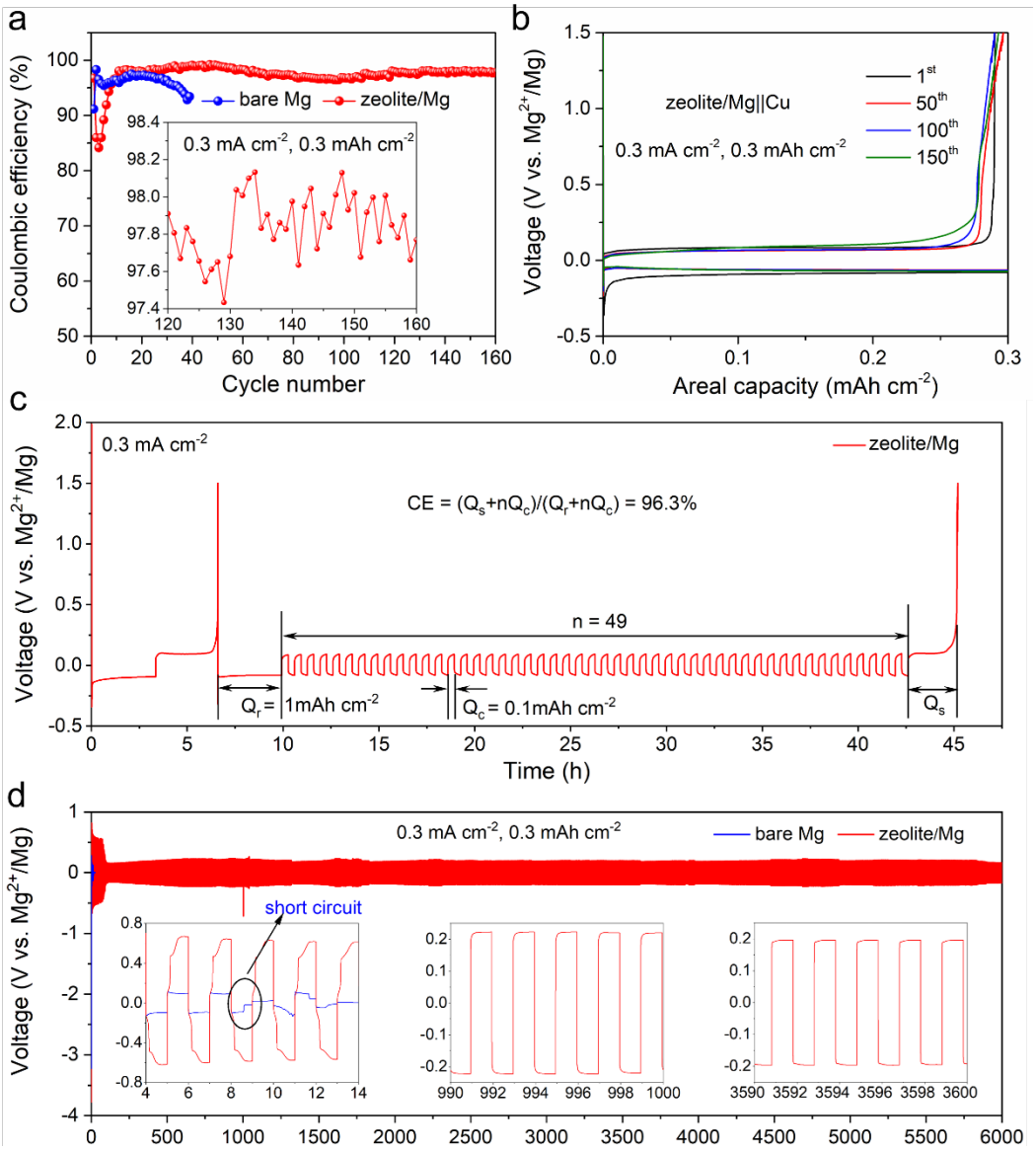

Figure 6.6 Electrochemical studies of Mg plating/stripping. **(a** and **b)** Evolution of coulombic efficiency on cycling in Cu||Mg and Cu||zeolite/Mg asymmetric cells and **(b)** corresponding voltage profiles of Cu||zeolite/Mg. The zeolite/Mg was activated in a symmetric cell for 20 cycles prior to being coupled with Cu. **(c)** Modified Aurbach measurement40 of coulombic efficiency in a Cu||zeolite/Mg cell. **(d)** Long-term cycling of Mg||Mg and zeolite/Mg||zeolite/Mg symmetric cells. Cycling conditions are at 0.3 mA cm^{-2} with a stripping/plating capacity of 0.3 mAh cm^{-2}.

both interfacial resistance (**Figure 6.2g**) and ion transport resistance (**Figure 6.2h)** decrease during the electrochemical conditioning process that typically exists in Mg electrolytes.[155] The gradually increased bulk ion conductivity is probably due to the electrolyte wetting and/or reconfiguration of the Mg^{2+} solvation structure within the zeolite membrane. To further investigate the electrochemical process at electrolyte-zeolite/Mg interface, we fitted the impedance with a bulk electrolyte resistance (R_s) and three interfacial resistances (**Figure 6.2g**): zeolite membrane resistance ($R_{zeolite}$) at high frequency, SEI resistance (R_{SEI}) at medium frequency, and charge transfer resistance (R_{CT}) at low frequency. These resistances remain stable at different hours, confirming the superiority of zeolite membrane to stabilize Mg plating/stripping during long-term cycling.

6.4 Highly Reversible Mg Plating/Stripping

To further examine the reversibility of the zeolite/Mg anode under realistic conditions, we galvanostatically measured the coulombic efficiency (CE) of Mg plating/stripping of asymmetric cells on a Cu substrate at a moderate current density of 0.3 mA cm^{-2} and areal capacity of 0.3 mAh cm^{-2}. The CE for zeolite/Mg quickly increases to > 98% after the initial 10 cycles and is sustained for over 160 cycles (**Figure 6.6a-b** and **6.7**). With bare Mg, the

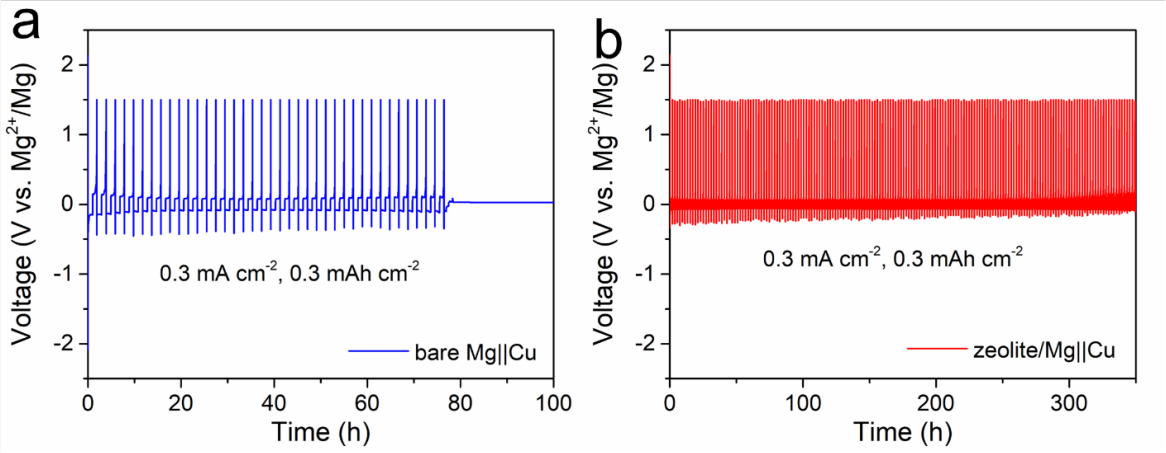

Figure 6.7 Voltage profiles of **(a)** Cu||Mg and **(b)** Cu||zeolite/Mg asymmetric cells at 0.3 mA cm^{-2} and 0.3 mAh cm^{-2}. The zeolite/Mg electrode was activated in a symmetric cell for 20 cycles prior to being coupled with Cu.

Mg||Cu cell fails after only 39 cycles due to short circuits (**Figure 6.6a**). The CE was also measured with a modified Aurbach method in asymmetric cells,[156] with an areal capacity of 1 mAh cm^{-2} as a Mg reservoir. With zeolite/Mg, an average 96.3% CE can be obtained (**Figure 6.6c**). The long-term stability of the zeolite/Mg anode was further evaluated in symmetric cells. We record a cell cycling lifetime of over 6000 hours (8.3 months or 3000 cycles) without significant increase of polarization: more than 750-fold vs. that of bare Mg (**Figure 6.6d**). We note the plating/stripping curves with zeolite membrane gradually changed to semi-rectangular shape during the activation process and remain constant for thousands of hours, where the possibility of soft short has been ruled out by previous impedance studies (**Figure 6.2f-h**). The origin of this change is probably due to the difference in nucleation/growth model between initial Mg plating/stripping and after activation, which is beyond the scope of this study and will be examined in future studies. To the best of our knowledge, we believe this is one of the longest lifetimes of a Mg anode in organoborate or chloride-based electrolyte. At more challenging conditions of 0.5 mA cm^{-2} and 0.5 mAh cm^{-2}, the cell still shows very stable cycling for over 2500 hours (3.5 months or 1250 cycles; **Figure 6.8**).

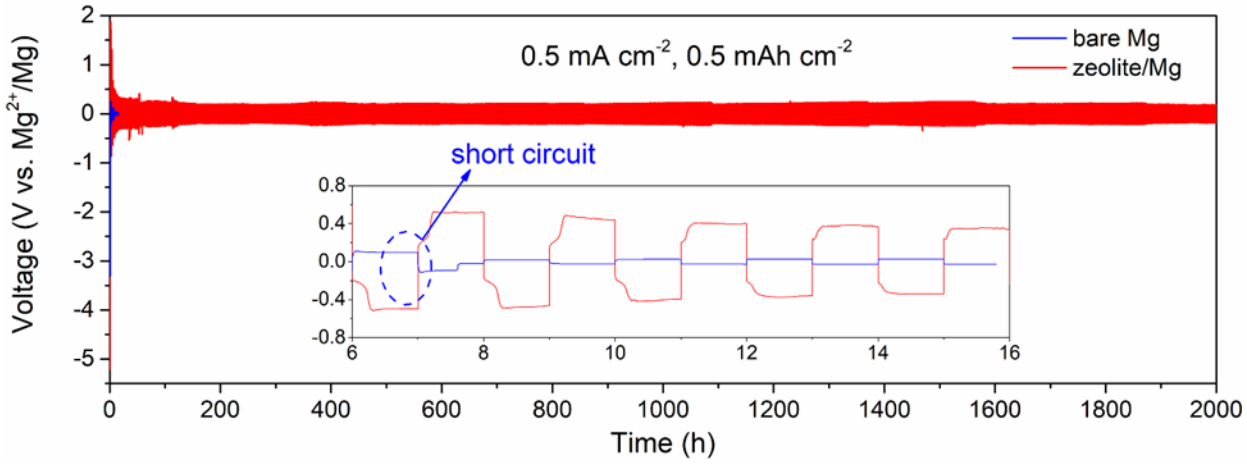

Figure 6.8 Long-term cycling of Mg||Mg and zeolite/Mg||zeolite/Mg symmetric cells at 0.5 mA cm^{-2} and 0.5 mAh cm^{-2}.

6.5 Dendrite-free Mg Plating Morphology

To examine the Mg deposition morphology under the protection of zeolite, Cu electrodes with plated Mg were carefully retrieved and analyzed by scanning electron microscopy (SEM), where insulating zeolite membrane was peeled off from Cu collector prior to the imaging experiments. A smooth and homogeneous Mg deposit was observed on Cu protected by zeolite membrane (**Figure 6.9a-c**), showing a two-dimensional (2D) Mg deposition layer merged by micro-size globules (**Figure 6.9b**) with nanoscale Mg nuclei (**Figure 6.9a**). For the Mg deposited on the bare Cu collector (**Figure 6.9d-f**), to the contrary, an inhomogeneous and three-dimensional (3D) island (**Figure 6.9e**) was observed with much larger Mg nuclei (**Figure 6.9d**). Such a 3D island growth of Mg was reported with similar negative impact to dendrite growth and can easily induce the early-onset shorting of asymmetric cells (**Figure 6.6a**).[130] The undesirable morphology was also observed on cycled

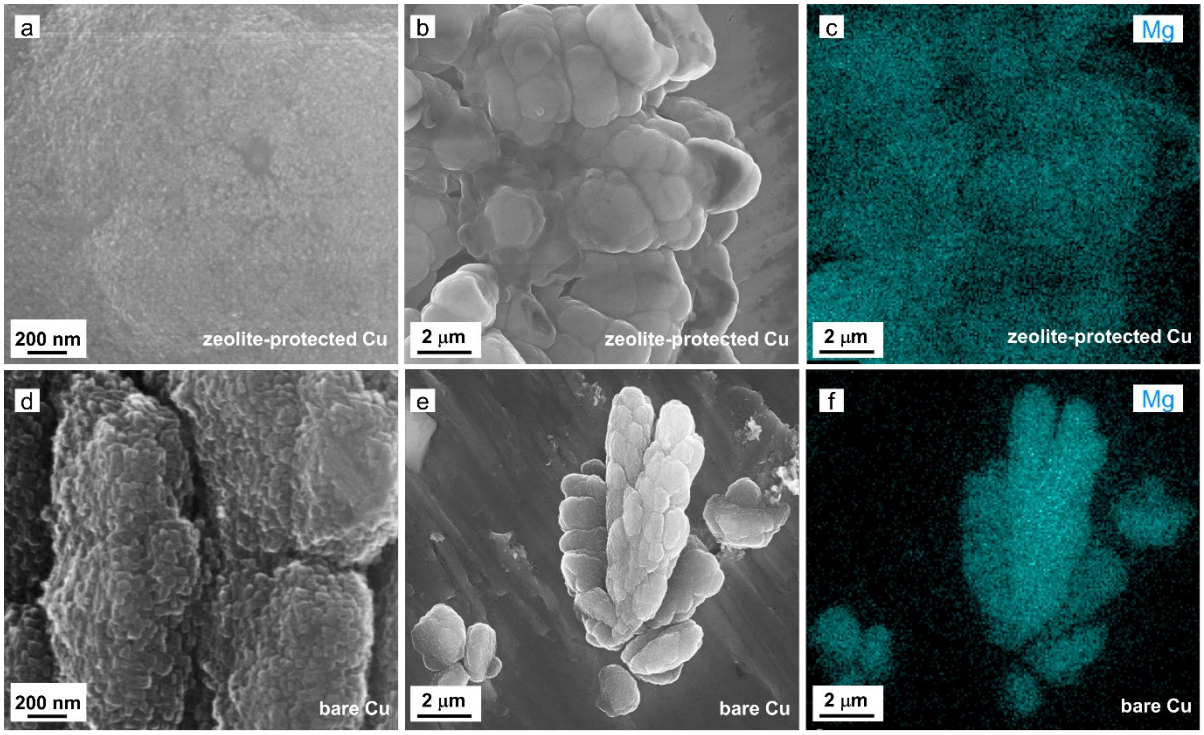

Figure 6.9 (a, b, d, e) SEM and **(c, d)** corresponding EDX images of Cu electrodes with deposited Mg at a current density of 0.3 mA cm^{-2} (0.3 mAh cm^{-2}): **(a-c)** zeolite-protected Cu and **(d-f)** bare Cu. Please note the zeolite membrane was removed prior to image the Mg morphology on zeolite-protected Cu.

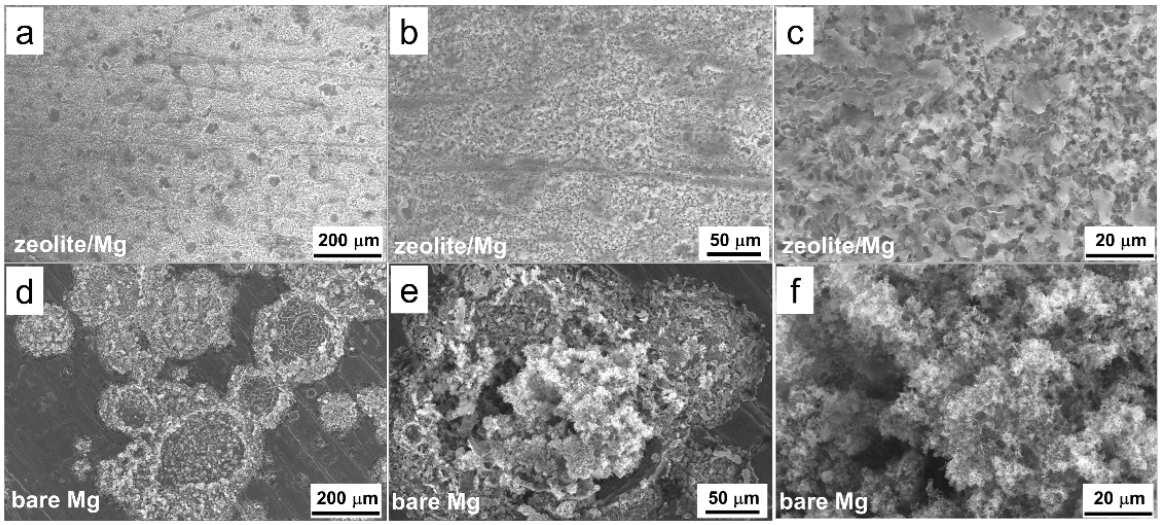

Figure 6.11 (a-f) SEM images of Mg metal deposited at a current density of 0.3 mA cm^{-2} (0.3 mAh cm^{-2}) after 10 cycles using **(a-c)** zeolite/Mg and **(d-f)** a bare Mg anode.

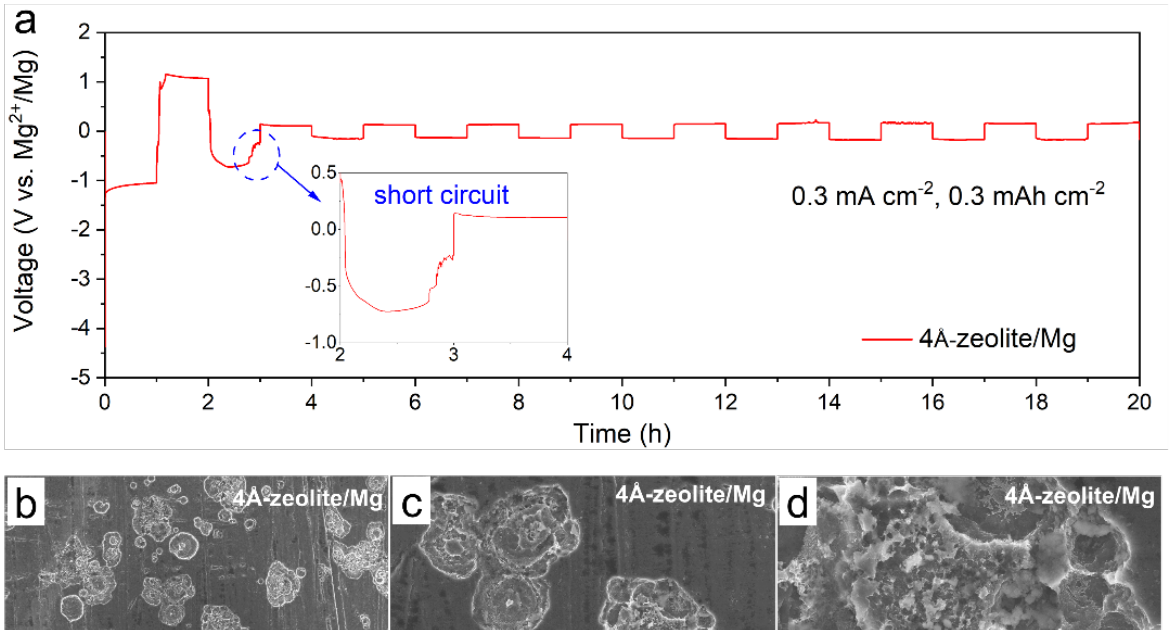

Figure 6.10 (a) Voltage profile of a Mg symmetric cell with a zeolite 4A/Mg anode and **(b-d)** corresponding SEM images of the poorly plated Mg.

bare Mg metal foil (**Figure 6.10**) that can be partly ascribed to the high reactivity of free G2 solvent molecules, which decompose on the Mg surface (see XPS studies below). In contrast,

by limiting the free G2 activity using a 3Å zeolite membrane, the solvent decomposition reaction is suppressed and yields a very smooth Mg deposition morphology. It should be noted that the 3Å pore size of the selective molecular sieves plays a key role in enabling stable

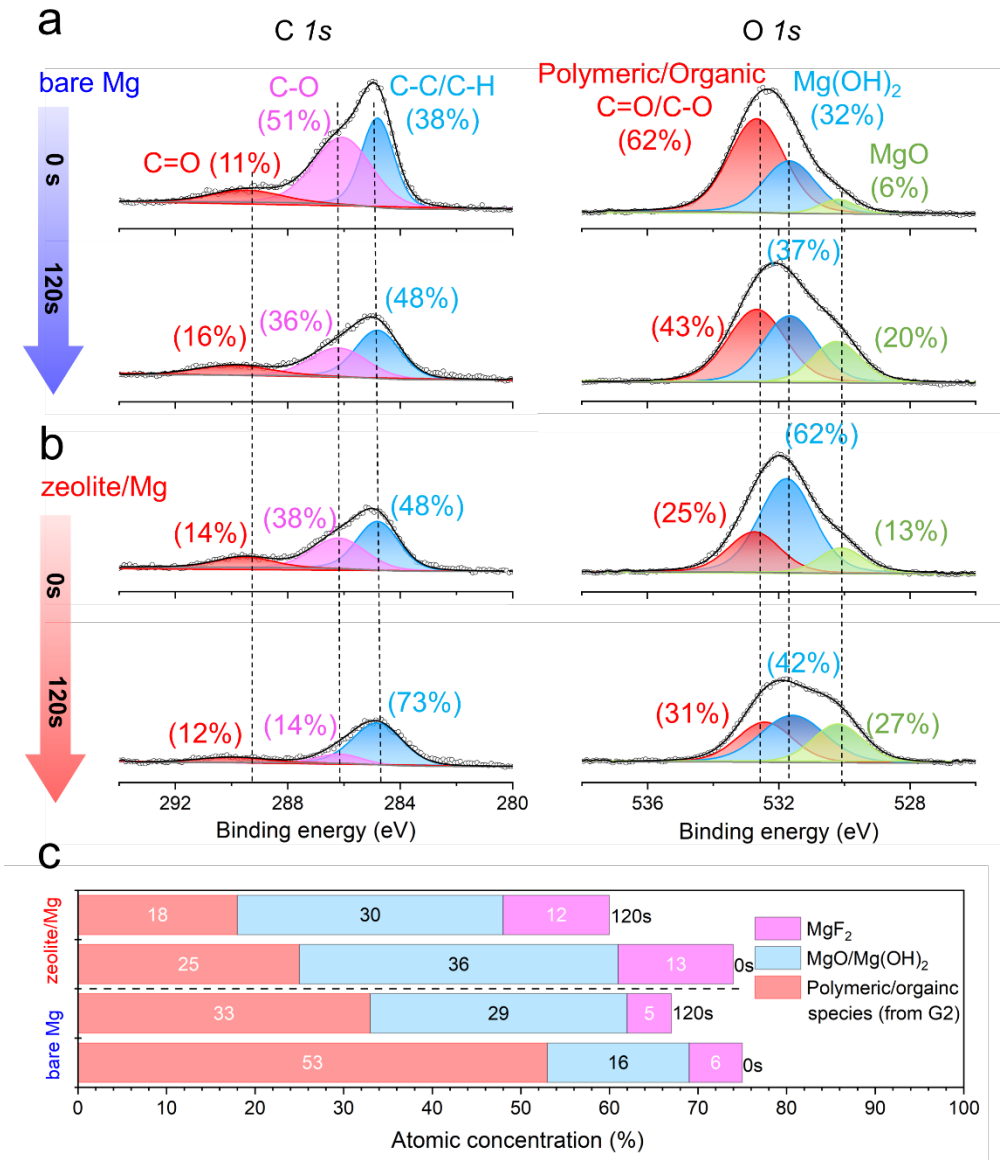

Figure 6.12 (a and **b)** Depth-profiling XPS spectra in the C 1s and O 1s regions for Mg plated on the 10th cycle on **(a)** bare and **(b)** zeolite-protected anodes at 0.3 mA cm^{-2} (0.3 mAh cm^{-2}). **(c)** The relative fractions of different species identified on the cycled electrodes. The peaks of C=O and C-O in the C1s and O1s spectra correspond to polymeric/organic decomposition products from the G2 solvent

cycling of these cells, as the use of 4Å zeolite membrane leads to very poor Mg plating/stripping performance and undesirable deposition morphologies (**Figure 6.11**). This is discussed in detail below.

6.6 XPS studies of interfacial SEIs

The surface composition of the deposited Mg is directly correlated to electrolyte decomposition. To prove this, we carried out high-resolution X-ray photoelectron spectroscopy (XPS) on the topmost and Ar^+-sputtered surface of retrieved Mg electrodes with/without zeolite protection. As shown in **Figure 6.12a**, in the O1s region of bare Mg, a peak at 532.7 eV corresponding to polymeric/organic C=O/C-O accounts for over 62% of the peak area, along withfeatures in the C *1s* region (C-O at 286.1 eV (51%) and C=O at 289.5 eV (11 %)). These can be ascribed to the decomposition of G2 at the Mg/electrolyte interface.[60,62] Two additional peaks for $Mg(OH)_2$ (531.7 eV, 32%) and MgO (530.2 eV, 6%) were also identified, which originate from the native oxide passivation surface or trace moisture in the electrolyte. MgF_2 (685.9 eV) and B-O (192.5 eV) species that result from $B(Ohfip)_4^-$ decomposition were

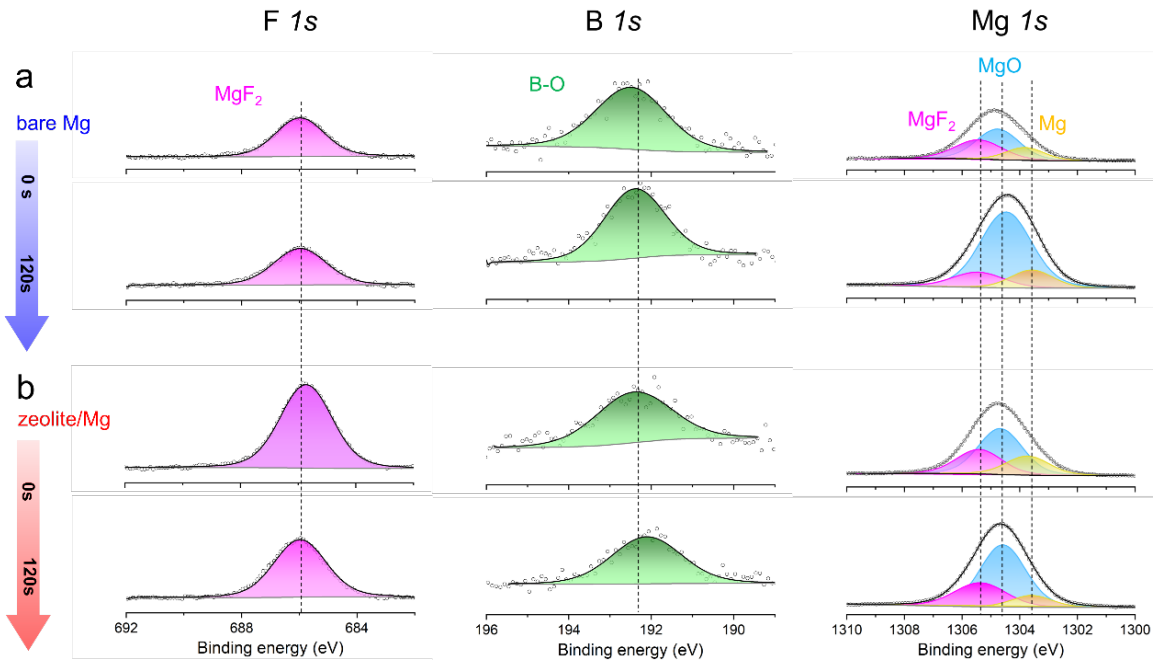

Figure 6.13 XPS F1s, B1s and Mg 1s spectra of deposited Mg metal on **(a)** bare Mg and **(b)** zeolite/Mg.

also confirmed in the F1s and B1s region (**Figure 6.13**). Whereas for zeolite/Mg, the intensity of C-O/C=O peaks related to G2 decomposition significantly decreases in both the C1s and O1s region (**Figure 6.12b**), indicating alleviated side reactions. After sputtering for 120 seconds, the percentage of these species for both bare and protected Mg significantly decreased (**Figure 6.12c**); however, the polymeric/organic fraction for zeolite/Mg is still much less than that of bare Mg. This is further evidence of the effectiveness of the zeolite membrane in protecting Mg from G2 decomposition on plating/stripping.

The proposed mechanism of suppressed G2 decomposition and Mg^{2+} diffusion pathway via the zeolite-3A membrane is shown in **Figure 6.14**. The G2 molecule in the

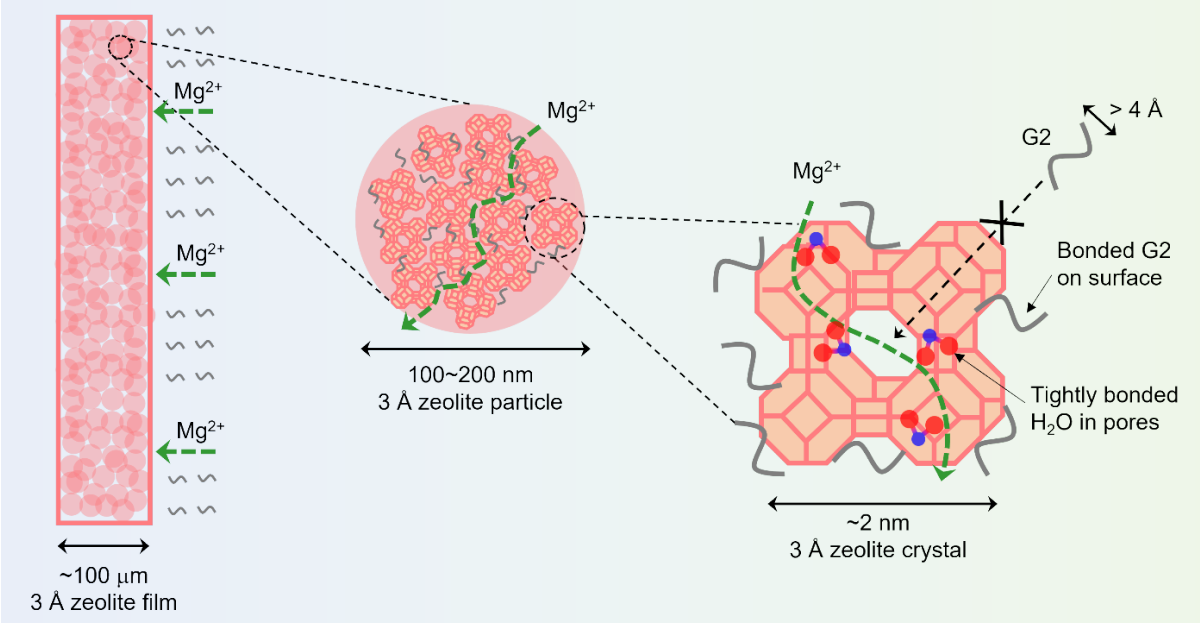

Figure 6.14 Proposed mechanism of suppressed G2 activity and Mg^{2+} diffusion pathway. The decreased free G2 in the zeolite membrane is due to surface adsorption by methoxy groups of G2 on zeolite. Mg^{2+} can diffuse either through surface adsorbed G2 along zeolite surface, or through the pores in the zeolite crystals with the assistance of transport via H_2O molecules which reside within the cages.

electrolyte cannot enter the zeolite through its 3 Å windows due to its large molecular size (> 4 Å diameter of the linear chain), as verified by thermogravimetric analysis (TGA, **Figure 6.15a**). However, glyme has been shown to strongly adsorb on the surface of zeolite crystals by interaction between the methoxy groups of G2 and the oxygen atoms of the zeolite.[157]

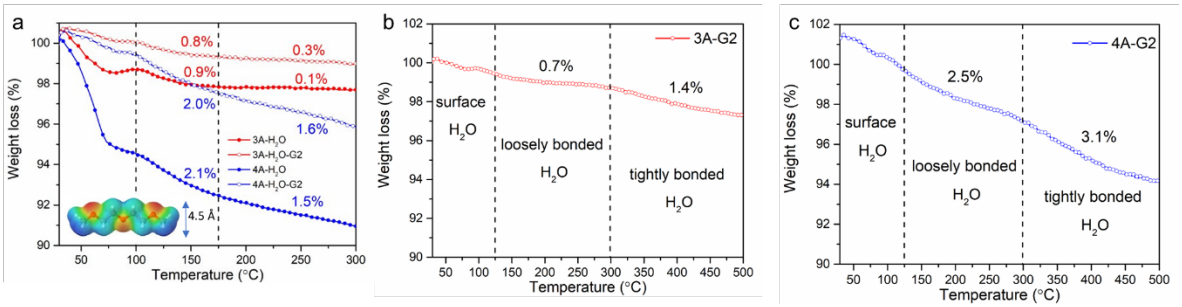

Figure 6.15 (a) TG analysis of zeolites 3A and 4A. Zeolites 3A-H_2O and 4A-H_2O were prepared by soaking zeolite 3A or 4A powder in H_2O overnight, then filtering the suspension and drying it at 60 °C. 3 Zeolites 3A-H_2O-G2 and 4A-H_2O-G2 were prepared by soaking Zeolites 3A-H_2O and 4A-H_2O in G2 overnight, followed by washing by THF three times, and drying the suspension at 60 °C. Before and after soaking in G2, zeolites 3A-H_2O and 4A-H_2O show similar weight loss in both the 100-175 °C region and 175-300 °C region, indicating G2 is not exchanged into either 3A or 4A zeolite. Inset shows the electrostatic surface of G2 calculated by DFT (http://atb.uq.edu.au), indicating a cross-sectional dimension of ~ 4.5 Å. **(b)** TG analysis of zeolite 3A powder after mixing it with G2 overnight. Before the TGA measurement, the sample was washed with THF three times to remove any residual surface solvent and dried in 60 °C overnight**. (c)** TGA analysis of zeolite 4A powder after mixing it with G2 overnight. Before the measurement, the sample was washed with THF three times to remove any residual surface solvent and dried at 60 °C overnight.

Indeed, the existence of little free G2 content in the zeolite 3A membrane was clearly shown by FTIR (**Figure 6.2b**). Such surface binding favorably reduces the decomposition of G2 available at the interface (**Figure 6.12**). Furthermore, strong interaction of G2 with the zeolite surface would promote desolvation of the diglyme coordinated to Mg^{2+}. In turn, this could promote diffusion of Mg^{2+} along the zeolite crystal surface. In addition, significant fractions of Mg^{2+} are readily exchanged with K^+ within the zeolite at room temperature (**Table 6.1**). This suggests the existence of a possible second Mg^{2+} diffusion pathway within the zeolite crystal,[158] which could take place by hopping along H_2O molecules in the cages.[84] Two different Mg^{2+} diffusion pathways were consistent with the solid-state ^{25}Mg MAS NMR results (**Figure 6.2c**), with both G2-solvated and hydrated Mg^{2+} showing significant mobility

Table 6.1 EDX elemental atomic percentage of pristine zeolite 3A powder, ion-exchanged 3A, pristine 4A and ion-exchanged 4A. To prepare ion-exchanged samples, the zeolite powders were immersed in a large excess of 0.25 M $MgCl_2$ aqueous solution at room temperature overnight. After the samples were washed with deionized water and ethanol, the powders were dried at 60 °C in an oven overnight prior to the EDX measurements.

Atomic percentage (%)	Na	Mg	K	Al	Na/Al	Mg/Al	Na/Mg
3 Å	1.86	0.38	0.47	1.67	1.11	0.22	4.89
Ion-exchanged 3 Å	4.29	1.12	0.07	3.71	1.15	0.30	3.83
4 Å	5.05	0.54	0	2.82	1.79	0.19	9.35
Ion-exchanged 4 Å	8.6	2.38	0	8.6	1	0.27	3.61

at room temperature. We note that those tightly bonded H_2O molecules in zeolite 3A can only be removed well above 300 °C (**Figure 6.15b**), and thus are not free to react with the Mg surface. Indeed, using zeolite 4A (where the water in the α cages is more loosely bound, see **Figure 6.15c)** in place of 3A reproducibly results in almost immediate cell failure (**Figure 6.11**). We speculate that here, the H_2O exchanges into the electrolyte to passivate the Mg anode by forming $Mg(OH)_2$/MgO.

6.7 Electrochemistry of Mg||Mo_3S_4 and Mg||PANI Full Cells

The stability of the zeolite/Mg anode was further evaluated in prototype full cells with Chevrel-phase Mo_3S_4 (or Mo_6S_8) as the cathode (**Figure 6.16**), a widely reported material for nonaqueous Mg batteries.[39,159,160] We first measured the cyclic voltammetry (CV) curves of the Mo_3S_4||Mg and Mg_3S_4||zeolite/Mg cells at a scan rate of 0.1 mV s^{-1} (**Figure 6.17a**). Both cells display similar redox behavior characteristic of the Chevrel phase; however, a slightly higher polarization is observed for zeolite/Mg due to the insulating nature of the zeolite

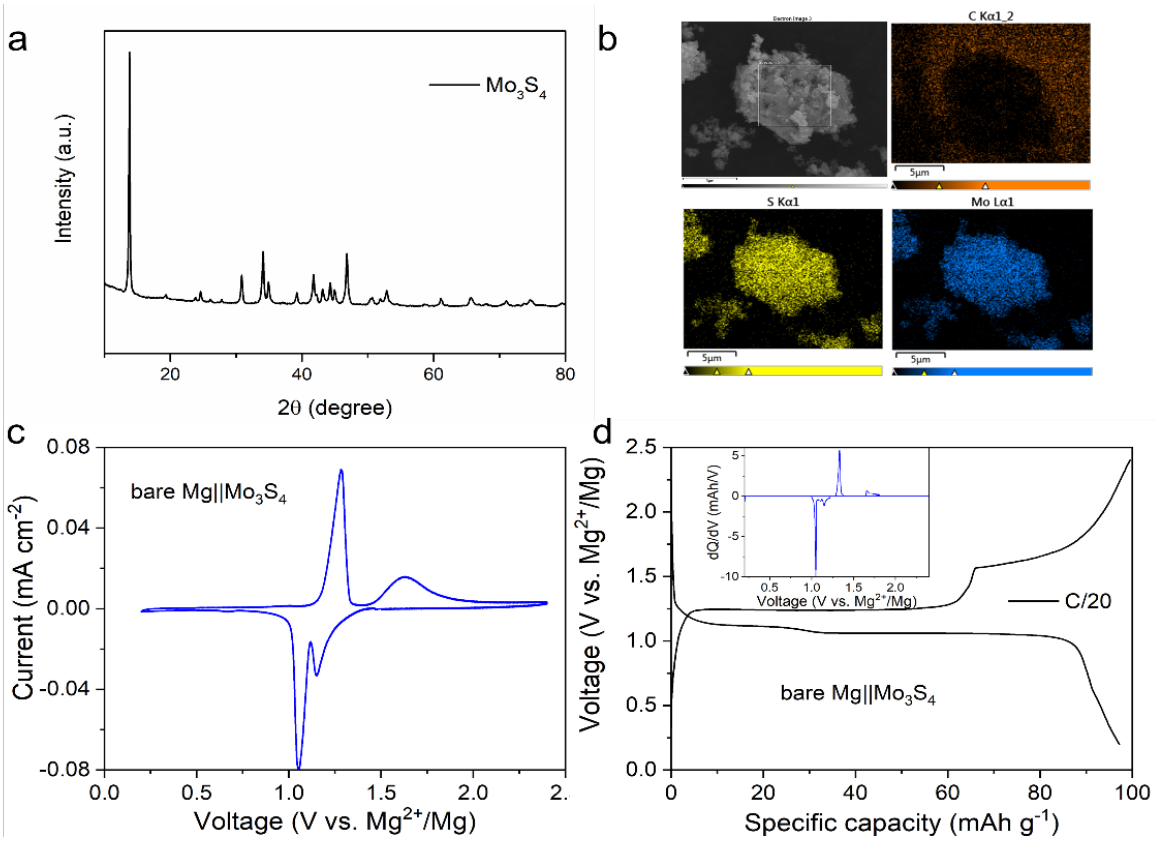

Figure 6.16 (a) XRD and **(b)** EDX mapping of Mo_3S_4 crystallites. **(c)** CV curves at 0.01 mV $s^{-1}$and **(d)** voltage profiles at C/20 of bare Mg||Mo_3S_4 (Inset shows the corresponding dQ/dV curve).

membrane. The Mo_3S_4||zeolite/Mg cell was investigated under galvanostatic control at rates of C/20 (1C = 128 mAh g_{Mo3S4}^{-1}), C/10 and C/5, providing discharge capacities of 96, 88 and 76 mAh g_{Mo3S4}^{-1}, respectively (**Figure 6.17b**). This rate performance is similar to that of a Mo_3S_4||Mg cell (**Figure 6.18**), showing good compatibility between the zeolite membrane and Mg anode under realistic full cell conditions. The long-term cycling stability of these full cells was evaluated at C/5 in the voltage range of 0.2-2.4 V under the same conditions. As shown in **Figure 6.17c**, in contrast to the rapid failure of Mg||Mo_3S_4 after only 16 cycles, the zeolite/Mg||Mo_3S_4 cell shows stable cycling for over 200 cycles with a capacity retention of 91%. It should be noted that Mo_3S_4 functions very well in $MgCl_2$-based electrolytes,[39,60] where the Mg anode can sustain long-term Mg plating/stripping. The observed rapid shorting of the

Mo_3S_4||Mg cell in this study is mainly due to the poor stability of the bare Mg anode in $Mg(B(Ohfip)_4)_2$/G2.

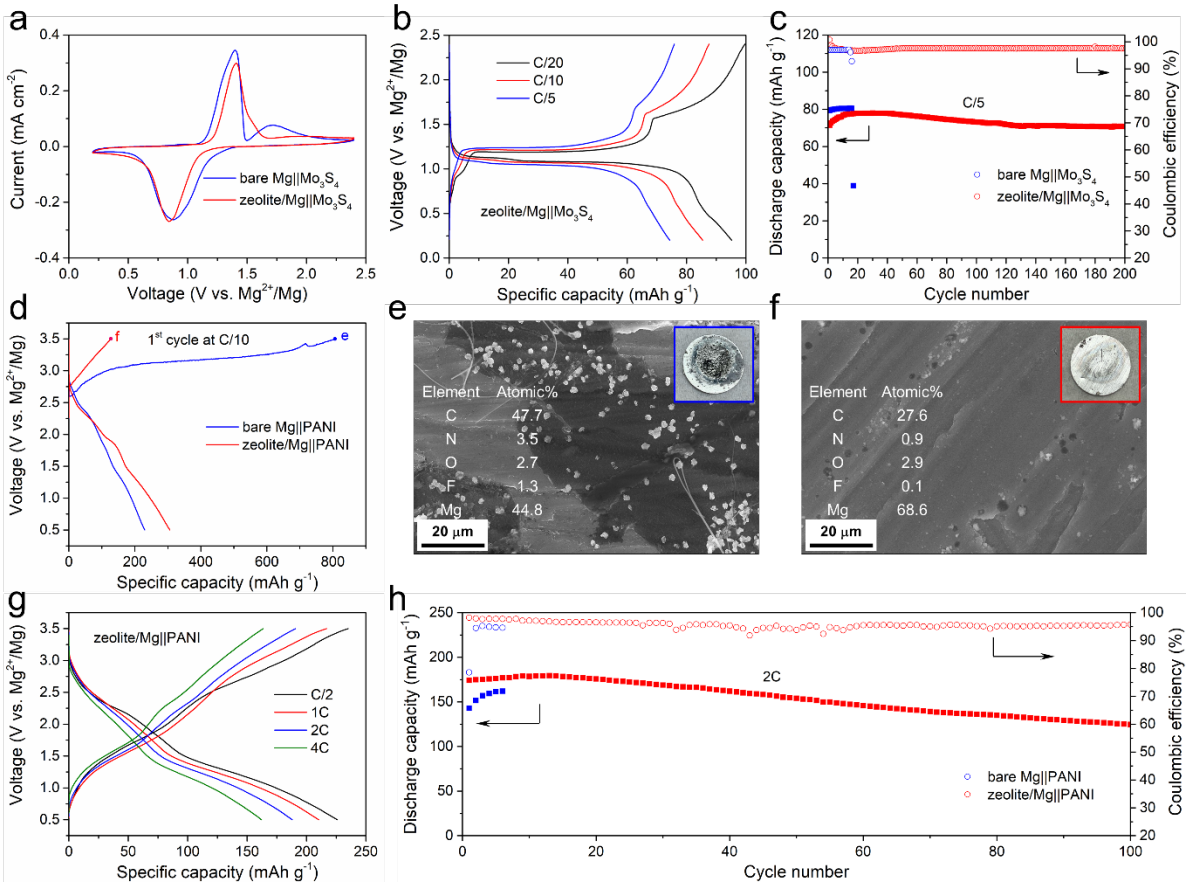

Figure 6.17 Electrochemical performance of full cells**. (a)** CV curves of Mo_3S_4 cathodes with bare Mg and zeolite/Mg at a scan rate of 0.1 mV s^{-1}. **(b)** Voltage profiles of Mo_3S_4|| zeolite/Mg at different rates (1C = 128 mAh g_{Mo3S4}^{-1}). **(c)** Discharge capacity and corresponding coulombic efficiency of a Mo_3S_4 cathode with bare Mg and zeolite/Mg as a function of cycle number at C/5. **(d)** First cycle of PANI||Mg and PANI|| zeolite/Mg at C/10 (1C = 250 mA g_{PANI}^{-1}). **(e** and **f)** SEM images and element ratios measured by EDX of **(e)** bare Mg and **(f)** zeolite-protected Mg that were retrieved from full cells after the initial charge. **(g)** Voltage profiles of PANI|| zeolite/Mg at different rates. **(h)** Discharge capacity and corresponding coulombic efficiency of PANI|| zeolite/Mg and PANI||Mg as a function of cycle number at a 2C rate. Prior to rate and long-term cycling measurements, all Mo_3S_4 and PANI cathodes were activated at C/20 and C/10, respectively.

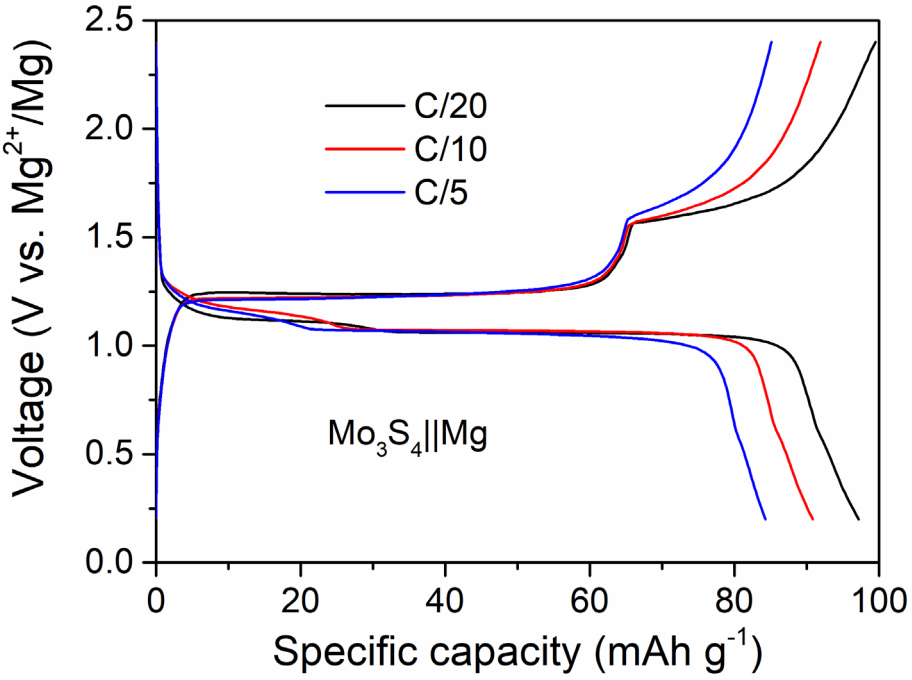

Figure 6.18 First cycle voltage profiles of Mo_3S_4||Mg at rates of C/20, C/10 and C/5 in the voltage range 0.2 - 2.4V.

To evaluate the stability of the zeolite/Mg anode in high-voltage cells, we employed organic polyaniline (PANI) as a platform cathode and measured the electrochemical performance over a voltage range of 0.5-3.5 V. Cells with zeolite/Mg||PANI exhibited a charge capacity of 127 mAh g_{PANI}^{-1} at C/10 (1C = 250 mA g_{PANI}^{-1}; **6.17d**). By reducing fully oxidized PANI to its reduced state at 0.5 V in the subsequent discharge process, a much higher discharge capacity of 305 mAh g_{PANI}^{-1} was obtained due to the association of Mg^{2+} cations with PANI (**Figure 6.19**). In contrast, an unprotected Mg anode PANI||Mg cell shows a very high initial charge capacity of over 806 mAh g_{PANI}^{-1}, with a subsequent discharge capacity of only 230 mAh g_{PANI}^{-1}. The observed overcharge is resulted from the aggravated dissolution/reduction of residual PANI monomers in the electrolyte, which shuttle through the glassfiber separator to the anode side and react with Mg to form a carbon/nitrogen-rich interface (**Figure 6.16e**). Such consumption of monomers on the anode side thus leads to the decreased discharge capacity in the subsequent process. In the presence of the zeolite membrane on the Mg surface (**Figure**

6.17f), the shuttling effect is significantly suppressed, as verified by the much lower fraction of carbon/nitrogen species in the EDX analysis and cleaner Mg surface after the first charge.

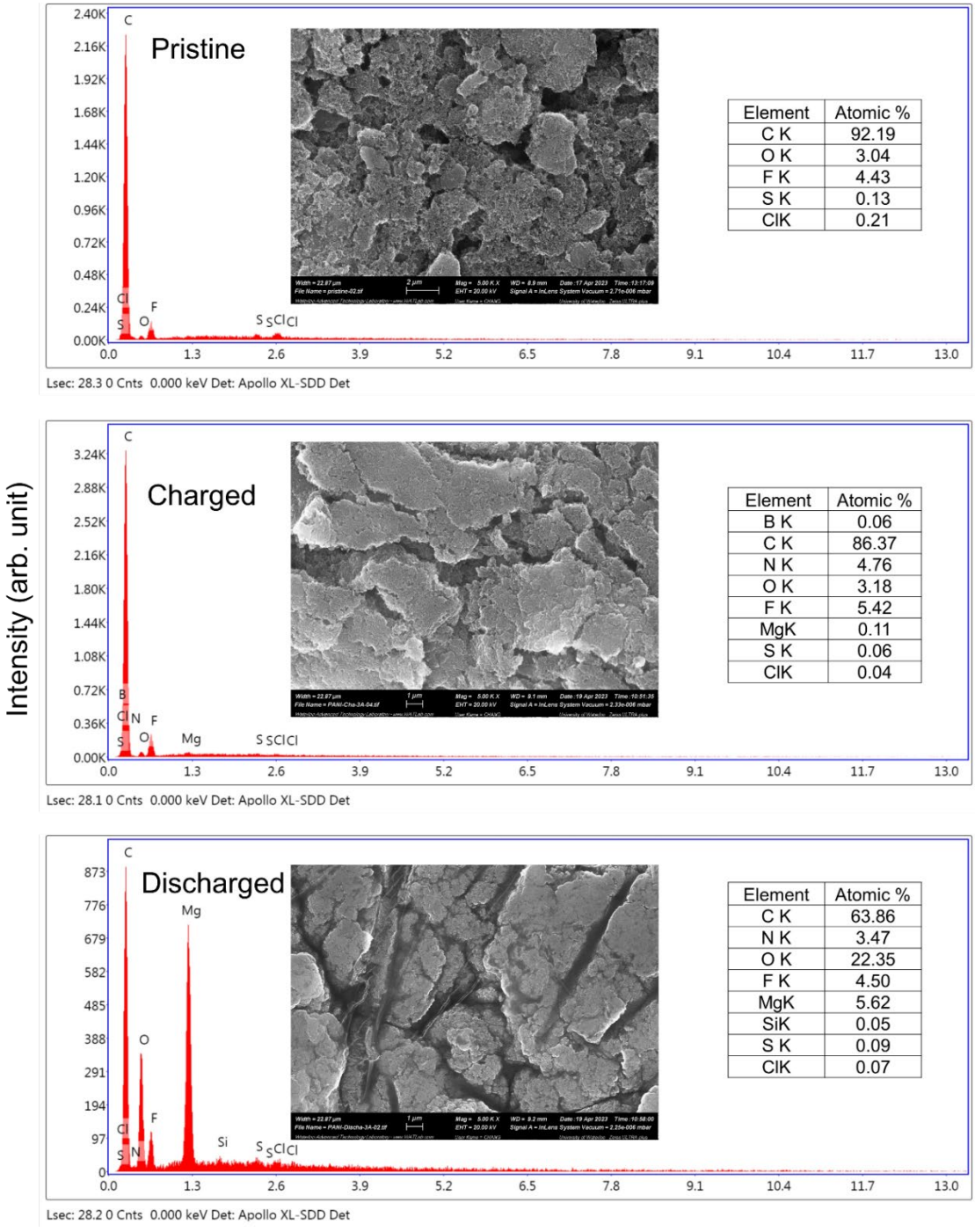

Figure 6.19 EDX of pristine, charged and discharged PANI (with a zeolite/Mg anode) at C/10.

After initial activation at C/10, the zeolite/Mg||PANI cell shows a high discharge capacity of 226 mAh g_{PANI}^{-1} at C/2 with an average discharge voltage of 1.4 V (**Figure 6.17g**). This correlates to a high energy density up to ~ 320 Wh kg_{PANI}^{-1}. In addition, we note that Mg^{2+} cation association/dissociation chemistry dominates the energy storage process (**Figure 6.19**), which is different from previous reported anion storage chemistry in chloride-based[161] and $Mg(TFSI)_2$-based[162] electrolyte. This likely originates from the bulky $B(Ohfip)_4)_2^-$ anion that only weakly associates with PANI, compared to the smaller and electron localized Cl^-/$TFSI^-$ anion. Nonetheless, the cation-type association/dissociation chemistry of organic PANI still obviates the sluggish Mg^{2+} solid-state diffusion exhibited in intercalative-type inorganic cathodes.[44,163] This results in a very good rate capability with a specific capacity of 210, 188 and 162 mAh g_{PANI}^{-1} at 1C, 2C and 4C, respectively, and power density of 1320 W kg_{PANI}^{-1} at a 4C rate. **Figure 6.17h** show the long-term cycling of a PANI||zeolite/Mg full cell at a moderate rate of 2C, demonstrating stable cycling with ~70% capacity retention for over 100 cycles, in contrast to the quick failure of PANI|| Mg due to both aggressive dissolution/shuttling of PANI and instability of bare Mg.

6.8 Conclusions

We report a low-cost zeolite membrane as an effective protective interface for a Mg metal anode, leading to dendrite-free and highly stable Mg plating/stripping in a 0.25 M $Mg(B(Ohfip)_4)_2$/G2 electrolyte with a ultralong lifetime of over 6000 hours (> 8 months). The function of this zeolite membrane is to reduce the free solvent content on the Mg/electrolyte interface, resulting in alleviated solvent decomposition. The superiority of the zeolite membrane-protected Mg anode is verified in full cells - with not only a prototype Mo_3S_4 cathode - but also a high-voltage PANI cathode owing to suppressed shuttling of free monomers. This strategy represents a viable and cost-effective avenue for stabilizing plating/stripping of metal anodes via interface modification, thus paving the way for the development of high-voltage magnesium-metal batteries.

Chapter 7 A Weakly Ion Pairing Electrolyte Designed for High Voltage Magnesium Batteries

7.1 Introduction

Among many aforementioned unaddressed challenges for practical MMBs, designing better electrolytes is one key to their successful commercialization.[37,38,164,165] The charge-dense Mg^{2+} cation results in: 1) a high desolvation penalty due to the slow kinetics of ion pair dissociation;[51] and 2) very slow ion migration kinetics because of a thick SEI on the Mg surface which impedes the interfacial charge transfer process.[60] Therefore, transferring electrolyte design principles from LIBs directly to MMBs is not possible. Utilizing conventional carbonate-based solvents and fluorinated anions such as BF_4^- and PF_6^- usually results in tightly bonded contact ion pairs (CIPs) that aggravate passivation of the Mg anode via pronounced electrolyte decomposition.[60] Classical Mg electrolytes rely on concentrated chloride species to unlock reversible Mg plating/stripping,[39] however, they are oxidatively unstable (~2.5 V vs. Mg^{2+}/Mg) and highly corrosive to current collectors or battery casings. Their dominant intercalation species - $Mg_xCl_y^+$ - also lowers the energy density compared to genuine Mg^{2+} storage.[166,167] The halide-free Mg salts with bulky alkoxyborate/aluminate or carborane anions show high reversibility for Mg plating/stripping with over 99% coulombic efficiency (CE) and oxidative stability over 3.5 V vs. Mg^{2+}/Mg.[56–59] however, are either expensive due to the reagents needed for their complex synthesis and purification procedures, where trace impurities can cause short lifetimes for Mg plating/stripping.[131,168,169] Conventional magnesium bis(trifluoromethanesulfonimide) ($Mg(TFSI)_2$ with high oxidative stability[170,171] (approaching 4 V vs. Mg^{2+}/Mg) contributes to large portions of CIPs that are easily reduced during Mg plating (**Figure 7.1a**).[134,172–174] The resulting inorganic products (for example, MgF_2 amd MgS), together with other solvent-derived polymeric/organic species, lead to a thick impedance layer on the Mg surface that passivates Mg^{2+}/Mg charge transfer. Currently, only a few studies have shown reversible Mg plating/stripping in such electrolytes,[62,63,129] where

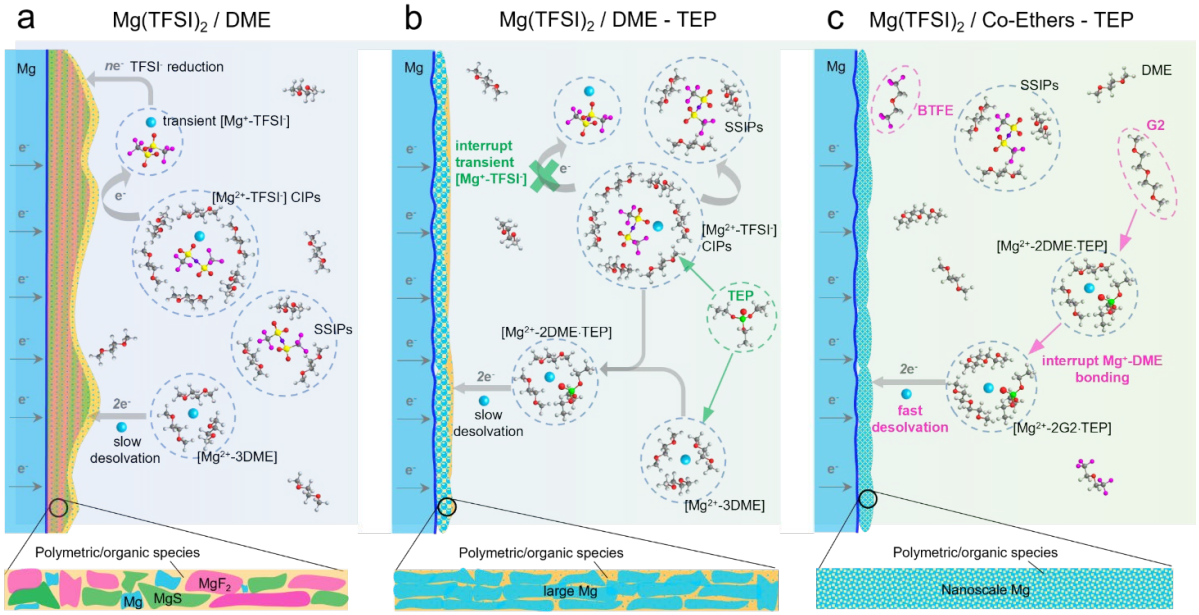

Figure 7.1 Electrolyte design principles. **(a)** In a conventional $Mg(TFSI)_2$/DME electrolyte, the high content of CIPs leads to the formation of transient [Mg^+-$TFSI^-$] clusters which are easily reduced during Mg plating. This results in a thick passivation layer consisting of inorganic MgF_2, MgS and polymeric organic species. The strong Mg^{2+}-DME interaction also induces slow desolvation of Mg^{2+}. **(b)** With the presence of the TEP additive in $Mg(TFSI)_2$/DME electrolyte, the CIPs are significantly interrupted with consequently much less decomposition of the $TFSI^-$ anion. Slow desolvation of the Mg^{2+} solvation sheath is still an issue, nonetheless, leading to large Mg crystal deposits. **(c)** The adoption of co-ethers changes the solvation structure of Mg^{2+}, leading to a more facile desolvation process that allows the formation of dendrite-free, nanoscale Mg nucleation and growth.

deeper understandings towards electrolyte network are needed to design efficient $Mg(TFSI)_2$-based electrolytes.

In this chapter, I designed a new co-ethereal phosphate electrolyte (CEPE) system that enables fast and highly stable Mg^{2+}/Mg redox activity at the anode and facile anion storage chemistry at the cathode using commercial $Mg(TFSI)_2$ as the salt. A family of methyl phosphates ($(CH_3)_3(CH_2)_nPO_4$, n = 0 - 4) with high dielectric constants and donor numbers were selected as electrolyte additives to interrupt [Mg^{2+}-$TFSI^-$] CIPs (**Figure** 7.**1b**). This results in suppressed $TFSI^-$ reduction, which limits the thickness of the passivation layer and

greatly lowers the voltage hysteresis for Mg plating/stripping. To further improve the Mg anode reversibility and stability, different ethers were chosen as co-solvents to tune the Mg^{2+} solvation sheath, thus facilitating desolvation and nanoscale Mg nucleation/growth (**Figure 7.1c**). By combining advanced spectroscopy techniques, molecular dynamics (MD) simulations, and density-functional-theory (DFT) calculations, the Mg^{2+} solvation structure and its interaction with anions or solvents are disclosed in depth. The optimized CEPE electrolytes sustain highly reversible Mg plating/stripping behavior at a range of current densities. We demonstrate ultra-stable Mg plating/stripping for over 7000 hours (9.7 months) at a practical current density of 2 mA cm^{-2} and an areal capacity of 2 mAh cm^{-2}. Importantly, the 4 V anodic stability of these electrolytes enables polyaniline||Mg full cells to run up to 3.5 V for over 400 cycles at a fast 2C rate with excellent capacity retention.

I proposed the idea, planned the experiments, performed all electrochemical measurements and wrote the original manuscript. Dr. Rishabh D. Guha. and Dr. Kristin A. Persson performed molecular dynamics and DFT calculation. Abhinandan Shyamsunder performed NMR measurements.

7.2 Experimental Approaches

7.2.1 Preparation of electrolytes

$Mg(TFSI)_2$ (Solvionic, 99.5%) was dried in a Buchi vacuum oven at 150 °C for over three days. DME (Sigma-Aldrich, 99.5%), G2 (Sigma-Aldrich, 99.5%), DEE (Sigma-Aldrich, 99.5%), BTFE (Synquest Labs), TMP (Sigma-Aldrich, ≥99%), TEP (Sigma-Aldrich, ≥99.8%), TPP (Sigma-Aldrich, 99%), TBP (Sigma-Aldrich, ≥99%) and TAP (Fisher scientific, 98%) were dried by molecular sieves (Sigma-Aldrich, 3Å) for over 24 hours before use. All salts, solvents and additives were stored in an Ar-filled glove box with H_2O and O_2 levels less than 0.1 ppm. As shown in **Table 7.1**, a specific mass of $Mg(TFSI)_2$ was mixed with various solvents at specific volume ratios and stirred at 25 °C for 2 min to fully dissolve the salt. Phosphate additives were added to the above solution and continuously stirred for half an hour to obtain the electrolytes.

Table 7.1 The compositions of different electrolytes. To prepare each electrolyte, 0.5 mmol $Mg(TFSI)_2$ was dissolved in 1 ml ethereal solvent with/out additional 0.1 ml TEP, to yield a total electrolyte volume of ~1.2 ml and a molarity of ~ 0.4 M.

Electrolytes (0.4 M $Mg(TFSI)_2$)	**Solvents**			
	DME (vol%)	G2 (vol%)	BTFE (vol%)	TEP (vol%)
$Mg(TFSI)_2$/DME	100	-	-	-
$Mg(TFSI)_2$/DME:TEP	100	-	-	10
$Mg(TFSI)_2$/CEPE	47.5	47.5	5	10

7.2.2 Electrochemical measurements

Coin cells (2032) were used in this study. Mg foils were polished by sandpaper before being punched into small disks (diameter: 12.7 mm) for cell assembly, and glass fiber separators were used (diameter: 16 mm) with 100 μL electrolyte in each cell. A VMP3 potentiostat/galvanostat station (Bio-Logic) was employed for linear sweep voltammetry (LSV) studies at a sweep rate of 5 mV s^{-1}, using three-electrode PFA-based Swagelok-type cells with Mg as the reference electrode, and Al foil (diameter: 11 mm) as both working and counter electrodes.

To accurately measure the coulombic efficiency, Mg||Au asymmetric cells were assembled and tested based on a previously reported protocol. Specifically, the Au substrates (diameter: 11 mm) were preconditioned for 10 cycles at a current density of 0.5 mA cm^{-2} with plating for 15 min and stripping at a cut-off voltage of 1.5 V. Another 15 min Mg plating cycle was used to establish a reservoir (Q_r), followed by 3 min stripping/plating (Q_c) for 10 cycles (n), and a final complete strip (Q_s) at 1.5 V. The average CE can be calculated as $(nQ_c + Q_s)/(nQ_c + Q_r)$.

For PANI||Mg or PTO||Mg full cells, PANI (Fisher Scientific, emeraldine base) or PTO (Chemscene) was first ball milled with Ketjen black™ carbon at a weight ratio of 4:5 for 100 min at 250 rpm. Then, the PANI electrode was fabricated by mixing the above mixture with polytetrafluoroethylene (Sigma-Aldrich, 60 wt% dispersion in H_2O) at a weight ratio of 9:1

using isopropanol as the dispersion agent. Due to the poor electronic conductivity, the relatively high carbon content is used to fabricate electrodes based on previous studies. The obtained free-standing PANI cathode was dried at 60 °C overnight and punched into small disks (diameter: 8 mm) with an active material loading of around 2.5 mg cm^{-2}. The cathode was pressed on Ti mesh (diameter: 11mm) before being tested in full cells under different C-rates at 25 °C.

The charge transfer resistance of two-electrode Mg||Mg symmetric coin cells in different electrolytes was measured by electrochemical impedance spectroscopy (EIS) with a voltage amplitude of 10 mV in the frequency range of 1 MHz to 100 mHz. The cell was cycled for 10 cycles at 0.1 mA cm^{-2} (0.1 mAh cm^{-2}) and rested for 10 min to reach equilibrium before the EIS measurement. All equivalent circuit fits were performed using the RelaxIS software package V3.

7.2.3 Materials Characterization

Raman spectra were collected using a 532 nm laser (Raman HORIBA HR800). Spectra were obtained using 3-5 accumulations with a total acquisition time ranging from 10-20 minutes under a 10x objective lens. NMR experiments were carried on a Bruker Advance 300 MHz instrument. The scanning electron microscopy (SEM) images of Mg plating/stripping morphologies and energy-dispersive X-ray spectra (EDX) were collected on a Zeiss Ultra field emission SEM instrument. XPS experiments were conducted on a Thermo Scientific K-Alpha XPS instrument. CasaXPS software was used to conduct XPS data analysis, where the C *1s* peak of 284.8 eV was used to calibrate the binding energies. Spectral fitting was based on Gaussian-Lorentzian functions and a Shirley-type background.

TEM sample preparation was performed by the Canadian Centre for Electron Microscopy using a Zeiss Crossbeam 350 FIB-SEM. Due to the suspected sensitivity of the surface material to both the ion and electron beams, the samples were coated with a relatively thick plasma-sputtered chromium coating prior to the FIB-SEM work. This coating protected the surface during the electron beam-induced deposition and subsequent ion beam-induced deposition of the tungsten protection layer. The TEM samples were extracted from the particles

by conventional FIB methods. The thinning necessary for electron transmission was performed under cryogenic conditions at approximately -135°C. The final ion beam probe of the 30 kV thinning was 40 pA. This was followed by a ~7° glancing-angle low voltage cleaning step applied to both sides with a 2 kV 50 pA ion beam. The resulting TEM sample was loaded into a Spectra Ultra 30-300kV TEM (Thermo Fisher Scientific) equipped with a Cs probe and image aberration correctors that was operated at 200 kV. An attached Ultra-X EDS detector was used to map Mg interface and collect EELS data. The EDS Maps were post-processed using Velox Software. All electrodes disassembled from the cells were washed three times with DME and dried at room temperature *in vacuo* overnight before each study.

7.3 Highly reversible and stable Mg plating/stripping in CEPE

We considered three electrolytes to evaluate their Mg plating/stripping behavior: a) 0.4 M $Mg(TFSI)_2$/DME as the baseline conventional electrolyte; b) 0.4 M $Mg(TFSI)_2$/DME: triethyl phosphate (TEP) [10:1 in vol, denoted as $Mg(TFSI)_2$/DME:TEP]; and c) tailor-designed $Mg(TFSI)_2$/CEPE [0.4 M $Mg(TFSI)_2$/DME: diethylene glycol dimethyl ether (G2): bis(2,2,2-trifluoroethyl) ether (BTFE): TEP, 19:19:2:4 in vol]. Instead of alkoxyborate/aluminate or carborane-based Mg salts, commercially available $Mg(TFSI)_2$ was chosen as the target salt, both on the basis of cost and owing to its strong ion pairing in ether-type electrolytes which we sought to disrupt with electrolyte design. TEP was chosen as a stronger coordinating solvent than glyme, while BTFE is a non-coordinating solvent. These choices of salt and solvents give us a good platform to understand the effect of cation/anion-solvent interaction on interfacial charge transfer in Mg plating/stripping. **Figure 7.2a, b** shows the voltage profiles of these electrolytes in Mg||Mg symmetric cells at a current density of 0.1 mA cm^{-2}. In $Mg(TFSI)_2$/CEPE, a very low Mg plating/stripping overpotential of ~ 0.15 V was obtained - nearly two-fold lower than in $Mg(TFSI)_2$/DME:TEP (~ 0.3 V) - whereas in $Mg(TFSI)_2$/DME more than a magnitude higher overpotential of ~ 1.85 V was observed. The

superiority of $Mg(TFSI)_2$/CEPE was further confirmed by the fast-kinetics of Mg plating/stripping at different current densities (**Figure 7.2c** and **7.3**), which reveals a low Mg

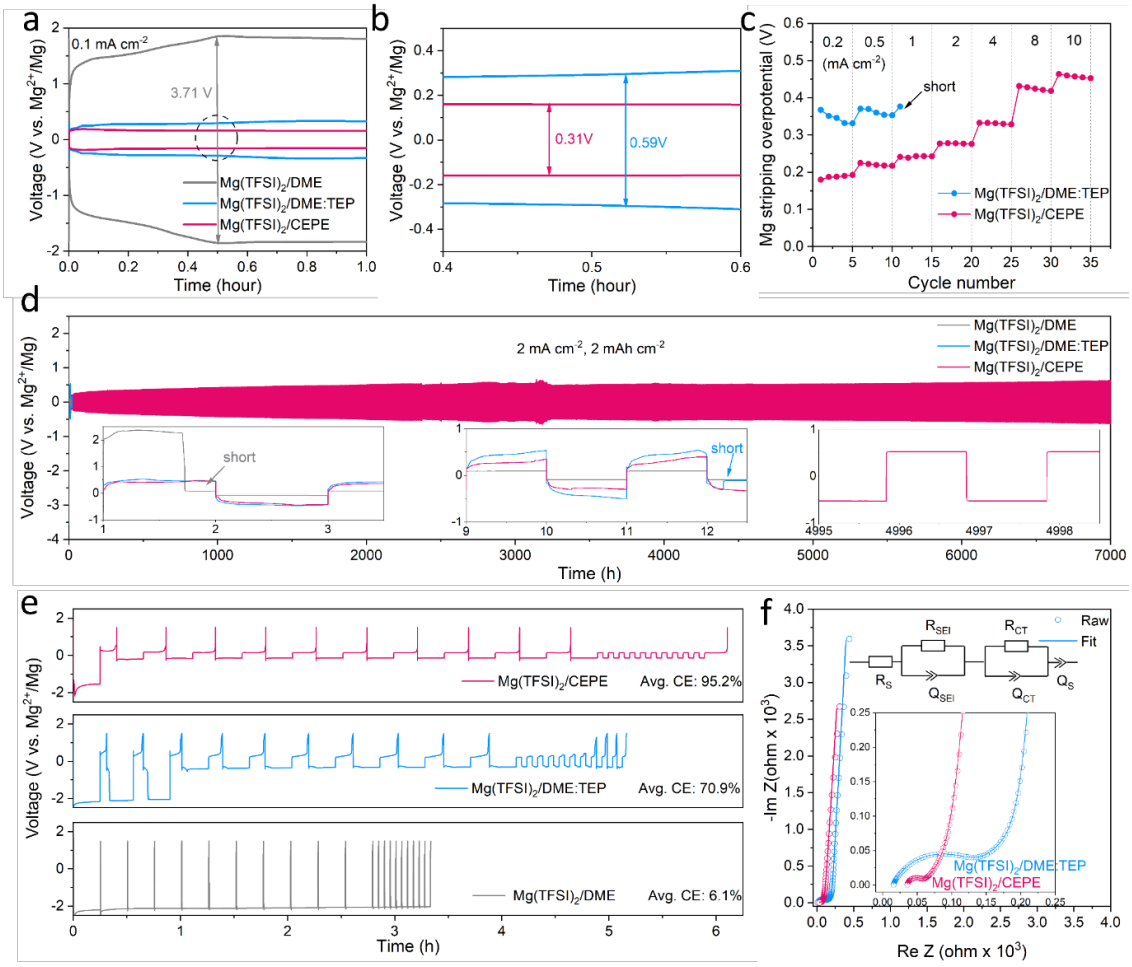

Figure 7.2 (**a, b**) The 10th voltage profiles of Mg||Mg symmetric cells with different electrolytes at a current density of 0.1 mA cm^{-2} for 1.0 h, with **(b)** the magnified views of circled regions. (**c**) Rate performance of Mg||Mg symmetric cells. The areal capacity was fixed at 0.1 mAh cm^{-2}, and the stripping overpotential at the central point was collected. (**d**) Long-term stability of Mg plating/stripping in different electrolytes at 2 mA cm^{-2} (2 mAh cm^{-2}). The rectangular profile with an overpotential of 0.5 V in the symmetric cell at ultra-long cycling times is characteristic of a low energy for nucleation of Mg on Mg metal that is not fully stripped on the previous cycle and after thousands of hours, accumulates. **(e)** Voltage profiles of Mg||Au asymmetric cells with different electrolytes at 0.5 mA cm^{-2}. (**f**) Nyquist plots of the Mg||Mg symmetric cell after 10 cycles in TEP-based electrolytes. The data were fit (shown by line) with the indicated equivalent circuit.

plating/stripping overpotential of < 0.5 V even at a high current density of 10 mA cm^{-2}. In contrast, the cell with $Mg(TFSI)_2$/DME:TEP quickly shorted at 1 m A cm^{-2} (**Figure 7.2c**) and $Mg(TFSI)_2$/DME shows a continuously high overpotential up to ~ 3.5 V (**Figure 7.4**).

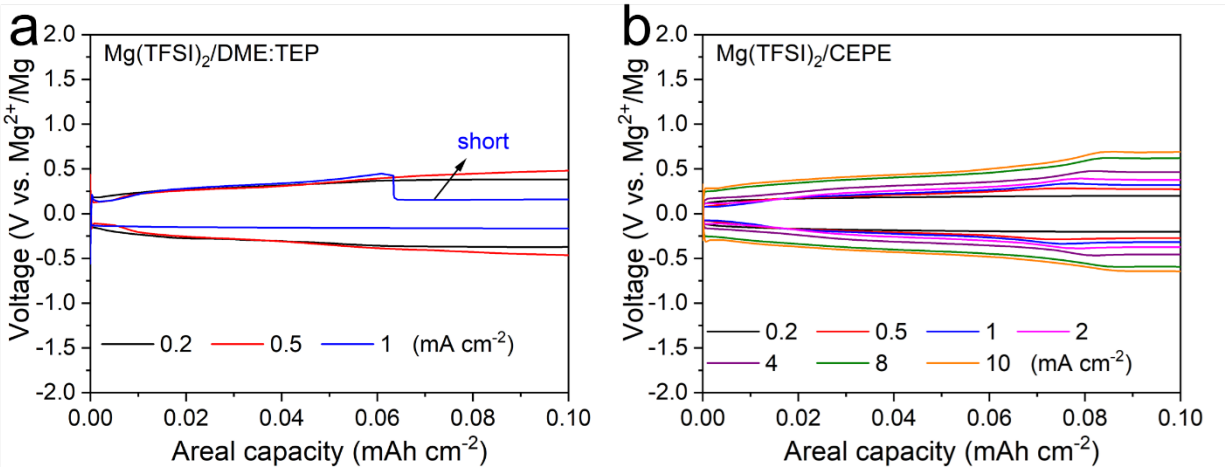

Figure 7.4 Selected voltage profiles of TEP-based electrolytes at different current densities in Mg symmetric cells: **(a)** $Mg(TFSI)_2$/DME:TEP; **(b)** $Mg(TFSI)_2$/CEPE.

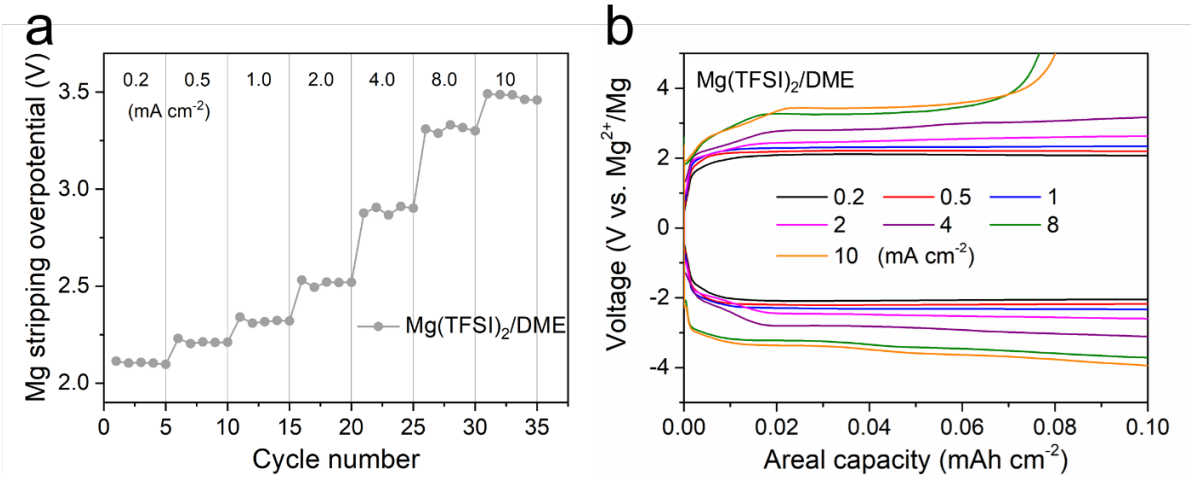

Figure 7.3 The rate performance of $Mg(TFSI)_2$/DME in Mg symmetric cells. **(a)** Mg stripping overpotentials at different current densities; **(b)** selected voltage profiles at 0.2-10 mA cm^{-2} with a fixed areal capacity of 0.1 mAh cm^{-2}.

While we observe improved Mg reversibility with TEP, the stability of the Mg anode during long-term cycling is of even greater importance.[60,62,63,129] We investigated Mg||Mg symmetric cell behaviour in different electrolytes. At a practical current density of 2 mA cm^{-2} and areal capacity of 2 mAh cm^{-2} (**Figure 7.2d**), $Mg(TFSI)_2$/DME and $Mg(TFSI)_2$/DME:TEP undergo rapid short circuiting of cells after only 2 and 12 hours, respectively. In contrast, cells employing $Mg(TFSI)_2$/CEPE undergo robust stripping/plating for over 7000 hours (9.7 months) without significant increase in voltage hysteresis, and exhibit a total cumulative capacity of over 10 Ah/cm^{-2}. The overpotential of Mg plating/stripping stabilizes at around 500 mV with no significant sudden voltage drops, ruling out the possibility of (soft) short circuits, as also confirmed by a charge transfer resistance of about 400 Ω attained after 7000 hours

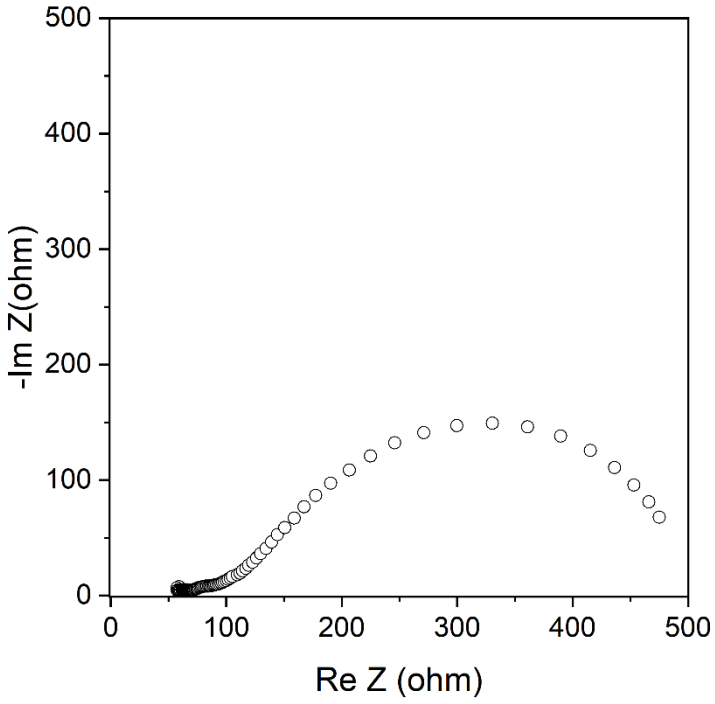

Figure 7.5 Nyquist plot of a Mg||Mg symmetric cell in $Mg(TFSI)_2$/CEPE after 7000 hours at 2 mA cm^{-2} and 2 mAh cm^{-2}. The measurement was conducted immediately after cycling to prevent the potential overlook for any soft short, because resting the cell may cause the soft short can not be discovered as demonstrated in previous work.[72] The exhibited charge transfer resistance of around 400 Ω confirms the absence of any (soft) short.

(**Figure 7.5**). To the best of our knowledge, this represents unprecedented stability and performance of Mg plating/stripping under such demanding conditions, suggesting good promise for long-life practical MMBs. The coulombic efficiency (CE) of Mg plating/stripping was investigated using Mg||Au asymmetric cells by a modified Aurbach method reported by Zhang *et al.*[156] The highest CE of 95.2% was achieved in $Mg(TFSI)_2$/CEPE (**Figure 7.2e**), which is significantly greater that of $Mg(TFSI)_2$/DME:TEP (70.9%). The baseline $Mg(TFSI)_2$/DME electrolyte, in contrast, shows very limited Mg plating/stripping reversibility with only 6.1% CE due to pronounced electrolyte decomposition. While the increase in CE in moving from DME/TEP to CEPE is remarkable, the latter value is not quite as high as achieved in bulky-anion salt alkoxyborate/aluminate or carborane-based electrolytes. This is probably due to the persistence of a low fraction of [Mg^{2+}-$TFSI^-$] contact-ion pairs (despite the major

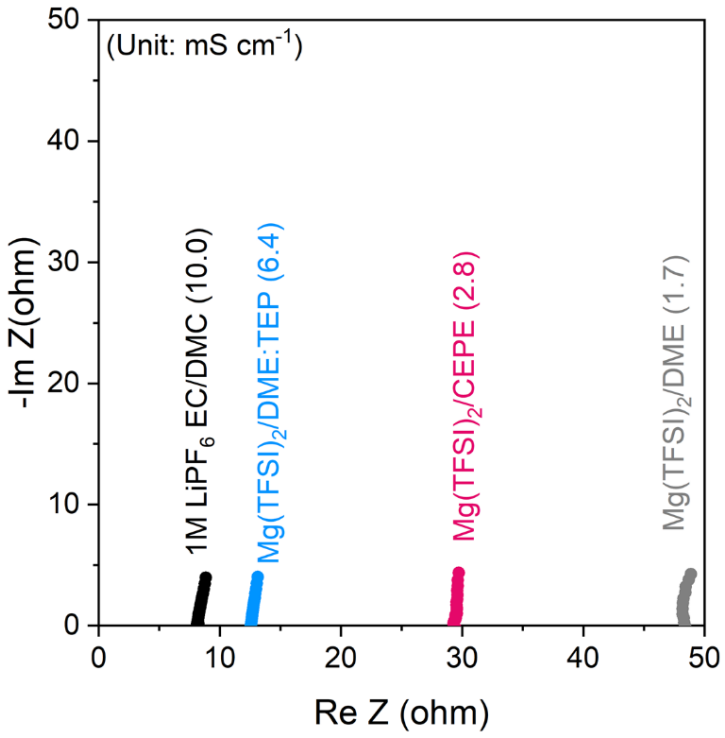

Figure 7.6 The ionic conductivity of different electrolytes measured in Pt||Pt symmetric cells using 1 M $LiPF_6$ in EC/DMC (10 mS cm^{-1}) as the reference electrolyte.

disruption of their formation, see discussion below), which are more easily reduced on the Mg surface.

The charge transfer process at the Mg/electrolyte interface was further explored by electrochemical impedance spectroscopy (EIS) studies (**Figure 7.2f**). In $Mg(TFSI)_2$/CEPE, a

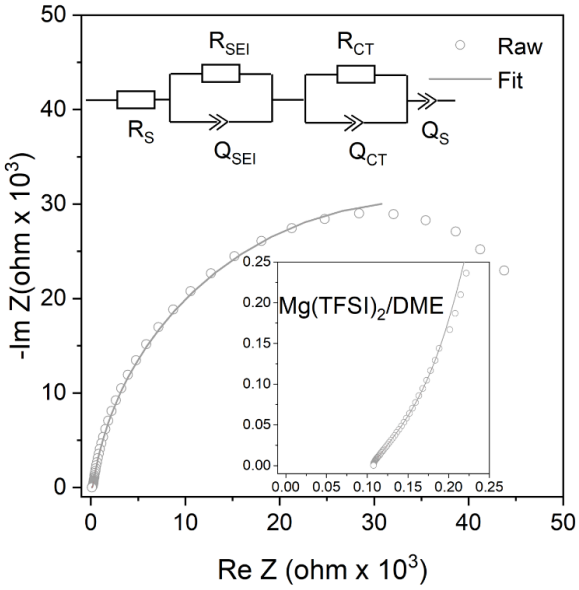

Figure 7.7 Nyquist plots of a Mg||Mg symmetric cell after 10 cycles in $Mg(TFSI)_2$/DME. The data were fit (shown by line) with the indicated equivalent circuit.

very low charge transfer resistance (R_{CT}) was observed in a Mg||Mg symmetric cell, consistent with its superior rate performance. On the other hand, $Mg(TFSI)_2$/DME:TEP, despite exhibiting the highest ionic conductivities of 6.4 mS cm^{-1} among three electrolytes (**Figure 7.6**), shows significantly higher R_{CT} than $Mg(TFSI)_2$/CEPE. This suggests interfacial electrochemistry plays a dominant role during Mg plating/stripping. Indeed, diffusion-limited tails ascribed to ion diffusion via as-formed interfacial Mg^{2+}-conducting SEIs[175] were observed in the low-frequency region in both electrolytes. In $Mg(TFSI)_2$/DME, however, the very large charge transfer resistance is similar to that of many previous reports (**Figure 7.7**).[129,130] This is

due to electrolyte decomposition on the Mg surface that forms an interfacial (Mg^{2+}-insulating) passivation layer, which leads to the absence of a diffusion-limited tail.

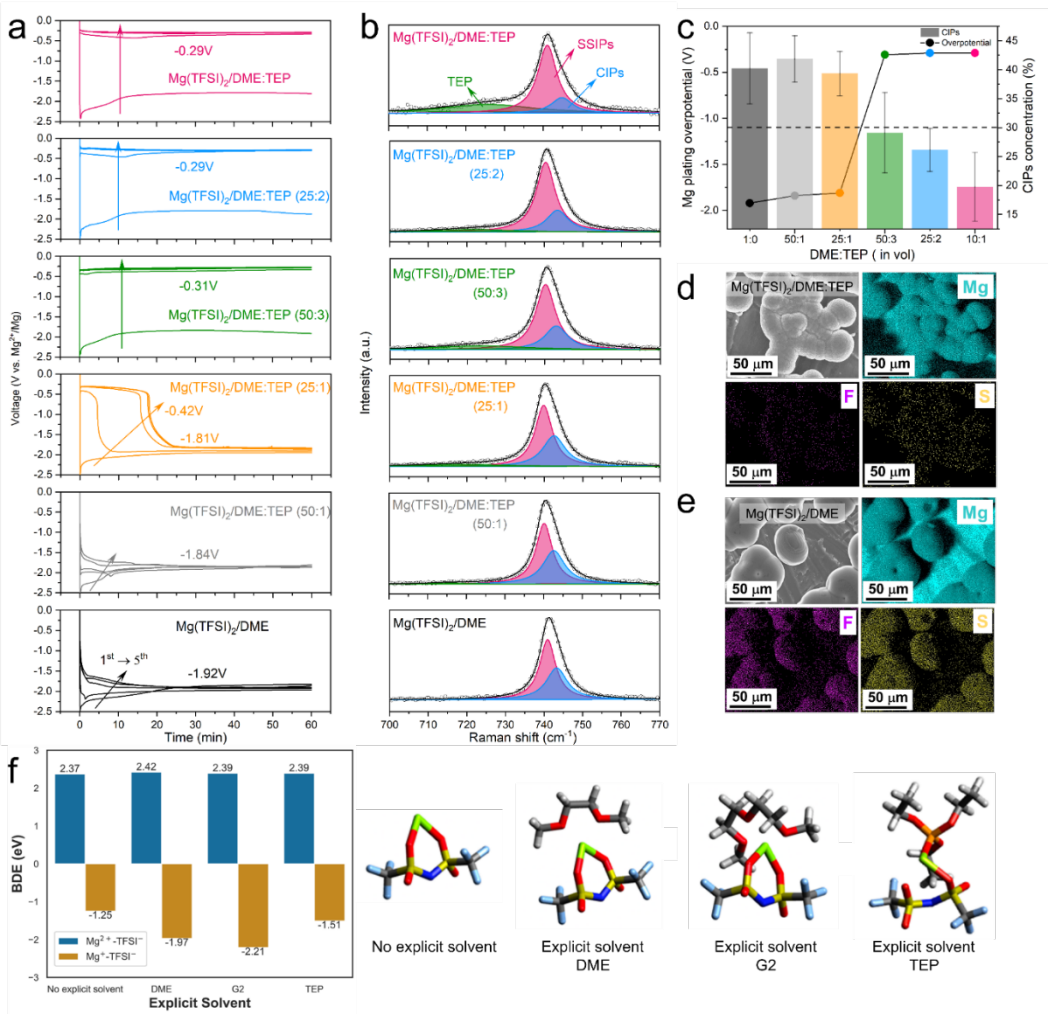

Figure 7.8 (a, b) The initial five plating profiles of $Mg(TFSI)_2$/DME in Mg||Mg symmetric cells with different DME:TEP ratios at a current density of 0.1 mA cm^{-2} **(b)** corresponding Raman spectra of different electrolytes in the 700-770 cm^{-1} range (the overall fit (black) has three components: TEP-green, SSIPs-pink and CIPs-blue). All fits were based on a Lorentzian peak function with coefficient of determination $R^2 > 0.997$**. (c)** The Mg plating overpotential and the ratio of CIP content as a function of DME:TEP ratio. **(d, e)** SEM images and EDX mappings of plated Mg in **(d)** $Mg(TFSI)_2$/DME:TEP and (e) $Mg(TFSI)_2$/DME. **(f)** DFT calculations of C-S bond dissociation energies of [Mg^{2+}-$TFSI^-$] and transient [Mg^+-$TFSI^-$] CIPs in different coordinating environments with the explicit solvent coordinated structure shown on the right.

7.4 Minimized anion activity by phosphates

The role of TEP in CEPE was systematically explored by controlling the DME:TEP ratio, which is directly correlated to Mg^{2+}/Mg redox activity. **Figure 7.8a** shows the Mg plating curves of the initial five cycles of Mg||Mg symmetric cells with different DME:TEP ratios. The Mg plating overpotential shows a TEP concentration-dependent behavior, identifying a DME:TEP ratio of 50:3 as an effective "sweet" spot to unlock fast Mg plating/stripping. This is directly correlated to the CIP fraction in the electrolytes, as revealed by fitting Raman spectra of the $TFSI^-$ band in the 700-770 cm^{-1} region based on a well-established theory of SSIPs and CIPs (**Figure 7.8b**).[129,147] An abrupt decrease in CIP fraction from 40% to < 30% is observed in DME:TEP (50:3), matching the sharp drop in plating overpotential to -0.32 V (**Figure 7.8c**). This indicates a threshold in CIP fraction where facile Mg^{2+}/Mg redox activity is unlocked below that limit, and Mg^{2+} desolvation from coordinated solvents at the interface starts to play a critical role (see below). Indeed, previous studies report that significant reduction of CIPs at the Mg surface suppresses $TFSI^-$ activity.[172] This is verified by the remarkable decrease of F/S signals from decomposed $TFSI^-$ in the energy-dispersive X-ray spectra (EDX, **Figure 7.8d**) of $Mg(TFSI)_2$/DME:TEP, in contrast to the strong F/S signals in $Mg(TFSI)_2$/DME (**Figure 7.8e**).

To reveal the functionality of TEP in suppressing anion reduction activity, density-functional-theory (DFT) calculations were performed. In an implicit solvent, thermodynamically endergonic C-S bond dissociation was observed in the [Mg^{2+}-$TFSI^-$] CIPs (bond dissociation energy (BDE): 2.37 eV, **Figure 7.8f**), whereas partially reduced transient [Mg^+-$TFSI^-$] CIPs show exergonic C-S bond dissociation (BDE: -1.25 eV), consistent with previous studies.[172] The C-S bond dissociation accompanies complete reduction of Mg^+ to Mg^0 (**Figure 7.9**) and essentially enables an irreversible plating process. More exergonic C-S bond cleavage was obtained for [Mg^+-$TFSI^-$] CIPs surrounded by one explicit DME (BDE: -1.97 eV) or G2 molecule (BDE: -2.21 eV), emphasizing the co-solvation during charge transfer does not protect the $TFSI^-$ anions from reduction. The BDE is also exergonic (-1.51 eV) for a transient CIP surrounded by an explicit TEP molecule. In the molecular dynamics (MD) results (see below), the paired Mg fraction decreases by ~50% in the CEPE system when compared to the $Mg(TFSI)_2$:DME system. These results, in conjunction with the Raman spectra (**Figure**

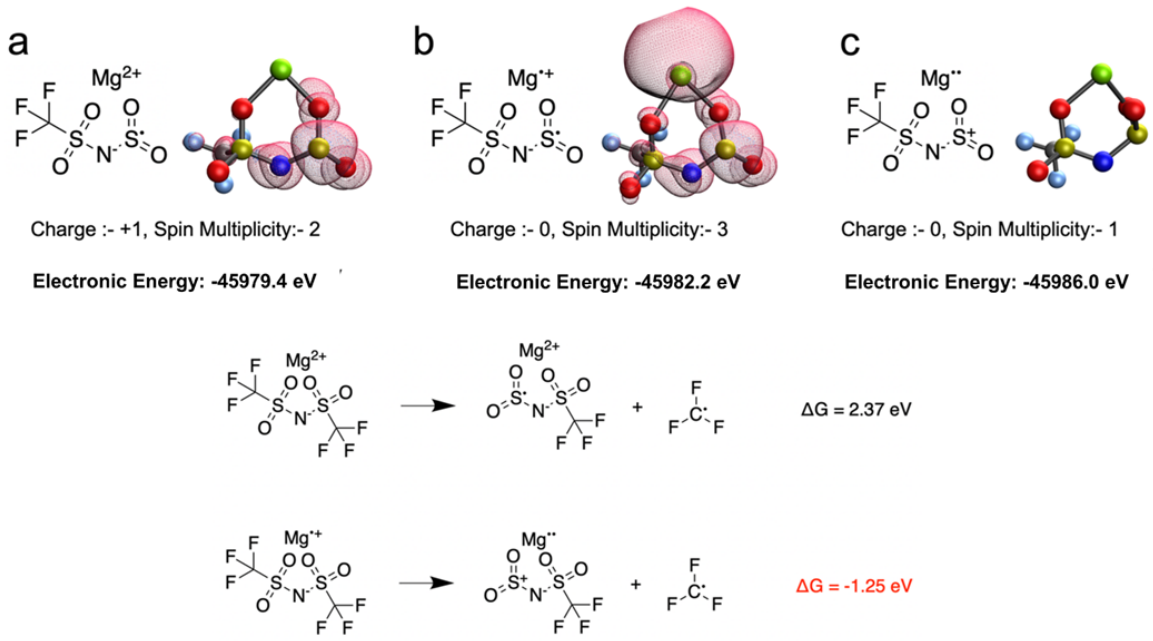

Figure 7.9 Unpaired electron spin densities and electronic energies for potential products after dissociation of partially reduced CIP. **(a)** radical with 1 unpaired electron; **(b)** radical with 2 unpaired electrons; **(c)** radical with 0 unpaired electrons. The lowest energy radical **(c)** is assumed to be the dissociation product for the BDE calculations of the partially reduced CIP.

7.8b), confirm that the introduction of TEP successfully outcompetes the $TFSI^-$ anions in the first solvation shell and significantly reduces the CIP concentration. Nonetheless, it is not reduced to zero. While the residual CIPs in CEPE could still induce limited anion decomposition, this may be further inhibited by applying interfacial protective coatings on the Mg surface, or by additional electrolyte design that is beyond the scope of this work.

Similar effects on activating reversible Mg^{2+}/Mg redox in single DME solvent extends to other phosphates with a formula of $(CH_3)_3(CH_2)_nPO_4$ (n=0 - 4, **Figure 7.10**). The co-ether engineering approach functions similarly (for example, TMP with n = 0), albeit with poorer rate characteristics relative to TEP (**Figure 7.11**). Nonetheless, these phosphates with different numbers of methylene groups can behave very differently. Previous reports indicate TMP primarily displaces one DME from the Mg^{2+} solvation structure to suppress DME reduction by forming TMP-reduced SEIs,[63,129] however, significant $TFSI^-$ decomposition still occurs

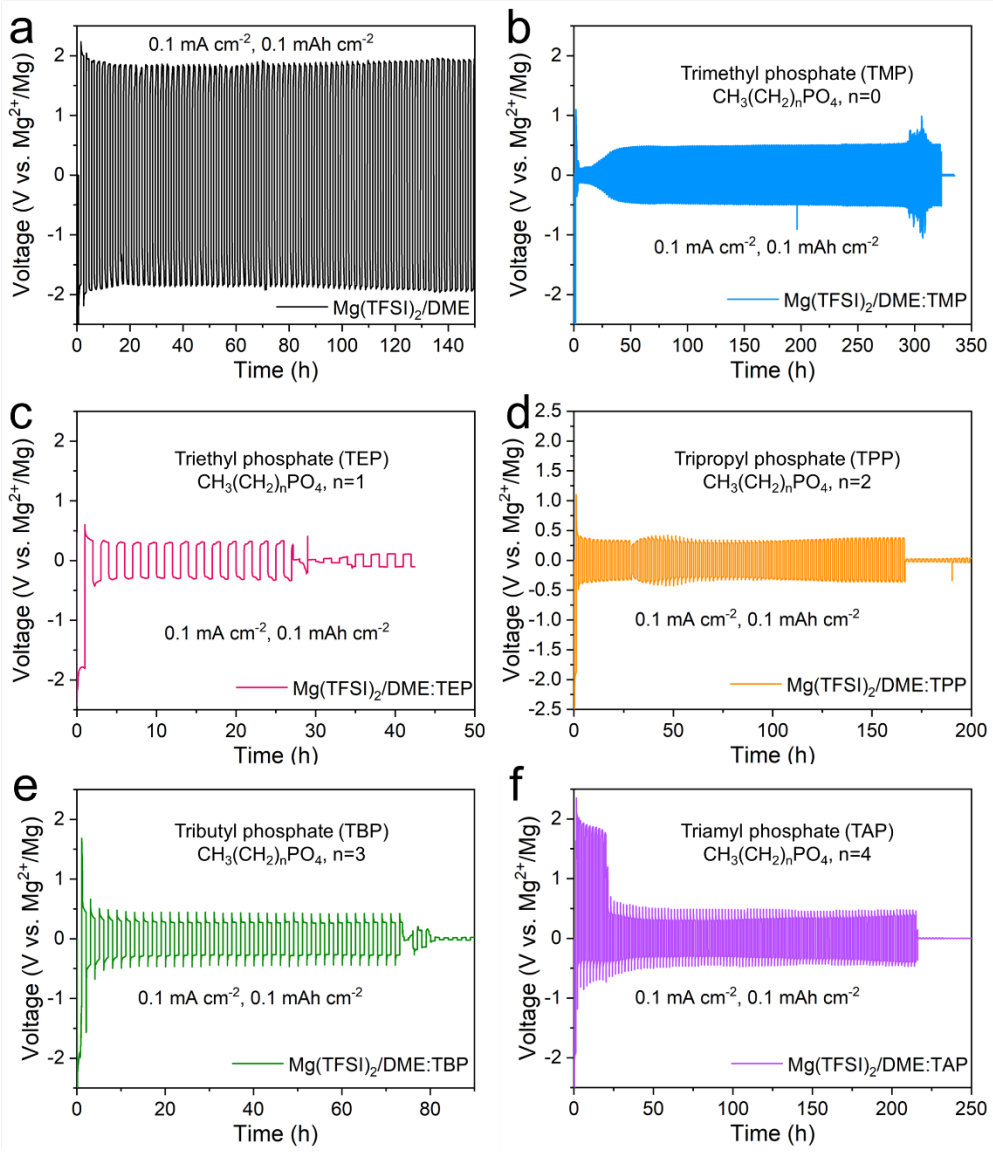

Figure 7.10 Galvanostatic cycling of Mg symmetric cells with different phosphates. **(a)** $Mg(TFSI)_2$/DME; **(b)** $Mg(TFSI)_2$/DME:TMP; **(c)** $Mg(TFSI)_2$/DME:TEP; **(d)** $Mg(TFSI)_2$/DME:TPP; **(e)** $Mg(TFSI)_2$/DME:TBP; **(f)** $Mg(TFSI)_2$/DME:TAP. The current density is 0.1 mA cm^{-2} with an areal capacity of 0.1 mAh cm^{-2}. The DME: phosphate ratio is 10:1 in all cases.

during Mg plating/stripping. The greater steric effect created by methylene groups in TEP may play a pivotal role in controlling interfacial activity of both $TFSI^-$ anion and these phosphates.

This directly relates to the electrochemical stability of the electrolytes (see the discussion below). More importantly, adding these phosphates to a single ether solvent (DME) delivers poor Mg anode stability even at a low current density of 0.1 mA cm^{-2} and areal capacity of 0.1 mAh cm^{-2} (**Figure 7.10**), which is inadequate for practically fast-charging Mg batteries. The optimized CEPE in this study represents a universal strategy to achieve benchmark-level Mg plating/stripping performance that applies to different phosphates (**Figure 7.11**). We further reveal the critical role of co-ethers in $Mg(TFSI)_2$/CEPE to modify the Mg^{2+} solvation structure and plating/stripping morphology below.

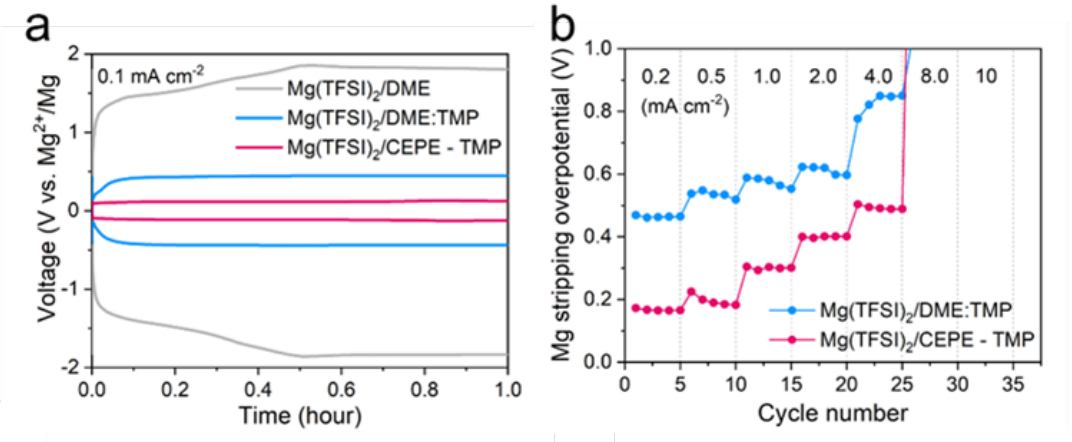

Figure 7.11 Electrochemical performance of Mg plating/stripping in TMP-based electrolytes. **(a)** The 20th voltage profiles of Mg||Mg symmetric cells with different electrolytes at a current density of 0.1 mA cm^{-2} for 1 h. **(b)** Rate performance of Mg||Mg symmetric cells.

7.5 Optimized solvation structures of Mg^{2+}

We carried out nuclear magnetic resonance (NMR) spectroscopy to understand the solvation structure of the electrolytes in these CEPE systems. **Figure 7.12a** displays the ^{13}C NMR spectra of various electrolytes at 298 K. In both $Mg(TFSI)_2$/CEPE and $Mg(TFSI)_2$/DME:TEP, the Mg^{2+}- TEP interaction leads to high frequency shifts of the -CH_2- groups in TEP by ~ 3.7 and ~ 3.4 ppm, respectively. This interaction is much stronger than that of Mg^{2+}-DME in $Mg(TFSI)_2$/DME that provokes only a 0.5 ppm *low* frequency shift of the DME -CH_2- group. This strong Mg^{2+}-TEP interaction results in a large decrease of the full

width at half maximum (FWHM) of DME (-CH_2- signal) by around 60%, a clear indication of

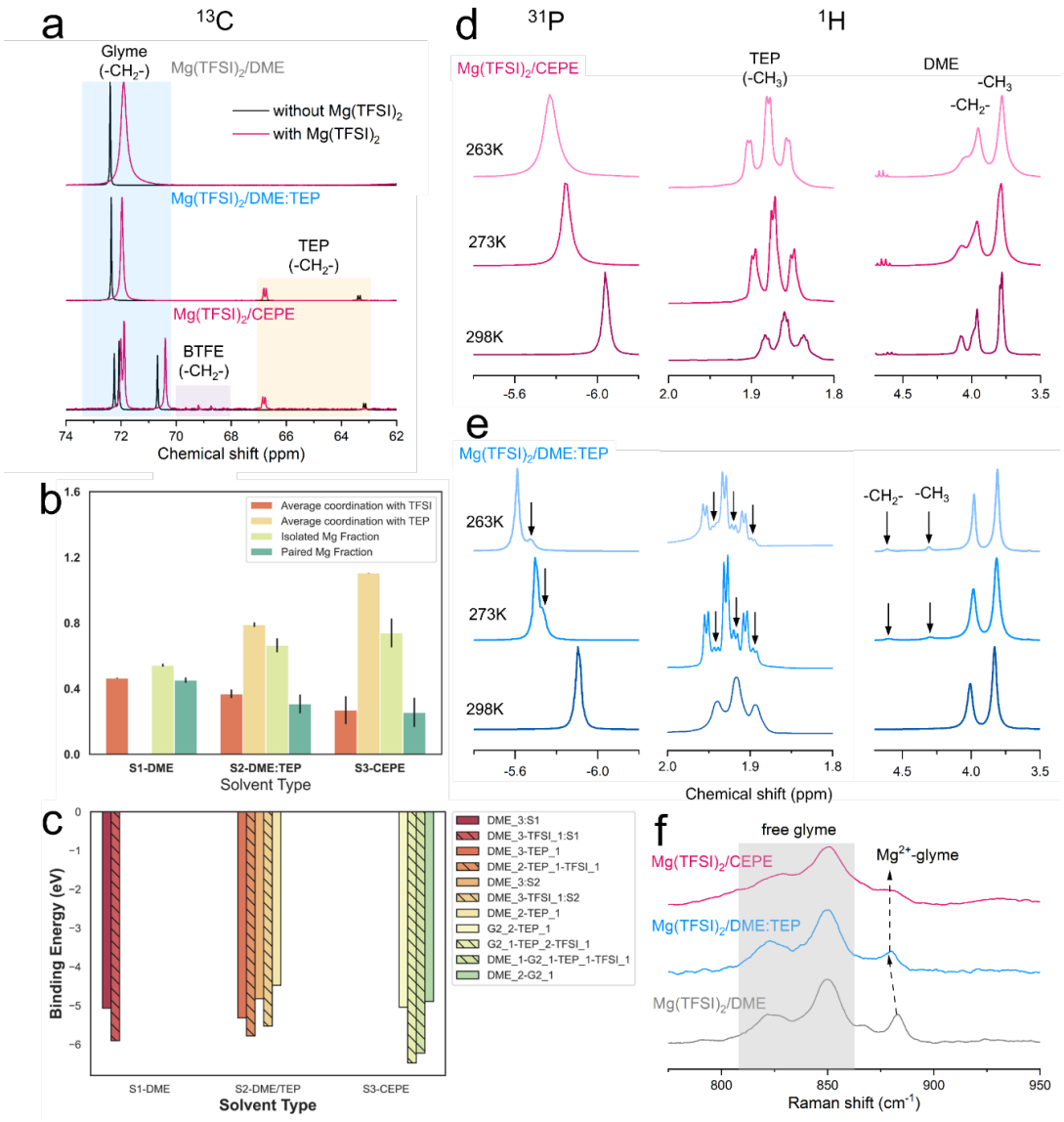

Figure 7.12 (a) ^{13}C NMR spectra of different electrolytes with/out $Mg(TFSI)_2$ at 298 K. **(b)** MD simulations of Mg^{2+} coordination environments in different electrolytes. The y-axis indicates either the average coordination numbers or the fraction of Mg^{2+} clusters. **(c)** DFT calculations of binding energies of predominant Mg^{2+} solvation shells. **(d, e)** Variable temperature ^{31}P and ^{1}H NMR spectra in **(d)** $Mg(TFSI)_2$/CEPE and **(e)** $Mg(TFSI)_2$/DME:TEP. Smaller peaks that were observed at lower temperature are indicated by black arrows. **(f)** Raman spectra of various electrolytes in regions of 775-950 cm^{-1}.

much lesser CIP fraction. This is in perfect accord with Raman analysis (**Figure 7.13**). A similar Mg^{2+}-TEP interaction was observed in both $Mg(TFSI)_2$/CEPE and $Mg(TFSI)_2$/DME:TEP electrolytes (**Figure 7.14**), suggesting the consistent effect of reducing CIPs in all electrolytes with the presence of TEP.

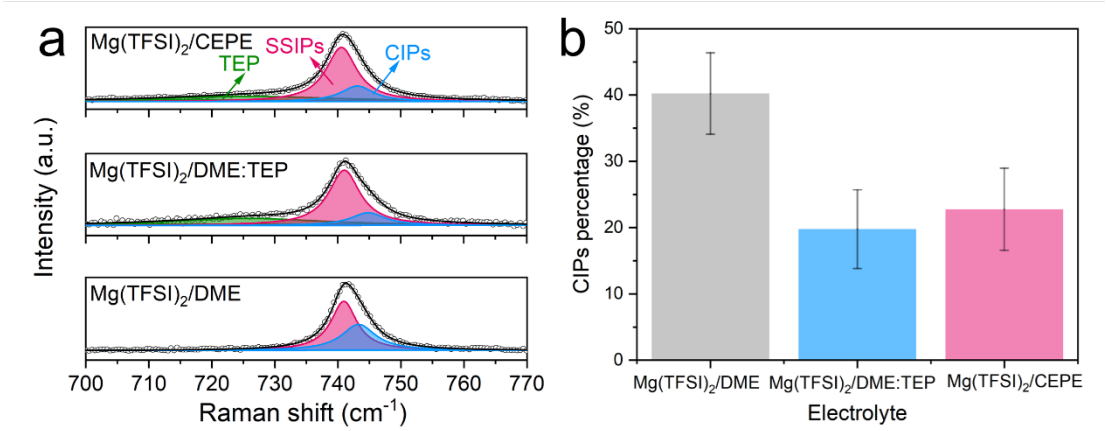

Figure 7.14 Raman analysis of different electrolytes. **(a)** Fitted Raman spectra of different electrolytes in the region of 700-770 cm^{-1}. **(b)** CIP fraction in different electrolytes.

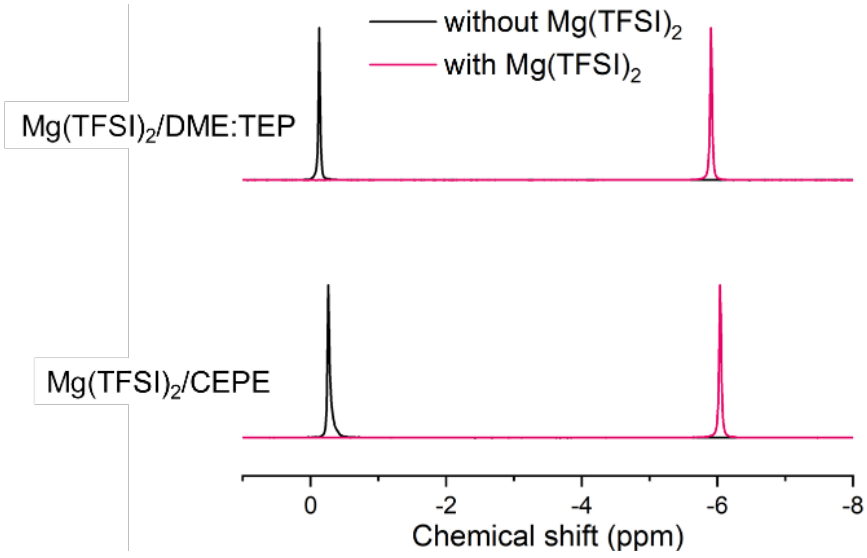

Figure 7.13 ^{31}P NMR spectra of $Mg(TFSI)_2$/DME:TEP and $Mg(TFSI)_2$/CEPE at 298 K.

The reduction in CIP formation by TEP is further upheld by classical MD simulations (**Figure 7.12b**). The average Mg^{2+}-TEP coordination increases from ~0.8 in $Mg(TFSI)_2$/DME:

TEP to ~1.1 in $Mg(TFSI)_2$/CEPE. The fractions of isolated and paired Mg^{2+} ions - defined by solvation shells with zero and one $TFSI^-$ anion - were also calculated. The paired Mg^{2+} fractions from MD closely matches with the experimental CIP concentrations, which is especially impressive with a non-polarizable forcefield: the average paired Mg^{2+} fraction decreases from ~ 0.45 in $Mg(TFSI)_2$/DME (experimental CIP concentration: ~40%) to ~ 0.26 in $Mg(TFSI)_2$/CEPE (experimental CIP concentration: ~23%). These results provide strong support to the experiment results and confirm the decrease of CIPs in both the $Mg(TFSI)_2$/DME:TEP and $Mg(TFSI)_2$/CEPE electrolytes.

DFT calculations were further performed to calculate the binding energies of the predominant clusters in these electrolytes. The results in **Figure 7.12c** demonstrate that the clusters with CIPs in the solvation shells (hatched bars) consistently exhibit a greater binding energy than the fully solvent-coordinated Mg^{2+}, in turn suggesting a higher desolvation energy for the charge transfer process.[176,177] The direct correlation between binding and desolvation energy is already established.[178] The trends in **Figure 7.12c** indicate that the large decrease in CIPs and increase in exclusively solvent-coordinated Mg^{2+} solvated clusters promote a facile desolvation process during charge transfer.[179] The results also affirm that the observed fast kinetics of Mg plating/stripping in the CEPE system is induced by higher exchange current densities and surface energies which in turn promotes uniform Mg electrodeposition (see below).[176]

The bulk dynamics of ethers and TEP in these electrolytes were explored by conducting variable temperature NMR. In both ^{31}P and ^{1}H spectra of $Mg(TFSI)_2$/CEPE, no new peaks were found at low temperature (**Figure 7.12d**). In $Mg(TFSI)_2$/DME:TEP, however, the single ^{31}P resonance at 298 K was gradually split into two at below 273 K (**Figure 7.12e**), along with the appearance of more $-CH_3$ and $-CH_2-$ signals of TEP in ^{1}H spectra at low temperature (**Figure 7.15**). This peak splitting suggests Mg^{2+} is undercoordinated with TEP (eg. fewer Mg^{2+}-TEP bonds in the presumably six-coordinated Mg^{2+} solvation sheath). In addition, the

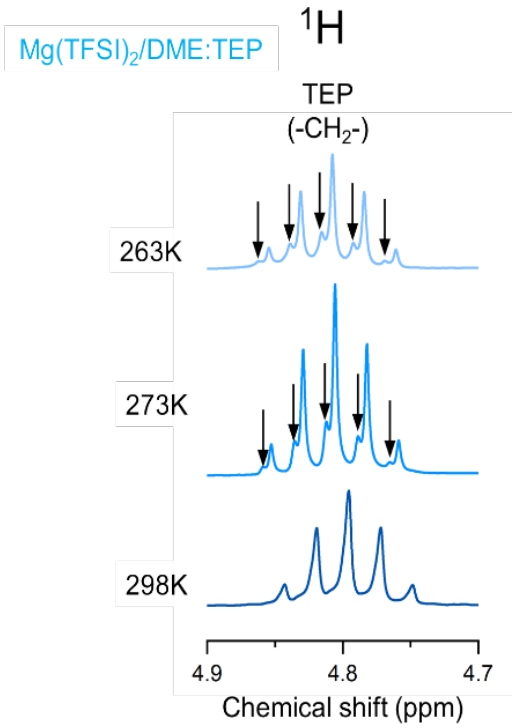

Figure 7.16 Variable temperature ^{1}H NMR spectra of $Mg(TFSI)_2$/DME:TEP

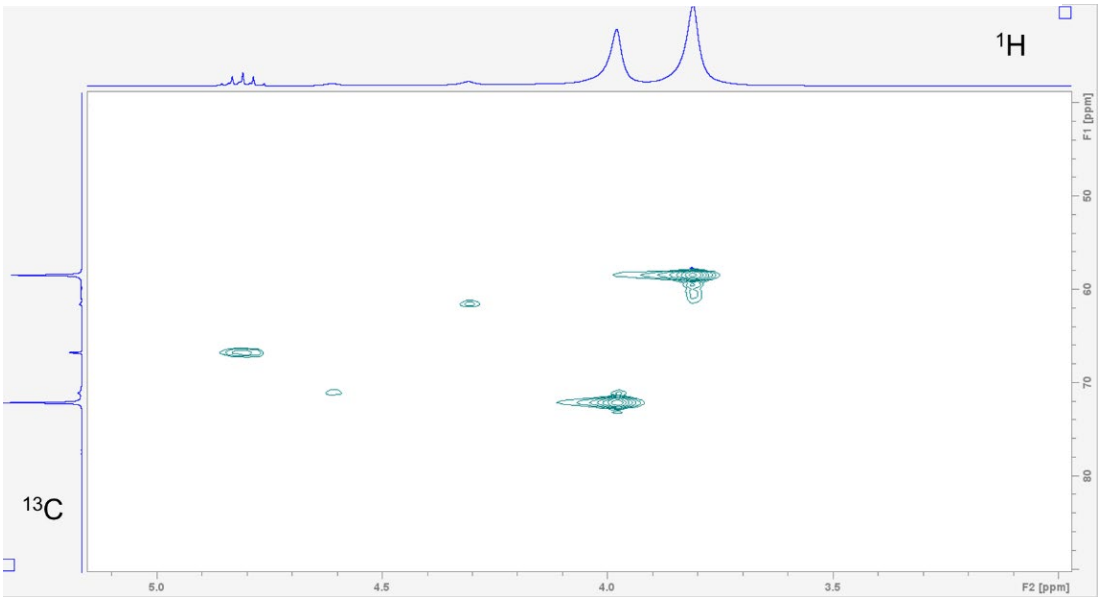

Figure 7.15 HSQC plot of $Mg(TFSI)_2$/DME:TEP at 263 K with ^{1}H spectra at the top and ^{13}C spectra at the left.

Mg^{2+}-DME interaction in $Mg(TFSI)_2$/DME:TEP shows similar undercoordination with two

new higher-frequency peaks appearing in ^{1}H spectra below 273 K, which were assigned to the -CH_2- and -CH_3 groups of DME by carrying out a Heteronuclear Single Quantum Coherence (HSQC) experiment (**Figure 7.16**). These new peaks can be ascribed to the slow exchange rate of DME molecules in different bound environments, leading to the peak separation at low temperatures.[134,180] The addition of G2 and BTFE in $Mg(TFSI)_2$/CEPE effectively enhances the exchange rate, owing to the absence of such undercoordination behavior. This is because G2 is known to exchange much faster than DME while BTFE barely coordinates with Mg^{2+}, in turn indicating decreased Mg^{2+}-glyme interaction by co-ethers. This is verified by the blue shift and decreased intensity of coordinated glyme signals in the Raman spectra (**Figure 7.12f**).[129] As a consequence, a lower desolvation penalty can be expected in $Mg(TFSI)_2$/CEPE, which explains the much enhanced kinetics of Mg plating/stripping relative to $Mg(TFSI)_2$/DME:TEP.

7.6 Tuning nanoscale and dendrite-free Mg plating/stripping morphology

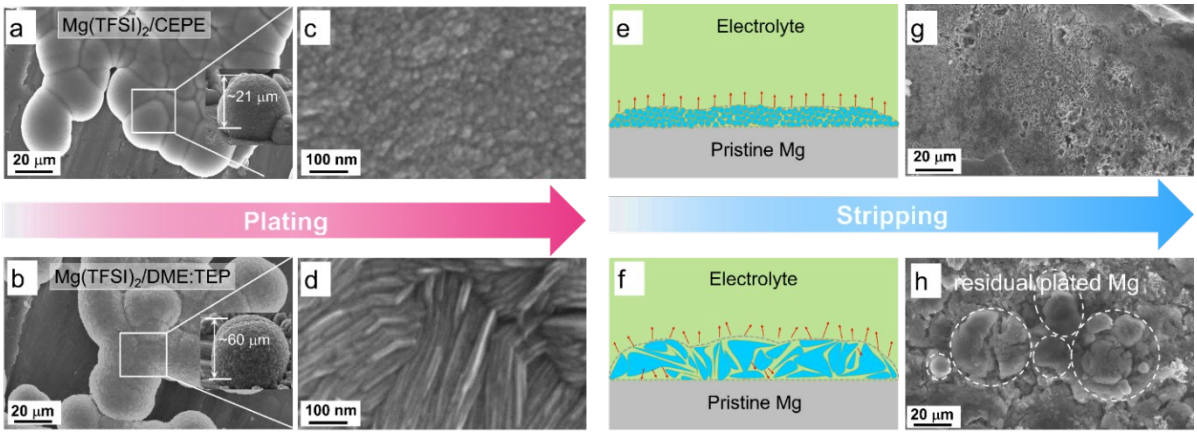

Figure 7.17 (a-d) Plated Mg morphologies (insets are the images of representative Mg globules with estimated thickness from a tilt angle of 60°). **(e-f)** Schematic illustration of stripping current distribution on plated Mg. g-h, Fully stripped Mg morphologies in different electrolytes: **(a, c, e, g)** $Mg(TFSI)_2$/CEPE; **(b, d, f, h)** $Mg(TFSI)_2$/DME:TEP. All electrodes were retrieved from the Mg||Mg symmetric cells that were cycled at a current density of 1 mA cm^{-2} and areal capacity of 1 mAh cm^{-2}.

To delve more into the function of co-ethers in sustained long-term Mg plating/stripping, we used scanning electron microscopy (SEM) coupled with EDX to probe

the Mg electrodes retrieved from the Mg||Mg symmetric cells. In $Mg(TFSI)_2$/CEPE, nanoscale Mg nuclei of around 10 nm were observed with much smoother surface morphology that merged in globules (**Figure 7.17a, c**). In $Mg(TFSI)_2$/DME:TEP, however, Mg deposits as microscale flaky crystals with a dimension of ~500 nm (**Figure 7.17b, d**). Mg plated in $Mg(TFSI)_2$/DME yielded a spherical morphology of core-shell multilayers (**Figure 7.8e** and **7.18**). The nanoscale nucleation and growth in $Mg(TFSI)_2$/CEPE leads to denser and thinner

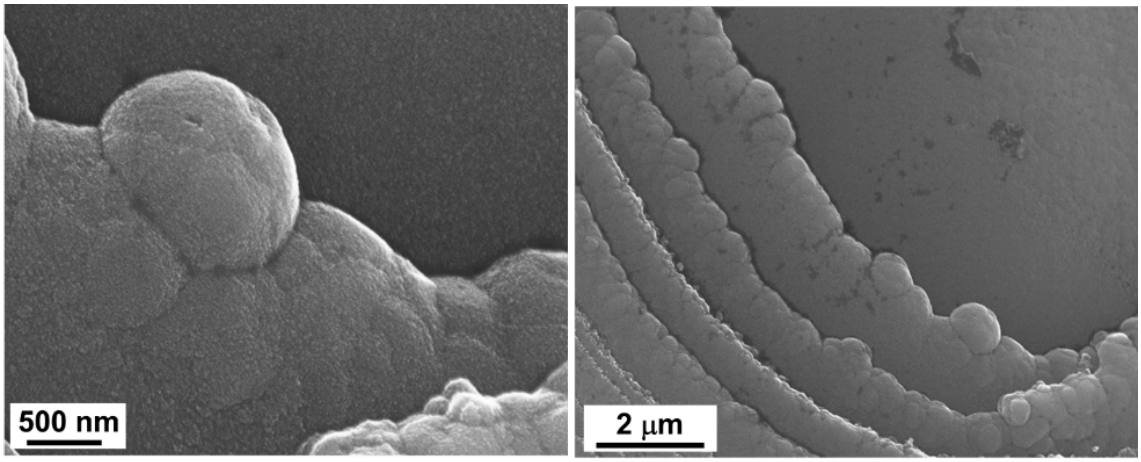

Figure 7.18 SEM images of plated Mg in $Mg(TFSI)_2$/DME.

hemisphere deposition with a thickness of ~ 20 μm, in contrast to ~ 60 μm in $Mg(TFSI)_2$/DME:TEP. The uniform deposition in CEPE can be attributed to the increase in isolated Mg^{2+} clusters with lower binding energies and weakened Mg^{2+}-DME interactions (**Figure 7.12**) that results in a faster desolvation process at the Mg/electrolyte interface. We thus expected a more homogeneous distribution of local interfacial currents during stripping (**Figure 7.17e, f**), which was verified by the smoother and cleaner stripping morphologies in $Mg(TFSI)_2$/CEPE (**Figure 7.17g**). In $Mg(TFSI)_2$/DME:TEP, by comparison, large quantities of cracked Mg globules were observed on the cycled electrode (**Figure 7.17h**). We believe that voids can be formed between the flaky crystals due to a non-uniform distribution of stripping current (**Figure 7.19**), which leads to electrolyte penetration through the plated Mg globules and results in inactive Mg.[181] With continuous plating/stripping, the accumulation of cracked globules leads to a mossy surface that can easily induce short circuits (**Figure 7.20**). Therefore,

Mg||Mg symmetric cells show outstanding stability with $Mg(TFSI)_2$/CEPE but quickly short with $Mg(TFSI)_2$/DME:TEP.

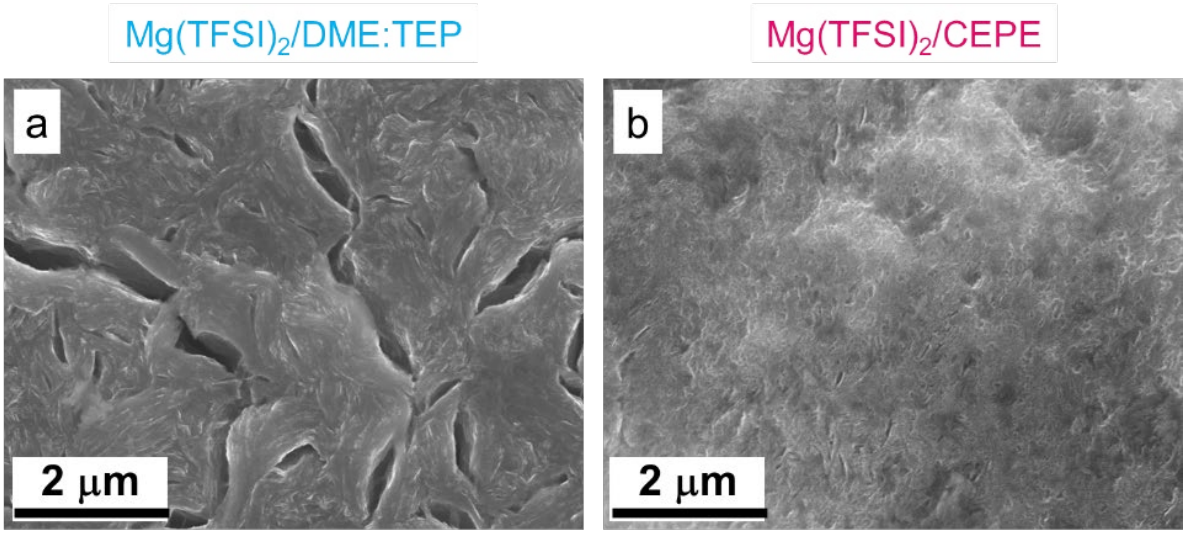

Figure 7.20 SEM images of a half-stripped Mg electrode in TEP-based electrolytes: **(a)** $Mg(TFSI)_2$/DME:TEP; **(b)** $Mg(TFSI)_2$/CEPE.

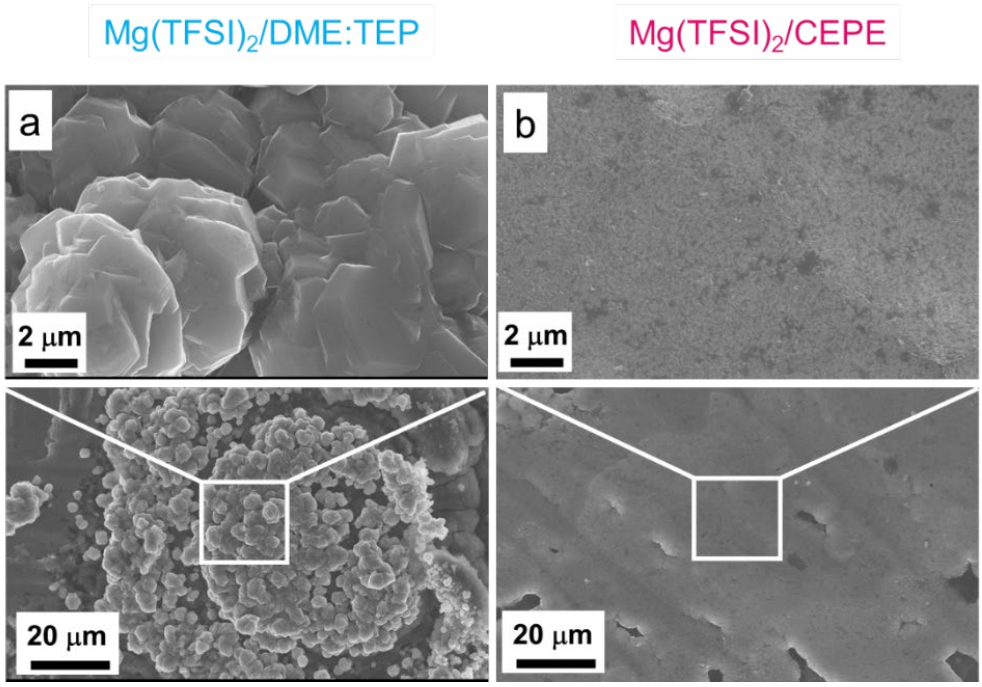

Figure 7.19 SEM images of multiple-cycled Mg in TEP-based electrolytes: **(a)** $Mg(TFSI)_2$/DME:TEP after 10 cycles; **(b)** $Mg(TFSI)_2$/CEPE after 50 cycles.

7.7 Interfacial SEI chemistry on plated Mg surface

High-resolution X-ray photoelectron spectroscopy (XPS) was used to investigate SEI compositions on the plated Mg surface in different electrolytes. For Mg cycled in the baseline $Mg(TFSI)_2$/DME (**Figure 7.21a**), we observed abundant surface species including MgF_2 (688.5 eV, F *1s*), MgS (163.2 eV, S *2p*), -CF (686.2 eV, F *1s*) and -SO_x (x <2, 167.4 eV, S *2p*). These likely result from the reduction of $TFSI^-$ anions. In addition, F-rich -CF_3 (688.6 eV, F *1s*) and -SO_2 (169.2 eV, S *2p*) signals imply copious adsorption of $TFSI^-$ anions on the Mg

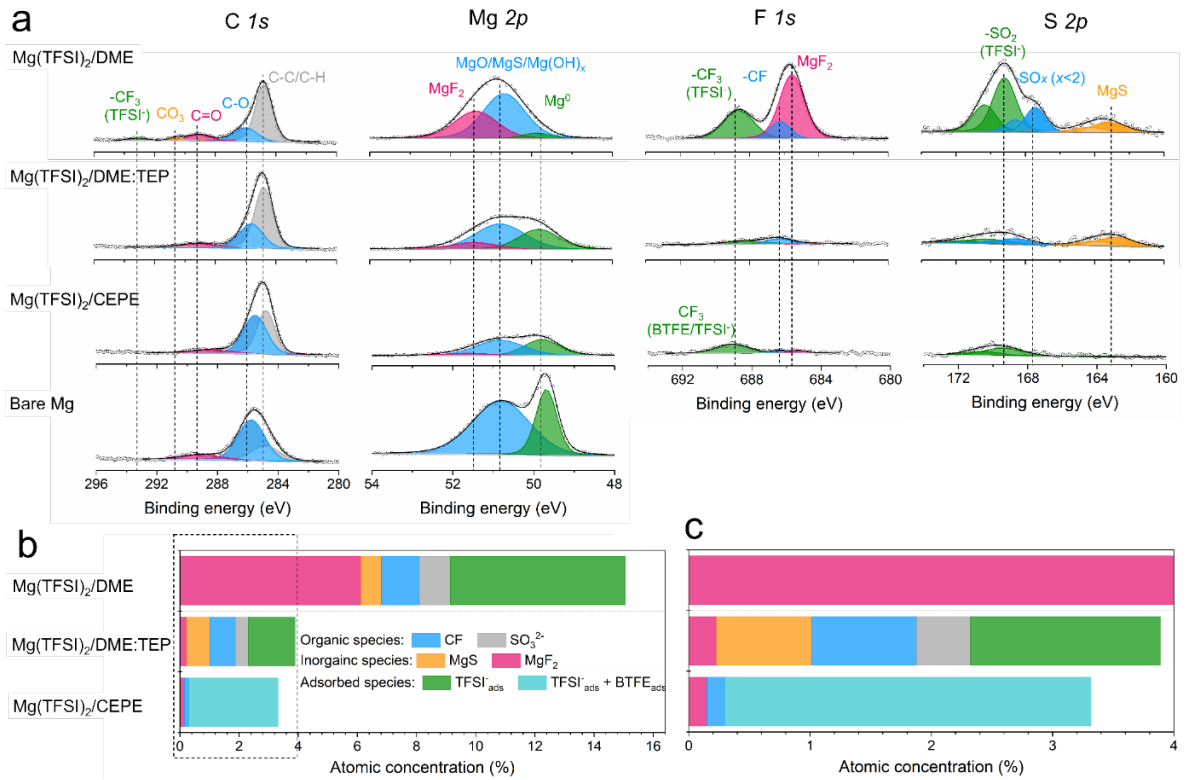

Figure 7.21 (a) XPS spectra of bare Mg and plated Mg in different electrolytes. **(b, c)** Atomic concentration of different $TFSI^-$-related species on the plated Mg surface and **(c)** magnified view of the circled region.

surface (**Figure 7.21b**). These results correlate with the large fraction of CIPs in the electrolyte, which facilitates the adsorption and reduction of $TFSI^-$ on the Mg surface to form the

passivation layer. Owing to the significantly decreased CIPs in $Mg(TFSI)_2$/DME:TEP, intensities in the F1s and S *2p* region are greatly diminished on plating Mg, showing effective suppression of these anion-related species. In $Mg(TFSI)_2$/CEPE, no evident anion-derived species were observed. We attribute this to the G2-optimized solvation structure and the

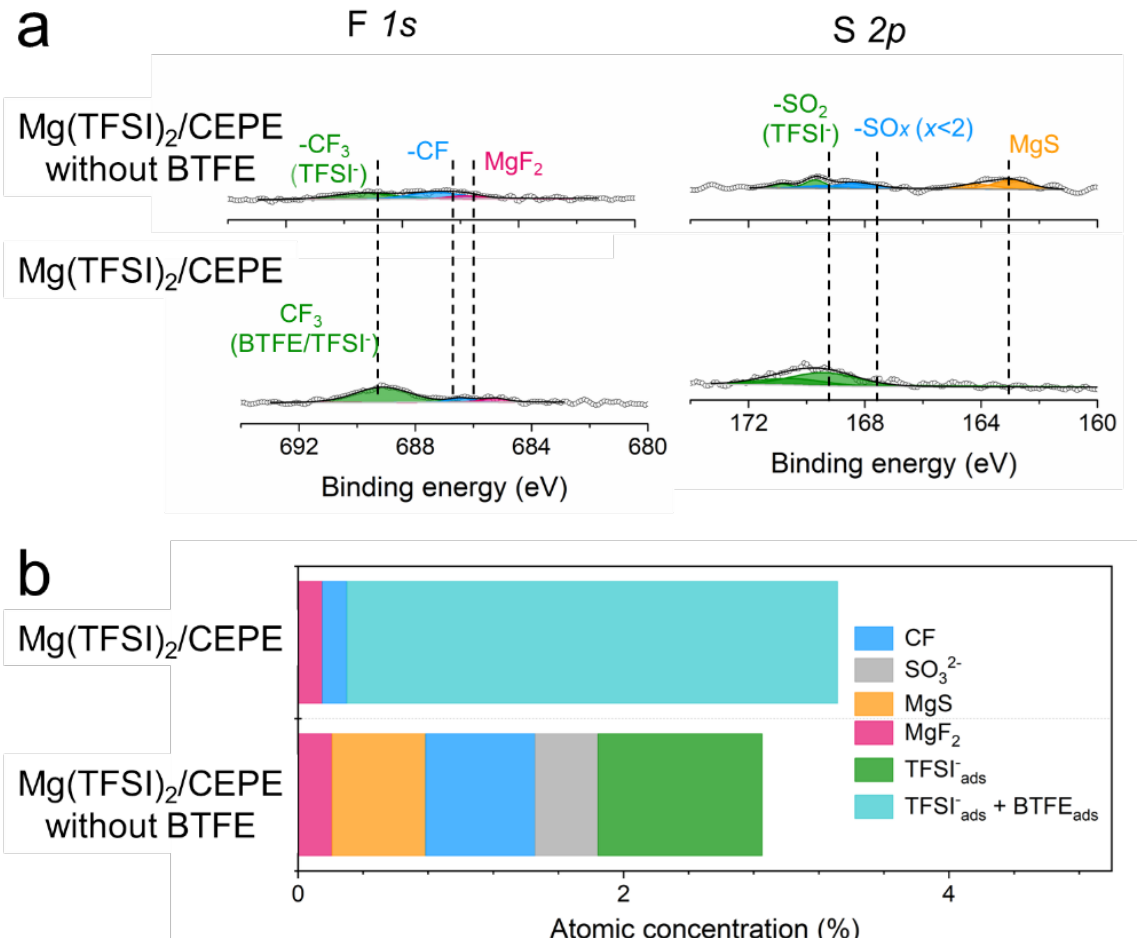

Figure 7.22 XPS analysis of plated Mg in $Mg(TFSI)_2$/CEPE with/out BTFE. **(a)** F 1s and S 2p XPS spectra of plated Mg. **(b)** Atomic concentration of different $TFSI^-$-related species on the plated Mg surface. The electrolyte composition of $Mg(TFSI)_2$/CEPE without BTFE is: 0.4 M $Mg(TFSI)_2$/DME:G2:TEP (5:5:1 in vol).

adsorption of BTFE on the Mg surface that further suppresses the decomposition of $TFSI^-$ (**Figure 7.21c**). Indeed, the $Mg(TFSI)_2$/CEPE without trace BTFE shows more electrolyte decomposition products (**Figure 7.22**), with significantly lower kinetics of Mg

plating/stripping (**Figure 7.23**). In addition, no phosphorus signals were found for electrodes retrieved from both $Mg(TFSI)_2$/DME:TEP and $Mg(TFSI)_2$/CEPE (**Figure 7.24**), suggesting TEP is not decomposed. This is in strong contrast to previous studies on the TMP additive that

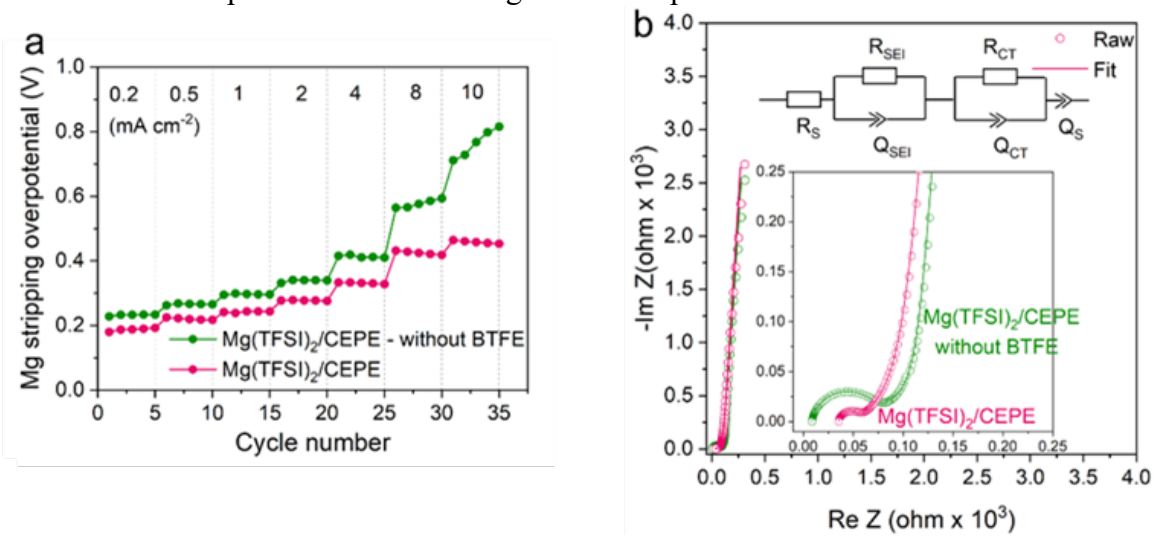

Figure 7.23 Electrochemical performance of Mg plating/stripping in $Mg(TFSI)_2$/CEPE with/out BTFE. **(a)** Rate performance of Mg||Mg symmetric cells. The areal capacity was fixed as 0.1 mAh cm^{-2}, and the stripping overpotential at the central point was collected. **(b)** Nyquist plots of Mg||Mg symmetric cell after 10 cycles. The data were fit (shown by line) with the indicated equivalent circuit.

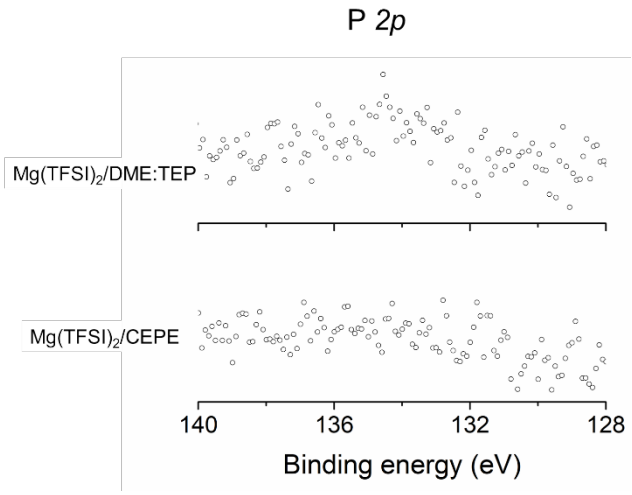

Figure 7.24 XPS in the P 2p region of plated Mg in different electrolytes.

showed its extensive reduction to form a $Mg_3(PO_4)_2$-rich interface,[63,129] which implies additive consumption causes the continuous increase of voltage hysteresis during Mg plating/stripping. While it is surprising that the additional -CH_2 group in TEP results in remarkably increased stability against electrochemical reduction, we speculate that this originates from a steric effect. This results in different Mg^{2+} solvation structures that presumably exist with higher stability.[182] Identifying the exact origin of this difference is beyond the scope of this work and will be part of a future study.

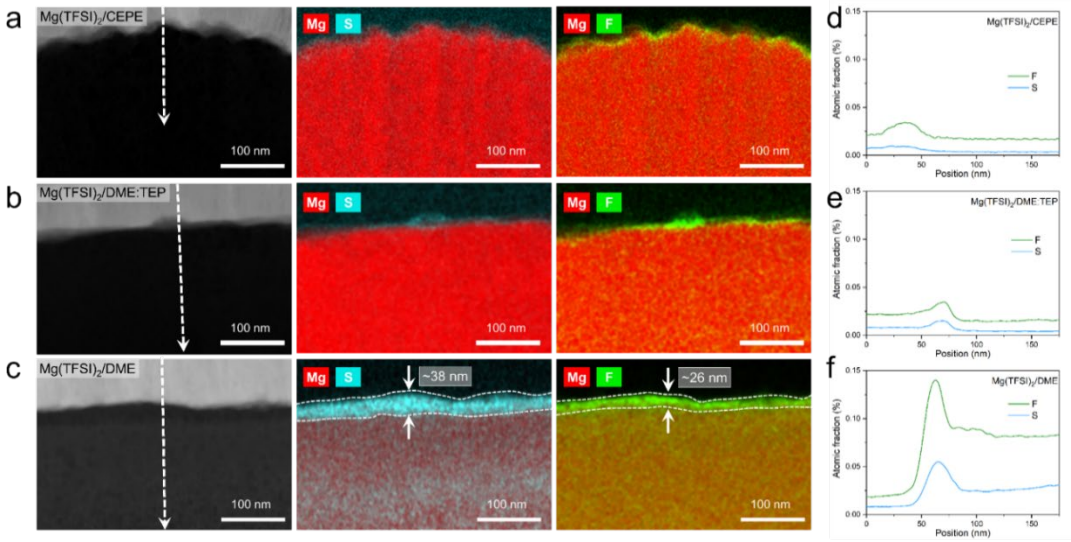

Figure 7.25 (a-c) STEM-HAADF images with Cr coating (white) on top of Mg samples (black) and corresponding EDX chemical maps with Mg/S and Mg/F overlap. **(d-f)** distribution of F and S by EELS line scan analysis taken along the indicated lines shown in STEM-HADDF images. **(a, d)** $Mg(TFSI)_2$/CEPE; **(b, e)** $Mg(TFSI)_2$/DME:TEP; **(c, f)** $Mg(TFSI)_2$/DME.

The structural characteristics and chemical mapping of these interfaces formed on Mg were further probed using cryogenic focused ion beam (Cryo-FIB) milling and transmission electron microscopy (TEM). **Figure 7.25a, b** shows the high-angle annular dark-field (HADDF) images at the surface of Mg deposited in $Mg(TFSI)_2$/CEPE and $Mg(TFSI)_2$/DME:TEP, along with color maps showing the Mg/S and Mg/F elemental distribution. Trace amounts of S and F can be observed on the Mg surface that originate from the formation of a very thin SEI. This is in good accord with the XPS results above. The

thickness cannot be well defined due to the low quantity of S/F present that is comparable to the background noise. In contrast, in baseline $Mg(TFSI)_2$/DME (**Figure 7.25c**), a ~30 nm thick S-rich and F-rich passivation layer is formed. In addition to the accumulation of S/F at the interface, significant amounts decorate the underlying Mg region. In both $Mg(TFSI)_2$/DME:TEP and $Mg(TFSI)_2$/CEPE, the S/F species were greatly diminished at both surface and Mg region, as confirmed by EELS line scan analysis (**Figure 7.25d-f** and **7.26**).

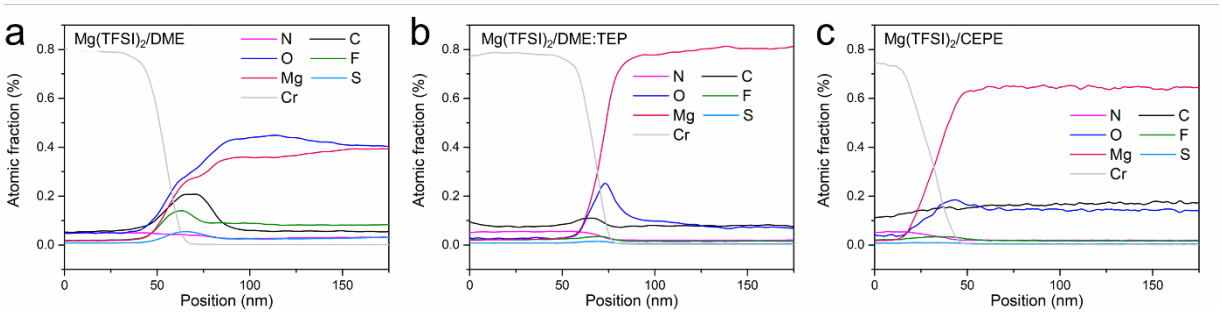

Figure 7.26 The elemental distribution of an EDX line scan analysis taken along the indicated lines shown in the STEM-HADDF images in Figure. 7.25

7.8 High-voltage stability in Mg-organic full cells

To assess the anodic stability of the CEPEs, linear scan voltammetry (LSV) was performed on three-electrode cells with commercial Al foil as a working/counter electrode and Mg as the reference electrode at a slow scan rate of 5 mV s^{-1}, as commonly utilized. All electrolytes exhibit an oxidation stability of around 4 V on Al foil **(Figure 7.27a**), consistent with previously reported $Mg(TFSI)_2$/glyme electrolyte systems. We chose polyaniline (PANI) as a readily available, high-voltage (~ 2.3 V) organic cathode material to benchmark the oxidative stability of the $Mg(TFSI)_2$/CEPE system. We demonstrate the cycling of a PANI||Mg cell up to a high cut-off voltage of 3.5 V **(Figure 7.27b**), providing a specific discharge capacity of 250 mAh g_{PANI}^{-1} at C/10 (1C = 250 mA g_{PANI}^{-1}) with an average discharge voltage of ~2.05 V. The dominant $TFSI^-$ anion storage chemistry is confirmed by EDX analysis (**Figure 7.28**), in accord with previous studies. A very large specific capacity of PANI is obtained in due to CEPE's good oxidative stability, whereas the use of chloride-based electrolytes in previous studies limits PANI's high-voltage application and hence gave rise to

a low specific capacity of less than 150 mAh g_{PANI}^{-1} in the range of 0.1-2.8 V.[161] More importantly, PANI in $Mg(TFSI)_2$/CEPE shows excellent rate capability, with a capacity of 239,

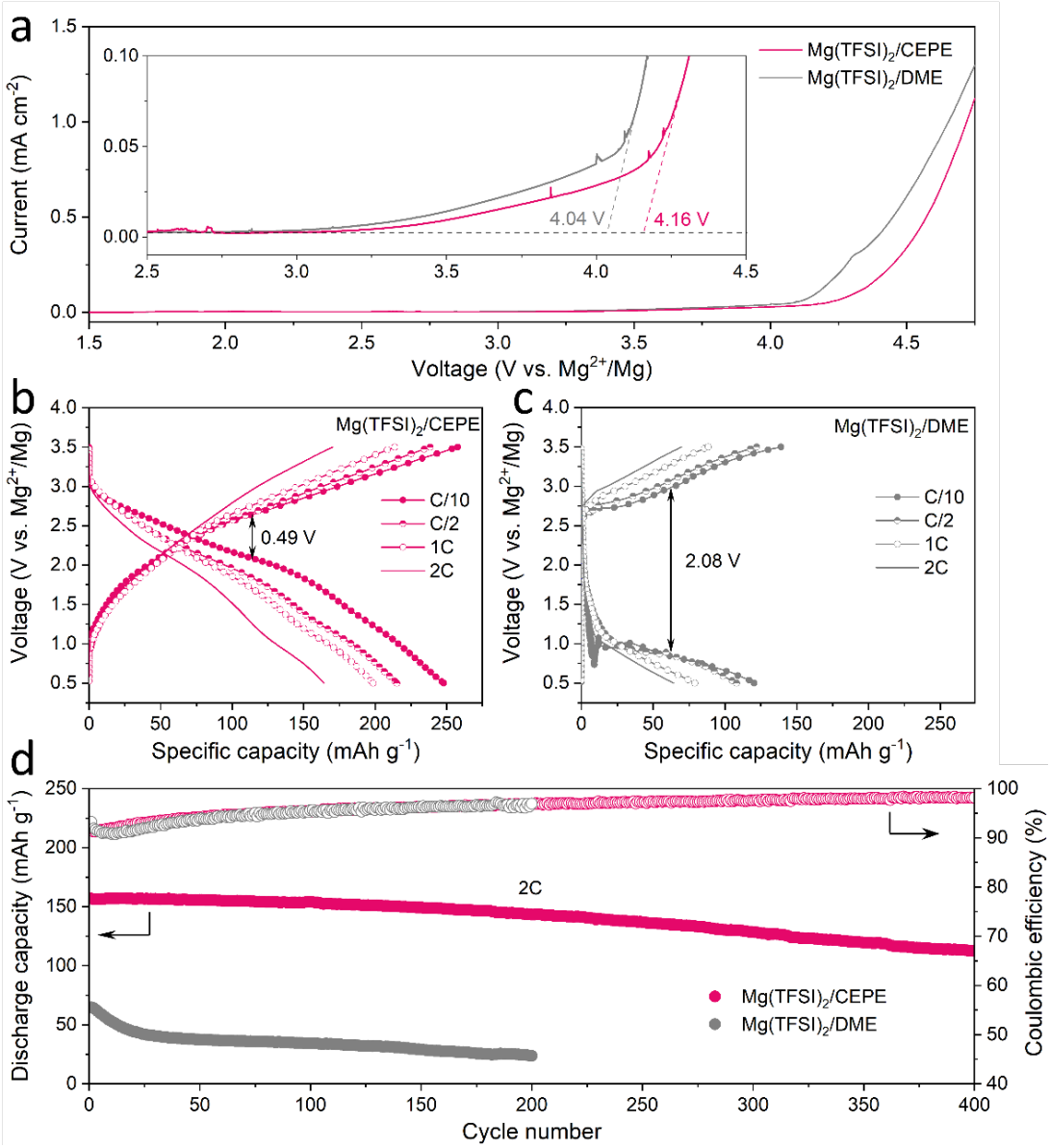

Figure 7.27 (a) LSV curves of $Mg(TFSI)_2$/CEPE and $Mg(TFSI)_2$/DME at a scan rate of 5 mV s^{-1}. The onset of oxidation in CEPE is slightly higher at 4.16 V. **(b, c)** Charge-discharge curve of PANI||Mg cells at different rates (1C = 250 mA g_{PANI}^{-1}) in **(b)** $Mg(TFSI)_2$/CEPE and **(c)** $Mg(TFSI)_2$/DME. **(d)** Long-term cycling of PANI||Mg cells at 2C in different electrolytes.

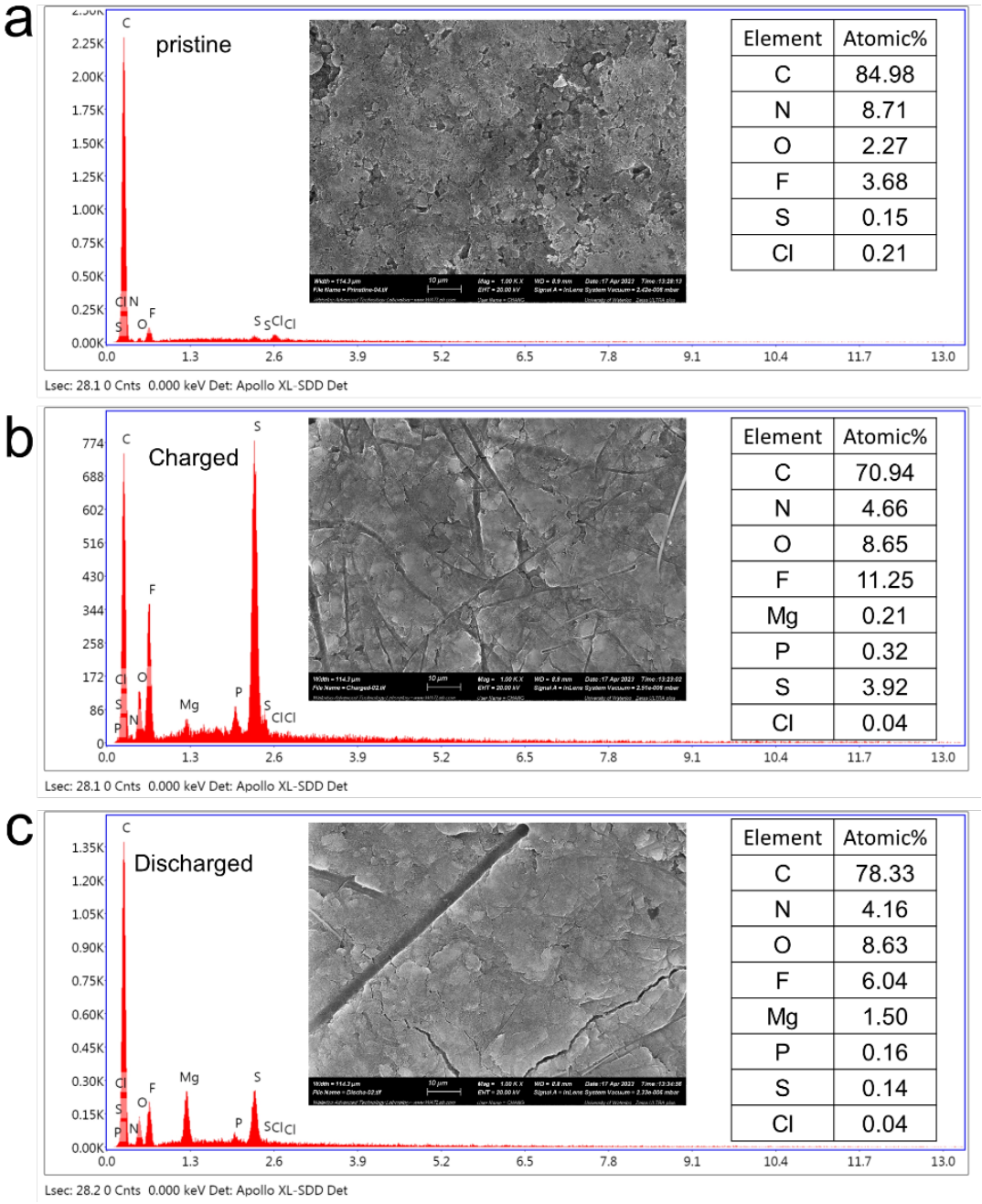

Figure 7.28 SEM and EDX of **(a)** pristine, **(b)** charged and **(c)** discharged PANI in $Mg(TFSI)_2$/CEPE at C/10.

215, and 165 mAh g_{PANI}^{-1} at C/2, 1C, and 2C, respectively. In the baseline $Mg(TFSI)_2$/DME electrolyte, however, a high voltage polarization of around 2.08 V was observed for the

PANI||Mg cell at C/10 (**Figure 7.27c**), yielding a discharge capacity of only 120 mAh g^{-1}. The long-term cycling stability of PANI||Mg cell was further investigated at a 2C rate (**Figure 7.27d)**. In $Mg(TFSI)_2$/CEPE, the cell retains a high discharge capacity of ~ 113 mAh g^{-1} with 99% CE after 400 cycles, corresponding to a capacity retention of over 72%. In contrast, a low discharge capacity of only 65 mAh g^{-1} was obtained in $Mg(TFSI)_2$/DME, which quickly drops to around 24 mAh g^{-1} after 200 cycles due to the poor kinetics of Mg plating/stripping. The desirable performance of PANI in CEPE under high voltage conditions confirms the high oxidative stability of CEPE and suggests a facile anion desolvation process due to suppressed CIP formation. This in turn simultaneously results in fast desolvation of Mg^{2+} at the cathode side, as proven by using an n-type pyrene-4,5,9,10-tetraone (PTO) cathode that also shows good rate performance (**Figure 7.29**). However, the PTO||Mg cell shows limited cycling stability due to the relatively high solubility of Mg_1PTO as reported,[Error! Bookmark not defined.] and was not pursued further in this study.

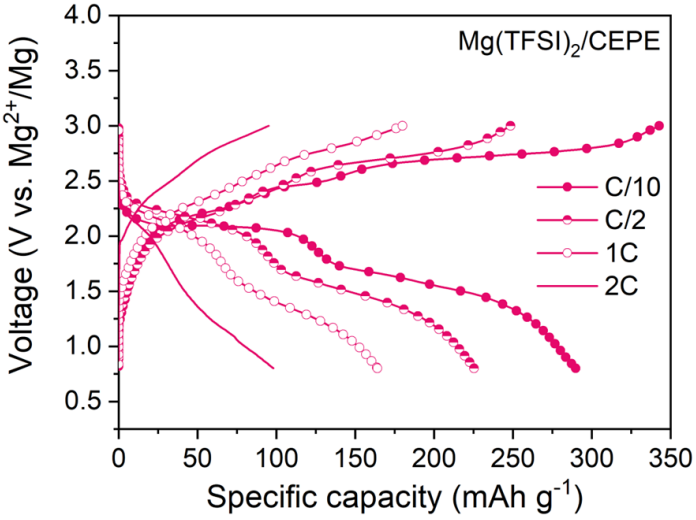

Figure 7.29 Charge-discharge curve of PTO||Mg cells at different rates (1C = 408 mA g_{PTO}^{-1}) in $Mg(TFSI)_2$/CEPE

7.9 Conclusions

A new type of co-ethereal phosphate electrolyte (CEPE) system is developed for stable and high-voltage Mg batteries. This electrolyte system relies on two key components: ethyl

phosphate additives to unlock the activity of Mg^{2+}/Mg redox and co-ether solvents to improve the kinetics and stability of Mg plating/stripping. The complex interactions between cation, anion and solvents were revealed by advanced spectroscopies and MD simulations, providing new design principles for efficient Mg electrolytes. In addition, the use of cost-effective and commercially available Mg salts simplifies scalability and expedites the development of MMBs. The assembled PANI||Mg batteries show excellent electrochemical performance with high cycling stability at an operating voltage of 3.5 V. Our design opens up new frontiers for low-cost and high-voltage electrolyte development that could take advantage of facile desolvation processes at the interfaces, and can establish a platform for new avenues of investigation for next generation energy storage in MMBs.

Chapter 8 Summary and Future Prospects

8.1 Summary

This thesis presents the investigations of a series of electrolyte engineering approaches to tackle the dilemmas on electrolyte/electrode interface and to achieve fast-kinetic and long-lived AZMBs and MMBs that are functioned at practical current densities and areal capacities. That also includes the development of fundamental understandings of divalent-ion solvation structures and their effect on electrode/electrolyte interface, which plays critical role in stabilizing both cathode and anode in the long-term cycling.

Dendrite Zn formation can shorten the lifetime of batteries and is one of most challenging issues for AZMBs. A novel DOTf additive was developed for a cost-effective and low-concentration 2 M $ZnSO_4$ electrolyte. The use of this modified electrolyte leads to dendrite-free and highly reversible Zn plating/stripping with ~100% average CE of Zn plating/stripping under a practical cycling condition of a high current density of 4 mA cm^{-2} and a high areal capacity of 4 mAh cm^{-2}. By using multiple advanced ex/in-situ microscopy and spectroscopy characterization techniques, a robust nanostructured SEI layer was revealed and lead to the suppression of detrimental LDHs and a nanoscale nucleation-growth process during Zn electrodeposition, thus enhancing the superior Zn stability and reversibility. The origin of this Zn^{2+}-conducting SEI is speculated to be a result of the water assisted dissociation of DOTf into neutral ion pairs, resulting in the interfacial acidic environment during initial cycles. Zn||$Zn_{0.25}V_2O_5 \cdot nH_2O$ full cells at low N:P ratios based on this electrolyte exhibit excellent cycling performance with different depth of proton intercalation.

Proton intercalation into the Zn cathode hosts has been rarely studied and overlooked phenomena in the early studies of AZMBs, and attracted more attention recently. The consequence of proton intercalation is the poor cycling stability of AZMBs at practical and moderate current densities. LVP was chosen as the example cathode to comprehensively study this phenomenon. The existence of phase transition induced by H^+ intercalation of LVP was confirmed in 4 m $Zn(OTf)_2$. Through the comparison between 4 m $Zn(OTf)_2$ and $ZnCl_2$ WiSE, such H^+ intercalation is revealed to be effectively suppressed by altering the Zn^{2+} solvation

sheath to weaken the hydrogen bonding network of H_2O. Dominant Zn^{2+} intercalation in LVP host was confirmed quantitatively by both Rietveld refinement and EDX. In addition, a PEG-based hybrid aqueous Zn electrolyte was proposed to replace $ZnCl_2$ WiSE for a low-cost AZMBs application, where 70PEG shows excellent reversibility and stability for Zn stripping/plating. Further evaluation of LVP in 70PEG showed that H^+ intercalation was effectively suppressed and dominant Zn^{2+} insertion/extraction chemistry worked steadily. These unique properties can be ascribed to the strong interaction between PEG and water, resulting in a similar weaker hydrogen bonding and stronger O-H covalent bond of water. Our work not only successfully solves the detrimental H^+ intercalation that has obsessed the detailed charge storage mechanisms research in this emerging area, but also builds up a new avenue to design appropriate Zn electrolytes from Zn^{2+} solvation structure point of view, aiming for real Zn^{2+} intercalation and highly reversible Zn utilization. This work lays the foundation of the discovery of sulfolane-based hybrid electrolyte.

With a practical goal of constructing high areal loading metal oxide electrodes that function under moderate rates, a sulfolane-based hybrid Zn electrolyte was developed. This electrolyte greatly suppresses the proton interaction and achieves dominant Zn^{2+} intercalation that stabilizes the ZVO at a high areal capacity of over 4 mAh cm^{-2}. Simultaneously, a fully hydrated Zn^{2+} solvation structure was revealed to enable a facile interfacial desolvation process at the solid/electrolyte interface, which assists to achieve highly reversible Zn plating/stripping with a sulfolane-derived SEI, and demonstrate excellent low-rate cycling stability of practical-level *anode-free* cells. This work represents a practical strategy to stabilize both electrodes by tuning the hybrid electrolyte network and also provides an understanding of Zn^{2+}-(de)intercalation in conventional oxide cathodes which could expedite the commercialization of practical AZMBs.

Realizing reversible and stable Mg plating/stripping of Mg metal anode for non-aqueous MMBs is much more challenging compared to that of Zn metal anode in AZMBs. This is mostly due to the parasitic reaction between Mg anode and electrolyte during Mg electrodeposition. The resulting undesirable interface on Mg leads to the non-uniform Mg

deposition morphologies in the state-of-art electrolyte with bulky alkoxy-borates. A low-cost zeolite membrane was discovered as an effective protective interface for a Mg metal anode in this type of electrolytes, leading to dendrite-free and highly stable Mg plating/stripping with an ultralong lifetime. Reduced free solvent content on the Mg/electrolyte interface was revealed with the presence of this membrane, resulting in alleviated solvent decomposition. More exciting is the verified superiority of the zeolite membrane-protected Mg anode in high-voltage full cells that can be cycled stably at fast rates.

The state-of-the-art alkoxy-borates/aluminates-based Mg electrolytes suffer from difficult-accessibility and expensiveness due to the reagents needed for their complex synthesis and purification procedures. Designing Mg electrolytes that are commercially available is of necessity. A cost-effective and commercially available co-ethereal phosphate electrolyte (CEPE) system is developed for stable and high-voltage Mg batteries based on ethyl phosphate additives to unlock the activity of Mg^{2+}/Mg redox and co-ether solvents to improve the kinetics and stability of Mg plating/stripping. The complex interactions between cation, anion and solvents were revealed by advanced spectroscopies and MD simulations, providing new design principles for efficient Mg electrolytes. The assembled PANI||Mg batteries show excellent electrochemical performance with high cycling stability at an operating voltage of 3.5 V.

8.2 Future Prospects

Aiming to tackle the fundamental issues in current AZMBs, I developed the electrolyte engineering strategy as the solution to these obstacles step by step. The electrolyte was initially designed for only anode (**chapter 3**) or cathode (**chapter 4**), nonetheless, laying the foundation of deep understanding towards the relationship between electrolyte network and electrode/electrolyte interface. This finally leads to the very practical electrolyte recipe (**chapter 5**) that can simultaneously support both state-of-art metal oxide cathode and Zn anode under realistic conditions. However, the challenges remain on the sluggish solid-state Zn^{2+} diffusion in these oxide cathodes, which may not be a concern for a long-duration energy storage scenario, but indeed significantly limits the reversible capacity and rate capacity for high-power applications that requires charging and discharging batteries in short time. For the

next generation of AZMBs, more practical considerations directly related to realistic working scenarios should be included when we design the electrolytes and electrodes.

To design the next generation of aqueous Zn electrolyte, the consumption of electrolytes during cell cycling needs to be considered. In the practical situation, lean electrolyte condition is needed to decrease the volume and weight of the cell to maximize the energy density, which requires the minimum electrolyte loss during the long-term cycling of batteries. The consumption of aqueous electrolytes normally originates from the loss of water solvent due to OER and HER, and the loss of salt due to the formation of SEIs, LDHs and other parasitic interfacial reactions. The formation of a functional SEI on Zn surface have been proved to effectively suppress these side reactions over limited cycles, nonetheless, it can also lose it efficacy due to the continuously change of electrode volume over cycling that leads to the breakdown of SEI, and finally cause cell failure. Therefore, new design principles of forming robust SEI with seal-healing ability that can stand high-areal-capacity cycling (high electrode volume change) are needed. The conventional WISEs can effectively suppress OER and enhance the anodic stability of aqueous Zn electrolytes, nonetheless, suffers from the high cost, corrosivity and low kinetics. The aqueous-nonaqueous solvent electrolyte is a feasible strategy to obviate these difficulties. Its future research direction should focus more on the choice of aqueous-nonaqueous solvent that requires low-cost, nonflammable and environmentally friendly on a basis of good compatibility with both Zn anode and cathodes.

To commercialize MMBs so that it can be a replacement for the state-of-art LIBs, lowering down the cost of electrolyte is one of the biggest challenges, which requires the exploration of conceptual new electrolytes based on the low-cost salts and solvents. The development of CEPEs in this thesis is a starting point towards this goal, where the fundamental understandings of the interaction between cation, anion and solvents was established, and its relevance with Mg/electrolyte interface was revealed as the core to achieve reversible and stable Mg plating/stripping. However, in this newly designed electrolyte, the CE of Mg plating/stripping is insufficient and well below the state-of-art alkyoxy-borates/aluminates or chloride-based electrolytes. Aiming for high-energy-density MMBs, the

CE is one of most important factors that determines the amounts of Mg metal anode required in the full cell. Therefore, increasing the CE of Mg plating/stripping in these cost-effective Mg electrolyte systems should be the goal in future studies.

The CE of Mg plating/stripping is determined by several reaction during Mg deposition, including the reduction of Mg^{2+} to Mg and the anion or solvent decomposition activity. To achieve high CE, highest possible Mg^{2+}/Mg redox activity and lowest possible anion/solvent decomposition activity is needed. Therefore, two different strategies can be applied when designing high efficient Mg electrolyte: (1) controlling Mg2+ solvation structures that facilitate fast Mg2+ desolvation process and subsequent Mg^{2+}/Mg redox kinetic, which can be tuned by selecting polarized solvents or additives to interrupt the original Mg^{2+} solvation structures; (2) selecting or designing the structure of anions that can easily dissociate with Mg^{2+} cation and are electrochemical stable during Mg^{2+} plating. Theoretically, a synergetic strategy that can simultaneously facilitate fast Mg^{2+}/Mg redox activity and low anion decomposition is expected to achieve high CE of Mg plating/stripping. In addition, designing functional interface at Mg anode surface that only allows Mg^{2+} to travel is a feasible way to suppress the solvent/salt decomposition, thus enhancing high CE.

In order to commercialize AZMBs and MMBs, it is also highly needed and important to rationally design the next generation of high-voltage Zn cathodes and Mg cathodes, which is an even more challenging task for practical divalent metal batteries. As mentioned above, the sluggish Zn^{2+} and Mg^{2+} solid state diffusion in most inorganic intercalative-type cathode hosts plagues their commercialization. Strategies including pre-intercalation of functional ions or molecules in the layered-type cathodes and heteroatom doping can probably reduce the strong interaction between Zn^{2+} and cathode hosts. Conventional method of downsizing the active materials particle could shorten the diffusion length of divalent ions. However, these strategies inevitably increase the cost and complexity of producing active materials, and lower the volumetric energy densities of batteries. New protype divalent-ion cathode materials for are of necessity. For AZMBs, the use of MnO_2/Mn^{2+} redox at cathode side attracts intense academic interests due to its high theoretical capacity (> 600 mAh g^{-1}), high voltage (~2 V vs. Zn^{2+}/Zn) and the low cost of manganese.[183–185] To achieve reversible and stable MnO_2/Mn^{2+}

redox reaction, however, very acidic environment (pH < 1) with dilute aqueous electrolyte is usually needed, which directly causes the chemical dissolution of Zn metal, severe HER and other corrosion issues towards battery casing. Therefore, the new electrolyte that can tackle these issues is also needed in this emerging area. For MMBs, with the discovery of more Mg electrolyte with high oxidative stability, developing high-voltage Mg cathode becomes increasingly urgent, which can be foreseen as an even more difficult challenge due the sluggish Mg^{2+} solid state diffusion in most inorganic oxide cathodes as mentioned above. The feasibility of using these high-voltage oxides for MMBs is still in question. Most of reported high-voltage cathodes only show reversible charge/discharge in electrolytes that are incompatible with Mg anodes, but are not functional in Mg-compatible electrolytes. Future research direction in this area probably should first focus on verifying the Mg^{2+} (de)intercalation in these oxides and understanding its mechanism in the newly designed, Mg compatible and highly efficient electrolytes. Only when these academic problems are tackled can the MMBs technology come into the consideration of commercialization for some certain areas.

References

(1) Armand, M.; Tarascon, J.-M. Building Better Batteries. *Nature* **2008**, *451*, 652–657.

(2) Liu, Z.; Huang, Y.; Huang, Y.; Yang, Q.; Li, X.; Huang, Z.; Zhi, C. Voltage Issue of Aqueous Rechargeable Metal-Ion Batteries. *Chem. Soc. Rev.* **2020**, 49, 180-232.

(3) Verma, V.; Kumar, S.; Manalastas, W.; Satish, R.; Srinivasan, M. Progress in Rechargeable Aqueous Zinc- and Aluminum-Ion Battery Electrodes: Challenges and Outlook. *Adv. Sustain. Syst.* **2018**, 1800111.

(4) Demir-Cakan, R.; Rosa Palacin, M.; Croguennec, L. Rechargeable Aqueous Electrolyte Batteries: From Univalent to Multivalent Cation Chemistry. *J. Mater. Chem. A* **2019**, *7* (36), 20519–20539.

(5) Ellis, B. L.; Lee, K. T.; Nazar, L. F. Positive Electrode Materials for Li-Ion and Li-Batteries. *Chem. Mater.* **2010**, *22* (3), 691–714.

(6) Choi, J. U.; Voronina, N.; Sun, Y.-K.; Myung, S.-T. Recent Progress and Perspective of Advanced High-Energy Co-Less Ni-Rich Cathodes for Li-Ion Batteries: Yesterday, Today, and Tomorrow. *Adv. Energy Mater.* **2020**, *10* (42), 2002027.

(7) Lin, D.; Liu, Y.; Cui, Y. Reviving the Lithium Metal Anode for High-Energy Batteries. *Nat. Nanotechnol.* **2017**, *12* (3), 194–206.

(8) Cheng, X.-B.; Zhang, R.; Zhao, C.-Z.; Zhang, Q. Toward Safe Lithium Metal Anode in Rechargeable Batteries: A Review. *Chem. Rev.* **2017**, *117* (15), 10403–10473.

(9) Tian, Y.; Zeng, G.; Rutt, A.; Shi, T.; Kim, H.; Wang, J.; Koettgen, J.; Sun, Y.; Ouyang, B.; Chen, T.; Lun, Z.; Rong, Z.; Persson, K.; Ceder, G. Promises and Challenges of Next-Generation "Beyond Li-Ion" Batteries for Electric Vehicles and Grid Decarbonization. *Chem. Rev.* **2021**, *121* (3), 1623-1669.

(10) Li, C.; Jin, S.; Archer, L. A.; Nazar, L. F. Toward Practical Aqueous Zinc-Ion Batteries for Electrochemical Energy Storage. *Joule* **2022**, *6*, 1727-1742.

(11) Shoji, T.; Hishinuma, M.; Yamamoto, T. Zinc-Manganese Dioxide Galvanic Cell Using Zinc Sulphate as Electrolyte. Rechargeability of the Cell. *J. Appl. Electrochem.* **1988**, *18* (4), 521–526.

(12) Kundu, D.; Vajargah, S. H.; Wan, L.; Adams, B.; Prendergast, D.; Nazar, L. F. Aqueous vs. Nonaqueous Zn-Ion Batteries: Consequences of the Desolvation Penalty at the Interface. *Energy Environ. Sci.* **2018**, *11* (4), 881–892.

(13) Kundu, D.; Adams, B. D.; Duffort, V.; Vajargah, S. H.; Nazar, L. F. A High-Capacity and Long-Life Aqueous Rechargeable Zinc Battery Using a Metal Oxide Intercalation Cathode. *Nat. Energy* **2016**, *1* (10).

(14) Wan, F.; Zhang, L.; Dai, X.; Wang, X.; Niu, Z.; Chen, J. Aqueous Rechargeable Zinc/Sodium Vanadate Batteries with Enhanced Performance from Simultaneous Insertion of Dual Carriers. *Nat. Commun.* **2018**, *9* (1), 1656.

(15) Wang, F.; Blanc, L. E.; Li, Q.; Faraone, A.; Ji, X.; Chen-Mayer, H. H.; Paul, R. L.; Dura, J. A.; Hu, E.; Xu, K.; Nazar, L. F.; Wang, C. Quantifying and Suppressing Proton Intercalation to Enable High-Voltage Zn-Ion Batteries. *Adv. Energy Mater.* **2021**, *11* (41), 2102016.

(16) Shi, H.-Y.; Song, Y.; Qin, Z.; Li, C.; Guo, D.; Liu, X.-X.; Sun, X. Inhibiting $VOPO_4 \cdot xH_2O$ Decomposition and Dissolution in Rechargeable Aqueous Zinc Batteries to Promote Voltage and Capacity Stabilities. *Angew. Chem. Int. Ed.* **2019**. *58* (45), 16057-16061.

(17) Oberholzer, P.; Tervoort, E.; Bouzid, A.; Pasquarello, A.; Kundu, D. Oxide versus Nonoxide Cathode Materials for Aqueous Zn Batteries: An Insight into the Charge Storage Mechanism and Consequences Thereof. *ACS Appl. Mater. Interfaces* **2019**, *11* (1), 674–682.

(18) Pan, H.; Shao, Y.; Yan, P.; Cheng, Y.; Han, K. S.; Nie, Z.; Wang, C.; Yang, J.; Li, X.; Bhattacharya, P.; Mueller, K. T.; Liu, J. Reversible Aqueous Zinc/Manganese Oxide Energy Storage from Conversion Reactions. *Nat. Energy* **2016**, *1* (5), 16039.

(19) Fang, G.; Zhou, J.; Pan, A.; Liang, S. Recent Advances in Aqueous Zinc-Ion Batteries. *ACS Energy Lett.* **2018**, *3* (10), 2480–2501.

(20) Zheng, S.; Shi, D.; Yan, D.; Wang, Q.; Sun, T.; Ma, T.; Li, L.; He, D.; Tao, Z.; Chen, J. Orthoquinone–Based Covalent Organic Frameworks with Ordered Channel Structures

for Ultrahigh Performance Aqueous Zinc–Organic Batteries. *Angew. Chem. Int. Ed. 61* (12), e202117511.

(21) Wan, F.; Zhang, L.; Wang, X.; Bi, S.; Niu, Z.; Chen, J. An Aqueous Rechargeable Zinc-Organic Battery with Hybrid Mechanism. *Adv. Funct. Mater.* **2018**, *28* (45), 1804975.

(22) Wan, F.; Zhou, X.; Lu, Y.; Niu, Z.; Chen, J. Energy Storage Chemistry in Aqueous Zinc Metal Batteries. *ACS Energy Lett.* **2020**, 3569–3590.

(23) Hao, J.; Li, X.; Zhang, S.; Yang, F.; Zeng, X.; Zhang, S.; Bo, G.; Wang, C.; Guo, Z. Designing Dendrite-Free Zinc Anodes for Advanced Aqueous Zinc Batteries. *Adv. Funct. Mater.* **2020**, 2001263.

(24) Hao, J.; Yuan, L.; Ye, C.; Chao, D.; Davey, K.; Guo, Z.; Qiao, S. Boosting Zn Electrode Reversibility in Aqueous Electrolyte Using Low-Cost Antisolvents. *Angew. Chem. Int. Ed. 60* (13), 7366-7375.

(25) Wang, Z.; Huang, J.; Guo, Z.; Dong, X.; Liu, Y.; Wang, Y.; Xia, Y. A Metal-Organic Framework Host for Highly Reversible Dendrite-Free Zinc Metal Anodes. *Joule* **2019**, *3* (5), 1289-1300.

(26) Zheng, J.; Zhao, Q.; Tang, T.; Yin, J.; Quilty, C. D.; Renderos, G. D.; Liu, X.; Deng, Y.; Wang, L.; Bock, D. C.; Jaye, C.; Zhang, D.; Takeuchi, E. S.; Takeuchi, K. J.; Marschilok, A. C.; Archer, L. A. Reversible Epitaxial Electrodeposition of Metals in Battery Anodes. *Science* **2019**, *366* (6465), 645–648.

(27) Zhang, W.; Zhao, Q.; Hou, Y.; Shen, Z.; Fan, L.; Zhou, S.; Lu, Y.; Archer, L. A. Dynamic Interphase–Mediated Assembly for Deep Cycling Metal Batteries. *Sci. Adv. 7* (49), eabl3752.

(28) Wang, F.; Borodin, O.; Gao, T.; Fan, X.; Sun, W.; Han, F.; Faraone, A.; Dura, J. A.; Xu, K.; Wang, C. Highly Reversible Zinc Metal Anode for Aqueous Batteries. *Nat. Mater.* **2018**, *17* (6), 543.

(29) Cao, L.; Li, D.; Deng, T.; Li, Q.; Wang, C. Hydrophobic Organic-Electrolyte-Protected Zinc Anodes for Aqueous Zinc Batteries. *Angew. Chem. Int. Ed.* **2020**, *59* (43), 19292–19296.

(30) Cao, L.; Li, D.; Pollard, T.; Deng, T.; Zhang, B.; Yang, C.; Chen, L.; Vatamanu, J.; Hu, E.; Hourwitz, M. J.; Ma, L.; Ding, M.; Li, Q.; Hou, S.; Gaskell, K.; Fourkas, J. T.; Yang, X.-Q.; Xu, K.; Borodin, O.; Wang, C. Fluorinated Interphase Enables Reversible Aqueous Zinc Battery Chemistries. *Nat. Nanotechnol.* **2021**, *16*, 902–910.

(31) Han, J.; Euchner, H.; Kuenzel, M.; Hosseini, S. M.; Groß, A.; Varzi, A.; Passerini, S. A Thin and Uniform Fluoride-Based Artificial Interphase for the Zinc Metal Anode Enabling Reversible Zn/MnO_2 Batteries. *ACS Energy Lett.* **2021**, *6* (9), 3063–3071.

(32) Han, D.; Cui, C.; Zhang, K.; Wang, Z.; Gao, J.; Guo, Y.; Zhang, Z.; Wu, S.; Yin, L.; Weng, Z.; Kang, F.; Yang, Q.-H. A Non-Flammable Hydrous Organic Electrolyte for Sustainable Zinc Batteries. *Nat. Sustain.* **2022,** 5, 205-213.

(33) Li, H. Practical Evaluation of Li-Ion Batteries. *Joule* **2019**, *3* (4), 911–914.

(34) Crawford, A. J.; Huang, Q.; Kintner-Meyer, M. C. W.; Zhang, J.-G.; Reed, D. M.; Sprenkle, V. L.; Viswanathan, V. V.; Choi, D. Lifecycle Comparison of Selected Li-Ion Battery Chemistries under Grid and Electric Vehicle Duty Cycle Combinations. *J. Power Sources* **2018**, *380*, 185–193.

(35) Li, C.; Shyamsunder, A.; Hoane, A. G.; Long, D. M.; Kwok, C. Y.; Kotula, P. G.; Zavadil, K. R.; Gewirth, A. A.; Nazar, L. F. Highly Reversible Zn Anode with a Practical Areal Capacity Enabled by a Sustainable Electrolyte and Superacid Interfacial Chemistry. *Joule* **2022**, *6* (5), 1103–1120.

(36) Li, C.; Kingsbury, R.; Zhou, L.; Shyamsunder, A.; Persson, K. A.; Nazar, L. F. Tuning the Solvation Structure in Aqueous Zinc Batteries to Maximize Zn-Ion Intercalation and Optimize Dendrite-Free Zinc Plating. *ACS Energy Lett.* **2022**, *7* (1), 533–540.

(37) Mohtadi, R.; Tutusaus, O.; Arthur, T. S.; Zhao-Karger, Z.; Fichtner, M. The Metamorphosis of Rechargeable Magnesium Batteries. *Joule* **2021**, *5* (3), 581-617.

(38) Liang, Y.; Dong, H.; Aurbach, D.; Yao, Y. Current Status and Future Directions of Multivalent Metal-Ion Batteries. *Nat. Energy* **2020**, *5*, 646-656.

(39) Aurbach, D.; Lu, Z.; Schechter, A.; Gofer, Y.; Gizbar, H.; Turgeman, R.; Cohen, Y.; Moshkovich, M.; Levi, E. Prototype Systems for Rechargeable Magnesium Batteries. *Nature* **2000**, *407* (6805), 724–727.

(40) Novák, P.; Imhof, R.; Haas, O. Magnesium Insertion Electrodes for Rechargeable Nonaqueous Batteries — a Competitive Alternative to Lithium? *Electrochimica Acta* **1999**, *45* (1), 351–367.

(41) Sun, X.; Duffort, V.; Mehdi, B. L.; Browning, N. D.; Nazar, L. F. Investigation of the Mechanism of Mg Insertion in Birnessite in Nonaqueous and Aqueous Rechargeable Mg-Ion Batteries. *Chem. Mater.* **2016**, *28* (2), 534–542.

(42) Amatucci, G. G.; Badway, F.; Singhal, A.; Beaudoin, B.; Skandan, G.; Bowmer, T.; Plitz, I.; Pereira, N.; Chapman, T.; Jaworski, R. Investigation of Yttrium and Polyvalent Ion Intercalation into Nanocrystalline Vanadium Oxide. *J. Electrochem. Soc.* **2001**, *148* (8), A940.

(43) Levi, E.; Lancry, E.; Mitelman, A.; Aurbach, D.; Ceder, G.; Morgan, D.; Isnard, O. Phase Diagram of Mg Insertion into Chevrel Phases, $Mg_xMo_6T_8$ (T = S, Se). 1. Crystal Structure of the Sulfides. *Chem. Mater.* **2006**, *18* (23), 5492–5503.

(44) Sun, X.; Bonnick, P.; Duffort, V.; Liu, M.; Rong, Z.; Persson, K. A.; Ceder, G.; Nazar, L. F. A High Capacity Thiospinel Cathode for Mg Batteries. *Energy Environ. Sci.* **2016**, *9* (7), 2273–2277.

(45) Sun, X.; Bonnick, P.; Nazar, L. F. Layered TiS_2 Positive Electrode for Mg Batteries. *ACS Energy Lett.* **2016**, *1* (1), 297–301. https://doi.org/10.1021/acsenergylett.6b00145.

(46) Liu, M.; Rong, Z.; Malik, R.; Canepa, P.; Jain, A.; Ceder, G.; A. Persson, K. Spinel Compounds as Multivalent Battery Cathodes: A Systematic Evaluation Based on Ab Initio Calculations. *Energy Environ. Sci.* **2015**, *8* (3), 964–974.

(47) Kim, C.; Phillips, P. J.; Key, B.; Yi, T.; Nordlund, D.; Yu, Y.-S.; Bayliss, R. D.; Han, S.-D.; He, M.; Zhang, Z.; Burrell, A. K.; Klie, R. F.; Cabana, J. Direct Observation of Reversible Magnesium Ion Intercalation into a Spinel Oxide Host. *Adv. Mater.* **2015**, *27* (22), 3377–3384.

(48) Liu, M.; Jain, A.; Rong, Z.; Qu, X.; Canepa, P.; Malik, R.; Ceder, G.; Persson, K. A. Evaluation of Sulfur Spinel Compounds for Multivalent Battery Cathode Applications. *Energy Environ. Sci.* **2016**, *9* (10), 3201–3209.

(49) Hu, L.; Jokisaari, J. R.; Kwon, B. J.; Yin, L.; Kim, S.; Park, H.; Lapidus, S. H.; Klie, R. F.; Key, B.; Zapol, P.; Ingram, B. J.; Vaughey, J. T.; Cabana, J. High Capacity for Mg2+ Deintercalation in Spinel Vanadium Oxide Nanocrystals. *ACS Energy Lett.* **2020**, *5* (8), 2721–2727.

(50) Kotobuki, M.; Yan, B.; Lu, L. Recent Progress on Cathode Materials for Rechargeable Magnesium Batteries. *Energy Storage Mater.* **2023**, *54*, 227–253.

(51) Dong, H.; Tutusaus, O.; Liang, Y.; Zhang, Y.; Lebens-Higgins, Z.; Yang, W.; Mohtadi, R.; Yao, Y. High-Power Mg Batteries Enabled by Heterogeneous Enolization Redox Chemistry and Weakly Coordinating Electrolytes. *Nat. Energy* **2020**, *5* (12), 1043–1050.

(52) Gaddum, L. W.; French, H. E. THE ELECTROLYSIS OF GRIGNARD SOLUTIONS1. *J. Am. Chem. Soc.* **1927**, *49* (5), 1295–1299.

(53) Mizrahi, O.; Amir, N.; Pollak, E.; Chusid, O.; Marks, V.; Gottlieb, H.; Larush, L.; Zinigrad, E.; Aurbach, D. Electrolyte Solutions with a Wide Electrochemical Window for Rechargeable Magnesium Batteries. *J. Electrochem. Soc.* **2007**, *155* (2), A103.

(54) Blázquez, J. A.; Maça, R. R.; Leonet, O.; Azaceta, E.; Mukherjee, A.; Zhao-Karger, Z.; Li, Z.; Kovalevsky, A.; Fernández-Barquín, A.; Mainar, A. R.; Jankowski, P.; Rademacher, L.; Dey, S.; Dutton, S. E.; Grey, C. P.; Drews, J.; Häcker, J.; Danner, T.; Latz, A.; Sotta, D.; Palacin, M. R.; Martin, J.-F.; Lastra, J. M. G.; Fichtner, M.; Kundu, S.; Kraytsberg, A.; Ein-Eli, Y.; Noked, M.; Aurbach, D. A Practical Perspective on the Potential of Rechargeable Mg Batteries. *Energy Environ. Sci.* **2023**, *16*, 1964-1981.

(55) Mohtadi, R.; Matsui, M.; Arthur, T. S.; Hwang, S.-J. Magnesium Borohydride: From Hydrogen Storage to Magnesium Battery. *Angew. Chem. Int. Ed.* **2012**, *51* (39), 9780–9783.

(56) Tutusaus, O.; Mohtadi, R.; Arthur, T. S.; Mizuno, F.; Nelson, E. G.; Sevryugina, Y. V. An Efficient Halogen-Free Electrolyte for Use in Rechargeable Magnesium Batteries. *Angew. Chem. Int. Ed.* **2015**, *54* (27), 7900–7904.

(57) Zhao-Karger, Z.; Bardaji, M. E. G.; Fuhr, O.; Fichtner, M. A New Class of Non-Corrosive, Highly Efficient Electrolytes for Rechargeable Magnesium Batteries. *J. Mater. Chem. A* **2017**, *5* (22), 10815–10820.

(58) Luo, J.; Bi, Y.; Zhang, L.; Zhang, X.; Liu, T. L. A Stable, Non-Corrosive Perfluorinated Pinacolatoborate Mg Electrolyte for Rechargeable Mg Batteries. *Angew. Chem.* **2019**, *131* (21), 7041–7045.

(59) Herb, J. T.; Nist-Lund, C. A.; Arnold, C. B. A Fluorinated Alkoxyaluminate Electrolyte for Magnesium-Ion Batteries. *ACS Energy Lett.* **2016**, *1* (6), 1227–1232.

(60) Sun, Y.; Wang, Y.; Jiang, L.; Dong, D.; Wang, W.; Fan, J.; Lu, Y.-C. Non-Nucleophilic Electrolyte with Non-Fluorinated Hybrid Solvents for Long-Life Magnesium Metal Batteries. *Energy Environ. Sci.* **2023**, *16* (1), 265–274.

(61) Nguyen, D.-T.; Eng, A. Y. S.; Ng, M.-F.; Kumar, V.; Sofer, Z.; Handoko, A. D.; Subramanian, G. S.; Seh, Z. W. A High-Performance Magnesium Triflate-Based Electrolyte for Rechargeable Magnesium Batteries. *Cell Rep. Phys. Sci.* **2020**, *1* (12), 100265.

(62) Hou, S.; Ji, X.; Gaskell, K.; Wang, P.; Wang, L.; Xu, J.; Sun, R.; Borodin, O.; Wang, C. Solvation Sheath Reorganization Enables Divalent Metal Batteries with Fast Interfacial Charge Transfer Kinetics. *Science* **2021**, *374* (6564), 172-178.

(63) Wang, S.; Wang, K.; Zhang, Y.; Jie, Y.; Li, X.; Pan, Y.; Gao, X.; Nian, Q.; Cao, R.; Li, Q.; Jiao, S.; Xu, D. High-Entropy Electrolyte Enables High Reversibility and Long Lifespan for Magnesium Metal Anodes. *Angew. Chem. Int. Ed. 62* (31), e202304411.

(64) Zhang, D.; Wang, Y.; Yang, Y.; Zhang, Y.; Zhao, Y.; Pan, M.; Sun, Y.; Chen, S.; Liu, X.; Wang, J.; NuLi, Y. Constructing Efficient $Mg(CF_3SO_3)_2$ Electrolyte via Tailoring Solvation and Interface Chemistry for High-Performance Rechargeable Magnesium Batteries. *Adv. Energy Mater. 13* (39), 2301795.

(65) Du, Y.; Chen, Y.; Tan, S.; Chen, J.; Huang, X.; Cui, L.; Long, J.; Wang, Z.; Yao, X.; Shang, B.; Huang, G.; Zhou, X.; Li, L.; Wang, J.; Pan, F. Strong Solvent Coordination Effect Inducing Gradient Solid-Electrolyte-Interphase Formation for Highly Efficient Mg Plating/Stripping. *Energy Storage Mater.* **2023**, *62*, 102939.

(66) Ma, L.; Schroeder, M. A.; Borodin, O.; Pollard, T. P.; Ding, M. S.; Wang, C.; Xu, K. Realizing High Zinc Reversibility in Rechargeable Batteries. *Nat. Energy* **2020**, 5, 743-749.

(67) Wang, D.; Gao, X.; Chen, Y.; Jin, L.; Kuss, C.; Bruce, P. G. Plating and Stripping Calcium in an Organic Electrolyte. *Nat. Mater.* **2018**, *17* (1), 16–20.

(68) *Crystallography. Scattering and diffraction. The Bragg's Law*. https://www.xtal.iqfr.csic.es/Cristalografia/parte_05_5-en.html (accessed 2023-09-27).

(69) Akhtar, K.; Khan, S. A.; Khan, S. B., Asiri, A. M. Scanning Electron Microscopy: Principle and Applications in Nanomaterials Characterization. In: Sharma, S. (eds) Handbook of Materials Characterization. *Springer*, *Cham*. **2018**, 113-145.

(70) Zeng, X.; Mao, J.; Hao, J.; Liu, J.; Liu, S.; Wang, Z.; Wang, Y.; Zhang, S.; Zheng, T.; Liu, J.; Rao, P.; Guo, Z. Electrolyte Design for In Situ Construction of Highly Zn^{2+}-Conductive Solid Electrolyte Interphase to Enable High-Performance Aqueous Zn-Ion Batteries under Practical Conditions. *Adv. Mater. 33* (11), 2007416.

(71) Cao, L.; Li, D.; Hu, E.; Xu, J.; Deng, T.; Ma, L.; Wang, Y.; Yang, X.-Q.; Wang, C. Solvation Structure Design for Aqueous Zn Metal Batteries. *J. Am. Chem. Soc.* **2020**, *142* (51), 21404-21409.

(72) Li, Q.; Chen, A.; Wang, D.; Pei, Z.; Zhi, C. "Soft Shorts" Hidden in Zinc Metal Anode Research. *Joule* **2022**, *6* (2), 273-279.

(73) Jin, Y.; Han, K. S.; Shao, Y.; Sushko, M. L.; Xiao, J.; Pan, H.; Liu, J. Stabilizing Zinc Anode Reactions by Polyethylene Oxide Polymer in Mild Aqueous Electrolytes. *Adv. Funct. Mater.* **2020**, *30* (43), 2003932.

(74) Huang, C.; Zhao, X.; Liu, S.; Hao, Y.; Tang, Q.; Hu, A.; Liu, Z.; Chen, X. Stabilizing Zinc Anodes by Regulating the Electrical Double Layer with Saccharin Anions. *Adv. Mater. 33* (38), 2100445.

(75) Glatz, H.; Tervoort, E.; Kundu, D. Unveiling Critical Insight into the Zn Metal Anode Cyclability in Mildly Acidic Aqueous Electrolytes: Implications for Aqueous Zinc Batteries. *ACS Appl. Mater. Interfaces* **2020**, *12* (3), 3522–3530.

(76) Huang, J.-F.; Baker, G. A.; Luo, H.; Hong, K.; Li, Q.-F.; Bjerrum, N. J.; Dai, S. Brønsted Acidic Room Temperature Ionic Liquids Derived from N,N-Dimethylformamide and Similar Protophilic Amides. *Green Chem* **2006**, *8* (7), 599–602.

(77) Zhang, L.; Li, H.; Wang, Y.; Hu, X. Characterizing the Structural Properties of N,N-Dimethylformamide-Based Ionic Liquid: Density-Functional Study. *J. Phys. Chem. B* **2007**, *111* (37), 11016–11020.

(78) Cottineau, T.; Richard-Plouet, M.; Mevellec, J.-Y.; Brohan, L. Hydrolysis and Complexation of N,N-Dimethylformamide in New Nanostructurated Titanium Oxide Hybrid Organic–Inorganic Sols and Gel. *J. Phys. Chem. C* **2011**, *115* (25), 12269–12274.

(79) Wang, N.; Dong, X.; Wang, B.; Guo, Z.; Wang, Z.; Wang, R.; Qiu, X.; Wang, Y. Zinc–Organic Battery with a Wide Operation-Temperature Window from −70 to 150 °C. *Angew. Chem.* **2020**, *132* (34), 14685–14691.

(80) Tsierkezos, N. G.; Roithová, J.; Schröder, D.; Molinou, I. E.; Schwarz, H. Solvation of Copper(II) Sulfate in Binary Water/ *N,N* -Dimethylformamide Mixtures: From the Solution to the Gas Phase. *J. Phys. Chem. B* **2008**, *112* (14), 4365–4371.

(81) Jia, R.; Song, X.; Yang, T.; Yang, H.; Liang, D.; Liang, Z. Electrochemical Synthesis of Trimethylamine by Cathodic Reduction of Dimethylformamide Using Cu and Pd Cathodes. *J. Electroanal. Chem.* **2015**, *741*, 32–35.

(82) Ma, L.; Pollard, T. P.; Zhang, Y.; Schroeder, M. A.; Ding, M. S.; Cresce, A. V.; Sun, R.; Baker, D. R.; Helms, B. A.; Maginn, E. J.; Wang, C.; Borodin, O.; Xu, K. Functionalized Phosphonium Cations Enable Zn Metal Reversibility in Aqueous Electrolytes. *Angew. Chem. 60* (22), 12438-12445.

(83) Kotula, P. X-Ray and EELS Imaging. In *Transmission Electron Microscopy: Diffraction, Imaging, and Spectrometry*; Carter, C. B., Williams, D. B., Eds.; Springer International Publishing: Cham, 2016; pp 439–466.

(84) Yang, H.; Qiao, Y.; Chang, Z.; Deng, H.; Zhu, X.; Zhu, R.; Xiong, Z.; He, P.; Zhou, H. Reducing Water Activity by Zeolite Molecular Sieve Membrane for Long-Life Rechargeable Zinc Battery. *Adv. Mater. 33* (38), 2102415.

(85) Pei, A.; Zheng, G.; Shi, F.; Li, Y.; Cui, Y. Nanoscale Nucleation and Growth of Electrodeposited Lithium Metal. *Nano Lett.* **2017**, *17* (2), 1132–1139.

(86) Zhang, Q.; Luan, J.; Fu, L.; Wu, S.; Tang, Y.; Ji, X.; Wang, H. The Three-Dimensional Dendrite-Free Zinc Anode on a Copper Mesh with a Zinc-Oriented Polyacrylamide Electrolyte Additive. *Angew. Chem. Int. Ed.* **2019**, *58* (44), 15841–15847.

(87) Huang, J.; Wang, Z.; Hou, M.; Dong, X.; Liu, Y.; Wang, Y.; Xia, Y. Polyaniline-Intercalated Manganese Dioxide Nanolayers as a High-Performance Cathode Material for an Aqueous Zinc-Ion Battery. *Nat. Commun.* **2018**, *9* (1), 2906.

(88) Park, M. J.; Yaghoobnejad Asl, H.; Manthiram, A. Multivalent-Ion versus Proton Insertion into Battery Electrodes. *ACS Energy Lett.* **2020**, *5* (7), 2367–2375.

(89) Liu, X.; Euchner, H.; Zarrabeitia, M.; Gao, X.; Elia, G. A.; Groß, A.; Passerini, S. Operando pH Measurements Decipher H^+/Zn^{2+} Intercalation Chemistry in High-Performance Aqueous Zn/δ-V_2O_5 Batteries. *ACS Energy Lett.* **2020**, *5* (9), 2979–2986.

(90) Na, M.; Oh, Y.; Byon, H. R. Effects of Zn^{2+} and H^+ Association with Naphthalene Diimide Electrodes for Aqueous Zn-Ion Batteries. *Chem. Mater.* **2020**, *32* (16), 6990-6997.

(91) Sun, W.; Wang, F.; Hou, S.; Yang, C.; Fan, X.; Ma, Z.; Gao, T.; Han, F.; Hu, R.; Zhu, M.; Wang, C. Zn/MnO_2 Battery Chemistry With H^+ and Zn^{2+} Coinsertion. *J. Am. Chem. Soc.* **2017**, *139* (29), 9775–9778.

(92) Zhang, L.; Rodríguez-Pérez, I. A.; Jiang, H.; Zhang, C.; Leonard, D. P.; Guo, Q.; Wang, W.; Han, S.; Wang, L.; Ji, X. $ZnCl_2$ "Water-in-Salt" Electrolyte Transforms the Performance of Vanadium Oxide as a Zn Battery Cathode. *Adv. Funct. Mater.* **2019**, *29* (30), 1902653.

(93) Ko, J. S.; Paul, P. P.; Wan, G.; Seitzman, N.; DeBlock, R. H.; Dunn, B. S.; Toney, M. F.; Nelson Weker, J. NASICON $Na_3V_2(PO_4)_3$ Enables Quasi-Two-Stage Na^+ and Zn^{2+} Intercalation for Multivalent Zinc Batteries. *Chem. Mater.* **2020**, *32* (7), 3028-3035.

(94) Wang, F.; Hu, E.; Sun, W.; Gao, T.; Ji, X.; Fan, X.; Han, F.; Yang, X.-Q.; Xu, K.; Wang, C. A Rechargeable Aqueous Zn^{2+}-Battery with High Power Density and a Long Cycle-Life. *Energy Environ. Sci.* **2018**, *11* (11), 3168–3175.

(95) Park, M. J.; Asl, H. Y.; Therese, S.; Manthiram, A. Structural Impact of Zn-Insertion into Monoclinic V2(PO4)3: Implications for Zn-Ion Batteries. *J. Mater. Chem. A* **2019**, *7* (12), 7159–7167.

(96) Pan, A.; Liu, J.; Zhang, J.-G.; Xu, W.; Cao, G.; Nie, Z.; Arey, B. W.; Liang, S. Nano-Structured $Li_3V_2(PO_4)_3$/Carbon Composite for High-Rate Lithium-Ion Batteries. *Electrochem. Commun.* **2010**, *12* (12), 1674–1677.

(97) Weppner, W.; Huggins, R. A. Determination of the Kinetic Parameters of Mixed-Conducting Electrodes and Application to the System Li_3Sb. *J. Electrochem. Soc.* **1977**, *124* (10), 1569.

(98) Yin, S.-C.; Grondey, H.; Strobel, P.; Anne, M.; Nazar, L. F. Electrochemical Property: Structure Relationships in Monoclinic $Li_{3-y}V_2(PO_4)_3$. *J. Am. Chem. Soc.* **2003**, *125* (34), 10402–10411.

(99) Asl, H. Y.; Sharma, S.; Manthiram, A. The Critical Effect of Water Content in the Electrolyte on the Reversible Electrochemical Performance of Zn–VPO_4F Cells. *J. Mater. Chem. A* **2020**, *8* (17), 8262–8267.

(100) Zhang, C.; Shin, W.; Zhu, L.; Chen, C.; Neuefeind, J. C.; Xu, Y.; Allec, S. I.; Liu, C.; Wei, Z.; Daniyar, A.; Jiang, J.-X.; Fang, C.; Greaney, P. A.; Ji, X. The Electrolyte Comprising More Robust Water and Superhalides Transforms Zn-Metal Anode Reversibly and Dendrite-Free. *Carbon Energy* **2021,** *3* (2), 339-348.

(101) Azri, A.; Giamarchi, P.; Grohens, Y.; Olier, R.; Privat, M. Polyethylene Glycol Aggregates in Water Formed through Hydrophobic Helical Structures. *J. Colloid Interface Sci.* **2012**, *379* (1), 14–19.

(102) Yuan, Y.; Sharpe, R.; He, K.; Li, C.; Saray, M. T.; Liu, T.; Yao, W.; Cheng, M.; Jin, H.; Wang, S.; Amine, K.; Shahbazian-Yassar, R.; Islam, M. S.; Lu, J. Understanding Intercalation Chemistry for Sustainable Aqueous Zinc–Manganese Dioxide Batteries. *Nat. Sustain.* **2022**, *5*, 890-898.

(103) Xie, J.; Liang, Z.; Lu, Y.-C. Molecular Crowding Electrolytes for High-Voltage Aqueous Batteries. *Nat. Mater.* **2020**, *19*, 1006-1011.

(104) Wang, Y.; Wang, T.; Dong, D.; Xie, J.; Guan, Y.; Huang, Y.; Fan, J.; Lu, Y.-C. Enabling High-Energy-Density Aqueous Batteries with Hydrogen Bond-Anchored Electrolytes. *Matter* **2022**, *5* (1), 162–179.

(105) Liu, J.; Yang, C.; Chi, X.; Wen, B.; Wang, W.; Liu, Y. Water/Sulfolane Hybrid Electrolyte Achieves Ultralow-Temperature Operation for High-Voltage Aqueous Lithium-Ion Batteries. *Adv. Funct. Mater. 32* (1), 2106811.

(106) Cheng, X.; Yuan, J.; Hu, J.; Chen, S.; Yan, H.; Yang, W.; Li, W.; Dai, Y. 2.5 V High-Performance Aqueous and Semi-Solid-State Symmetric Supercapacitors Enabled by 3 m Sulfolane-Saturated Aqueous Electrolytes. *Energy Technol.* **2022**, *10* (6), 2200157.

(107) Yang, W.; Du, X.; Zhao, J.; Chen, Z.; Li, J.; Xie, J.; Zhang, Y.; Cui, Z.; Kong, Q.; Zhao, Z.; Wang, C.; Zhang, Q.; Cui, G. Hydrated Eutectic Electrolytes with Ligand-Oriented Solvation Shells for Long-Cycling Zinc-Organic Batteries. *Joule* **2020**, *4* (7), 1557–1574.

(108) Chang, N.; Li, T.; Li, R.; Wang, S.; Yin, Y.; Zhang, H.; Li, X. An Aqueous Hybrid Electrolyte for Low-Temperature Zinc-Based Energy Storage Devices. *Energy Environ. Sci.* **2020**, *13* (10), 3527–3535.

(109) Ma, G.; Miao, L.; Yuan, W.; Qiu, K.; Liu, M.; Nie, X.; Dong, Y.; Zhang, N.; Cheng, F. Non-Flammable, Dilute, and Hydrous Organic Electrolytes for Reversible Zn Batteries. *Chem. Sci.* **2022**, *13* (38), 11320–11329.

(110) Lin, X.; Zhou, G.; Robson, M. J.; Yu, J.; Kwok, S. C. T.; Ciucci, F. Hydrated Deep Eutectic Electrolytes for High-Performance Zn-Ion Batteries Capable of Low-Temperature Operation. *Adv. Funct. Mater. 32* (14), 2109322.

(111) Zhao, X.; Zhang, X.; Dong, N.; Yan, M.; Zhang, F.; Mochizuki, K.; Pan, H. Advanced Buffering Acidic Aqueous Electrolytes for Ultra-Long Life Aqueous Zinc-Ion Batteries. *Small* **2022**, *18* (21), 2200742.

(112) Wang, M.; Ma, J.; Meng, Y.; Sun, J.; Yuan, Y.; Chuai, M.; Chen, N.; Xu, Y.; Zheng, X.; Li, Z.; Chen, W. High-Capacity Zinc Anode with 96% Utilization Rate Enabled by Solvation Structure Design. *Angew. Chem. Int. Ed.* **2023***, 62* (3), e202214966.

(113) Li, M.; Wang, X.; Hu, J.; Zhu, J.; Niu, C.; Zhang, H.; Li, C.; Wu, B.; Han, C.; Mai, L. Comprehensive H_2O Molecules Regulation via Deep Eutectic Solvents for Ultra-Stable Zinc Metal Anode. *Angew. Chem. Int. Ed.* **2023**, *62* (18), e202215552.

(114) Zhang, N.; Cheng, F.; Liu, Y.; Zhao, Q.; Lei, K.; Chen, C.; Liu, X.; Chen, J. Cation-Deficient Spinel $ZnMn_2O_4$ Cathode in $Zn(CF_3SO_3)_2$ Electrolyte for Rechargeable Aqueous Zn-Ion Battery. *J. Am. Chem. Soc.* **2016**, *138* (39), 12894–12901.

(115) Zhang, N.; Cheng, F.; Liu, J.; Wang, L.; Long, X.; Liu, X.; Li, F.; Chen, J. Rechargeable Aqueous Zinc-Manganese Dioxide Batteries with High Energy and Power Densities. *Nat. Commun.* **2017**, *8* (1), 405.

(116) Yuan, D.; Zhao, J.; Ren, H.; Chen, Y.; Chua, R.; Jie, E. T. J.; Cai, Y.; Edison, E.; Manalastas, W.; Wong, M. W.; Srinivasan, M. Anion Texturing Towards Dendrite-Free Zn Anode for Aqueous Rechargeable Batteries. *Angew. Chem. Int. Ed. 60* (13), 7213-7219.

(117) Zhang, Q.; Ma, Y.; Lu, Y.; Zhou, X.; Lin, L.; Li, L.; Yan, Z.; Zhao, Q.; Zhang, K.; Chen, J. Designing Anion-Type Water-Free Zn^{2+} Solvation Structure for Robust Zn Metal Anode. *Angew. Chem. Int. Ed. 60* (43), 23357-23364.

(118) Kirby, B. J.; Jungwirth, P. Charge Scaling Manifesto: A Way of Reconciling the Inherently Macroscopic and Microscopic Natures of Molecular Simulations. *J. Phys. Chem. Lett.* **2019**, *10* (23), 7531–7536.

(119) Leontyev, I.; Stuchebrukhov, A. Accounting for Electronic Polarization in Non-Polarizable Force Fields. *Phys. Chem. Chem. Phys.* **2011**, *13* (7), 2613–2626.

(120) Yoo, H. D.; Jokisaari, J. R.; Yu, Y.-S.; Kwon, B. J.; Hu, L.; Kim, S.; Han, S.-D.; Lopez, M.; Lapidus, S. H.; Nolis, G. M.; Ingram, B. J.; Bolotin, I.; Ahmed, S.; Klie, R. F.; Vaughey, J. T.; Fister, T. T.; Cabana, J. Intercalation of Magnesium into a Layered Vanadium Oxide with High Capacity. *ACS Energy Lett.* **2019**, *4* (7), 1528–1534.

(121) Mukherjee, A.; Ardakani, H. A.; Yi, T.; Cabana, J.; Shahbazian-Yassar, R.; Klie, R. F. Direct Characterization of the Li Intercalation Mechanism into α-V2O5 Nanowires Using in-Situ Transmission Electron Microscopy. *Appl. Phys. Lett.* **2017**, *110* (21), 213903.

(122) Varela, M.; Oxley, M. P.; Luo, W.; Tao, J.; Watanabe, M.; Lupini, A. R.; Pantelides, S. T.; Pennycook, S. J. Atomic-Resolution Imaging of Oxidation States in Manganites. *Phys. Rev. B* **2009**, *79* (8), 085117.

(123) Mishra, R.; Kim, Y.-M.; He, Q.; Huang, X.; Kim, S. K.; Susner, M. A.; Bhattacharya, A.; Fong, D. D.; Pantelides, S. T.; Borisevich, A. Y. Towards Spin-Polarized Two-

Dimensional Electron Gas at a Surface of an Antiferromagnetic Insulating Oxide. *Phys. Rev. B* **2016**, *94* (4), 045123.

(124) Park, J.-H.; Hyun Park, S.; Joung, D.; Kim, C. Sustainable Biopolymeric Hydrogel Interphase for Dendrite-Free Aqueous Zinc-Ion Batteries. *Chem. Eng. J.* **2022**, *433*, 133532.

(125) Liang, G.; Zhu, J.; Yan, B.; Li, Q.; Chen, A.; Chen, Z.; Wang, X.; Xiong, B.; Fan, J.; Xu, J.; Zhi, C. Gradient Fluorinated Alloy to Enable Highly Reversible Zn-Metal Anode Chemistry. *Energy Environ. Sci.* **2022**, 15, 1086-1096.

(126) Ma, L.; Li, Q.; Ying, Y.; Ma, F.; Chen, S.; Li, Y.; Huang, H.; Zhi, C. Toward Practical High-Areal-Capacity Aqueous Zinc-Metal Batteries: Quantifying Hydrogen Evolution and a Solid-Ion Conductor for Stable Zinc Anodes. *Adv. Mater.* **2021**, *33* (12), 2007406.

(127) Wang, W.; Yang, C.; Chi, X.; Liu, J.; Wen, B.; Liu, Y. Ultralow-Water-Activity Electrolyte Endows Vanadium-Based Zinc-Ion Batteries with Durable Lifespan Exceeding 30 000 Cycles. *Energy Storage Mater.* **2022**, *53*, 774–782.

(128) Yang, Y.; Liang, S.; Lu, B.; Zhou, J. Eutectic Electrolyte Based on N-Methylacetamide for Highly Reversible Zinc–Iodine Battery. *Energy Environ. Sci.* **2022**, 15, 1192-1200.

(129) Zhao, W.; Pan, Z.; Zhang, Y.; Liu, Y.; Dou, H.; Shi, Y.; Zuo, Z.; Zhang, B.; Chen, J.; Zhao, X.; Yang, X. Tailoring Coordination in Conventional Ether-Based Electrolytes for Reversible Magnesium Metal Anodes. *Angew. Chem. Int. Ed.* **2022**, *61* (30), e202205187.

(130) Eaves-Rathert, J.; Moyer, K.; Zohair, M.; Pint, C. L. Kinetic- versus Diffusion-Driven Three-Dimensional Growth in Magnesium Metal Battery Anodes. *Joule* **2020**, *4* (6), 1324–1336.

(131) Tang, K.; Du, A.; Dong, S.; Cui, Z.; Liu, X.; Lu, C.; Zhao, J.; Zhou, X.; Cui, G. A Stable Solid Electrolyte Interphase for Magnesium Metal Anode Evolved from a Bulky Anion Lithium Salt. *Adv. Mater.* **2020**, *32* (6), 1904987.

(132) Ding, M. S.; Diemant, T.; Behm, R. J.; Passerini, S.; Giffin, G. A. Dendrite Growth in Mg Metal Cells Containing Mg(TFSI)2/Glyme Electrolytes. *J. Electrochem. Soc.* **2018**, *165* (10), A1983.

(133) Liu, Y.; Zhao, W.; Pan, Z.; Fan, Z.; Zhang, M.; Zhao, X.; Chen, J.; Yang, X. Interfacial Engineering of Magnesiophilic Coordination Layer Stabilizes Mg Metal Anode. *Angew. Chem. Int. Ed.* **2023**, *62* (25), e202302617.

(134) Hahn, N. T.; Kamphaus, E. P.; Chen, Y.; Murugesan, V.; Mueller, K. T.; Cheng, L.; Zavadil, K. R. Magnesium Battery Electrolytes with Improved Oxidative Stability Enabled by Selective Solvation in Fluorinated Solvents. *ACS Appl. Energy Mater.* **2023**, *6* (6), 3264-3277.

(135) Häcker, J.; Rommel, T.; Lange, P.; Zhao-Karger, Z.; Morawietz, T.; Biswas, I.; Wagner, N.; Nojabaee, M.; Friedrich, K. A. Magnesium Anode Protection by an Organic Artificial Solid Electrolyte Interphase for Magnesium-Sulfur Batteries. *ACS Appl. Mater. Interfaces* **2023**, *15* (27), 33013–33027.

(136) Zhao-Karger, Z.; Liu, R.; Dai, W.; Li, Z.; Diemant, T.; Vinayan, B. P.; Bonatto Minella, C.; Yu, X.; Manthiram, A.; Behm, R. J.; Ruben, M.; Fichtner, M. Toward Highly Reversible Magnesium–Sulfur Batteries with Efficient and Practical Mg[B(Hfip)4]2 Electrolyte. *ACS Energy Lett.* **2018**, *3* (8), 2005–2013.

(137) Zhang, J.; Liu, J.; Wang, M.; Zhang, Z.; Zhou, Z.; Chen, X.; Du, A.; Dong, S.; Li, Z.; Li, G.; Cui, G. The Origin of Anode-Electrolyte Interfacial Passivation in Rechargeable Mg-Metal Batteries. *Energy Environ. Sci.* **2023**, *16*, 1111-1124.

(138) Zhang, Y.; Li, J.; Zhao, W.; Dou, H.; Zhao, X.; Liu, Y.; Zhang, B.; Yang, X. Defect-Free Metal–Organic Framework Membrane for Precise Ion/Solvent Separation toward Highly Stable Magnesium Metal Anode. *Adv. Mater.* **2022**, *34* (6), 2108114.

(139) Bae, J.; Park, H.; Guo, X.; Zhang, X.; H. Warner, J.; Yu, G. High-Performance Magnesium Metal Batteries via Switching the Passivation Film into a Solid Electrolyte Interphase. *Energy Environ. Sci.* **2021**, *14*, 4391-4399.

(140) Son, S.-B.; Gao, T.; Harvey, S. P.; Steirer, K. X.; Stokes, A.; Norman, A.; Wang, C.; Cresce, A.; Xu, K.; Ban, C. An Artificial Interphase Enables Reversible Magnesium Chemistry in Carbonate Electrolytes. *Nat. Chem.* **2018**, *10* (5), 532–539.

(141) Li, Y.; Zhou, X.; Hu, J.; Zheng, Y.; Huang, M.; Guo, K.; Li, C. Reversible Mg Metal Anode in Conventional Electrolyte Enabled by Durable Heterogeneous SEI with Low Surface Diffusion Barrier. *Energy Storage Mater.* **2022**, *46*, 1–9.

(142) Zhang, J.; Guan, X.; Lv, R.; Wang, D.; Liu, P.; Luo, J. Rechargeable Mg Metal Batteries Enabled by a Protection Layer Formed in Vivo. *Energy Storage Mater.* **2020**, *26*, 408–413.

(143) Zhao, Y.; Du, A.; Dong, S.; Jiang, F.; Guo, Z.; Ge, X.; Qu, X.; Zhou, X.; Cui, G. A Bismuth-Based Protective Layer for Magnesium Metal Anode in Noncorrosive Electrolytes. *ACS Energy Lett.* **2021**, *6* (7), 2594–2601.

(144) Lv, R.; Guan, X.; Zhang, J.; Xia, Y.; Luo, J. Enabling Mg Metal Anodes Rechargeable in Conventional Electrolytes by Fast Ionic Transport Interphase. *Natl. Sci. Rev.* **2020**, *7* (2), 333–341.

(145) Wang, Y. Measurements and Modeling of Water Adsorption Isotherms of Zeolite Linde-Type A Crystals. *Ind. Eng. Chem. Res.* **2020**, *59* (17), 8304–8314.

(146) Chang, Z.; Qiao, Y.; Yang, H.; Cao, X.; Zhu, X.; He, P.; Zhou, H. Sustainable Lithium-Metal Battery Achieved by a Safe Electrolyte Based on Recyclable and Low-Cost Molecular Sieve. *Angew. Chem. Int. Ed.* **2021**, *60* (28), 15572–15581.

(147) Lu, Z.; Yang, H.; Yang, Q.-H.; He, P.; Zhou, H. Building a Beyond Concentrated Electrolyte for High-Voltage Anode-Free Rechargeable Sodium Batteries. *Angew. Chem. Int. Ed.* **2022**, *61* (20), e202200410.

(148) Lu, Z.; Geng, C.; Yang, H.; He, P.; Wu, S.; Yang, Q.-H.; Zhou, H. Step-by-Step Desolvation Enables High-Rate and Ultra-Stable Sodium Storage in Hard Carbon Anodes. *Proc. Natl. Acad. Sci.* **2022**, *119* (40), e2210203119.

(149) Shyamsunder, A.; Blanc, L. E.; Assoud, A.; Nazar, L. F. Reversible Calcium Plating and Stripping at Room Temperature Using a Borate Salt. *ACS Energy Lett.* **2019**, *4* (9), 2271–2276.

(150) Sun, X.; Lee, H. S.; Yang, X. Q.; McBreen, J. A New Additive for Lithium Battery Electrolytes Based on an Alkyl Borate Compound. *J. Electrochem. Soc.* **2002**, *149* (3), A355.

(151) Mao, M.; Lin, Z.; Tong, Y.; Yue, J.; Zhao, C.; Lu, J.; Zhang, Q.; Gu, L.; Suo, L.; Hu, Y.-S.; Li, H.; Huang, X.; Chen, L. Iodine Vapor Transport-Triggered Preferential Growth of Chevrel Mo_6S_8 Nanosheets for Advanced Multivalent Batteries. *ACS Nano* **2020**, *14* (1), 1102–1110.

(152) Fujii, K.; Sogawa, M.; Yoshimoto, N.; Morita, M. Structural Study on Magnesium Ion Solvation in Diglyme-Based Electrolytes: IR Spectroscopy and DFT Calculations. *J. Phys. Chem. B* **2018**, *122* (37), 8712–8717.

(153) Sa, N.; Kinnibrugh, T. L.; Wang, H.; Sai Gautam, G.; Chapman, K. W.; Vaughey, J. T.; Key, B.; Fister, T. T.; Freeland, J. W.; Proffit, D. L.; Chupas, P. J.; Ceder, G.; Bareno, J. G.; Bloom, I. D.; Burrell, A. K. Structural Evolution of Reversible Mg Insertion into a Bilayer Structure of V2O5·nH2O Xerogel Material. *Chem. Mater.* **2016**, *28* (9), 2962–2969.

(154) Yim, T.; Woo, S.-G.; Lim, S.-H.; Yoo, J.-Y.; Cho, W.; Park, M.-S.; Han, Y.-K.; Kim, Y.-J.; Yu, J. Magnesium Anode Pretreatment Using a Titanium Complex for Magnesium Battery. *ACS Sustain. Chem. Eng.* **2017**, *5* (7), 5733–5739.

(155) See, K. A.; Liu, Y.-M.; Ha, Y.; Barile, C. J.; Gewirth, A. A. Effect of Concentration on the Electrochemistry and Speciation of the Magnesium Aluminum Chloride Complex Electrolyte Solution. *ACS Appl. Mater. Interfaces* **2017**, *9* (41), 35729–35739.

(156) Adams, B. D.; Zheng, J.; Ren, X.; Xu, W.; Zhang, J.-G. Accurate Determination of Coulombic Efficiency for Lithium Metal Anodes and Lithium Metal Batteries. *Adv. Energy Mater.* **2018**, *8* (7), 1702097.

(157) Lad, J. B.; Makkawi, Y. T. Adsorption of Dimethyl Ether (DME) on Zeolite Molecular Sieves. *Chem. Eng. J.* **2014**, *256*, 335–346.

(158) Chi, X.; Li, M.; Di, J.; Bai, P.; Song, L.; Wang, X.; Li, F.; Liang, S.; Xu, J.; Yu, J. A Highly Stable and Flexible Zeolite Electrolyte Solid-State Li–Air Battery. *Nature* **2021**, *592* (7855), 551–557.

(159) Long, J.; Tan, S.; Wang, J.; Xiong, F.; Cui, L.; An, Q.; Mai, L. Revealing the Interfacial Chemistry of Fluoride Alkyl Magnesium Salts in Magnesium Metal Batteries. *Angew. Chem. Int. Ed.* **2023**, *62* (21), e202301934.

(160) Wang, D.; Du, X.; Chen, G.; Song, F.; Du, J.; Zhao, J.; Ma, Y.; Wang, J.; Du, A.; Cui, Z.; Zhou, X.; Cui, G. Cathode Electrolyte Interphase (CEI) Endows Mo_6S_8 with Fast Interfacial Magnesium-Ion Transfer Kinetics. *Angew. Chem. Int. Ed.* **2023**, *62* (14), e202217709.

(161) Tang, J.; Xu, F. Polyaniline Cathode for Dual-Ion Rechargeable Mg Batteries. *Mater. Lett.* **2022**, *320*, 132365.

(162) Goswami, S.; Nandy, S.; Fortunato, E.; Martins, R. Polyaniline and Its Composites Engineering: A Class of Multifunctional Smart Energy Materials. *J. Solid State Chem.* **2023**, *317*, 123679.

(163) Blanc, L.; Bartel, C. J.; Kim, H.; Tian, Y.; Kim, H.; Miura, A.; Ceder, G.; Nazar, L. F. Toward the Development of a High-Voltage Mg Cathode Using a Chromium Sulfide Host. *ACS Mater. Lett.* **2021**, *3* (8), 1213–1220.

(164) Meng, Y. S.; Srinivasan, V.; Xu, K. Designing Better Electrolytes. *Science* **2022**, *378* (6624), eabq3750.

(165) Zhang, H.; Qiao, L.; Armand, M. Organic Electrolyte Design for Rechargeable Batteries: From Lithium to Magnesium. *Angew. Chem. Int. Ed.* 2022, *61* (52), e202214054.

(166) Dong, H.; Liang, Y.; Tutusaus, O.; Mohtadi, R.; Zhang, Y.; Hao, F.; Yao, Y. Directing Mg-Storage Chemistry in Organic Polymers toward High-Energy Mg Batteries. *Joule* **2018**, *3* (3), 782-793.

(167) Yoo, H. D.; Liang, Y.; Dong, H.; Lin, J.; Wang, H.; Liu, Y.; Ma, L.; Wu, T.; Li, Y.; Ru, Q.; Jing, Y.; An, Q.; Zhou, W.; Guo, J.; Lu, J.; Pantelides, S. T.; Qian, X.; Yao, Y. Fast Kinetics of Magnesium Monochloride Cations in Interlayer-Expanded Titanium Disulfide for Magnesium Rechargeable Batteries. *Nat. Commun.* **2017**, *8* (1), 339.

(168) Mandai, T. Critical Issues of Fluorinated Alkoxyborate-Based Electrolytes in Magnesium Battery Applications. *ACS Appl. Mater. Interfaces* **2020**, *12* (35), 39135–39144.

(169) Ren, W.; Wu, D.; NuLi, Y.; Zhang, D.; Yang, Y.; Wang, Y.; Yang, J.; Wang, J. An Efficient Bulky $Mg[B(Otfe)_4]_2$ Electrolyte and Its Derivatively General Design Strategy for Rechargeable Magnesium Batteries. *ACS Energy Lett.* **2021**, *6* (9), 3212–3220.

(170) Ha, S.-Y.; Lee, Y.-W.; Woo, S. W.; Koo, B.; Kim, J.-S.; Cho, J.; Lee, K. T.; Choi, N.-S. Magnesium(II) Bis(Trifluoromethane Sulfonyl) Imide-Based Electrolytes with Wide Electrochemical Windows for Rechargeable Magnesium Batteries. *ACS Appl. Mater. Interfaces* **2014**, *6* (6), 4063–4073.

(171) Salama, M.; Shterenberg, I.; Gizbar, H.; Eliaz, N. N.; Kosa, M.; Keinan-Adamsky, K.; Afri, M.; Shimon, L. J. W.; Gottlieb, H. E.; Major, D. T.; Gofer, Y.; Aurbach, D. Unique Behavior of Dimethoxyethane (DME)/Mg($N(SO_2CF_3)_2$)$_2$ Solutions. *J. Phys. Chem. C* **2016**, *120* (35), 19586–19594.

(172) Rajput, N. N.; Qu, X.; Sa, N.; Burrell, A. K.; Persson, K. A. The Coupling between Stability and Ion Pair Formation in Magnesium Electrolytes from First-Principles Quantum Mechanics and Classical Molecular Dynamics. *J. Am. Chem. Soc.* **2015**, *137* (9), 3411–3420.

(173) Baskin, A.; Prendergast, D. Exploration of the Detailed Conditions for Reductive Stability of $Mg(TFSI)_2$ in Diglyme: Implications for Multivalent Electrolytes. *J. Phys. Chem. C* **2016**, *120* (7), 3583–3594.

(174) Yang, Y.; Wang, J.; Du, X.; Jiang, H.; Du, A.; Ge, X.; Li, N.; Wang, H.; Zhang, Y.; Chen, Z.; Zhao, J.; Cui, G. Cation Co-Intercalation with Anions: The Origin of Low Capacities of Graphite Cathodes in Multivalent Electrolytes. *J. Am. Chem. Soc.* **2023**, *145* (22), 12093-12104.

(175) Fan, S.; Cora, S.; Sa, N. Evolution of the Dynamic Solid Electrolyte Interphase in Mg Electrolytes for Rechargeable Mg-Ion Batteries. *ACS Appl. Mater. Interfaces* **2022**, *14* (41), 46635-46645.

(176) Boyle, D. T.; Kim, S. C.; Oyakhire, S. T.; Vilá, R. A.; Huang, Z.; Sayavong, P.; Qin, J.; Bao, Z.; Cui, Y. Correlating Kinetics to Cyclability Reveals Thermodynamic Origin of Lithium Anode Morphology in Liquid Electrolytes. *J. Am. Chem. Soc.* **2022**, *144* (45), 20717–20725.

(177) Wu, Y.; Wang, A.; Hu, Q.; Liang, H.; Xu, H.; Wang, L.; He, X. Significance of Antisolvents on Solvation Structures Enhancing Interfacial Chemistry in Localized High-Concentration Electrolytes. *ACS Cent. Sci.* **2022**, *8* (9), 1290–1298.

(178) Holoubek, J.; Liu, H.; Wu, Z.; Yin, Y.; Xing, X.; Cai, G.; Yu, S.; Zhou, H.; Pascal, T. A.; Chen, Z.; Liu, P. Tailoring Electrolyte Solvation for Li Metal Batteries Cycled at Ultra-Low Temperature. *Nat. Energy* **2021**, *6* (3), 303–313.

(179) Nan, B.; Chen, L.; Rodrigo, N. D.; Borodin, O.; Piao, N.; Xia, J.; Pollard, T.; Hou, S.; Zhang, J.; Ji, X.; Xu, J.; Zhang, X.; Ma, L.; He, X.; Liu, S.; Wan, H.; Hu, E.; Zhang, W.; Xu, K.; Yang, X.-Q.; Lucht, B.; Wang, C. Enhancing Li+ Transport in NMC811||Graphite Lithium-Ion Batteries at Low Temperatures by Using Low-Polarity-Solvent Electrolytes. *Angew. Chem. Int. Ed.* **2022**, *61* (35), e202205967.

(180) Chen, Y.; Atwi, R.; Han, K. S.; Ryu, J.; Washton, N. M.; Hu, J. Z.; Rajput, N. N.; Mueller, K. T.; Murugesan, V. Role of a Multivalent Ion–Solvent Interaction on Restricted Mg2+ Diffusion in Dimethoxyethane Electrolytes. *J. Phys. Chem. B* **2021**, *125* (45), 12574–12583.

(181) Fang, C.; Lu, B.; Pawar, G.; Zhang, M.; Cheng, D.; Chen, S.; Ceja, M.; Doux, J.-M.; Musrock, H.; Cai, M.; Liaw, B.; Meng, Y. S. Pressure-Tailored Lithium Deposition and Dissolution in Lithium Metal Batteries. *Nat. Energy* **2021**, *6* (10), 987–994.

(182) Chen, Y.; Yu, Z.; Rudnicki, P.; Gong, H.; Huang, Z.; Kim, S. C.; Lai, J.-C.; Kong, X.; Qin, J.; Cui, Y.; Bao, Z. Steric Effect Tuned Ion Solvation Enabling Stable Cycling of High-Voltage Lithium Metal Battery. *J. Am. Chem. Soc.* **2021**, *143* (44), 18703-18713.

(183) Wang, M.; Meng, Y.; Xu, Y.; Chen, N.; Chuai, M.; Yuan, Y.; Liu, Z.; Sun, J.; Zheng, X.; Zhang, Z.; Li, D.; Chen, W. Aqueous All-Manganese Batteries. *Energy Environ. Sci.* **2023**, *16*, 5284-5293.

(184) Chao, D.; Zhou, W.; Ye, C.; Zhang, Q.; Chen, Y.; Gu, L.; Davey, K.; Qiao, S.-Z. An Electrolytic Zn-MnO_2 Battery for High-Voltage and Scalable Energy Storage. *Angew. Chem. Int. Ed.* **2019**, *58* (23), 7823–7828.

(185) Zhong, C.; Liu, B.; Ding, J.; Liu, X.; Zhong, Y.; Li, Y.; Sun, C.; Han, X.; Deng, Y.; Zhao, N.; Hu, W. Decoupling Electrolytes towards Stable and High-Energy Rechargeable Aqueous Zinc–Manganese Dioxide Batteries. *Nat. Energy* **2020**, *5*, 440-449.